Chapter 1. Introduction

1.1. Background on Induction Motors

An electric motor is a machine that converts electrical energy into kinetic energy. Electric motors are widely used in many areas from household equipment such as air conditioning fans to industrial applications such as in manufacturing processes. For example, electric motors in the United States consume 59% of all generated electricity in the country with 78% of the electrical energy used in industrial systems, 43% used in commercial buildings, and 37% used in residential houses [1]. In addition, three phase induction motors consume typically 40% to 50% of all generated electrical energy in a country [2]. Therefore induction motors are one of the most significant items of machinery in industrialised nations.

Induction motors are reliable and require minimum maintenance. However duty cycle, installation, manufacturing factors, and environmental influences can deteriorate and reduce the efficiency of the motors [3-5]. In extreme cases, motors may have unexpected downtime which can significantly increase the running cost or even be catastrophic in mission critical applications. In other cases, the efficiency of the motors may have been reduced due to the presence of various motor faults but the motors may still operate. This kind of failure may have a significant cost if not handled promptly and properly. For example an induction machine, which its efficiency reduced from 80% to 70%, would produce an additional electricity cost of about 14% per year. These factors give rise to the need for maintenance approaches.

In industry, there are three basic maintenance approaches: corrective maintenance, time based maintenance, and condition based maintenance [6, 7]. Corrective maintenance only fixes the problems when they occur. The advantages of the corrective maintenance approach are that it has the lowest maintenance cost and the machine is utilised for its full life span. However, the disadvantage of the corrective maintenance approach is that the machine can fail at any time, so unexpected downtime cannot be avoided.

The second maintenance approach, time based maintenance, inspects the condition of a machine at a pre-defined time interval. The choice of the time interval is a trade-off between the cost of maintenance and the cost of an unexpected failure. The advantage of the time based maintenance approach is that it can reduce the rate of unexpected downtime in comparison to the corrective maintenance approach. However, the time based maintenance approach also increases the maintenance cost.

The third maintenance approach, condition based maintenance, inspects a machine only when it is known to be operating at a non-optimal condition. This approach has a variable time interval instead of fixed (time based maintenance). The time interval in this approach is determined based on the knowledge of the presence or absence of faults in the machine and the knowledge of the severity of the faults. As a result, the condition based maintenance has the potential to eliminate unexpected downtime and utilise the machine for its full life span with a maintenance cost that is less than the maintenance cost of the time based maintenance approach. The condition based maintenance approach combines the benefits of the other two approaches while minimising their drawbacks.

The key requirement of condition based maintenance is a condition monitoring system that can diagnose the condition of a motor in order to determine the types of faults as well as the severity of the faults. However, the present motor fault diagnosis techniques are not able to reliably detect the existence of various faults and their severity. Hence the novel aim of this research project is to investigate and develop fault diagnosis techniques using multiple sensor inputs that can improve the reliability of detecting the presence or absence of different types of faults in a motor and the severity of the faults while the motor is operating (on-line).

1.2. On-line Condition Monitoring

On-line condition monitoring is the process of inspecting and monitoring the condition of a machine while it is under a normal operating condition. As such, an on-line condition monitoring and fault diagnosis system should not be intrusive nor should it disrupt the normal operation of the machine. An online condition monitoring system should be able to detect any changes to the sensor signals, which indicate the presence and the severity of machine faults, and predict the need for maintenance before major breakdowns occur. As mentioned previously, an accurate online condition monitoring system is an integral part of successful condition based maintenance.

Common components of an on-line condition monitoring system are sensors, data acquisition, fault detection, fault classification, and fault diagnosis [8]. The sensors are used to capture meaningful signal data regarding the physical characteristics of the machine. These sensors can include voltage sensors, current sensors, flux sensors, vibration sensors, speed sensors, temperature sensors, etc.

The data acquisition system is used to amplify, condition, and sample the signal data captured by the sensors. Such system determines the amount of amplification, the cut-off frequency, the sampling rate, and the sampling time required for the fault detection system.

The fault detection system is used to process the signal data from the data acquisition system in order to extract features from the signal data that are sensitive to the machine faults. The fault detection system can be divided into two different types, which are based on model-reference and experimentation of the signal data. The model-reference methods usually derive fault features based on either first principles underlying the operation of the machine or a mathematical simulation of the machine such as finite element analysis [9]. On the other hand, methods using experimental signal data usually obtain fault features by applying various signal processing techniques, such as the Fourier transform (FT) and wavelet transform, to the signal data of machines, and finding parameters in the processed signal that can distinguish between the healthy and the faulty machines.

The fault classification system is used to process the fault features obtained from the fault detection system in order to determine whether a machine is faulty or not and to estimate the severity of the faults if the machine is found to be faulty. The fault classification system can be approached in two ways, one based on a prediction model and the other on threshold or trending. The prediction model approaches are usually based on artificial intelligence techniques, such as an artificial neural network and fuzzy logic [10-14]. These approaches usually involve training the prediction model by using fault features with known output conditions so that the prediction model can eventually predict the condition of the machine. However, this method usually requires a lot of learning data for the model to be accurate enough in practice. On the other hand, setting a threshold for a fault feature or trending of a fault feature do not require a lot of learning data, but the characteristics of the fault feature need to be known.

The fault diagnosis system is used to notify the operator when a fault has been detected, based on the analysis of the fault classification system. The fault diagnosis system needs to be able to classify the type of faults, such as broken bars, eccentricity, and shorted turn, and report the severity of the fault. Finally, the system should also be able to suggest solutions to the problems based on the severity of the fault. For example, if a particular fault is found to be very severe, the system may suggest to undertake maintenance immediately, but if the fault severity is minimal, the system may suggest that maintenance be delayed a while longer.

1.3. Literature Review of Motor's Faults

Faults in induction motors can be divided into 4 main categories; broken rotor bar faults, eccentricity faults, stator related faults, and bearing faults. The likelihood of each fault, based on the induction motor fault surveys in [15-17], is shown in Figure 1.1. An on-line condition monitoring system needs to be able to detect these incipient faults.

Common fault detection methods are generally based on the Fourier transform. The Fourier transform method relies on the principle that an induction motor is highly symmetrical and the presence of any kind of fault in the motor will disturb its symmetry. This distortion in symmetry will introduce characteristic fault frequencies in the spectra of various sensor signals [18-20]. As a result, it is possible to detect the motor faults by monitoring the amplitude of these characteristic fault frequencies, where the amplitude usually increases as the severity of the fault increases. However, these fault frequency components also exist in healthy motors and their amplitudes can vary between different healthy motors and as a function of load. As a consequence, it can be difficult to distinguish between healthy and faulty motors, not to mention distinguishing the different severities of the motor faults.

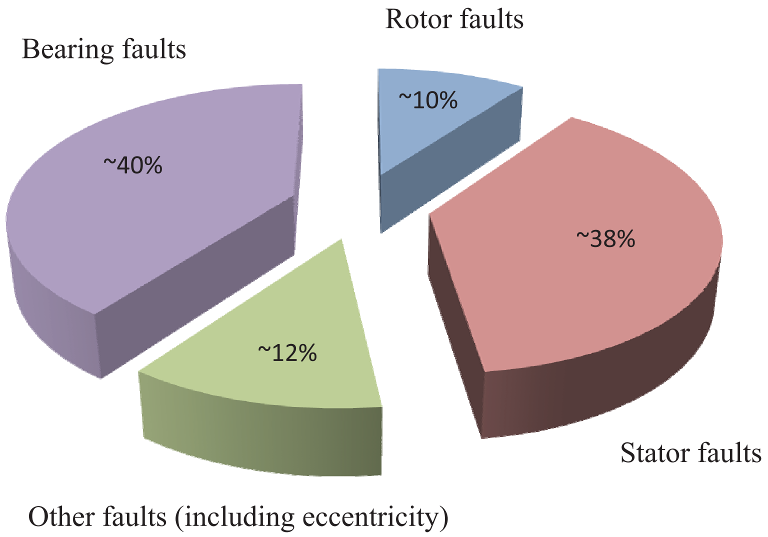

Figure 1.1 - Type of faults in induction motors.

1.3.1. Broken Rotor Bar Faults

Broken rotor bar faults can be caused by frequent direct on-line starting, pulsating mechanical loads, manufacturing defects, and thermal and mechanical stresses from high duty cycle operation [4, 6, 15, 21]. Broken rotor bar faults only account for about 10% of the total induction motor failures. However, the presence of a broken bar will also overheat the adjacent bars due to the change in the rotor current distribution and cause the broken bar fault to worsen. In a severe case, the broken pieces of the rotor bar may damage the stator windings or laminations during operation. In addition, the presence of broken rotor bar faults reduces the efficiency of the motor, which means an increase in the operational cost.

The broken rotor bar fault is one of the easiest induction motor faults to detect using the steady-state condition monitoring and has thus been widely studied in the literature. The presence of broken rotor bar faults in a motor produces characteristic fault frequencies (Eq. 1.1) in the stator current and axial leakage flux [3, 18, 22-24].

$$f_{brb} = f(1 \pm 2s) \qquad \text{(Eq. 1.1)}$$

where f_{brb} represents the broken rotor bar sideband frequencies, f is the supply frequency, and s is the per unit slip.

1.3.2. Eccentricity Faults

There are two types of eccentricity faults associated with induction motors: static eccentricity and dynamic eccentricity [4, 15, 25, 26]. Static eccentricity is where the air gap difference between the stator and the rotor varies but the position of the minimum air gap is fixed. Static eccentricity can be caused by manufacturing defects of the stator core (i.e. oval shape) and installation issues, where the rotor may not be fitted exactly in the centre of the stator. Dynamic eccentricity is where the air gap difference between the stator and rotor varies but the position of the minimum air gap rotates with the rotor. Dynamic eccentricity can be caused by manufacturing defects of the rotor, where the rotor diameter is not concentric with the centre of the shaft, and bearing issues, where there could be radial movement in the bearing due to wear or manufacturing defects.

Eccentricity faults only account for a small percentage of the total number of induction motor failures. However, eccentricity faults can potentially introduce other faults and become catastrophic. For example, the presence of eccentricity faults puts more stress on the bearings which can introduce bearing faults or reduce the bearing's life; and in extreme cases, the rotor can collide with the stator causing winding failure (i.e. shorted turn faults), thus damaging the laminations. In addition, eccentricity faults reduce the efficiency of the motor, which in turn increase the total operational cost.

Eccentricity faults are commonly detected using steady-state condition monitoring techniques. The presence of eccentricity faults produces characteristic fault frequencies in the stator current (Eq. 1.2) - (Eq. 1.3), axial leakage flux (Eq. 1.2) - (Eq. 1.3), and motor vibrations (Eq. 1.4) [3, 22, 24, 27-30].

$$f_{sede1} = f\left[(kR \pm n_d)\frac{(1-s)}{p} \pm v\right] \qquad \text{(Eq. 1.2)}$$

$$f_{sede2} = f \pm f_r \qquad \text{(Eq. 1.3)}$$

$$f_{de1} = f_r \qquad \text{(Eq. 1.4)}$$

where f_{sede1} is the eccentricity (static/dynamic) fault frequency 1, f_{sede2} is the eccentricity (static/dynamic) fault frequency 2, f_{de1} is the dynamic eccentricity fault frequency 1, k is any integer, R is the number of rotor bars, $n_d = 0$ (static eccentricity) and $n_d = 1, 2, 3\ldots$ (dynamic eccentricity), p is the number of pole pairs, v is the order of the stator time harmonics, and f_r is the frequency corresponding to the rotor mechanical speed.

1.3.3. Stator Related Faults

Stator related faults, also known as shorted turn faults, occur when the stator windings are shorted due to insulation failure. Shorted turn faults can be caused by collision between the stator and the rotor, voltage stress imposed by the fast switching of inverters, and insulation issues due to manufacturing defects, contamination, overheating, and wear [31-35]. There are 3 types of shorted turn faults, which are turn to turn fault, phase to phase turn fault, and phase to ground turn fault. A turn to turn fault occurs when the insulation between two coils in the same phase fails. A phase to phase turn fault occurs when the insulation between two coils in adjacent phases fails. A phase to ground turn fault occurs when the terminal of one of the stator windings is short circuited to ground. This causes two effects: firstly, the short-circuited winding will have significant currents induced in it from the other windings, and secondly the supply current will increase dramatically causing the circuit breaker to open. However, when a turn to turn fault or a phase to phase turn fault occurs, the motor may appear to be operating normally but at reduced efficiency. Therefore, these two types of shorted turn faults are where on-line fault detection needs to concentrate.

Stator related faults account for the second largest number of faults, about 38%, in induction motors. They are commonly detected using the steady-state condition monitoring techniques. The presence of stator faults produces characteristic fault frequency components in the stator current (Eq. 1.5), axial leakage flux (Eq. 1.5), and motor vibration (Eq. 1.6) [22, 36, 37].

$$f_{st1} = f\left[k\frac{(1-s)}{p} \pm v\right] \qquad \text{(Eq. 1.5)}$$

$$f_{st2} = 2f \qquad \text{(Eq. 1.6)}$$

where f_{st1} is the shorted turn fault frequency 1 and f_{st2} is the shorted turn fault frequency 2.

1.3.4. Bearing Faults

Bearing faults are the most common cause of faults in induction motors, which is about 40% of the total induction motor failures. They can be categorised into 3 different types, which are inner race fault, outer race fault, and rolling element fault [27, 38]. Other bearing related faults, such as brinelling, usually shift the position of the rotor. Therefore this kind of bearing related fault usually manifests itself as an eccentricity fault in the machine. Bearing faults are usually caused by manufacturing defects, installation errors, lack of lubrication, or wear.

A comprehensive analysis procedure for detecting bearing faults through the stator current, axial leakage flux, and motor vibration is demonstrated in [3, 27, 38]. Bearing faults are commonly detected by analysing the magnitude of the bearing fault frequency components during steady-state operation, where the component magnitudes tend to increase as the fault severity increases. However, bearing faults are not within the scope of this study and will not be investigated, mainly because of the time constraint of the research project.

1.4. Objectives of the Thesis

In order to perform accurate and reliable analysis on induction motors, the installation of the motors and the measurement of their sensor signals need to be reliable. Therefore, the **first aim** of this thesis is to design an experimental procedure and an experimental setup that can accurately repeat the measurements of sensor signals and can introduce a particular fault to the motor in isolation of other faults.

The most common fault detection technique in induction motors is based on the Fourier transform (FT). Fault detection based on the FT has the advantages that it is not computationally expensive and it is relatively simple to implement. Therefore fault detection based on the FT is suitable for an automated on-line condition monitoring system. The FT based techniques usually analyse and compare the magnitude of the fault frequency components, where the magnitude tends to increase as the severity of the fault increases. However, the fault frequency components also exist in healthy motors and their magnitudes may vary between different motors and between repeated measurements. Therefore, the **second aim** of this thesis is to utilise the FT technique in order to perform a baseline study of induction motors.

Furthermore, each type of motor faults may affect more than one fault frequency component (or feature) and presently there is no clear comparison as to which feature is the better choice for identifying a particular fault. Hence, the **third aim** of this thesis is to investigate and compare the performance of various fault frequency components in detecting a particular stator fault (i.e. eccentricity faults or shorted turn faults) under different loading conditions.

The previous research work described in *Section 1.3* only looks at features for detecting a particular fault from one or two sensor types, and there is no clear comparison of how each sensor type performs in detecting a particular fault. Therefore, the **fourth aim** of this thesis is to investigate and compare the performance of features from multiple sensor types in detecting a particular rotor or stator fault under different loading conditions. This thesis will attempt to identify which sensor type is the best choice for identifying a particular fault.

Similarly, the previous research work investigates the detection of a particular fault in isolation of other faults. Hence, the **fifth aim** of this thesis is to investigate how the presence of other common faults, such as supply imbalance and misalignment, affects the detection of a particular rotor or stator fault under different loading conditions.

Rotor fault detection based on the common FT technique has its limitations. For example, the reliability of detecting a rotor fault using the common FT technique depends on the loading conditions and the severity of the fault [4, 22, 28, 39]. If the loading condition is too low or the fault is not too severe, the FT technique may fail to identify the rotor fault. Therefore, the **final aim** of this thesis is to investigate new fault features using different techniques, such as the wavelet transform (WT), to find better features for detecting rotor faults under different loading conditions. This thesis will explore rotor fault detection techniques when the motor is in transient operation (i.e. starting and rundown).

In general, the scope of this thesis covers five main topics, which include investigations on the three main rotor and stator faults (eccentricity faults, shorted turn faults, and broken rotor bar faults) under different fault severities, loading conditions, and motor operating conditions (see Table 1.1). The investigations on the eccentricity faults and shorted turn faults will be performed under steady-state motor operation (Figure 1.2) by utilising the Fourier transform technique on the sensor signals from the stator current, the axial leakage flux, and the motor vibration. The investigations on the broken rotor bar faults will be performed under motor transient operation, such as starting (Figure 1.3) and rundown (Figure 1.4), by utilising the wavelet transform technique and Fourier transform technique on the signal data from the stator current and the flux linkage.

Table 1.1 – Scope of the thesis.

Topic	**Motor Operation**	**Signal Processing**	**Sensors**	**Features**
Rotor Speed and Rotor Slot Number Estimation	Steady-state	FT	Current Leakage flux Vibration	Frequency components
Baseline Study of Induction Motors	Steady-state	FT	Current Leakage flux Vibration	Frequency components
Eccentricity Faults	Steady-state	FT	Current Leakage flux Vibration	Frequency components
Shorted Turn Faults	Steady-state	FT	Current	Frequency components Extended Park's vector
			Leakage flux Vibration	Frequency components
Broken Rotor Bar Faults	Starting	WT	Current	Starting current envelope
	Rundown	WT	Current	Change in speed (torque)
		FT	Current	Harmonic content
			Flux linkage	Drop in magnitude Time constant Harmonic content

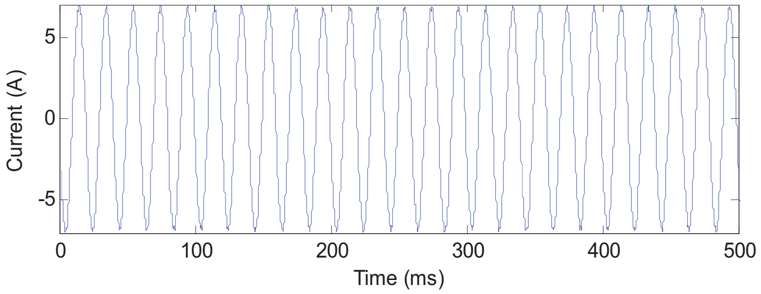

Faults: eccentricity and shorted turn faults.

Signal Processing: FT

Figure 1.2 – Example of a steady-state current waveform.

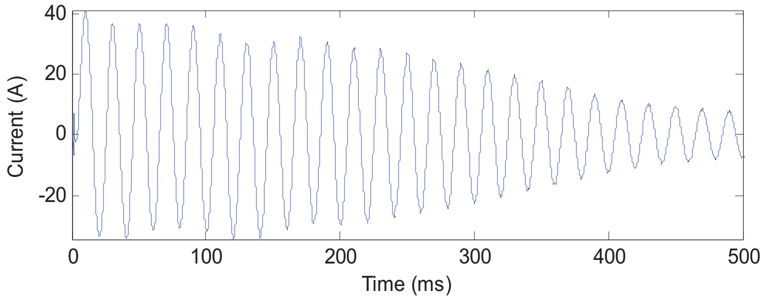

Faults: broken rotor bar faults.

Signal Processing: WT

Figure 1.3 – Example of a starting current waveform.

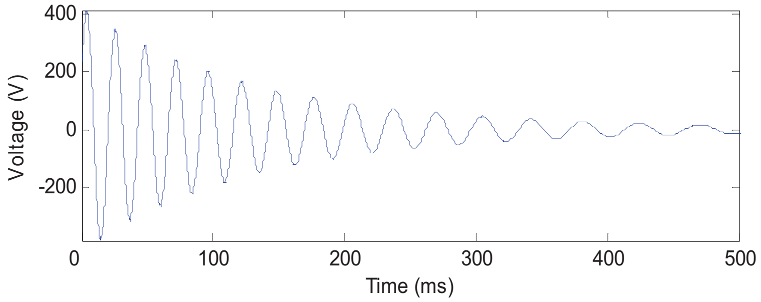

Faults: broken rotor bar faults.

Signal Processing: WT and FT

Figure 1.4 – Example of a rundown induced voltage waveform.

1.5. Features of the Experimental Setup Used in the Thesis

The tests described in this thesis were conducted on 6 new identical induction motors with the specification shown in Table 1.2. This motor specification was chosen because it was desired to have motors that could be practically installed in the lab with a rating as close as possible to the ratings that are commonly used in the industry. The motor test set-up was designed and built on a firm and rigid foundation in order to eliminate problems due to unwanted soft foot and vibration. Precise mounting of the motor was carried using a torque spanner (Norbar, 35 Nm) and accurate shaft alignment between the rotor and the DC load was ensured by using a precision laser alignment tool (Optalign Plus from Prűftechnik).

Table 1.2 – Motor specification.

No. of phases	3-phase distributed winding
Rated power	2.2 kW
Rated voltage	415 V
Rated frequency	50 Hz
Rated Current	4.9 A
Rated speed	1415 RPM
No. of poles	4
No. of rotor bars	32
No. of stator slots	36
Stator winding details	1 layer winding with no paths in parallel
No. of coils per phase	6 (concentric)
No. of turns/phase	282
No. of turns/slot	47
AWG	21 (0.7239 mm in diameter, bare copper)
Packing factor	22%
Slot area	87 mm^2
Stator winding connection type	Wye

Each of the six identical motors was numbered and every movable component in each motor was also numbered so that if a modification (i.e. introducing artificial faults) to the motor were required, it could be disassembled and re-assembled without the components getting mixed between the identical motors. Furthermore, the orientation of every movable component was also marked so that precise re-assembling of the motor could be done. This process was undertaken in order to ensure that the data of the healthy motor is comparable to the data obtained when faults are introduced to the same motor.

A separately-excited DC machine with a resistive load was used to load the test machines. This produced a load torque which varied approximately linearly with the motor speed. For example, when the machine was disconnected from the supply at full load, the load torque also decayed at a rate proportional to the motor speed. The % of rated slip was calculated using the slip of the machine during steady-state operation, which was also used to indicate the level of loading as shown in the results of this thesis. The motor test setup is shown in Figure 1.5.

Two voltage sensors, two current sensors, an axial leakage flux search coil and three vibration sensors were attached to the test motors. The position of the search coil was located around the motor housing near the non-drive end for easier access. The consistency of the orientation of the search coil was also ensured. The three vibration sensors were screw mounted to the motors through drilled taps on the motor's housing. All sensors were particularly chosen because they are non-invasive and could be easily installed. The specifications for the sensors are listed in Table 1.3.

The following variables were measured:

- Two line voltage signals (the third line voltage was calculated).
- Two phase stator current signals (the third phase was calculated assuming a three-wire connection).
- Three vibration signals, which were captured at 3 different positions: driving end horizontal (DEH) position, driving end vertical (DEV) position, and non-driving end horizontal (NDEH) position.
- One axial leakage flux signal, which is the magnetic flux that radiates out of the motor frame.

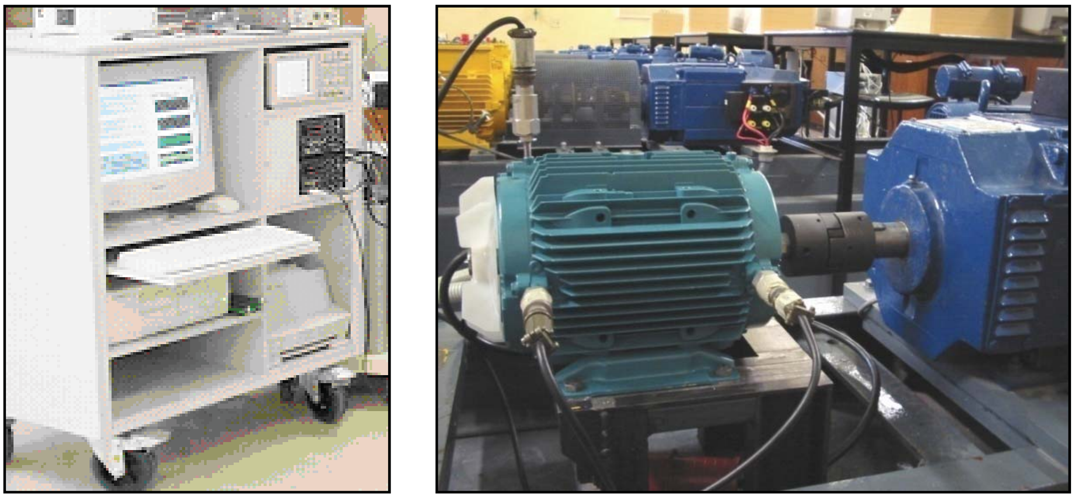

Figure 1.5 - Photograph of the data acquisition and data analysis hardware (left) and the motor test setup (right).

Table 1.3 – Specifications of the sensors.

PARAMETER	DEVICE	BANDWIDTH	INPUT RANGE
Voltage	Isolation amplifier	30 kHz	± 600 V
Current	Hall-effect clamp-on	50 kHz	± 10 A
Flux	100 turns, search coil	10 kHz	± 1 V
Vibration	CTC AC102-1A piezo-electric accelerometers	20 kHz	± 2 g

Each of the analogue signals from the sensors was passed to a variable gain amplifier and a low pass filter. The variable gain amplifier has 8 channels and each channel is able to adjust the gain (i.e. x1, x10, and x100) individually to amplify a weak signal. The low pass filter is an eight channel 8th order Butterworth analogue filter with a selectable cut-off frequency of either 100 Hz or 2 kHz. The cut-off frequency was chosen to satisfy the Nyquist Theorem, where the sampling rate must be at least twice the highest frequency present in the signal. The low pass filter was used to remove any unwanted high frequency components that could otherwise cause aliasing issues. The filtered signals were then passed to analogue to digital (A/D) converters, which are part of the data acquisition hardware, to obtain a set of digital data. The data acquisition hardware is a plug-in card from National Instruments (NI-PCI-6110, 12 bit, 5 MHz, simultaneous sampling). A simple flow diagram of the condition monitoring system is shown in Figure 1.6.

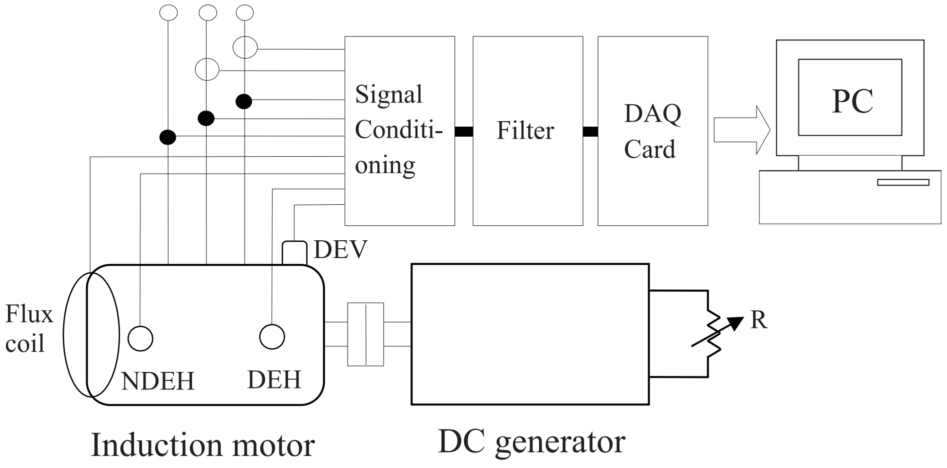

Figure 1.6 - Block diagram of the measurement hardware and the motor test setup with the sensors' locations.

Ideally, all sensors should be sampled at a sampling rate and sampling time as high as possible but these options are restricted by the hardware limitations. As a consequence, all sensors were sampled simultaneously with two different sampling rates and two different sampling times, which are chosen as follows:

- Low-frequency measurement at 400 Hz sampling frequency (which gives a Nyquist frequency of 200 Hz) with a sampling time of 100 s, which allows very high-resolution frequency analysis with a lower bandwidth (40,000 data points with 0.01 Hz resolution), and

- High-frequency measurement at 8000 Hz sampling frequency with a sampling time of 5 seconds, which allows high frequency analysis with a lower frequency resolution (40,000 data points with 0.2 Hz resolution).

These two sampling (and cut-off) frequencies were particularly chosen because most of the low frequency components that are of interest usually lie between 0 - 100 Hz and the high frequency components that are of interest usually lie below 2 kHz. Furthermore, the 40000 data points were chosen because of the limitations of the hardware processing power.

1.5.1. Simulation of Broken Rotor Bar Faults

Broken rotor bar faults were simulated by cutting a narrow slot through the end-ring next to the lamination stack using a small diameter milling cutter to break the electrical connection between the rotor bar and the end-ring. This method is used to minimise the disturbance to the rotor end-ring currents which would occur if the end-ring were completely removed.

The profile of the rotor bars in the test machine can be seen in Figure 1.7, where a section of the rotor end-ring has been cut completely away. A partial broken rotor bar fault was created by decreasing the depth of the slot to only remove a portion of the rotor bar cross-sectional area. For example, a 25% broken rotor bar means 25% of the rotor bar's cross-sectional area has been removed (Figure 1.7).

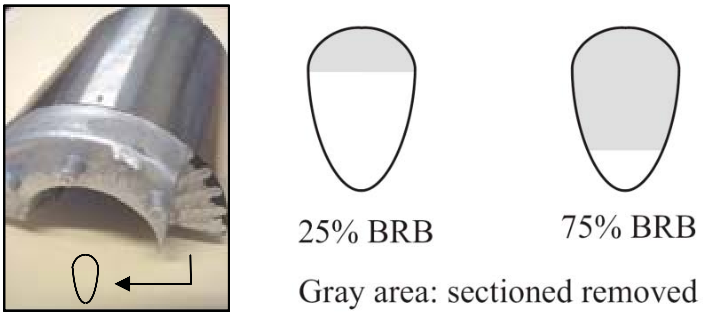

Figure 1.7 - Photograph of the rotor cross-section and the profile of the partially broken rotor bars.

1.5.2. Simulation of Eccentricity Faults

Figure 1.8 shows a sectioned view of the test motor with an adjustable static eccentricity facility. The test motor was designed to allow the introduction of repeatable and reliable static eccentricity adjustments. The test motor has the same specifications as the healthy motors.

As illustrated in Figure 1.8, the test motor consisted of custom-built motor end-plates which contain an adjustable bearing housing. The graduated screws in the motor setup allow the operator to raise or lower the rotor position in relation to the stator core. There are two graduated screws on the motor setup, which allow the operator to independently adjust the rotor position at either end of the rotor. The graduated screws are able to introduce static eccentricity with a resolution up to 0.01 mm, where the nominal airgap of the motor is 0.39 mm (based on the manufacturer's specifications). These values and the design of the adjustable bearing housing were verified based on the precise measurements of the necessary motor parts (eg. rotor diameter, stator diameter, bearing diameter, etc.) when the motor was disassembled.

The zero eccentricity (centred rotor) position was estimated by using the mid-point of the range of free movement of the rotor at each end. That is, the allowable movement of the rotor at each end-plate was found by adjusting the graduated screws until the rotor touched the stator laminations, and the average of the upper and lower values of this was assumed to correspond to centred operation.

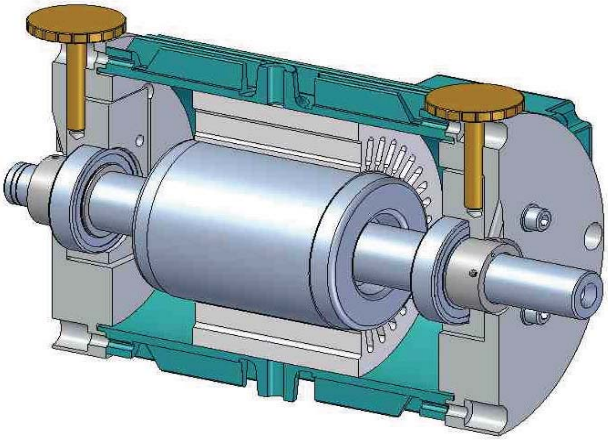

Figure 1.8 - Sectioned view of the test motor showing the adjustable static eccentricity arrangement.

1.5.3. Simulation of Shorted Turn Faults

The motor with adjustable shorted turn faults was built by rewinding the stator windings of a motor with the same specifications as the healthy motors, which have 282 turns per phase. The test motor (Figure 1.9) was rewound such that taps on the stator windings could be accessed from the external panel (i.e. R1 to R5 and B1 to B5). R1 is the external access to the end of the stator winding of phase A (see Figure 1.10). R2 is the external access to the 5 consecutive turns. Similarly, R3, R4, and R5 are the external accesses to the 10, 15, 20 consecutive turns respectively. As in the case for R1 to R5, B1 to B5 are the external accesses for the stator windings of phase B.

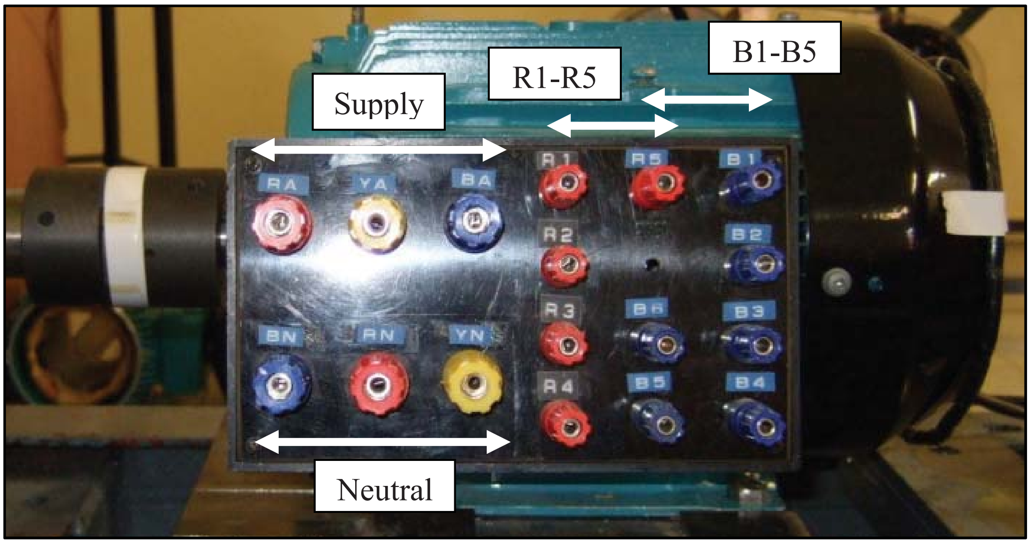

Figure 1.9 –Test motor showing the adjustable shorted turn arrangement.

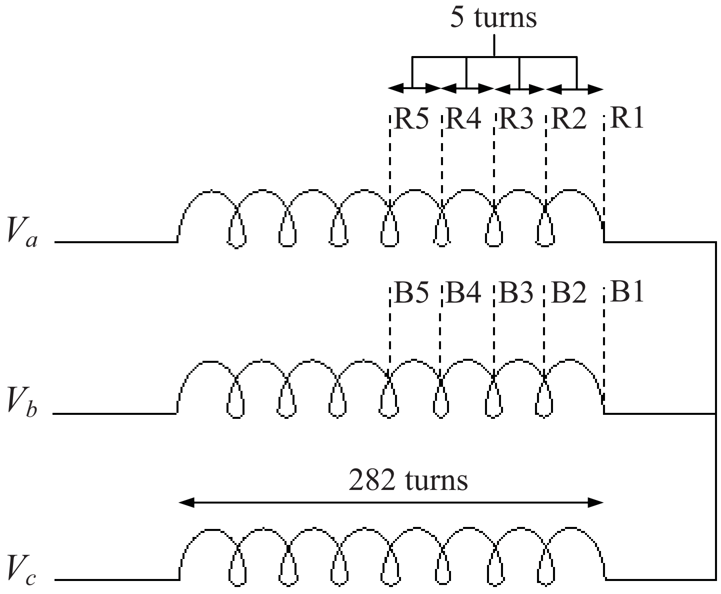

Figure 1.10 – Illustration of the stator winding external accesses.

Turn to turn faults can be simulated by short circuiting R1 to R2, R1 to R3, R1 to R4, or R1 to R5. For example, to short circuit 10 turns of the windings of phase A, a wire needs to be placed to short circuit R1 and R3. Phase to phase shorted turn faults can be simulated by short circuiting R2 to B2, R3 to B3, R4 to B4, or R5 to B5. For example, to introduce 10 turns phase to phase shorted turn fault, a wire needs to be placed to short circuit R3 and B3.

1.6. Contributions of the Thesis

Followings are a list of contributions of this research.

Rotor Speed and Rotor Slot Number Estimations

- Comparing the performance of four different speed estimation techniques from three different non-invasive sensor signal types; namely, stator current signal, axial leakage flux signal, and motor vibration signal.
- Investigating and comparing the possibility of estimating the number of rotor slots using the rotor slot harmonics in the stator current and axial leakage flux signals, and the rotor slot passing frequency in the motor vibration signal.
- Combining the different rotor slot number estimation techniques in order to improve the estimation capability.

Baseline Study

- Performing a baseline study of identical rating healthy motors, which examines the phase variation of common fault frequency components in the current signals, the motor repeatability of common fault frequency components, and the motor variability of common fault frequency components as a function of load.

Shorted Turn Fault Detection

- Comparing the performance of potential shorted turn fault features in the stator current, axial leakage flux, and motor vibration signals using five different fault severities and ten different loading conditions.

- Identifying and analysing the useful shorted turn features by utilising the motor variability tests in the baseline study in order to determine the loads and the fault severities for which the features can be reliably used to detect the faults.

Static Eccentricity Fault Detection

- Comparing the performance of potential static eccentricity fault features in the stator current, axial leakage flux, and motor vibration signals using nine different fault severities and ten different loading conditions.
- Identifying the useful static eccentricity features, and combining the useful static eccentricity features in order to produce a better fault indicator.
- Examining the possibility of detecting static eccentricity faults and estimating the fault severity using the combined features.
- Investigating the effects of misalignment faults on the useful static eccentricity features.

Broken Rotor Bar Fault Detection

- Investigating a new method for detecting broken rotor bar faults that is based on the wavelet transform of the motor starting current envelope.
- Examining the effects of unbalanced supply on the new broken rotor bar fault detection method.
- Investigating several methods for detecting broken rotor bar faults after supply disconnection that include two features from the rundown induced voltage; the harmonic content and the change in the motor output torque for a given value of slip, and three features from the stator flux linkage and its space vector components; the step change on disconnection, the rate of decay with time, and its spatially correlated harmonic content.

1.7. Organisation of the Thesis

Chapter 2 of the thesis provides descriptions of the signal processing techniques utilised in condition monitoring. The chapter discusses the limitations of practical Fourier transform and shows methods to minimise these limitations, such as windowing, zero padding, and spectral averaging. The basic principles of how the wavelet transform works and its advantages over the Fourier transform method in analysing transient signal are also discussed.

Chapter 3 presents several methods for detecting rotor speed and the number of rotor bars in an induction motor by utilising the different sensor signal types. The chapter then compares the performance of the different rotor speed and rotor slot number estimation techniques. In addition, a simple approach for combining the different methods using the different sensor signal types is presented and discussed.

Chapter 4 gives the baseline study of the six healthy induction motors utilised in this thesis. The baseline study examines how the common fault frequency components for detecting the rotor and stator faults vary under repeated tests and between the six identical healthy motors.

Chapter 5 examines the two types of shorted turn faults, which are turn to turn faults and phase to phase turn faults. This chapter introduces various features which are known to be able to detect shorted turn faults and provides a comparison of the different features as to find the best feature for detecting the faults under different loading conditions.

Chapter 6 examines the effects of static eccentricity faults on the known eccentricity fault frequency components. The chapter gives a comparison of the ability of the different frequency components in detecting eccentricity faults. The frequency components that are found to be good eccentricity indicators are then combined with a new approach in order to improve the overall fault detection capability. In addition, the effects of misalignment on the eccentricity features are investigated.

Chapter 7 introduces a novel approach for detecting broken rotor bar faults that are not affected by motor loading conditions. The approach utilises wavelet transform and the envelope of the starting current waveform in order to detect and distinguish different fault severities. In addition, the chapter also investigates the effects of unbalanced supply on the proposed approach.

Chapter 8 examines various new approaches for detecting broken rotor bar faults during motor rundown operation. The approaches described in this chapter utilise multiple signal processing techniques, such as the Fourier transform, wavelet transform, Park's vector, and order tracking analysis, in attempt to distinguish different fault severities under different loading conditions.

Finally, the last chapter in this thesis provides a summary of the investigations performed and gives suggestions for future research.

Chapter 2. Signal Processing Techniques

2.1. Introduction

As described in Chapter 1, the presence of faults in induction motors usually introduces or alters the characteristic fault frequency components in the spectrum of various sensor signals, such as stator current signals, leakage flux signals, and motor vibration signals. Therefore it is important to use signal processing techniques that can monitor these fault frequency components. Two signal processing techniques utilised extensively in this thesis are the Fourier transform and the wavelet transform. The nature of the Fourier transform allows the analysis of signal frequency components during motor steady-state operation, while the wavelet transform allows the analysis of signal components during motor transient operation.

2.2. Fourier Transform

The Fourier transform (FT) of a signal, $f(t)$, and its inverse Fourier transform are defined in (Eq. 2.1) and (Eq. 2.2) respectively [40].

$$\boldsymbol{F}(\omega) = \frac{1}{\sqrt{2\pi}} \int_{-\infty}^{\infty} f(t) e^{-j\omega t}\, dt \qquad \text{(Eq. 2.1)}$$

$$f(t) = \frac{1}{\sqrt{2\pi}} \int_{-\infty}^{\infty} \boldsymbol{F}(\omega) e^{j\omega t}\, d\omega \qquad \text{(Eq. 2.2)}$$

where ω is the angular frequency.

(Eq. 2.1) and (Eq. 2.2) show that the Fourier transform of a signal is the superposition of sinusoidal components of all possible frequencies and amplitudes of the signal. Therefore, the Fourier transform can extract the frequency information of a time signal and determine the strength/energy of a particular frequency component. The Fourier transform provides the frequency representation of a time signal.

2.2.1. Discrete Fourier Transform

When dealing with real applications, the signal data is not continuous but sampled at frequency f_s. Therefore discrete version of (Eq. 2.1) and (Eq. 2.2), known as the discrete Fourier transform (DFT), are required. (Eq. 2.3) shows the DFT of a sampled signal, $f[n]$, and (Eq. 2.4) shows its inverse DFT.

$$\boldsymbol{F}(k) = \frac{1}{N} \sum_{n=0}^{N-1} f[n] e^{-j\frac{2\pi kn}{N}} \qquad \text{(Eq. 2.3)}$$

$$f[n] = \frac{1}{N} \sum_{n=0}^{N-1} \boldsymbol{F}(k) e^{j\frac{2\pi kn}{N}} \qquad \text{(Eq. 2.4)}$$

where N is the number of samples of $f[n]$ and $k = 0,1,2 \ldots N\text{-}1$.

The sampled signal (and the analogue signal it represents) should ideally have a one to one mapping (i.e. unique representation). However, this is not always the case. In fact, analogue signals at frequencies of f_o and f_o+mf_s, where m is any integer, have identical digital signals (sampled signals) [7, 41, 42]. A simple example of this problem is illustrated in (Eq. 2.5), where the signal $\cos(2\pi f_o n t_s + \theta)$ and the signal $\cos(2\pi(f_o+mf_s)nt_s + \theta)$ have identical digital signals for all values of n. This problem is known as aliasing. Aliasing can be avoided and a unique mapping between an analogue signal and its digital signal can be preserved only if the frequency range of the analogue signal is restricted to lie between $-\frac{f_s}{2}$ and $\frac{f_s}{2}$. This is usually ensured by using an analogue low-pass filter (anti-aliasing filter), which should filter out any frequencies higher than $\frac{f_s}{2}$ before the analogue signal is sampled by an A/D converter.

$$cos\left(2\pi\left(f_o+\frac{m}{t_s}\right)nt_s+\theta\right)=cos\ (2\pi f_o nt_s+\theta+2\pi mn) \qquad \text{(Eq. 2.5)}$$

Based on (Eq. 2.3), it can be deduced that the spectrum (DFT) of a sampled signal is periodic with a period of the sampling frequency, f_s. The proof of this can be seen in (Eq. 2.6).

$$\begin{aligned}\boldsymbol{F}(f\pm mf_s)&=\sum_{n=-\infty}^{\infty}f[n]e^{-j2\pi nt_s(f\pm mf_s)}\\&=\sum_{n=-\infty}^{\infty}f[n]e^{-j2\pi nt_sf}e^{\pm j2\pi nm}\\&=\sum_{n=-\infty}^{\infty}f[n]e^{-j2\pi nt_sf}\\&=\boldsymbol{F}(f)\end{aligned} \qquad \text{(Eq. 2.6)}$$

For real data, $\boldsymbol{F}(f)=\boldsymbol{F}^*(f_s-f)$ (see (Eq. 2.7)), and hence to examine the spectrum of a real sampled signal, one only needs to look at frequencies between 0 and $f_s/2$.

$$\begin{aligned}\boldsymbol{F}(f_s-f)&=\sum_{n=-\infty}^{\infty}f[n]e^{-j2\pi nt_s(f_s-f)}\\&=\sum_{n=-\infty}^{\infty}f[n]e^{j2\pi nt_sf}e^{-j2\pi n}\\&=\left[\sum_{n=-\infty}^{\infty}f[n]e^{-j2\pi nt_sf}\right]^*\\&=\boldsymbol{F}^*(f)\end{aligned} \qquad \text{(Eq. 2.7)}$$

2.2.2. Fast Fourier Transform (FFT)

Evaluating the discrete Fourier transform of a signal with N samples can be computationally expensive. It requires a computation of the order of N^2 operations, as evaluating each frequency bin requires approximately N complex multiplication and addition (see (Eq. 2.3)).

The most common method to reduce the number of computation is the fast Fourier transform (FFT) algorithm by Cooley and Tukey [43]. The algorithm uses the fact that the DFT of a signal with N samples is equivalent to the combination (i.e. some simple reordering and arithmetic operations) of two DFTs of when the signal is divided into two blocks, each of $N/2$ samples. If N is chosen to be a power of 2, then each block can be further halved and the same algorithm can be applied again. This process can be repeated until the data block cannot be divided further. As a result, the algorithm reduces the DFT computation from the order of N^2 to the order of $N \log_2(N)$.

2.2.3. Limitations of Practical Fourier Transform

In real condition monitoring applications, practical Fourier transforms have three main hardware limitations. First, the captured sensor signals are not free of noise. Second, the data only has a finite number of samples. Third, a digital computer can only evaluate the Fourier transform at a finite size of frequency interval, Δf.

The first hardware limitation (i.e. noise issue) can cause weak frequency components in the signal to be masked by the random noise. As a consequence, the frequency analysis may not be able to correctly identify and detect the frequency components of a signal.

Ideally, the Fourier transform of a continuous signal results in delta functions at the frequencies that are present in the signal. However, the combined effects of the finite number of samples and the finite size of frequency interval can cause the frequency energy of the signal to be spread over a range of frequencies with a main lobe and subsidiary side lobes (i.e. similar to a sinc function translated to the frequency of the signal) if the frequency of the signal is not an integer multiple of Δf. This type of signal is termed as a non-centre cell signal. If the signal frequency is an integer multiple of Δf, then a delta function at the frequency of the signal can be obtained. This signal is named as a centre cell signal.

In real condition monitoring applications, the signals which are captured by the sensors are non-centre cell signals. There are two problems associated with non-centre cell signals, which are a resolution problem, due to the width of the main lobe, and a side lobe leakage problem. The first problem (i.e. resolution) arises when the signal contains two (or more) frequency components that are very close together such that the second frequency component lies inside the main lobe of the first frequency component. As a consequence, the frequency analysis cannot separate the two frequency components because they appear as a single frequency component. The second problem (i.e. side lobe leakage) arises when the amplitude of the side lobe of a particular frequency component overshadows the amplitude of the main lobe of another frequency component in the signal. This particular problem may occur if the signal contains two (or more) frequency components that are close together in frequency and the magnitude of the first component is much greater than the magnitude of the second component. As a consequence, the frequency analysis cannot correctly identify the magnitude (energy) of the second frequency component.

All of these hardware limitations reduce the accuracy in analysing the various frequency components of a signal. Therefore, it is important to minimise the effects of the hardware limitations. There are several methods that can be utilised to minimise the above mentioned problems and improve the frequency analysis of a signal. These methods include window functions, interpolation in the frequency domain (zero padding), and spectral averaging (spectral smoothing).

2.2.3.1. Window Functions

The resolution problem due to the width of the main lobe and the side lobe leakage problem can be minimised by applying a suitable window function. A window function can be applied by multiplying the signal data with a window function as to shape the signal data to match the window function (Eq. 2.8). Note that a captured sensor signal data which is not windowed is the same as a signal data with a rectangular window applied.

$$\boldsymbol{F}(f) = \frac{1}{N}\sum_{n=0}^{N-1} w[n]f[n]e^{-j2\pi n t_s f} \qquad \text{(Eq. 2.8)}$$

where $w[n]$ is the window function.

There are many different window functions available. The decision in choosing one window function over the others depends on:

- the resolution requirement, which is the width of the main lobe,
- the magnitude of the strongest side lobe, and
- the decay rate of the side lobe magnitudes with frequency.

A good overview and performance evaluation for each of the window functions are given in [7, 44, 45]. Some examples of the popular window functions include Rectangular, Hanning, Hamming, Bartlett, and Blackman windows.

The Hanning window, which is defined in (Eq. 2.9), is one of the most popular window functions because it is the window function which provides the most balanced characteristics. The Hanning window has a slightly broadened main lobe but its first side lobe is at 32 dB below the main peak and the side lobes decay very rapidly with frequency. The characteristics of the Hanning window fulfil our requirements for the frequency analysis of the sensor signals. Hence, the Hanning window is the window function that is utilised in this thesis.

$$w_{Hanning}[n] = \frac{1}{2}\left(1 - cos\left(\frac{2\pi(n+1)}{N+1}\right)\right) \qquad \text{(Eq. 2.9)}$$

where n=0, 1, ..., N-1.

The effects of applying the Hanning window to the sensor signal, which is the stator current of the healthy motor (see *section 1.5*) running at full load captured with a sampling frequency of 8 kHz and a sampling time of 5 seconds (see Figure 2.1), is demonstrated in Figure 2.2 and Figure 2.3. The vertical axis of the figures, $F(f)^*F(f)$, shows the magnitudes (powers) of the frequency components in the signal. The unit chosen for these magnitudes is dB so that the magnitudes from different sensor signals have an equal standing for each decade.

Figure 2.2 and Figure 2.3 clearly demonstrate that there are three effects of the window function. The first effect is that the Hanning window slightly broadens the width of the main peak. The main peak is the narrowest when no window function is applied (i.e. rectangular window). This means that the Hanning window slightly increases the resolution problem. However, the second and the third effects of applying the Hanning window compensate its drawback. The second effect is that the Hanning window significantly reduces the magnitude of the strongest side lobe. The third effect is that the Hanning window significantly increases the decay rate of the side lobes with frequency. The combination of the second and the third effects of the Hanning window clearly improve the detection of the frequency components in the signal.

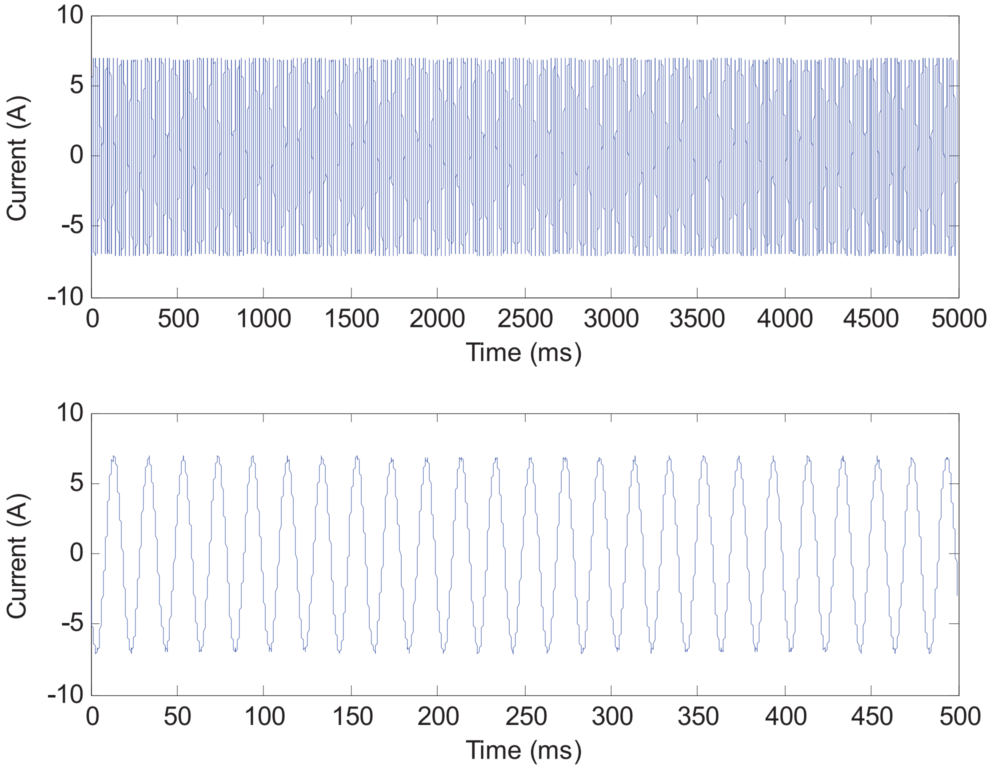

Figure 2.1 – Stator current signal of the healthy motor sampled at 8 kHz.

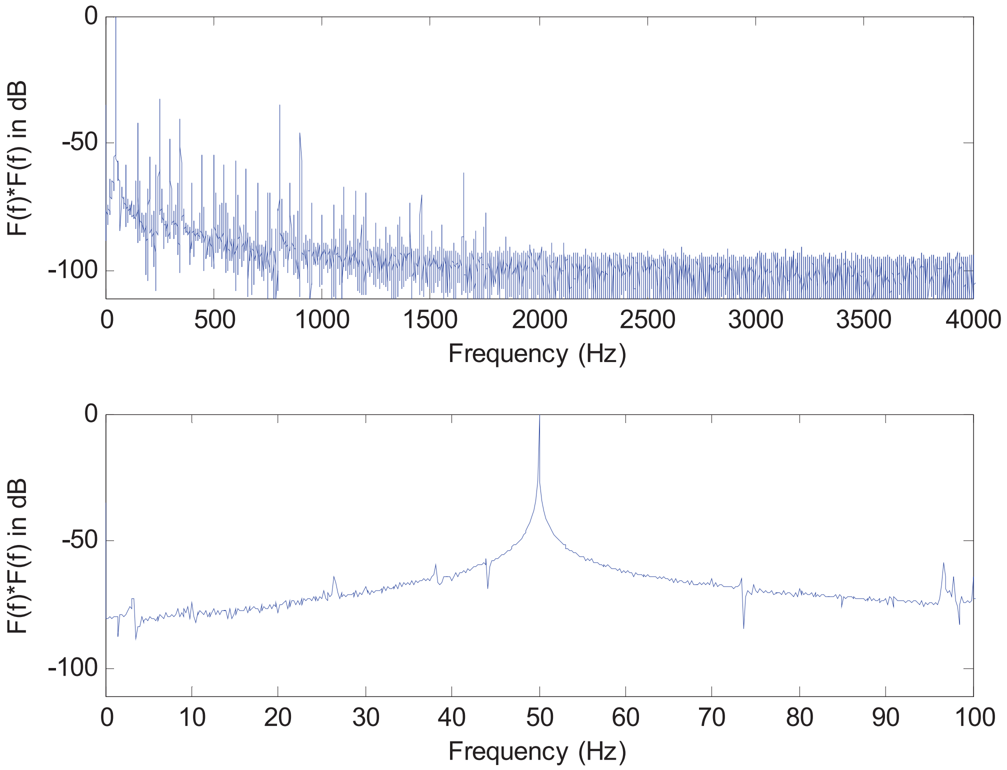

Figure 2.2 – Frequency spectrum of the stator current without any window function (or Rectangular window).

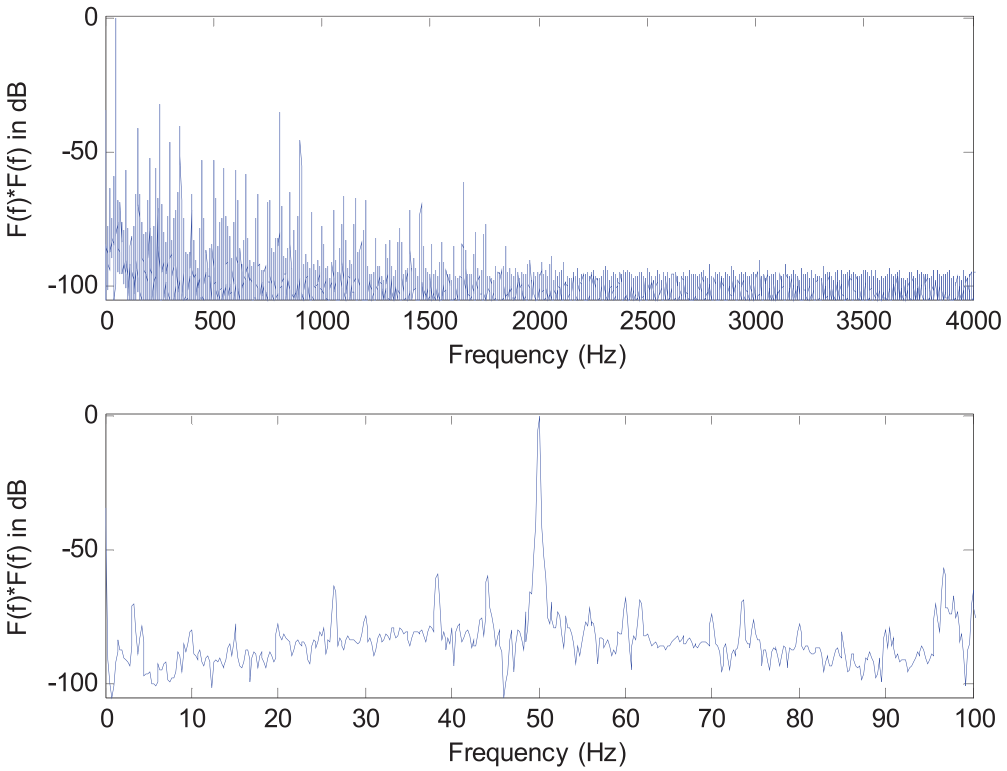

Figure 2.3 – Frequency spectrum of the stator current with Hanning window.

2.2.3.2. Interpolation in Frequency Domain

The practical limitations of the Fourier transform cause the frequency components in a signal to be detected as a main lobe and subsidiary side lobes instead of a single delta function. This main lobe can only be evaluated at a finite frequency interval of Δf. As a consequence, it is likely that the highest point of the main lobe is not at the frequency which is an integer multiple of Δf. Hence, the accuracy in detecting the frequency and the magnitude of the signal component is reduced. The worst case occurs when the highest point of the main lobe is located exactly halfway between two frequency bins.

One method to minimise the problem is to utilise interpolation in the frequency domain, which is also known as zero padding. Interpolation in the frequency domain is a technique where the Fourier transform is evaluated at a finer spacing than Δf by adding a block of $m*N$ zeros to the end of the signal data [46]. The resulting Fourier transform has the same Nyquist frequency and the same periodicity in the frequency domain because the sampling rate has not been changed. However, the resulting Fourier transform is now evaluated at a finer spacing of $\Delta f/(m+1)$. For example, if a $7N$ block of zeros is added to the end of the signal data, the resulting Fourier transform is then evaluated at a frequency interval of $\Delta f/8$.

The effects of interpolating the signal in the frequency domain are demonstrated in Figure 2.4. The figure only shows a portion of the complete spectrum which shows the main peak (main lobe) of the third harmonic of the fundamental, 150 Hz, component in the signal. The figure shows the limited frequency resolution when no zero padding is added. This is because the Fourier transform of the signal is evaluated at a rather limited frequency interval, Δf. When zero padding is added to the signal, the main lobe becomes rounder and smoother. The main lobe becomes even rounder and smoother as the amount of zero padding is increased. This shows that the Fourier transform of the signal is evaluated at finer frequency intervals as the amount of zero padding is increased. Figure 2.4 shows that when $7N$ zero padding is added to the signal, the frequency accuracy is improved by ~0.02 Hz and the magnitude accuracy is improved by ~0.1 dB. Yet, increasing the amount of zero padding to greater than $7N$ results in very limited improvements. Therefore, the frequency analysis results given in this thesis utilised either $7N$ or $15N$ zero padding.

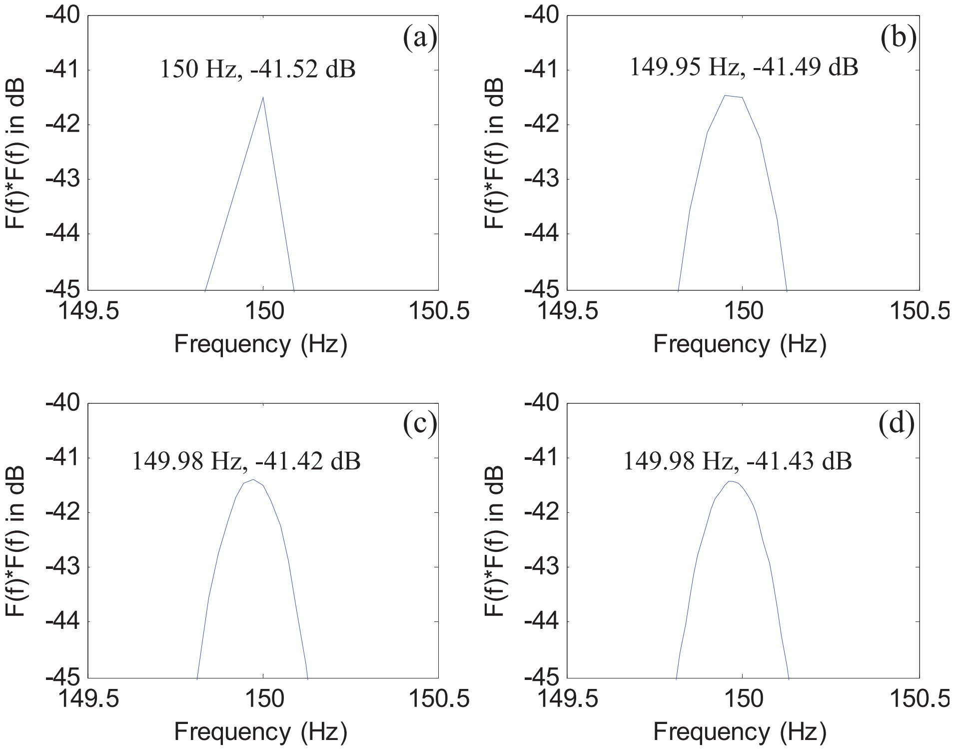

Figure 2.4 – Main peak (main lobe) of the fundamental component of the stator current with no zero padding (a), 3*N* zero padding (b), 7*N* zero padding (c), and 15*N* zero padding (d).

2.2.3.3. Spectral Averaging

The practical limitations of the Fourier transform can cause the presence of weak frequency components to be masked by random noise. One technique to minimise this problem is to utilise spectral averaging, also known as spectral smoothing. The principle of spectral averaging is to divide the signal data into *M* sub-blocks each with length *N*/*M*. All *M* sub-blocks are then Fourier transformed separately. The resultant spectra are used to calculate the spectral average (see (Eq. 2.10) and (Eq. 2.11)).

$$\boldsymbol{S}_{average} = \frac{1}{M}\sum_{m=1}^{M} \boldsymbol{S}_m(f) \qquad \text{(Eq. 2.10)}$$

where

$$\boldsymbol{S}_m(f) = |\boldsymbol{F_m}(f)|^2 \qquad \text{(Eq. 2.11)}$$

where $\boldsymbol{F_m}$ is the Fourier transform of the signal in each sub-block.

The effects of spectral averaging on the sensor signal, which is the stator current of the healthy motor running at full load captured with a sampling frequency of 400 Hz and a sampling time of 100 seconds, are demonstrated in Figure 2.5 - Figure 2.7. The figures show that the random noise is reduced when the spectral averaging technique is applied. Furthermore, the noise becomes lesser as the number of sub-blocks used in the spectral averaging is increased. As a result, this technique allows the detection of weak frequency components that may be masked by random noise, and allows a clearer distinction between the signal frequency components and the random noise. However, Figure 2.5 - Figure 2.7 also show that the main lobes of the signal frequency components widen when the spectral averaging technique is applied. The width of the main lobe increases with the number of sub-blocks used in the spectral averaging. This is to be expected as the width of the main lobe (i.e. the frequency resolution) depends on the length of the sub-block window (*N*/*M*), where the width of the main lobe increases (i.e. the frequency resolution reduces) as the length of the sub-block window reduces.

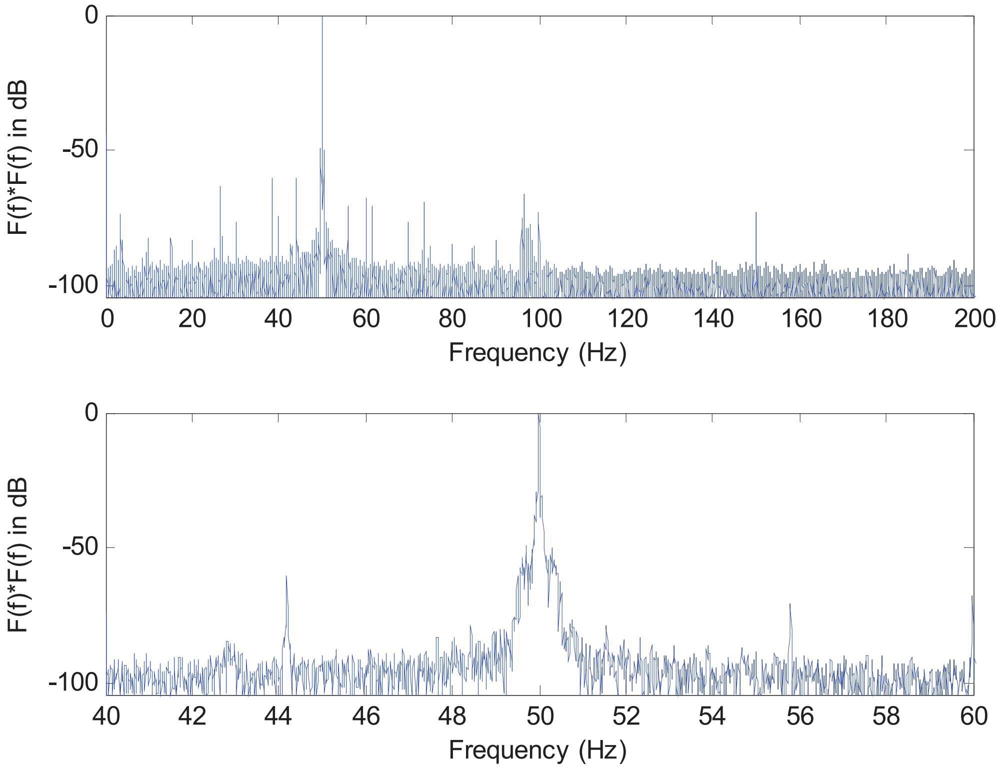

Figure 2.5 – Frequency spectrum of the stator current with no averaging.

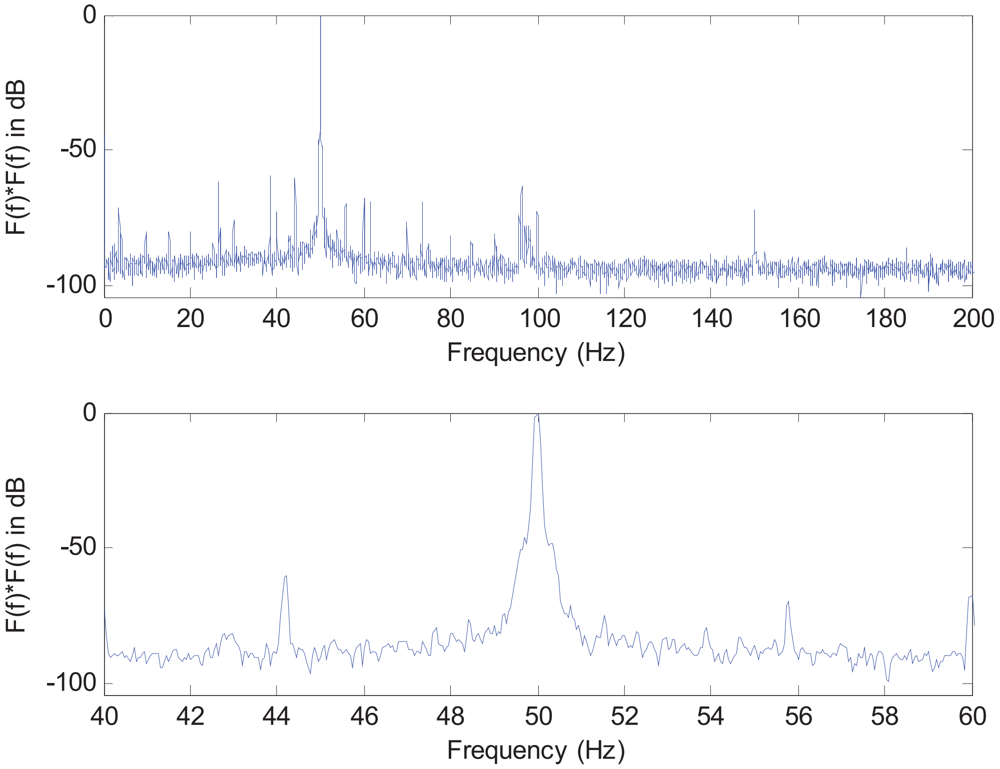

Figure 2.6 – Frequency spectrum of the stator current with 5 blocks averaging.

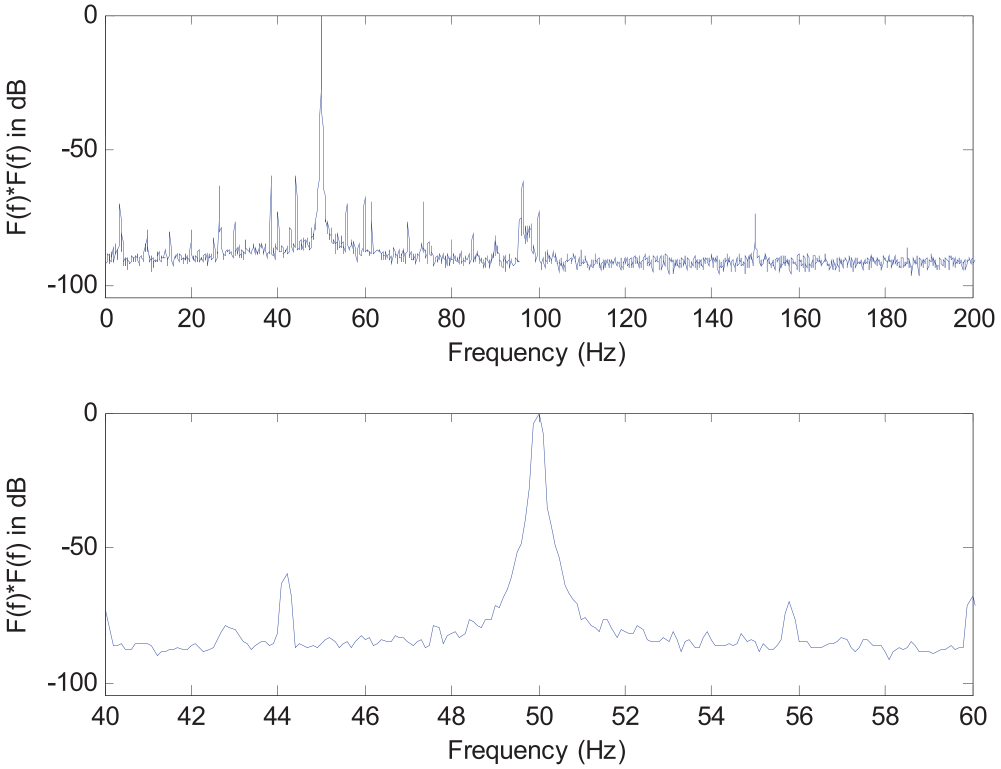

Figure 2.7 – Frequency spectrum of the stator current with 10 blocks averaging.

While spectral averaging can reduce the random noise, it also reduces the frequency resolution. Therefore, this thesis does not utilise spectral averaging for all the frequency analysis but only in certain cases where the signal data is known to have a high enough sampling time (i.e. frequency resolution) to accommodate for the loss of the frequency resolution. For example, the spectral averaging technique is utilised when the frequency analysis is only dealing with the low frequency measurement data (400 Hz, 100 s), which has a long sampling time.

2.3. Short-Time Fourier Transform

As described in the previous sections, the Fourier transform provides the frequency information of a signal but it loses its time information. This is because the Fourier transform is calculated over a whole captured signal (Eq. 2.1), which means the frequency information extracted from the signal represents the averages of the frequency components that exist in the signal over the whole time domain. As a consequence, the Fourier transform is only suitable for the analysis of motor steady-state operation and cannot be used to analyse the instantaneous frequency content of a signal, such as when the motor load varies.

In order to get a time-frequency representation of a captured sensor signal, the short-time Fourier transform (STFT) can be utilised. The principle of the STFT is to divide a time signal into equal length sub-blocks by using a sliding window function, $w(t)$ (Figure 2.8), and perform the Fourier transform on each of the sub-blocks separately (Eq. 2.12) [47]. As a result, the STFT can extract the frequency information of a signal while maintaining its time information. However, the STFT reduces the frequency resolution of the signal because the STFT divides the signal into smaller sub-blocks which represent less observation time. Hence the frequency and time resolution of the STFT technique depend on the length of the window. A longer window means higher frequency resolution but lower time resolution while a shorter window means lower frequency resolution but higher time resolution.

$$\boldsymbol{F_{ST}}(\omega, \varphi) = \frac{1}{\sqrt{2\pi}} \int_{-\infty}^{\infty} f(t) w(t - \varphi) e^{-j\omega t} \, dt \qquad \text{(Eq. 2.12)}$$

where φ is the window position.

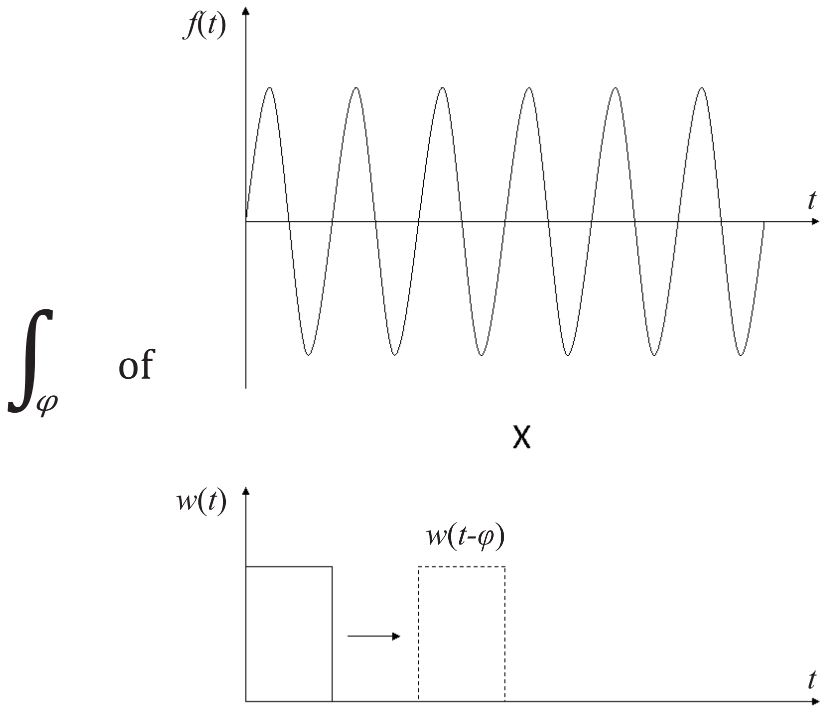

Figure 2.8 – Illustration of the principle of STFT.

2.3.1. Short-Time Discrete Fourier Transform

When dealing with real applications, the signal data is not continuous but sampled at frequency f_s. Therefore the discrete version of the STFT in (Eq. 2.12), known as the short-time discrete Fourier transform (STDFT), is shown in (Eq. 2.13).

$$\boldsymbol{F_{ST}}(k_\omega, k_\varphi) = \frac{1}{N}\sum_{n=0}^{N-1} f[n]w[n - k_\varphi \varphi_c]e^{-j\frac{2\pi k_\omega n}{N}} \qquad \text{(Eq. 2.13)}$$

where φ_c is the window position constant.

Examples of the STFT (spectrogram) analysis of the stator current (400 Hz, 100 s), used in Figure 2.5, are shown in Figure 2.9. The spectrogram analysis is performed by dividing the signal into 20 and 100 blocks using the Hanning window with no overlapping. The spectrogram of the 20 blocks division (Figure 2.9 top) shows that the time resolution is rather course and it can be observed that the time domain is divided into 20 bins. This spectrogram also shows that there is a strong component at a frequency of 50 Hz, represented by a thin red line. The thin line suggests that the frequency resolution is acceptable because the thinner the line, the higher the frequency resolution is. On the other hand, the spectrogram of the 100 blocks division (Figure 2.9 bottom) shows that the time resolution is quite high which can be observed by the smooth transition across the time bins. However, this spectrogram shows that the fundamental 50 Hz component is represented by a broader red line. The broader line suggests that the frequency resolution of this spectrogram is not as good as the frequency resolution of the spectrogram of the 20 blocks division. Based on these results, it can be concluded that there is a trade off between time resolution and frequency resolution when utilising the spectrogram analysis, and the trade off is controlled by the length of the window function.

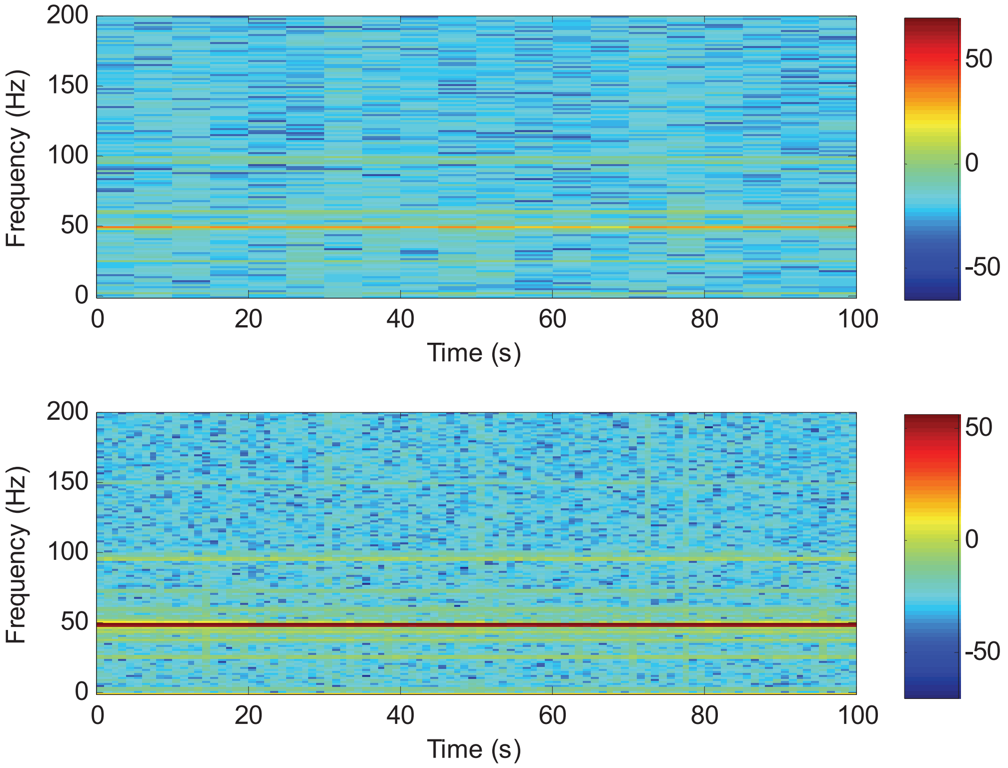

Figure 2.9 – Spectrogram of the stator current in Figure 2.1 with 20 blocks (top) and 100 blocks (bottom) division.

2.4. Wavelet Transform

As described in the previous section, the STFT can provide a time-frequency representation of a signal by using a fixed length window. However, the use of a fixed length window can lead to a poor frequency resolution especially if the observation time (sampling time) of the signal is limited, such as when capturing the sensor signals during motor transient operation. One solution is to utilise the wavelet transform (WT). The wavelet transform can provide both the frequency information and the time information of a signal by using a variable length window. As such, fault detection techniques based on the wavelet transform can be utilised to analyse motor transient operation, such as starting and rundown. The application of the wavelet transform to condition monitoring is still rather new and only accounts for about 2% of the total applications of the wavelet transform in power systems [48].

The wavelet transform of a signal, $f(t)$, is defined [49] as

$$\boldsymbol{W}_{cwt}(a,\varphi) = \frac{1}{\sqrt{a}}\int_{-\infty}^{\infty} f(t)\psi\left(\frac{t-\varphi}{a}\right)dt \qquad \text{(Eq. 2.14)}$$

where a is the wavelet scale, φ is the wavelet position, and $\psi(t)$ is the wavelet function.

The wavelet transform in (Eq. 2.14) is also known as the continuous wavelet transform (CWT) because it utilises a continuous range of scales (a) and shifts (φ). The definition of the CWT (Eq. 2.14) shows that the main concept of the wavelet transform is to divide a signal into its various scaled and shifted versions of the wavelet (Figure 2.10), in a similar fashion that the Fourier transform of a real variable divides a signal into its sinusoidal components of different frequencies with different or equal magnitudes and phases. The correlation between the signal and the wavelet function at each level of scaling and for various time shifts is termed the wavelet coefficient.

A high scale wavelet corresponds to a "stretched" wavelet, which has a slow rate of change and hence low frequency. On the other hand, a low scale wavelet corresponds to a "compressed" wavelet with rapidly changing detail and hence high frequency. The fact that the wavelet function can be scaled gives the wavelet transform its variable length window and the fact that the wavelet function can also be shifted gives the wavelet transform its ability to provide both the frequency (in term of scale) and time information of a signal.

There are some conditions that must be satisfied for a function to be considered as a wavelet function [50, 51]. These conditions require the function to be orthogonal, to be oscillatory, and to decay rapidly to zero. Some examples of the common wavelet functions include the wavelet functions from the Daubechies family, the Coiflets family, and the Symlet family (see Figure 2.11). The choice of the wavelet functions used in this thesis will be discussed in the related chapters (Chapter 7 and Chapter 8).

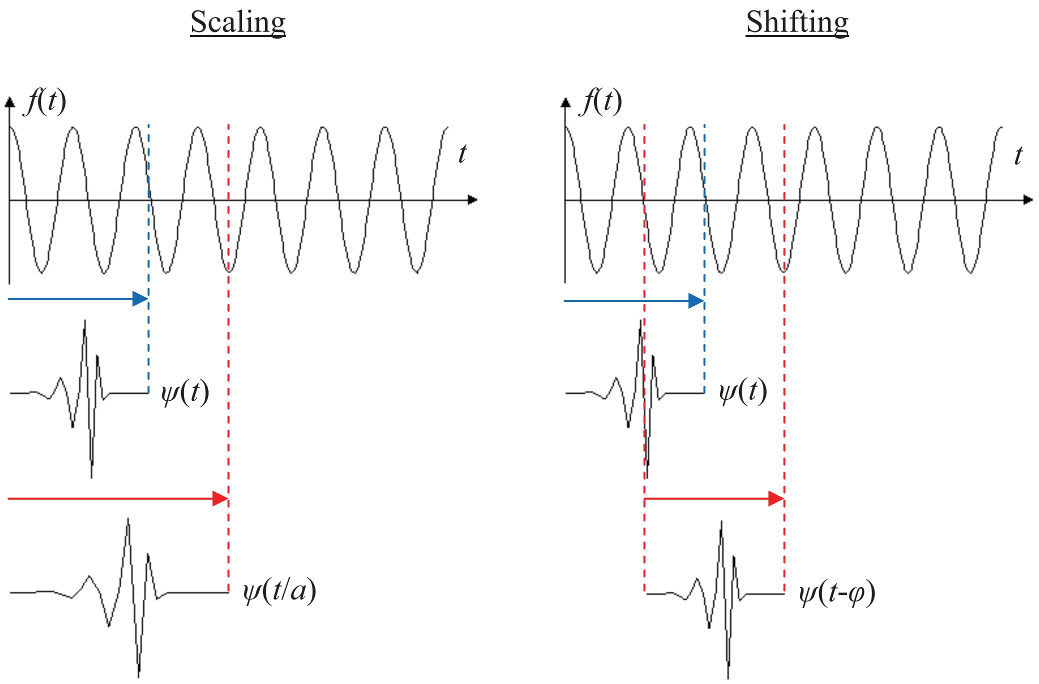

Figure 2.10 – Illustration of the principle of wavelet transform.

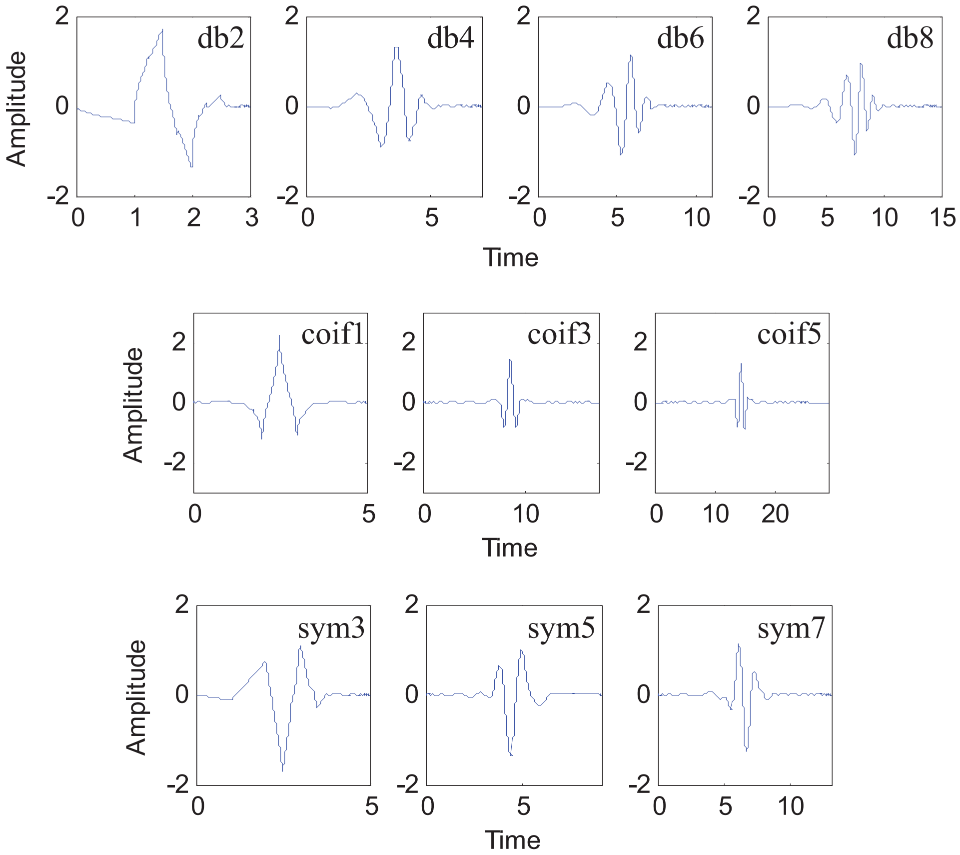

Figure 2.11 – Examples of wavelet functions from the Daubechies family (db), the Coiflets family (coif), and the Symlet family (sym).

2.4.1. Continuous Wavelet Transform

When dealing with real applications, the signal data is sampled at a frequency of f_s and the range of scales and shifts of the wavelet transform cannot be continuous. Therefore, the CWT in real applications utilises integer multiples of scales and shifts (Eq. 2.15).

$$\boldsymbol{W}_{CWT}(k_a, k_\varphi) = \frac{1}{\sqrt{k_a a_c}} \sum_n f[n]\ \psi\left[\frac{nt_s - k_\varphi \varphi_c}{k_a a_c}\right] \qquad \text{(Eq. 2.15)}$$

where a_c is the wavelet scale constant and φ_c is the wavelet position constant.

The results of applying the CWT to the stator current of a healthy motor running at full load, captured with a sampling frequency of 8 kHz and a sampling time of 5 seconds (Figure 2.12), are shown in Figure 2.13. The figure displays the magnitude of the wavelet coefficients (the legend in Figure 2.13) as functions of wavelet scale and wavelet shifts. The CWT plot in Figure 2.13 shows several distinct patterns, such as the strong horizontal pattern at scale around 141, the vertical pattern at the beginning of the plot, and the vertical pattern at the end of the plot. The horizontal pattern at scale around 141 is the strongest pattern in the CWT plot and it represents the fundamental component of the signal. The vertical patterns at the beginning and at the end of the CWT plot represent the discontinuities in the signal. In addition, the CWT plot shows that the horizontal patterns seem to be regular at all values of shifts, which suggest that there are no irregularities (like switching or frequency change) within the signal. As can be seen from this example, wavelet transform has the ability to analyse both the time information (shifts) and the frequency information (scale) of a signal with good resolution. As a result, the wavelet transform can be utilised to analyse the transient sensor signals during motor transient operations.

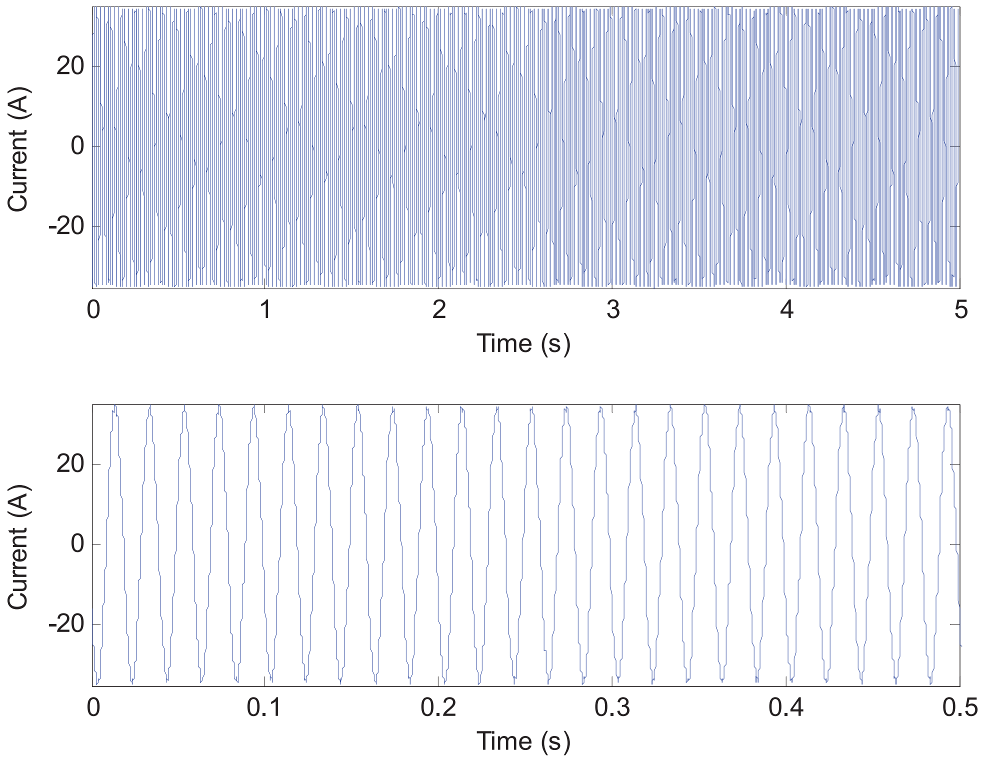

Figure 2.12 – Stator current signal of a healthy motor running at full load.

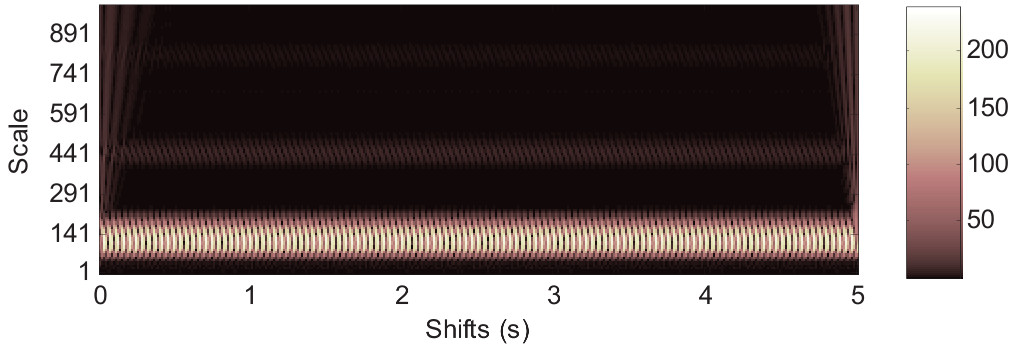

Figure 2.13 – CWT of the stator current signal.

2.4.2. Discrete Wavelet Transform

The CWT, which calculates scales and shifts at every possible integer up to some predetermined maximum value, may require significant processing power and processing time. The discrete wavelet transform (DWT) attempts to reduce the processing time while maintaining reasonable accuracy by calculating the scales and the shifts only at multiples of the power of 2 [50, 52]. The DWT is shown in (Eq. 2.16) and (Eq. 2.17).

$$a = 2^{\alpha}$$
$$\varphi = \beta 2^{\alpha} \qquad \text{(Eq. 2.16)}$$

Hence,

$$\boldsymbol{W}_{DWT}(\alpha,\beta) = 2^{-\alpha/2} \sum_{n} f[n]\ \psi[2^{-\alpha} n t_s - \beta] \qquad \text{(Eq. 2.17)}$$

where α and β are real integers.

A filtering interpretation of the discrete wavelet transform is illustrated in Figure 2.14. As shown in the figure, at each level of the wavelet decomposition, which is denoted by α in (Eq. 2.17), the signal is passed to both a high pass wavelet filter (h_{pf}) and a low pass wavelet filter (l_{pf}). The filtered signals are then down-sampled by a factor of 2 in order to keep the total number of samples the same as for the original signal data. The signal component which is extracted from the high pass filter is called the "detail" component (*cD*). This component consists of the high frequency component (in terms of the wavelet function used) of the signal. The high pass filter coefficients are the wavelet coefficients approximately scaled. The signal component which is extracted from the low pass filter is called the "approximation" component (*cA*). This component consists of the low frequency component (in terms of the wavelet function used) of the signal.

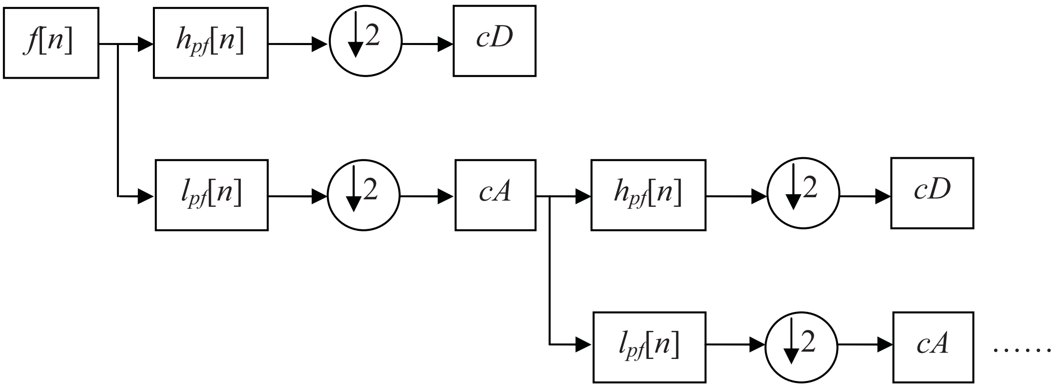

Figure 2.14 – Multiple level wavelet decomposition.

The DWT may reduce the processing power and the processing time but the wavelet analysis in this thesis utilises the continuous wavelet transform (CWT) because it provides more flexibility in terms of the scales and the shifts that can be used. As a result, the analysis based on the CWT is more detailed and customisable than its DWT counterpart. In addition, the advancement of computing technology allows greater processing power and less processing time, which in turn reduces the above mentioned drawbacks of the CWT.

2.5. Order Tracking Analysis

Another signal processing technique that is commonly utilised to analyse transient signals is the order tracking analysis. This technique is primarily used in vibration analysis for reducing the smearing effect in the spectrum of a transient signal [53, 54]. The technique can be implemented with two options. The first option is by using a speed sensor to control the signal sampling rate, thus allowing reasonably long records to be taken as the machine is changing speed. However, such analysis is only useful for tracking faults which are characterised by the frequency components that are proportional to the operating speed. This is because the sampling rate can only be synchronised to the motor speed. Due to this limitation and the additional speed sensor requirement, this technique is not considered in this study.

The second option is to resample the signal waveform such that each cycle (period) of the waveform contains exactly the same number of samples separated by a fixed spatial (linear) interval rather than a fixed time interval. This option has the advantage of not requiring a speed sensor but it involves interpolation of the original signal which may introduce unwanted approximation errors. This digital implementation of the order tracking and its trade-off will be further discussed in Chapter 8.

2.6. Summary

This chapter provided descriptions of the two principal signal processing techniques used extensively in the thesis; Fourier transform and wavelet transform. The practical use of the Fourier transform as a signal processing technique for condition monitoring was examined and its practical limitations were discussed. Methods used to minimise these limitations, such as window functions, interpolation in the frequency domain, and spectral averaging, were also presented. The Fourier transform is an important signal processing technique for fault detection in a condition monitoring system because it can provide detailed frequency information about a signal, and faults in induction motors usually manifest themselves as frequency components in the sensor signals. However, the Fourier transform of a signal loses its time information. Therefore, fault detection techniques based on the Fourier transform are only suitable for motor steady-state operation.

The chapter also examined the practical use of the wavelet transform as a signal processing method for condition monitoring. The differences between the continuous wavelet transform and the discrete wavelet transform were discussed. The wavelet transform is another important signal processing technique for fault detection in a condition monitoring system because it can provide both the frequency information and the time information of a signal. Therefore fault detection techniques based on the wavelet transform can be utilised to analyse motor transient operation, such as starting and rundown. This technique is utilised in this thesis to analyse broken rotor bar fault detection during motor starting and motor rundown operation in Chapter 7 and Chapter 8 respectively.

Chapter 3. Rotor Speed and Rotor Slot Number Estimation

3.1. Introduction

Identification of the exact frequency components corresponding to a fault often requires the knowledge about the operating speed and the number of rotor slots. For example, the broken rotor bar (BRB) sidebands in (Eq. 1.1) depend on the slip, which can be calculated if the rotor speed and the number of poles are known. The number of poles is usually given on the machine nameplate but the actual operating speed needs to be estimated from the machine sensor signals. In addition, it is not a common practice to provide the number of rotor slots in the machine nameplate. However, knowledge of the number of rotor slots is important because it is needed to calculate the eccentricity fault frequency components (Eq. 1.2), which can be used to detect static and dynamic eccentricity faults [27-29].

Furthermore, the combination of the number of rotor slots and the eccentricity fault frequency harmonics have also been used for speed estimation in the past [55-57]. It was reported in [56] that it is possible to estimate the steady-state speed of an inverter-driven motor (28 kW, 415 V, 50 A) by tracking the speed-dependent slot harmonic component, which is related to the number of rotor slots, within a certain frequency range. In this reference, the extracted slot harmonic was compared to the 19th harmonic of the fundamental frequency in order to determine the rotor rotational speed. It was also reported that the number of rotor slots could be determined by examining the stator current spectrum as the load was progressively decreased. As the load decreased, the speed dependent slot harmonic would reduce in amplitude and change in frequency. Hence, the speed dependent slot harmonic could be identified and the number of rotor slots could be calculated. However, the limitation of this technique is that it requires data to be taken under multiple loading conditions, which cannot be ensured in a practical operating condition.

A similar speed estimation technique on an inverter-driven induction motor (4 kW, 4 poles, 28 rotor slots) was also reported in [55]. The difference is that this work estimated the transient speed by utilising the short-time Fourier transform (STFT). In addition, the work also incorporated zero padding (i.e. interpolation in the frequency domain) into the FT in order to improve the detection of the speed dependent rotor slot harmonics. Another similar technique was utilised in [57] to estimate the rotor speed of an inverter-driven motor (7.46 kW, 4 poles). The difference is that this work used decimation to alias the rotor slot harmonics into a single frequency. This process improved the ability to detect the desired slot harmonic. It was also reported that the number of rotor slots could be found by finding the most significant slot harmonics in (Eq. 1.2) when the number of rotor slots, R, is varied between 30 - 54 (even numbers only), n_d is varied for 0 and ±1, and v is varied for ±5, ±3, ±1. However, the technique was not proven to function in a wide range of motors (i.e. motors with rotor slots other than 30 - 54) and the process was found to be computationally intensive.

The accuracy of the speed estimation techniques which are based on the speed dependent slot harmonic and the FT were found to be dependent on the number of samples of the captured data. The work in [58] showed a comparison of several methods, such as Blackman-Tukey [59], Steiglitz-McBride [60], and MUSIC (multiple signal classifier) [61], which can improve the speed estimation techniques so that the speed harmonic component can be extracted from a minimal number of data samples but with greater accuracy than the FT techniques. The work suggested that the MUSIC and Steiglitz-

McBride methods produced better frequency resolution results than the FT method when the number of samples was 16. However, it was found that when the number of samples was 32, the FT method significantly improved the frequency resolution.

Four other speed estimation techniques which did not utilise the rotor slot harmonics were also reported in the literature. In [62], the FT and the Hilbert transform demodulation approach were utilised to estimate the rotor speed. In [63] an extended Kalman filter (EKF) and a real-coded genetic algorithm (GA) optimisation were incorporated to estimate the rotor speed. The work in [64] involved injecting an extra rotor current with controllable frequency to the rotor windings and matching that frequency to the rotating frequency of the motor to estimate the rotor speed. The work in [65] estimated the rotor speed by examining the small ripple generated on the angular frequency of the rotor flux through injection of a high frequency stator current component.

In general, it can be concluded that most of the speed estimation techniques based on the rotor slot harmonics have focussed only on inverter-driven induction motors, under limited loading conditions, and have used only the stator current. Furthermore, the rotor slot number estimation techniques reported earlier either require data at multiple loads or are computationally intensive. Therefore, the work in this chapter aims to improve on the existing methods and to provide simple and accurate estimation of both the rotor speed and the rotor slot number by utilising the stator current, the axial leakage flux, or the vibration sensor signals. In the following sections, several methods for rotor speed and rotor slot number estimation based on different signal frequencies and sensor types are investigated and their performance are compared over a wide range of loads.

3.2. Rotor Speed Estimation Techniques

The rotor speed is an important piece of information in an on-line condition monitoring system as it is required to calculate the load and the fault frequencies. This section will examine several speed estimation techniques which utilise the stator current, the motor vibration, and the axial leakage flux signals.

3.2.1. Stator Current

The eccentricity fault frequency components (Eq. 1.2) are easily detected in the stator current [27-29] and the axial leakage flux signals. These fault frequencies are a function of the supply frequency, the number of rotor slots, the number of poles, and the slip. It is possible to reduce the eccentricity fault frequency equation into a function of only the supply frequency and the rotor frequency, f_r, by setting the variables $k = 0$, $n_d = \pm 1$, $v = 1$, as shown in (Eq. 3.1) [57]. This relation allows the rotor speed to be found using (Eq. 3.2).

$$f_{ecc1} = f\left[(\pm 1)\frac{(1-s)}{p} \pm 1\right] = f \pm f_r \qquad \text{(Eq. 3.1)}$$

$$f_r = |f - f_{ecc1}| \qquad \text{(Eq. 3.2)}$$

The frequency spectrum given in Figure 3.1 shows that the eccentricity fault frequency components in (Eq. 3.1) are not particularly strong in the current signal but they are still detectable and can be used to calculate the rotor speed. Furthermore, the experimental results suggest that the lower sideband is stronger than the upper sideband. Hence, the lower sideband will be used to calculate the speed.

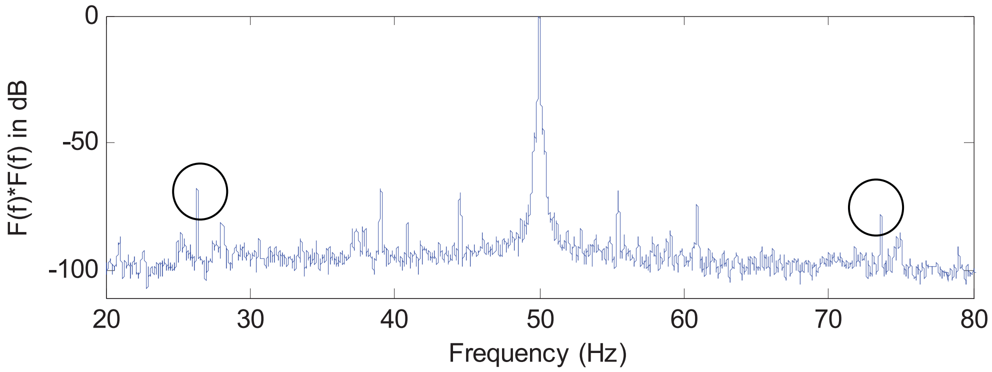

Figure 3.1 - Frequency spectrum of the stator current signal at full load illustrating the eccentricity harmonics (Eq. 3.1).

3.2.2. Motor Vibration

The motor vibration signal can be used to detect eccentricity faults and stator related faults, and is also useful for speed estimation. In particular, the vibration signal contains a comparatively large amplitude component at the rotor frequency f_r (see Figure 3.2). Based on the experimental results, this rotor frequency component has been proven to be strong under all loading conditions. As a result, the rotor speed can be readily estimated using the vibration signal.

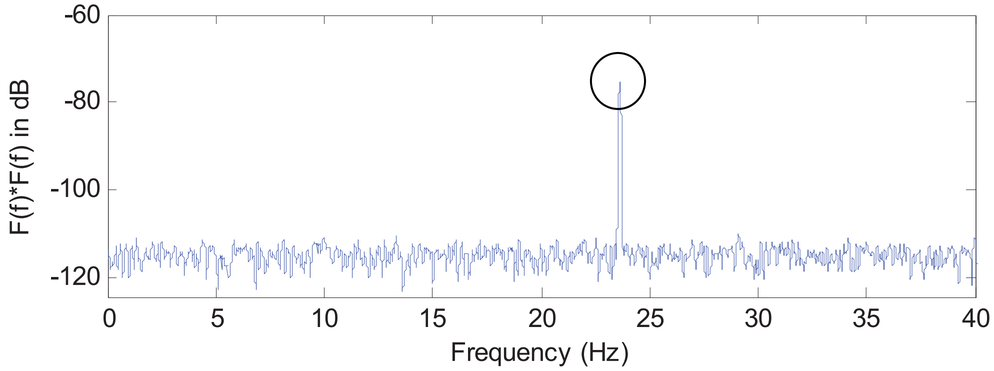

Figure 3.2 - Frequency spectrum of the vibration signal at full load showing the rotor frequency.

3.2.3. Axial Leakage Flux

There are two speed estimation methods that can be applied to the axial leakage flux signal. The first method is the same method as in the stator current signal, which is based on the eccentricity fault frequency harmonics in (Eq. 3.1). The second method uses the fact that the axial leakage flux from the rotor end-windings contains a strong component at the slip frequency, *sf*. This slip frequency can be used to determine the rotor speed through the relationship described in (Eq. 3.3) - (Eq. 3.5).

$$f_r = \frac{(n_s - s.n_s)}{60} \qquad \text{(Eq. 3.3)}$$

where the synchronous speed, n_s, is defined as

$$n_s = \frac{60 \times f}{p} \qquad \text{(Eq. 3.4)}$$

Hence,

$$f_r = \frac{(f - sf)}{p} = f\left(\frac{1-s}{p}\right) \qquad \text{(Eq. 3.5)}$$

Figure 3.3 (top) shows that the eccentricity harmonics, which are used for detecting the speed, are quite strong in the flux signal. The figure also suggests that the lower sideband is stronger than the higher sideband. Therefore, the lower sideband will be used to calculate the rotor speed.

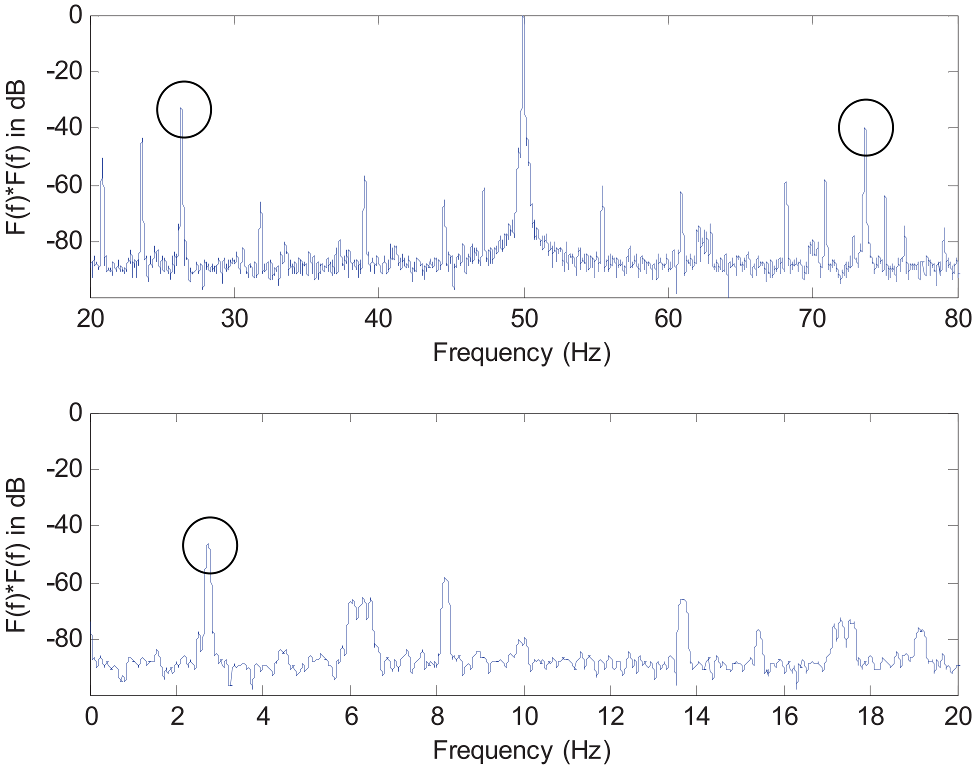

Figure 3.3 - Frequency spectrum of the axial leakage flux signal at full load showing: (top) the eccentricity harmonics (Eq. 3.1), and (bottom) the slip frequency.

Figure 3.3 (bottom) shows that the slip frequency component in the flux signal is detectable and so it can be used to calculate the speed. However, the slip frequency component is found to have lower magnitude than the speed related component of the first method, which is based on the eccentricity harmonics. Therefore, the first speed estimation method is considered more useful than the second method in the axial leakage flux signal.

3.2.4. Comparison of Rotor Speed Estimation Techniques

Table 3.1 presents a comparison of the performance of the speed estimation techniques discussed in the previous sections. The table shows measured results from the healthy motor under different loading conditions from no-load to full-load. The table shows the motor load (in %, defined by the slip), the measured rotor speed (n_{opt}, using an optical tachometer), the estimated rotor speed (n_{est}), and the rotor speed error (Δn, in %).

Table 3.1 – Comparison of the speed estimation techniques.

Tachometer	**Current: Eccentricity Harmonics**			**Vibration: Rotor Frequency**		
n_{opt} (RPM)	Load (%)	n_{est} (RPM)	Δn (%)	Load (%)	n_{est} (RPM)	Δn (%)
1498.0	2.0	1498.7	0.05	2.2	1498.5	0.03
1489.0	13.3	1488.8	0.01	13.6	1488.6	0.03
1472.0	33.1	1472.2	0.01	32.9	1472.4	0.03
1436.0	75.0	1436.3	0.02	75.0	1436.3	0.02
1424.0	88.8	1424.4	0.03	89.0	1424.3	0.02
1416.0	97.5	1417.1	0.08	97.5	1417.1	0.08

Tachometer	**Flux: Eccentricity Harmonics**			**Flux: Slip Frequency**		
n_{opt} (RPM)	Load (%)	n_{est} (RPM)	Δn (%)	Load (%)	n_{est} (RPM)	Δn (%)
1498.0	2.0	1498.7	0.05	-	-	-
1489.0	13.3	1488.8	0.01	13.6	1488.6	0.03
1472.0	33.1	1472.2	0.01	33.1	1472.3	0.02
1436.0	75.0	1436.3	0.02	75.1	1436.2	0.01
1424.0	89.0	1424.2	0.01	88.9	1424.3	0.02
1416.0	97.5	1417.1	0.08	97.6	1417	0.07

Table 3.1 shows that the estimated rotor speed from the different techniques may differ slightly. This is due to the frequency resolution of the captured signals. The results given in Table 3.1 show that the speed estimation methods based on the eccentricity harmonics and the rotor frequency are very accurate under all loading conditions. These speed estimation methods can detect the rotor speed with an accuracy of better than 0.1% when compared against the optical tachometer. This accuracy is well within the tolerance of the optical tachometer.

On the other hand, the speed estimation technique which is based on the slip frequency is found to be not as reliable as the other methods. The slip frequency method is found to be good for high loads but unreliable at light loads (i.e. less than 10%). At light loads, the slip frequency component is difficult to detect because its magnitude is small and it is very close to the DC component. Therefore at light loads, the slip frequency component will be overshadowed by the DC component and the peak detection algorithm will mistakenly detect the DC component as the slip frequency. As a consequence, the rotor speed estimation method which is based on the slip frequency cannot estimate the rotor speed when the load is less than 10%, as shown in Table 3.1.

Further clarification about how each of the speed estimation techniques performs at different loading conditions is shown in Figure 3.4. It shows that the signal to noise ratio (SNR), which is described in (Eq. 3.6), of the eccentricity harmonic based speed estimation techniques is better at light load, and the SNR reduces as the load increases. However, the techniques still maintain acceptable level of SNR under all loading conditions. The SNR of the rotor frequency and the slip frequency based speed estimation techniques generally improve as the load increases. The rotor frequency based technique shows good SNR under all loading conditions but the slip frequency based technique fails at very light load (less than 10%).

In general, simple and reliable rotor speed estimation can be achieved from any one of the stator current, the motor vibration, or the axial leakage flux signals. The most reliable speed estimation techniques are those which are based on the rotor frequency in the vibration signal and the eccentricity harmonics in the axial leakage flux signal because they have high SNR at all loading conditions. The speed estimation technique which is based on the slip frequency is found to be the worst because it has a low SNR at very light loads.

$$SNR_{rs}(dB) = Signal(dB) - Noise\ Level(dB) \qquad \text{(Eq. 3.6)}$$

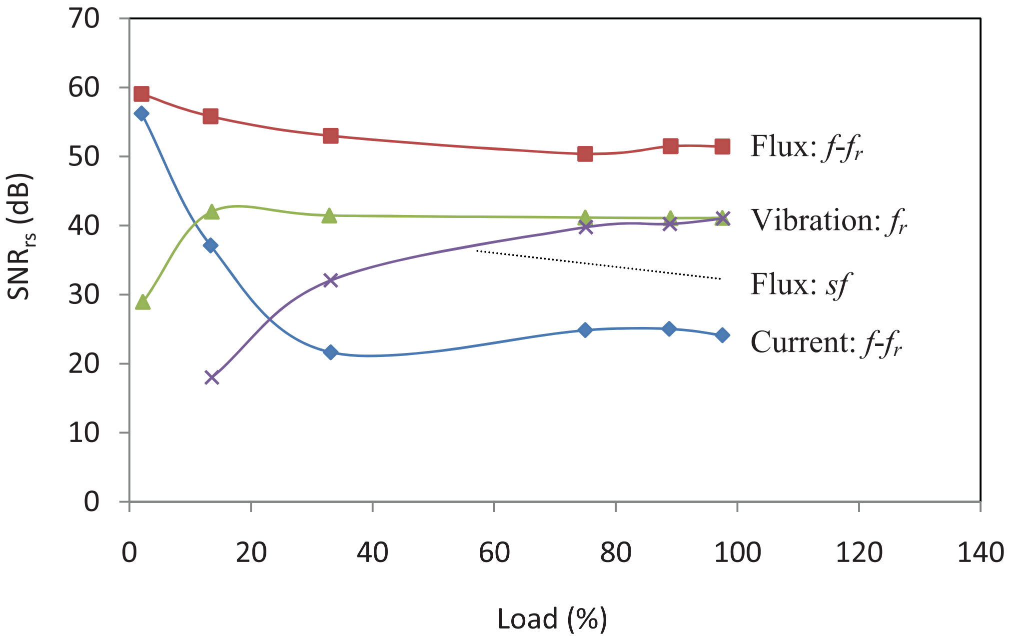

Figure 3.4 - SNR of the rotor speed estimation techniques as a function of load.

3.3. Rotor Slot Number Estimation Techniques

After the rotor speed has been identified, the number of rotor slots can then be estimated. There are two rotor slot number estimation techniques that will be investigated in this section. These techniques utilise the stator current, the axial leakage flux, and the motor vibration signals.

3.3.1. Stator Current and Axial Leakage Flux

The first rotor slot number estimation technique is based on the eccentricity fault frequency components in (Eq. 1.2), which are present in both the stator current and the axial leakage flux. This eccentricity fault frequency equation can be reduced to a combination of rotor frequency, supply frequency, and the number of rotor slots by setting $n_d = 0$ (normally for detecting static eccentricity) and $k = 1$. In addition, the experimental results suggest that the upper sideband of the first static eccentricity harmonic (i.e. $v = 1$) is one of the stronger and more reliable components. As such, the rotor slot number estimation technique will focus on this eccentricity fault frequency component (Eq. 3.7).

$$f_{ecc2} = f\left[R\frac{(1-s)}{p} + 1\right] = Rf_r + f \qquad \text{(Eq. 3.7)}$$

The relationship described in (Eq. 3.7) allows the estimation of the number of rotor slots (or bars), R, by determining the value of R which corresponds to the largest amplitude component in the current or flux spectrum, that is not a harmonic of the fundamental.

Figure 3.5 and Figure 3.6 show typical power spectra for the stator current and the axial leakage flux signals of a healthy motor running at full load. As highlighted in the figures, the eccentricity component (Eq. 3.7) is the most dominant component, other than the harmonics of the fundamental. This eccentricity component is also found to be consistently dominant across all tested loading conditions. Figure 3.5 and Figure 3.6 also reveal that the eccentricity component in the current spectrum is relatively stronger than the other components in the spectrum, while the eccentricity component in the flux spectrum is not much stronger than the other components. Therefore, the eccentricity component may be easier to be identified in the stator current than in the axial leakage flux.

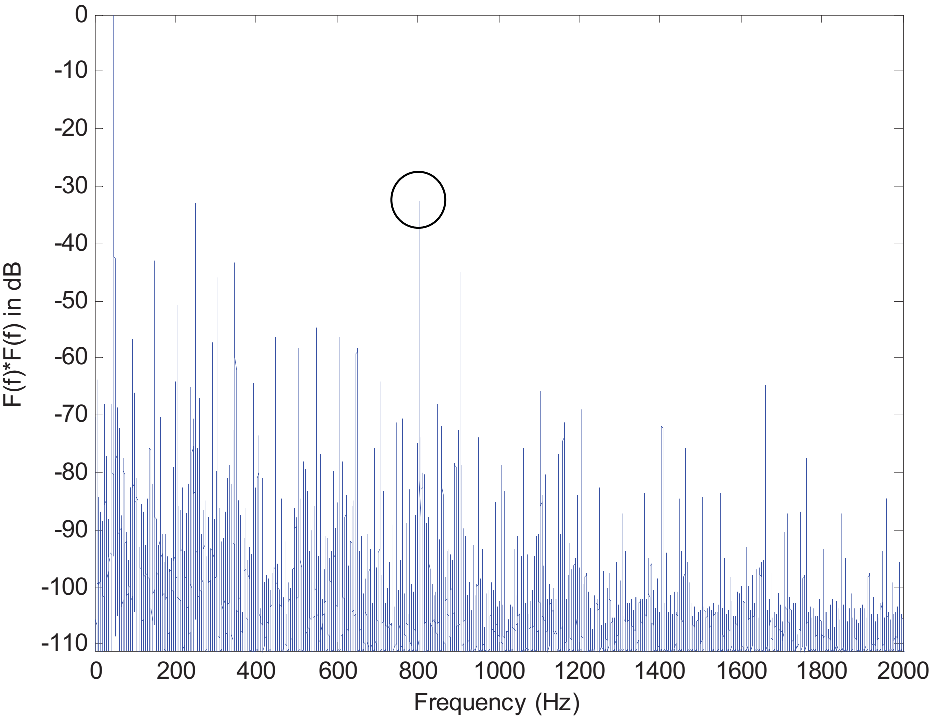

Figure 3.5 - Frequency spectrum of the stator current signal showing the eccentricity harmonic based on (Eq. 3.7).

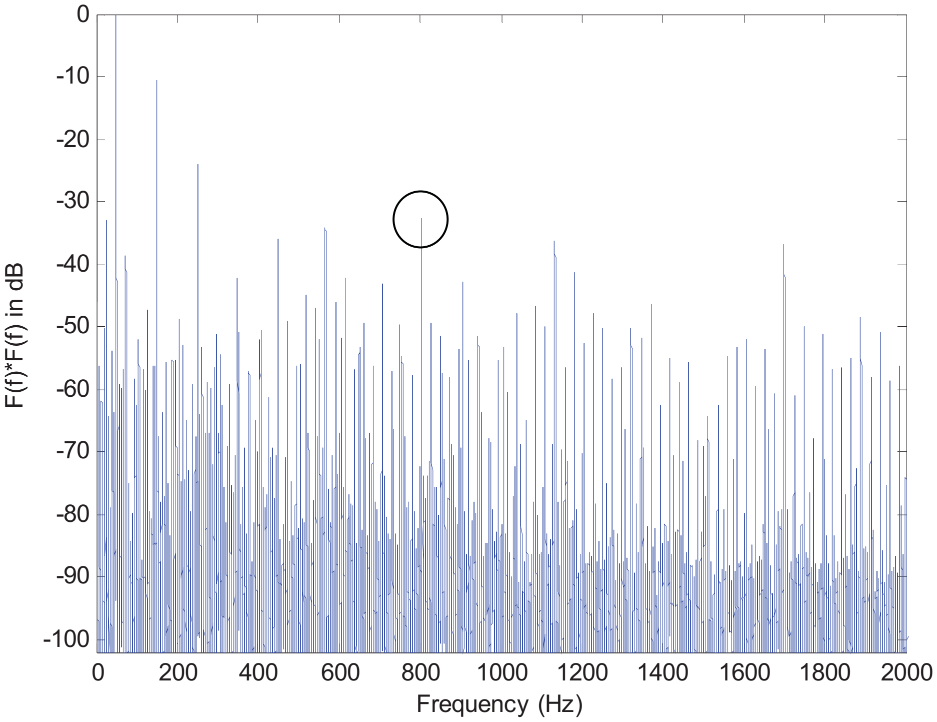

Figure 3.6 - Frequency spectrum of the axial leakage flux signal showing the eccentricity harmonic based on (Eq. 3.7).

Assuming that the number of rotor slots, R, is not known, the results of extracting the frequency components in (Eq. 3.7) with R varied for a range of possible values from the spectra in Figure 3.5 and Figure 3.6 are shown in Figure 3.7 and Figure 3.8. The figures show that the highest magnitude component in both the current and the flux spectra is achieved when the number of rotor slots is 32, which corresponds to the actual number of rotor slots of the test motor. Note that it is assumed that the number of rotor slots of less than 10 or greater than 60 is not practical for the motor specification used in this study, and the peak detection algorithm set the magnitude to -100 dB if there is no peak component detected or if the peak component is a harmonic of the fundamental.

Table 3.2 summarises the results of the rotor slot number estimation technique on two different motors. These include the healthy motor and the faulty motor with four broken rotor bars (BRB) under multiple loading conditions. The results indicate that the proposed rotor slot number estimation technique can successfully determine the number of rotor slots for the two test motors under all loading conditions. It was also proven that the rotor slot number estimation technique proposed here is equally effective in the current and the flux signals, although the current signal is preferred due to the stronger component as mentioned previously.

However, there are a few precautions that should be noted when utilising this rotor slot number estimation method. An issue may arise when the motor load is very low (less than 10%) and the number of rotor slots is few (less than 15 rotor slots). In this condition, the rotor frequency will be very close to the synchronous frequency and hence the frequency of the eccentricity component in (Eq. 3.7) may be very close to a strong harmonic of the fundamental. As a consequence, the two components can be difficult to distinguish. This problem can be reduced by making sure the sampling period is long enough to ensure a high frequency resolution.

In Table 3.2, there are slight differences between the calculated loads from the current signal and the flux signal. These differences come from the fact that the loads are calculated based on the rotor speed calculated from the corresponding signal. For example, the loads in the rotor slot number estimation using the current signal is also calculated from the current signal.

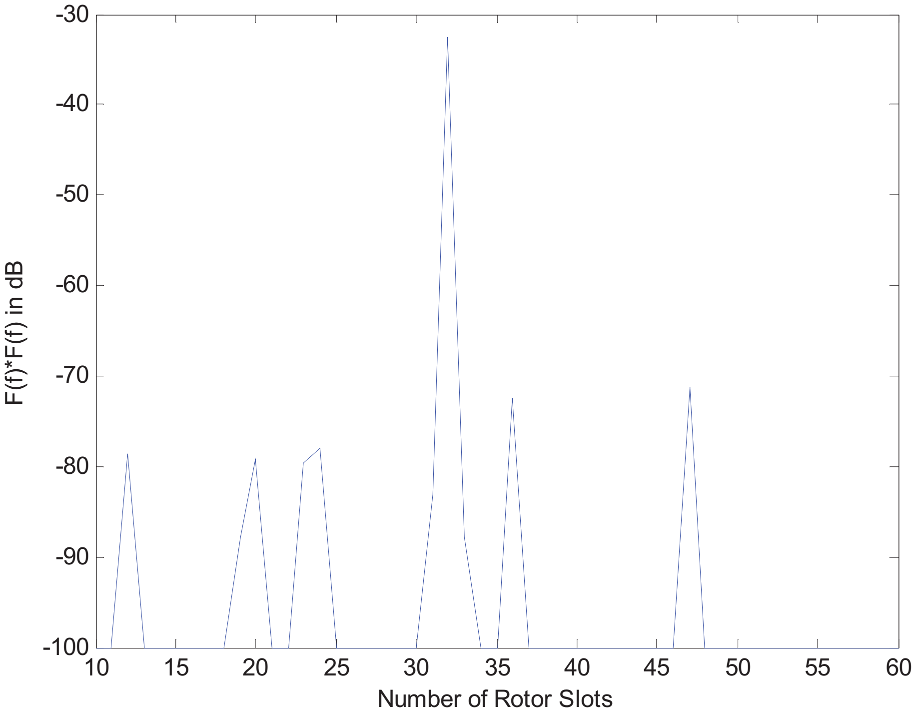

Figure 3.7 - Magnitudes of the possible eccentricity component (Eq. 3.7) against the possible number of rotor slots in the stator current spectrum.

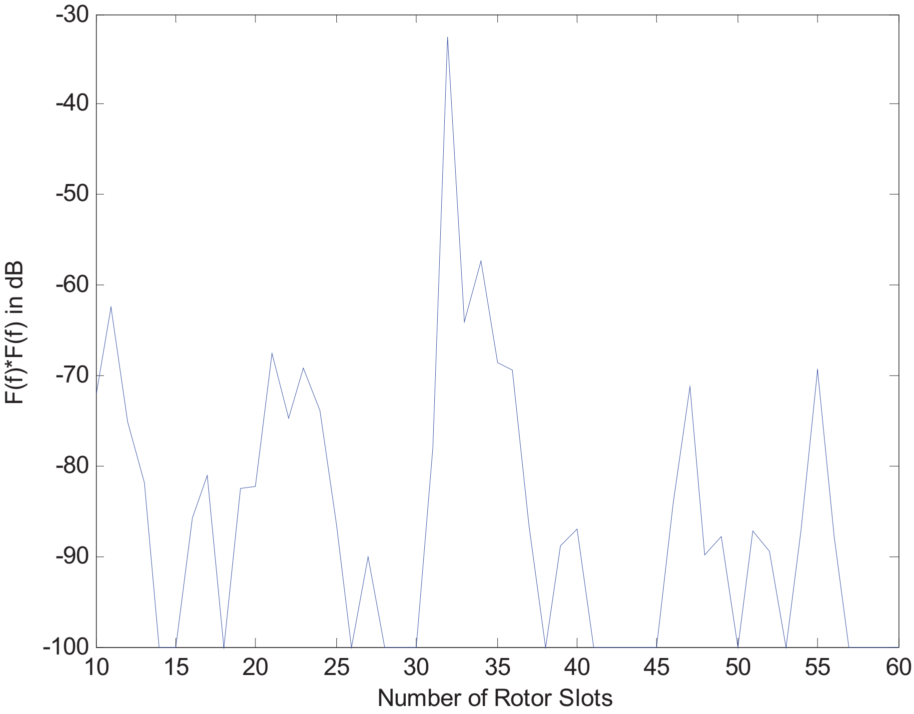

Figure 3.8 - Magnitudes of the possible eccentricity component (Eq. 3.7) against the possible number of rotor slots in the axial flux spectrum.

Table 3.2 - Rotor slot number estimates based on the eccentricity harmonics in current and flux signals.

Healthy motor				**Faulty motor (4 BRB)**			
Current		Flux		Current		Flux	
Load (%)	*R*	Load (%)	*R*	Load (%)	*R*	Load (%)	*R*
3.4	32	3.4	32	1.1	32	1.2	32
13.7	32	13.7	32	4.6	32	4.6	32
24.0	32	24.0	32	16.2	32	16.2	32
33.7	32	33.7	32	21.2	32	21.2	32
43.7	32	43.7	32	28.8	32	28.8	32
53.0	32	53.3	32	41.9	32	41.9	32
63.8	32	63.8	32	61.0	32	61.1	32
74.6	32	74.6	32	83.3	32	83.3	32
85.2	32	85.2	32	104.9	32	104.9	32
96.6	32	96.6	32	119.1	32	119.1	32

3.3.2. Motor Vibration

The rotor slot number estimation technique that is based on the eccentricity fault frequency component (Eq. 3.7) cannot be used on the motor vibration signal because this eccentricity component does not exist in the vibration signal.

The electromagnetic interaction between the stator and the rotor slots is known to produce a strong component at the rotor slot passing frequency, f_{rsp}, in the motor vibration sensor signal. The rotor slot passing frequency depends on the number of rotor slots and the rotor frequency as in (Eq. 3.8). This relationship allows the estimation of the number of rotor slots, R, by finding the largest amplitude component at the frequency given by (Eq. 3.8) that is not a harmonic of the fundamental when R is varied over the possible values. Note that the rotor slot passing frequency is a special case of the eccentricity fault frequency components given in (Eq. 1.2) when n_d is set to 0 (for static eccentricity), k to 1, and v to 0.

$$f_{rsp} = Rf_r \qquad \text{(Eq. 3.8)}$$

Figure 3.9 shows a typical power spectrum of a motor vibration signal, with the rotor slot passing frequency highlighted, when the healthy motor is operating at full load. The figure shows that the rotor slot passing component is the largest component in the spectrum. However, the magnitude of this component is found to be sensitive to the level of load. As a consequence, the rotor slot passing component may not be the largest amplitude component of all possible combinations of *R* under all loading conditions. Hence it is possible that this rotor slot number estimation technique may fail in certain conditions.

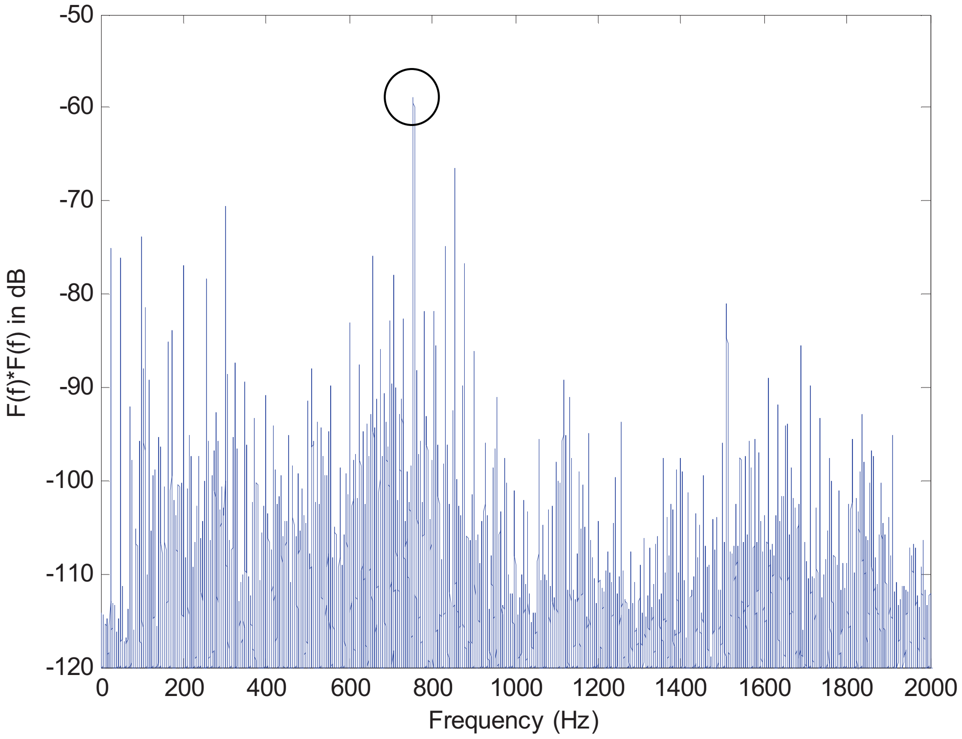

Figure 3.9 - Frequency spectrum of the motor vibration signal showing the rotor slot passing frequency (Eq. 3.8).

Assuming that the number of rotor slots, *R*, is not known, the results of extracting the frequency components in (Eq. 3.8) with *R* varied for a range of possible values from the spectrum in Figure 3.9 are shown in Figure 3.10. The definition and the usage of SNR in the figure will be discussed in *section 3.3.3*.

Figure 3.10 shows that the highest magnitude component is achieved when the number of rotor slots is 32, which corresponds to the actual number of rotor slots of the test motor.

Table 3.3 presents the results of the rotor slot number estimation technique, based on the rotor slot passing frequency, for the healthy motor and the faulty motor with 4 BRB. The table shows that the technique works 90% of the time for both the healthy motor and the faulty motor. The estimation technique fails for the healthy motor when the load is very low (i.e. 3.6%) and it also fails for the faulty motor when the load is at 21%. The results suggest that the rotor slot number estimation technique based on the rotor slot passing frequency can be unreliable when the load is low (i.e. less than 25%). The reasons for this failure are that the rotor slot passing frequency component is not significantly stronger than the other components in the vibration signal and the vibration signal may contain a number of other strong signal components. It should also be noted that if a number of different motor loads can be obtained, then the number of rotor slots can be found by ignoring the "odd" result.

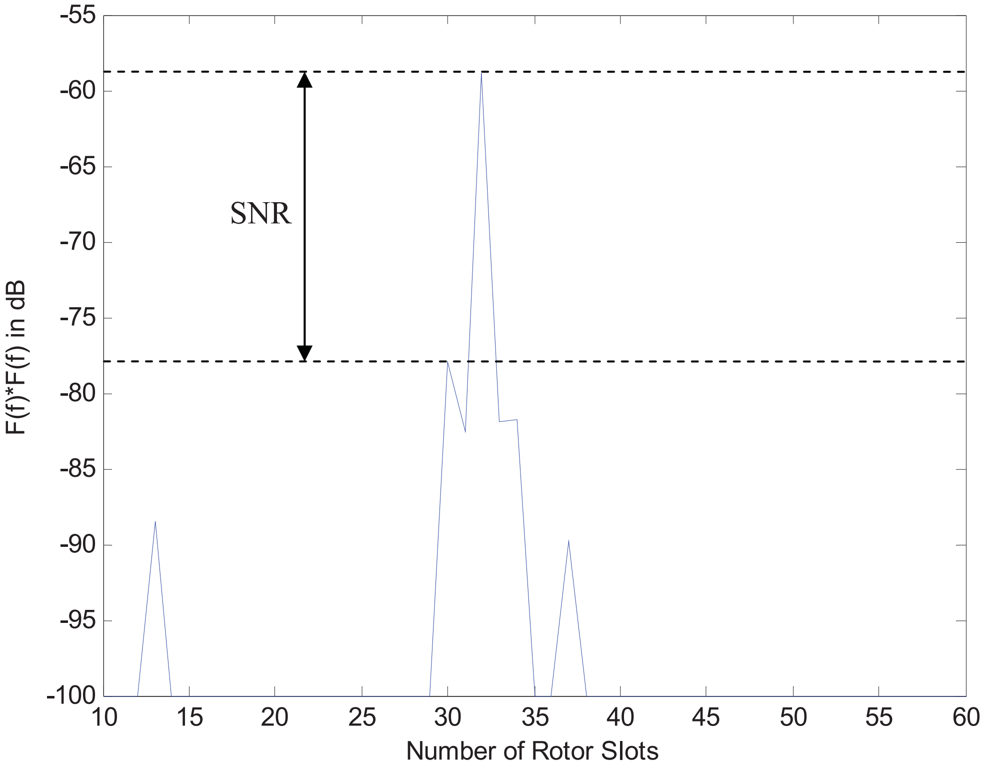

Figure 3.10 - Magnitudes of the possible rotor slot passing frequencies (Eq. 3.8) against the possible number of rotor slots in the vibration spectrum.

Table 3.3 - Rotor slot number estimates based on the rotor slot passing frequency.

Healthy motor		Faulty motor (4 BRB)	
Load (%)	*R*	Load (%)	*R*
3.6	**36**	1.7	32
13.8	32	4.7	32
23.2	32	16.1	32
33.3	32	21.0	**35**
43.4	32	29.2	32
53.0	32	41.4	32
63.4	32	61.3	32
74.0	32	83.9	32
85.3	32	105.3	32
96.9	32	119.0	32

3.3.3. Comparison of Rotor Slot Number Estimation Techniques

In order to measure the performance of the different rotor slot number estimation techniques, a signal to noise parameter as defined in (Eq. 3.9) is utilised. This parameter measures the signal to noise ratio between the eccentricity component (Eq. 3.7) or the rotor slot passing frequency component (Eq. 3.8) and the second highest magnitude of the possible eccentricity component or the possible rotor slot passing frequency component when R is varied (see Figure 3.10).

$$SNR_{rsne}(dB) = Signal(dB) - Noise(dB) \tag{Eq. 3.9}$$

Figure 3.11 shows how the three different rotor slot number estimation techniques perform on the healthy motor. The figure shows that the technique using the stator current gives the highest SNR on average and its SNR can reach 50 dB. However, the SNR drops when the load is at around 4% and 85% but the technique still manages to provide a positive SNR, which means the technique is still able to estimate the correct number of rotor slots. The SNR of the technique using the axial leakage flux is quite constant at around 20 dB. The SNR of the technique using the motor vibration seems to decrease as the load decreases. When the load is less than 4%, the technique actually fails as shown by the negative SNR. This shows that the technique from the motor vibration can be unreliable at very light loads for the healthy motor.

Figure 3.12 shows a similar comparison of the three estimation techniques using the faulty motor with 4 BRB. The figure demonstrates that the technique using the stator current gives the highest SNR on average and the SNR is quite constant at around 20 dB, especially at higher loads (greater than 20%). However, the SNR drops when the load is less than 5% and also at 21% but the technique is still able to produce the correct result. The SNR of the technique using the axial leakage flux is quite constant at around 10 dB, but the SNR of the technique using the motor vibration signal is found to be very low (barely positive). However, the vibration technique still manages to produce the correct result under most loading conditions, except at 21% load.

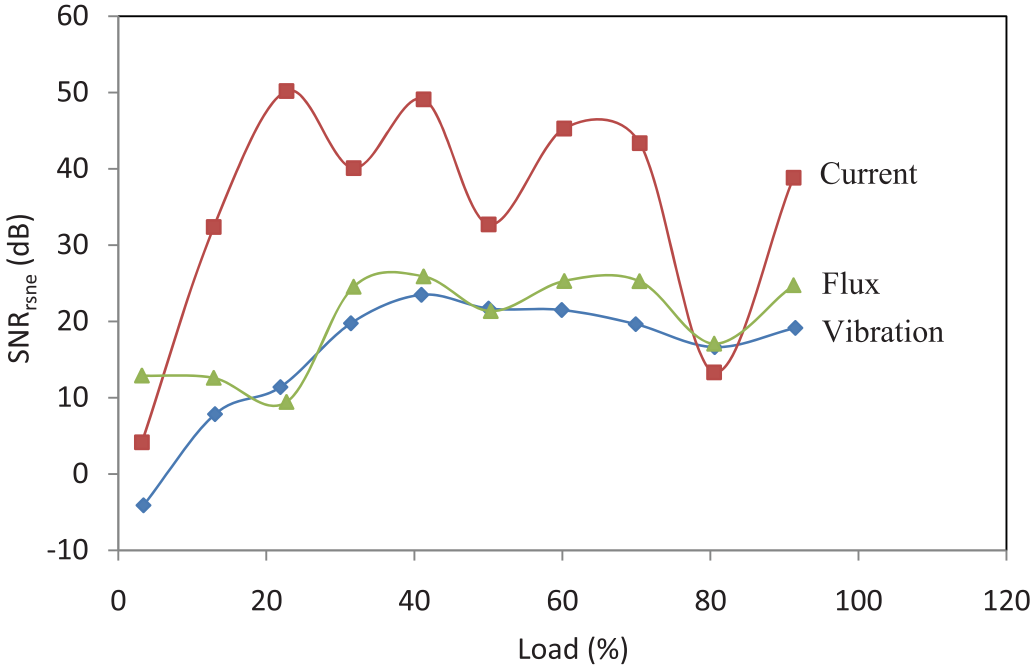

Figure 3.11 - SNR of the rotor slot number estimation techniques for the healthy motor.

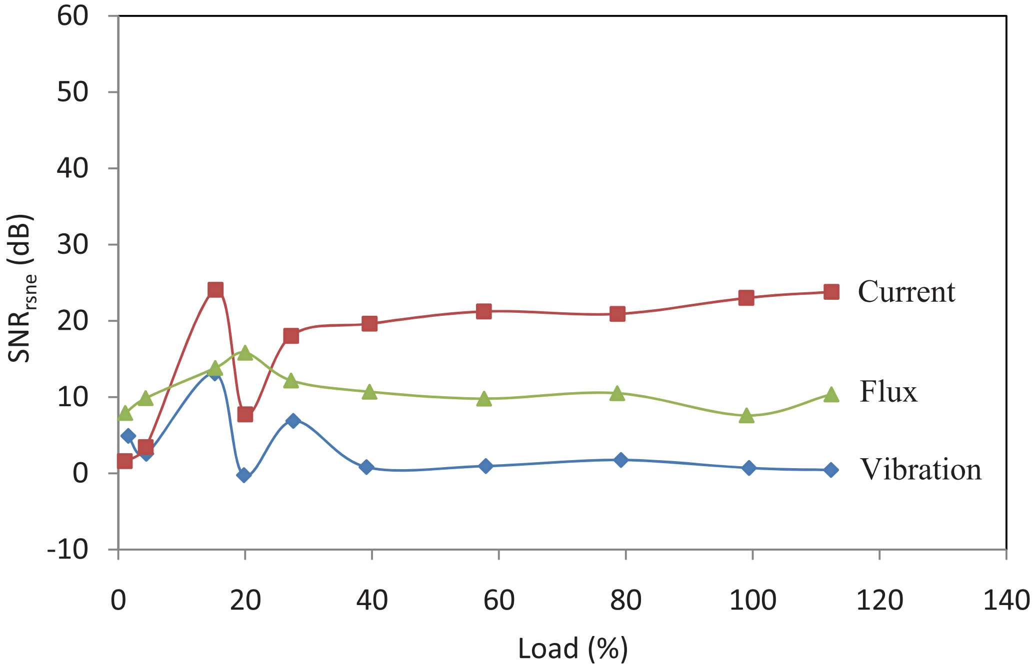

Figure 3.12 - SNR of the rotor slot number estimation techniques for the faulty motor (4 BRB).

Comparison of Figure 3.11 and Figure 3.12 shows that the presence of broken rotor bar faults reduces the effectiveness/performance of all three rotor slot number estimation techniques. The broken rotor bar faults can reduce the SNR by up to 30 dB (~60%) in the stator current signal, up to 15 dB (~60%) in the axial leakage flux signal, and up to 20 dB (~80%) in the motor vibration signal. However, the rotor slot number estimation technique, which is using the eccentricity component (Eq. 3.7), in the current and the flux signals can still detect the number of rotor slots (bars) reliably even if a fault of 4 BRB is present. In general, the technique using the stator current is the best method for both the healthy motor and the faulty motor as it provides the highest SNR on average.

3.3.4. Combining Rotor Slot Number Estimation Techniques

The performance of the individual rotor slot number estimation techniques can be further improved by combining the different techniques. The different rotor slot number estimation techniques can be combined by multiplying the component magnitudes of the possible rotor slot dependent frequencies from the three techniques (i.e. current, leakage flux, and vibration techniques), as given in (Eq. 3.10).

$$\begin{aligned} |F(f)|^2_{combined}(R) \\ &= |F(f_{ecc2})|^2_{current}(R) \times |F(f_{ecc2})|^2_{flux}(R) \\ &\times \left|F\left(f_{rsp}\right)\right|^2_{vibration}(R) \end{aligned} \qquad \text{(Eq. 3.10)}$$

where $|F(f)|^2$ is the magnitude of the signal component at frequency *f*.

Figure 3.13 shows a typical result of combining the three different estimation techniques for a range of possible number of rotor slots, R, on the healthy motor running at full load. The figure shows that the highest magnitude component is achieved when the number of rotor slots is 32, which corresponds to the actual number of rotor slots of the test motor.

Table 3.4 summarises the results of the combined rotor slot number estimation techniques on two different motors, the healthy motor and the faulty motor with four broken rotor bars (BRB), under multiple loading conditions. The results indicate that the combined rotor slot number estimation technique can successfully determine the number of rotor slots for the two test motors under the entire loading conditions.

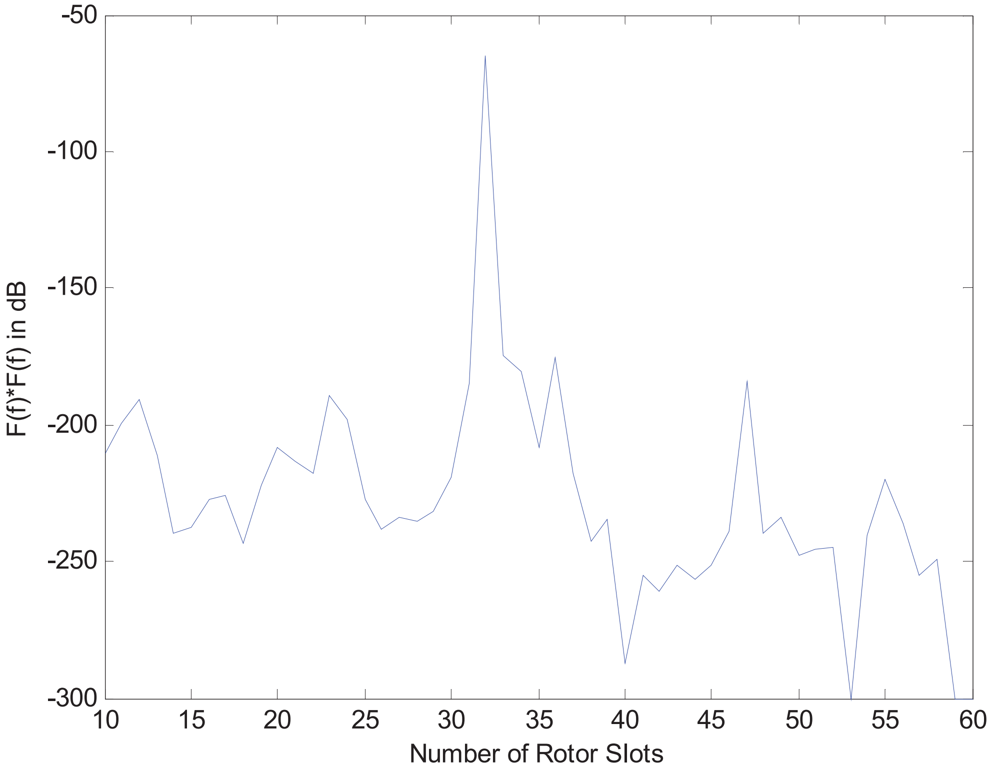

Figure 3.13 - Magnitudes of the combined rotor slot number estimation techniques using (Eq. 3.10) as a function of the possible number of rotor slots.

Table 3.4 - Rotor slot number estimates based on combining the rotor slot number estimation techniques.

Healthy motor		**Faulty motor (4 BRB)**	
Load (%)	*R*	Load (%)	*R*
3.2	32	1.0	32
12.9	32	4.3	32
22.7	32	15.3	32
31.8	32	20.0	32
41.2	32	27.2	32
50.0	32	39.6	32
60.2	32	57.6	32
70.4	32	78.7	32
80.5	32	99.0	32
91.2	32	112.4	32

Figure 3.14 shows how the combined rotor slot number estimation techniques perform on the healthy and faulty (4 BRB) motors. The figure shows that the SNR of the combined techniques for the healthy motor is significantly better (about 2 - 3 times higher) than the SNR of the individual techniques. Similarly, the SNR of the combined techniques for the faulty motor is about 3 - 6 times better than the SNR of the individual techniques.

However, as in the case of the individual techniques, the presence of broken rotor bar faults reduces the SNR of the combined technique, but only by about 35% instead of 60% – 80%.

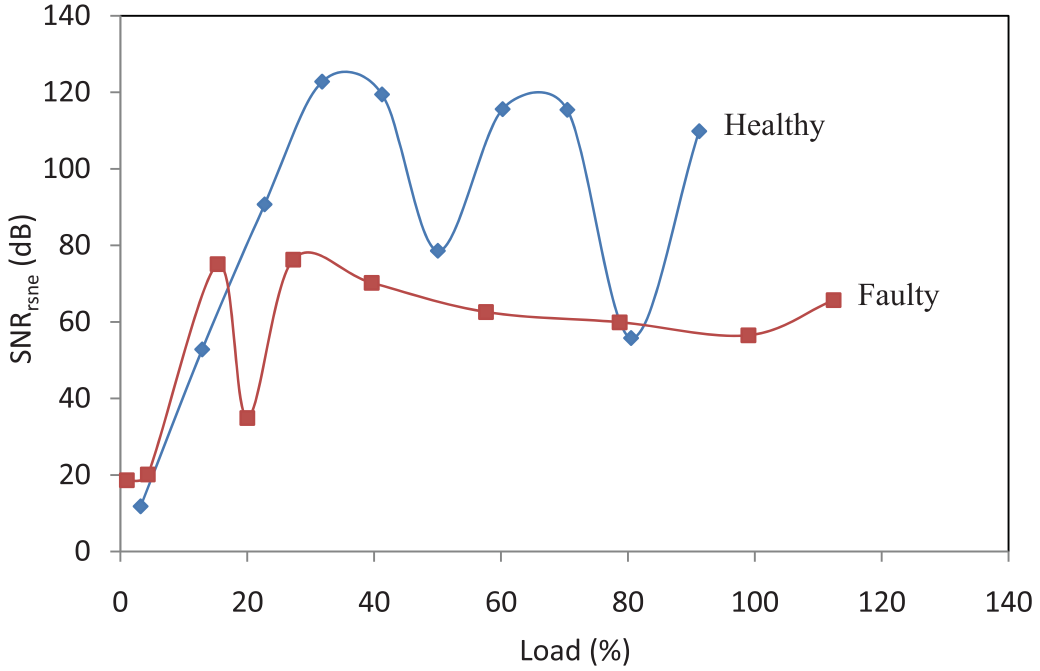

Figure 3.14 - SNR of the combined rotor slot number estimation techniques for the healthy and faulty (4 BRB) motors.

3.4. Summary

This chapter investigated the use of the stator current, the axial leakage flux, and the motor vibration sensor measurements to estimate the rotor speed and the number of rotor slots of a three-phase induction motor based on measurements obtained at a single operating point. Operating points varying from no-load to full-load were tested. The study investigated four different rotor speed estimation techniques, which were based on the eccentricity harmonics, slip frequency, and the rotor frequency. Similarly, rotor slot number estimation techniques based on the eccentricity harmonics and the rotor slot passing frequency were examined. A summary of the key results are as follows:

- The rotor speed can be accurately determined from any of the current, flux and vibration sensor measurements, at any value of load.
- The speed estimation techniques that utilise the eccentricity harmonics and the rotor frequency are able to operate down to very light loads compared to utilising the slip

frequency. As such, the work in this thesis will utilise the rotor frequency from the motor vibration signal in order to determine the rotor speed.

- The number of rotor slots can be detected accurately from the stator current and the axial leakage flux signals by utilising the rotor speed and the eccentricity harmonics.
- The rotor slot number estimation using the vibration signal is dependent on the loading conditions and the fault conditions of the motor.
- The presence of broken rotor bar faults reduces the SNR of the rotor slot number estimation techniques by about 60% - 80%.
- Combining the different rotor slot number estimation techniques significantly increases the SNR of finding the correct number of rotor slots and thus improves the rotor slot number estimation of both the faulty and healthy motors.

Chapter 4. Baseline Study of Induction Motors

4.1. Introduction

The reliability of condition monitoring techniques depends upon a thorough understanding of the electrical and mechanical characteristics of induction motors in both the healthy and faulty states. Although an induction motor is highly symmetrical, the presence of any kind of fault in it modifies its symmetrical property. This disruption to its symmetry produces characteristic fault frequencies in the measured sensor signals, where different types of faults produce different characteristic fault frequencies (see *Section 1.3*). The increase or decrease in the magnitude of the fault frequencies can be used for fault detection. However, it is observed that even healthy machines may have a detectable signal component at the fault frequencies. Furthermore, it is not well understood how a particular fault signal magnitude in a given machine and operating condition relates to the presence or absence of a specific fault. For example, the presence of broken rotor bars increases the amplitude of the broken rotor bar sidebands, which can be observed in the stator current and the axial leakage flux spectra. However, even healthy motors have a measurable amplitude at the relevant fault frequencies. Therefore, it is important to investigate and understand the characteristics of the magnitudes of the fault frequency components between the nominally identical healthy motors to be able to set threshold levels to distinguish between healthy and faulty motors.

The work in this chapter is a baseline study to develop a comprehensive database of the non-invasive sensor measurements corresponding to healthy motors. The work also aims to understand the behaviour of the characteristic fault frequency components of the healthy motors as a function of loading conditions.

4.2. Approach Used in Baseline Study

The baseline study is performed on six identical healthy induction motors under steady-state operation. As such, the Fourier transform technique is utilised to analyse the behaviour of the characteristic fault frequency components. The fault frequency components that are investigated (see Table 4.1) include:

- Broken rotor bar sidebands in the stator current and the axial leakage flux signals,
- Eccentricity fault frequencies in the stator current, the axial leakage flux, and the motor vibration signals, and
- Shorted turn fault frequencies in the stator current, the axial leakage flux, and the motor vibration signals.

Table 4.1 – Baseline study of fault frequency components.

Faults	**Sensors**	**Fault Frequency Components**
Broken rotor bar fault	Stator current	(Eq. 1.1)
	Axial leakage flux	(Eq. 1.1)
Eccentricity fault	Stator current	(Eq. 1.2) and (Eq. 1.3)
	Axial leakage flux	(Eq. 1.2) and (Eq. 1.3)
	Motor vibration	(Eq. 1.4)
Shorted turn fault	Stator current	(Eq. 1.5)
	Axial leakage flux	(Eq. 1.5)
	Motor vibration	(Eq. 1.6)

There are three issues that are investigated in this baseline study: phase variation, repeatability, and motor variation. The **phase variation** test measures how much the fault frequency components vary among the three current phases. The **repeatability** test measures the magnitude variation of the fault frequency components of a given healthy motor for 3 repeated measurements as a function of loading condition. Each repeatability test is conducted after the motor has been removed and then replaced again, thus testing the consistency of the test setup as well as the testing procedures. The **motor variation** test measures the magnitude variation of the fault frequency components between the 6 identical healthy motors under different loading conditions. The motor variation test results are displayed as the average magnitude of the fault frequency component for the 6 motors, its standard deviation (s.d.) plots, and the maximum magnitude deviation among the 6 motors for each load. The standard deviation plots (Eq. 4.1) are estimated by interpolating the magnitude of the fault frequency component for each load with a cubic spline fit and calculating the standard deviation of the magnitude between the 6 motors as a function of load. The maximum magnitude deviation (Eq. 4.2) is defined as the maximum magnitude of the fault frequency among the 6 motors for a given load minus the minimum magnitude of the frequency among the 6 motors for the same load.

$$\begin{aligned} lower\ s.d.curve &= mean - s.d. \\ upper\ s.d.curve &= mean + s.d. \end{aligned} \qquad \text{(Eq. 4.1)}$$

$$\begin{aligned} &max\_dev(load, frequency) \\ &\qquad = max(load, frequency, motor1\colon motor6) \\ &\qquad - \ min(load, frequency, motor1\colon motor6) \end{aligned} \qquad \text{(Eq. 4.2)}$$

Figure 4.1 - Figure 4.4 show examples of the measured waveforms obtained from each type of sensor in the data acquisition system with their corresponding frequency spectra when the healthy motor is operating at the rated load. The frequency spectra of the voltage, current, and leakage flux measurements were generated using the data sampled at 400 Hz to give a good resolution at frequencies below 100 Hz (the cut-off frequency), as most of the critical frequencies lie within this range in these three measurements. The vibration spectrum was generated using the data sampled at 8 kHz as most of the critical frequencies in the vibration signal are above 100 Hz but below 2 kHz (the cut-off

frequency). In the analysis, the magnitude of the peaks found is normalized to give a fundamental (50 Hz) peak of 0 dB, except for the magnitude from the vibration signals because its 50 Hz component is not the fundamental component. Instead, the magnitude of the vibration signals is not normalised (i.e. normalised against 0 dB).

The voltage spectrum or the current spectrum is used to determine an accurate value of the fundamental frequency of the mains supply. The vibration spectrum is used to determine the slip frequency and hence the amount of load placed on the motor. The combination of the fundamental frequency, the slip and the motor nameplate data is then used to identify the location of the fault frequencies. For example, the combination of the fundamental frequency and the slip can be used to calculate the broken rotor bar sidebands, which are highlighted in Figure 4.2.

Figure 4.1 - Figure 4.4 show that each sensor produces a different noise level. The voltage, the current, the leakage flux, and the vibration sensors have noise levels of about -95 dB, -90 dB, -60 dB, and -105 dB respectively. The difference in the noise level is due to the quantisation noise in each A/D converter, which depends on the number of bits that the A/D converter used to represent the analogue signal. The noise level can be reduced if an A/D converter with a higher number of bits is utilised.

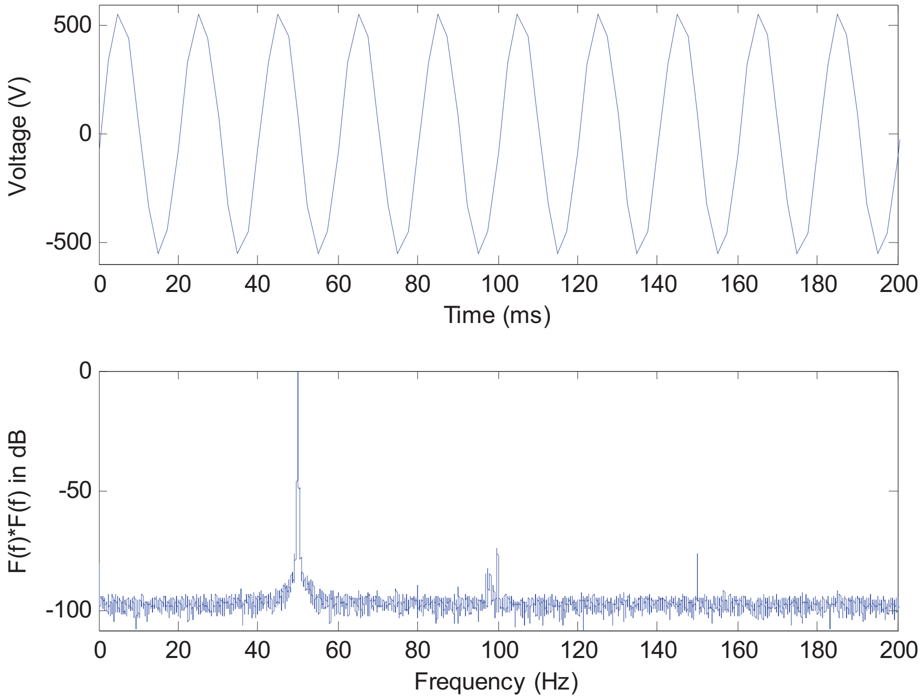

Figure 4.1 - Measured line voltage signal between phase A and B sampled at 400 Hz (top) and its corresponding frequency spectrum (bottom).

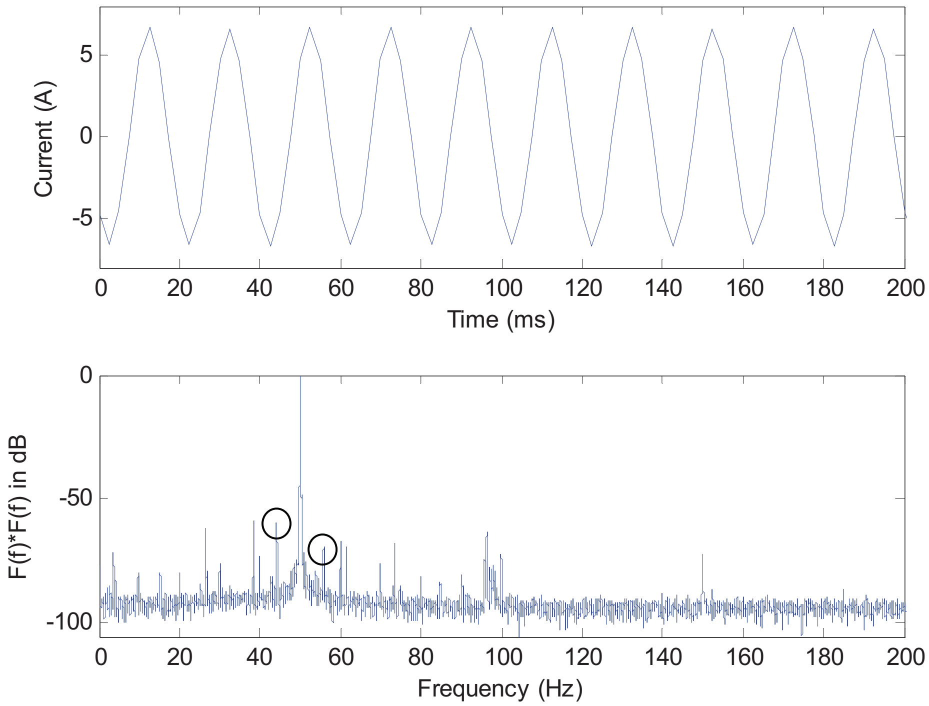

Figure 4.2 - Measured stator current signal of phase A sampled at 400 Hz (top) and its corresponding frequency spectrum (bottom).

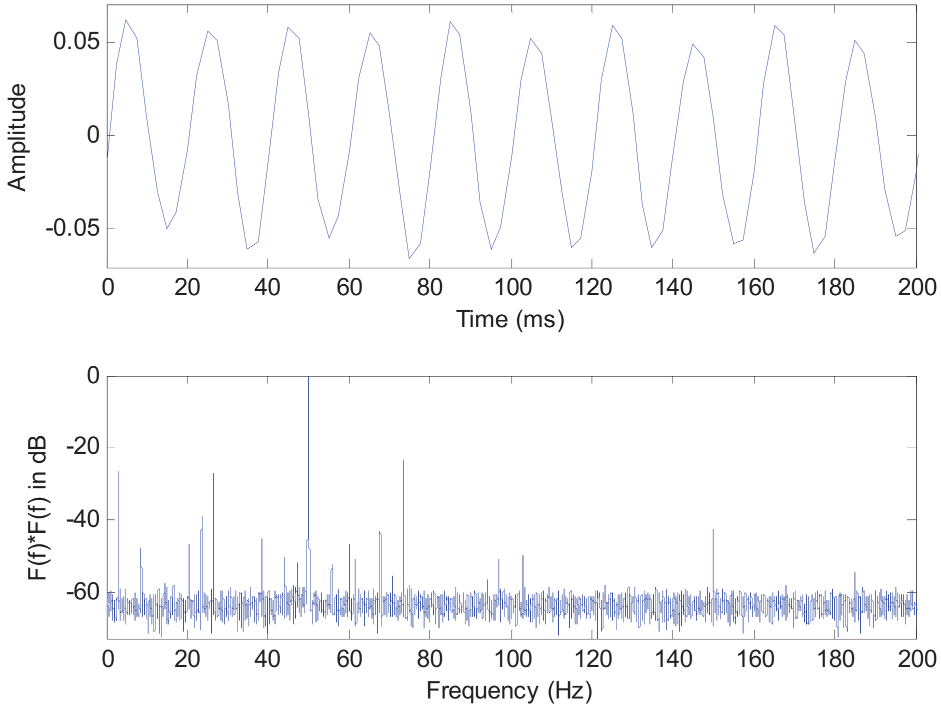

Figure 4.3 - Measured axial leakage flux signal sampled at 400 Hz (top) and its corresponding frequency spectrum (bottom).

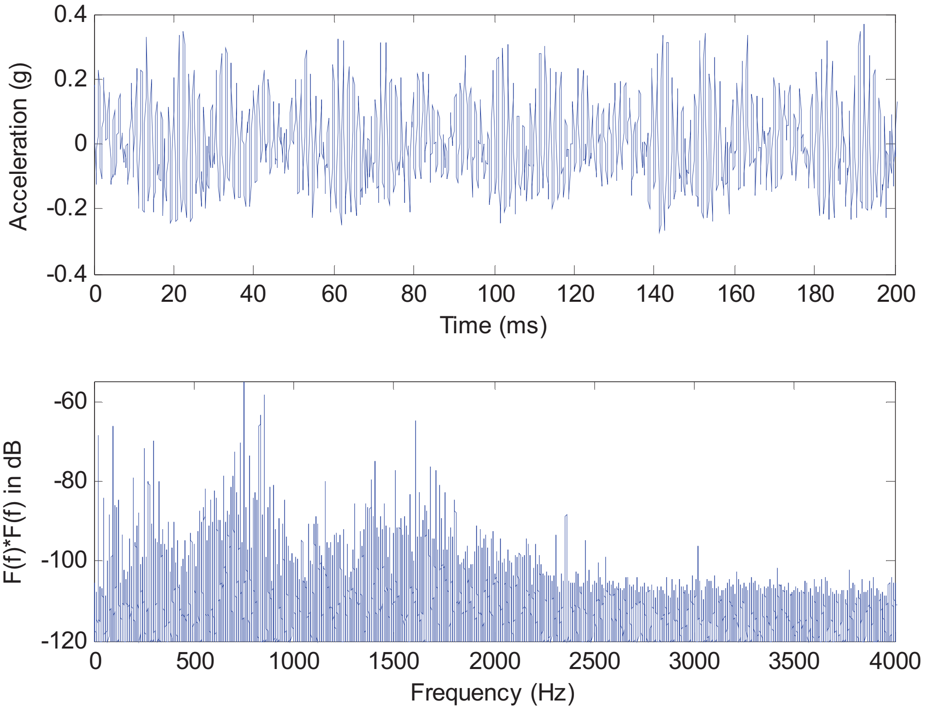

Figure 4.4 - Measured motor vibration signal at DEH sampled at 8 kHz (top) and its corresponding frequency spectrum (bottom).

4.3. Fundamental Frequency

Understanding the behaviour of the fundamental 50 Hz component as a function of load under the repeatability test and the motor variation test is important because the analysis in this thesis always normalises the current and flux fault frequency components to the fundamental. As such, this baseline study will include investigation of the behaviour of the un-normalised fundamental component in both stator current and leakage flux signals.

4.3.1. Repeatability Test

Figure 4.5 shows that the magnitude of the fundamental component from both the current and the leakage flux signals is very consistent among the 3 repeated measurements, indicated by the three different symbols. The magnitude variation around a particular load is on average less than 1 dB. This suggests that both current and leakage flux signals may not need to be normalised when comparing between repeated test measurements.

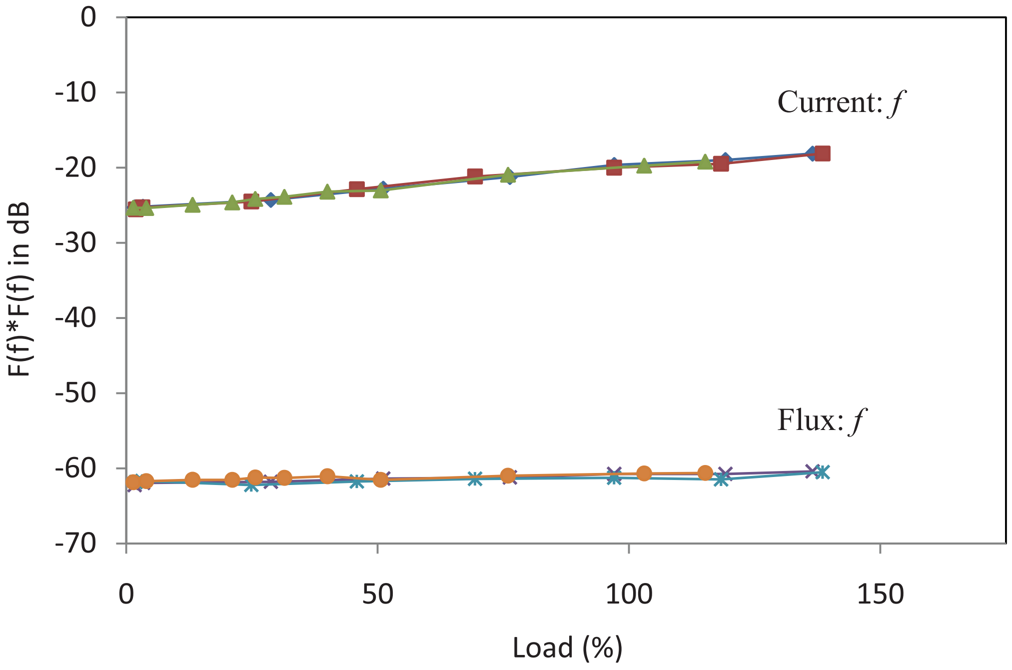

Figure 4.5 - Repeatability test of the fundamental component.

4.3.2. Motor Variation Test

Figure 4.6 shows that the magnitude of the fundamental in the stator current tends to increase with increasing load. This is because the magnitude of the fundamental component is proportional to the stator current while the current drawn increases as the load increases. On the other hand, the magnitude of the fundamental component in the leakage flux doesn't seem to be affected by the load. This is because the leakage flux is not only affected by the stator current but also by the rotor current, coil-end leakage inductance in the stator windings, and end-ring leakage inductance in the rotor cage.

The standard deviation plots of the fundamental component in the current signal (Figure 4.6) show that there is no observable magnitude variation among the identical motors, which means that the magnitude of the fundamental component doesn't change much between the different identical motors. This is to be expected because identical motors should produce similar stator current characteristics. This finding suggests that the current signal may not need to be normalised to the fundamental when comparing between identical motors. On the other hand, the standard deviation plots of the fundamental component in the leakage flux signal show that the magnitude of the fundamental does change among the identical motors. This is because the leakage flux is affected not only by the stator current but also by the combination of the stator current and the rotor current. As a consequence, the leakage flux signal should always be normalised to the fundamental when comparing the motors.

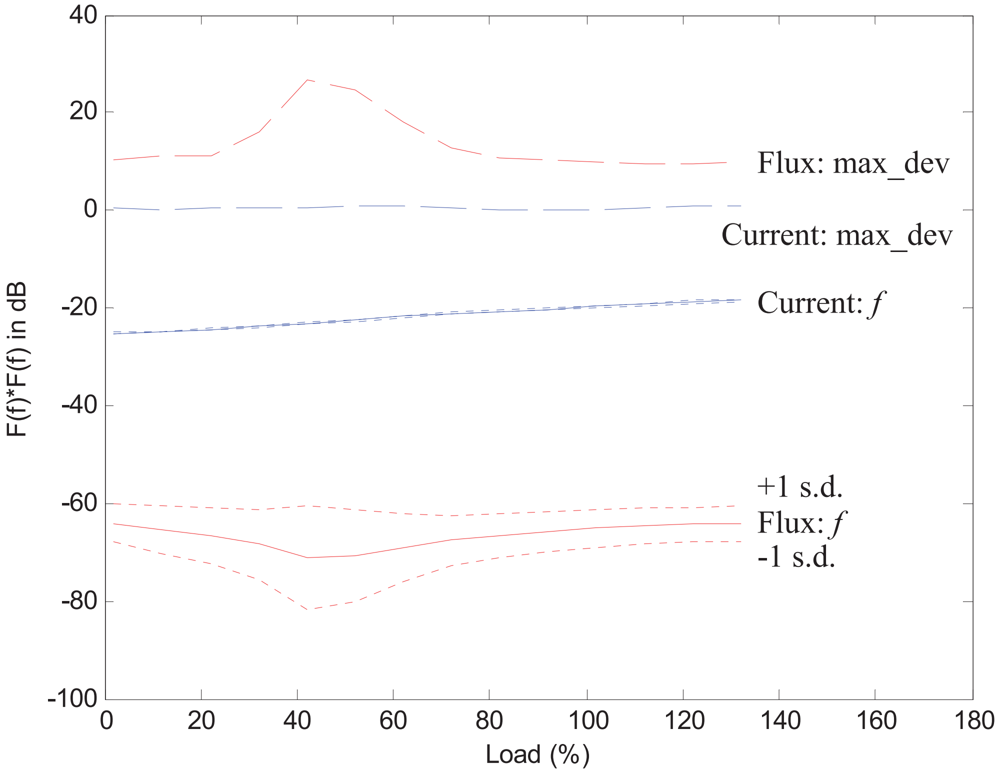

Figure 4.6 - Motor variation test of the fundamental component.

4.4. Broken Rotor Bar Fault Frequencies

The broken rotor bar sidebands, given in (Eq. 1.1), are commonly used to detect broken rotor bar faults. However, these sidebands are also present in healthy motors. Therefore, this baseline study will investigate the characteristics of both the upper and lower sidebands of the broken rotor bar fault frequencies from the stator current and the axial leakage flux in the healthy motors.

4.4.1. Phase Variation Test

Figure 4.7 shows that the magnitudes of the BRB sidebands do not vary much between the different current phases of the motor for all tested loading conditions. The phase variation is observed to be always less than 1 dB. Therefore, it is possible to examine only one of the current phases when investigating BRB faults.

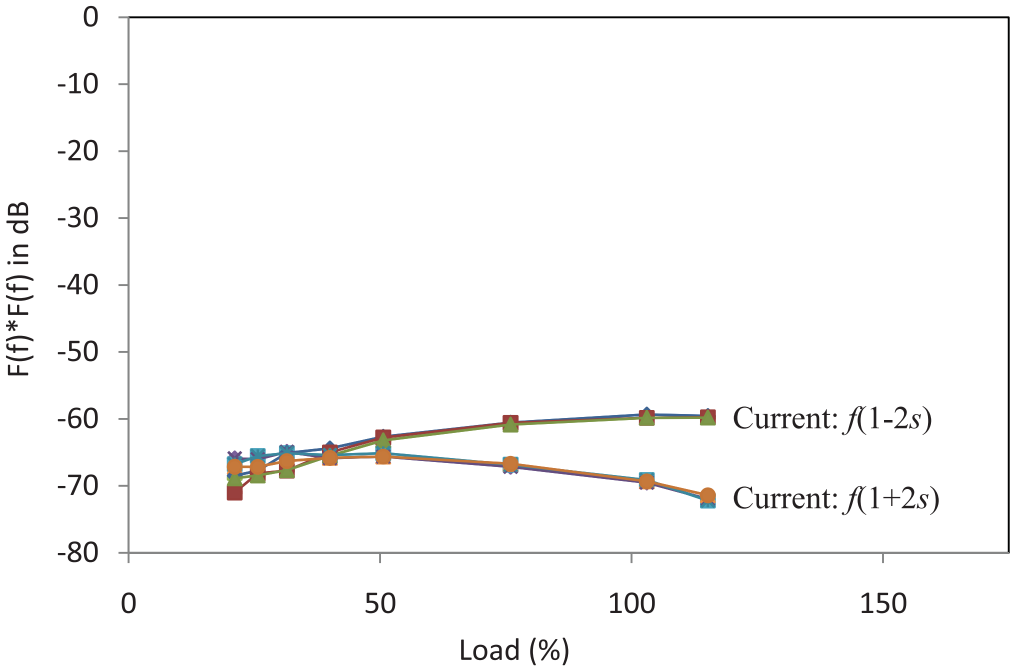

Figure 4.7 – Phase variation test of the BRB sidebands.

4.4.2. Repeatability Test

Figure 4.8 and Figure 4.9 show that the magnitude of the broken rotor bar sidebands from both the current and the leakage flux signals is very consistent among the 3 repeated measurements. The magnitude variation around a particular load is less than 1 dB. These findings suggest that trending of the feature, which is a process to measure the feature continuously or regularly to detect any changes to the feature, is possible.

Figure 4.8 and Figure 4.9 also indicate that it can be difficult to identify the BRB sidebands when the motor is operating at very light loads (less than 15%). When the load is very low, the measured BRB sidebands are very close to the fundamental component (50 Hz) and the magnitude of the BRB sidebands is relatively weak. As a consequence, the fundamental component will overshadow the BRB sidebands, rendering them undetectable. This issue seems to affect both the current and the leakage flux measurements.

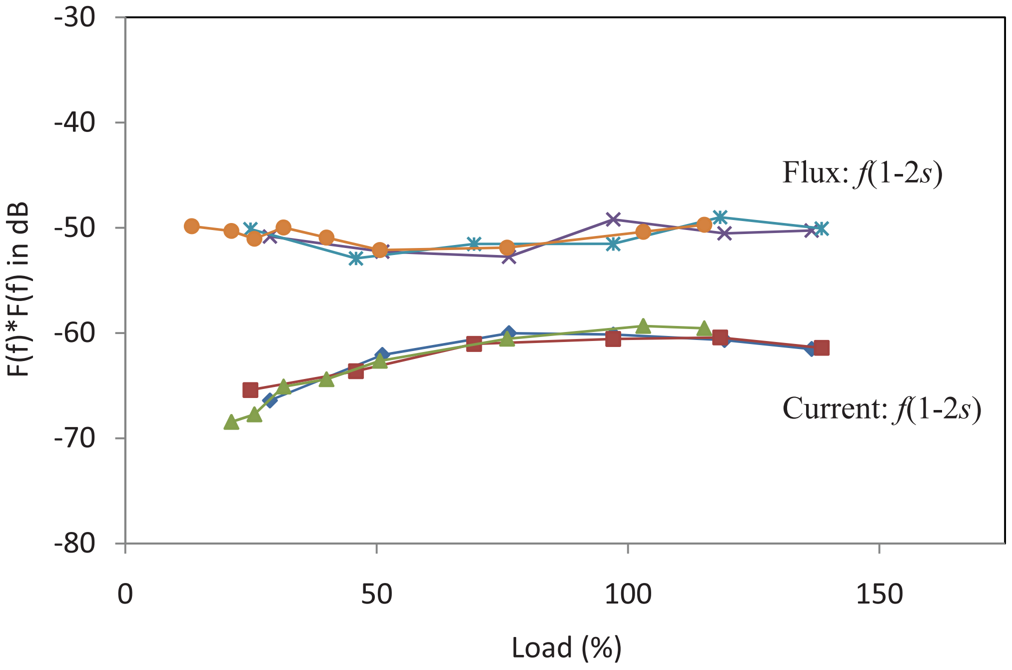

Figure 4.8 – Repeatability test of the lower BRB sidebands.

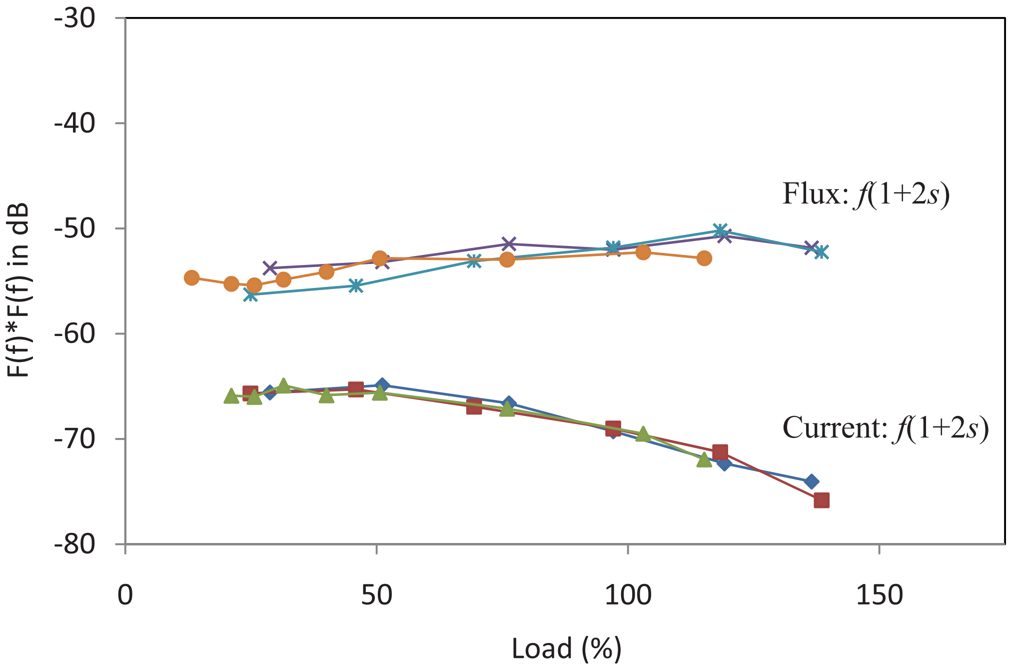

Figure 4.9 – Repeatability test of the upper BRB sidebands.

4.4.3. Motor Variation Test

The analysis of Figure 4.10 - Figure 4.12 shows that the average magnitude of the BRB sidebands seems to be fairly consistent at around -70 dB for the stator current signal and at around -50 dB for the axial leakage flux signal. However, this does not mean that the BRB sidebands are easier to detect in the leakage flux signal than the current signal because the noise level of the leakage flux signal is higher than the noise level of the current signal.

The standard deviation plots of the lower and upper BRB sidebands from the current signal are within about 5 dB of the average magnitude. This shows that the magnitude of the BRB sidebands for two-thirds of the healthy motor population lies within about 5 dB of the average magnitude. The standard deviation plots of the lower BRB sideband from the leakage flux signal reveal that the magnitude for two-thirds of the motor population lies within about 10 dB of the average magnitude. The standard deviation plots of the upper BRB sideband from the leakage flux signal seem to be better, where the magnitude for two-thirds of the motor population lies about 5 dB of the average magnitude.

The maximum deviation plots of the BRB sidebands from the current signal show that the maximum magnitude variation among the 6 motors for each load is about 15 dB. However, the maximum deviation plot of the lower BRB sideband seems to increase with the load, while the maximum deviation plot of the upper BRB sideband is fairly consistent under different loading conditions. The maximum deviation plots of the lower BRB sideband from the leakage flux signal show that the maximum magnitude deviation for each load is about 25 dB. The maximum deviation plots of the upper BRB sideband for the leakage flux signal seem to be better, where that the maximum magnitude deviation for each load is about 15 dB.

These findings show that the upper BRB sideband from either the current or the leakage flux is more consistent (i.e. less magnitude variation) than the lower BRB sideband. The lower BRB sideband from the current signal is also acceptable but its magnitude variation between the identical motors gets larger as the load increases. In general, the magnitude variation of the BRB sidebands among the 6 healthy motors is quite significant, which may prove that setting a threshold level for this feature could be difficult.

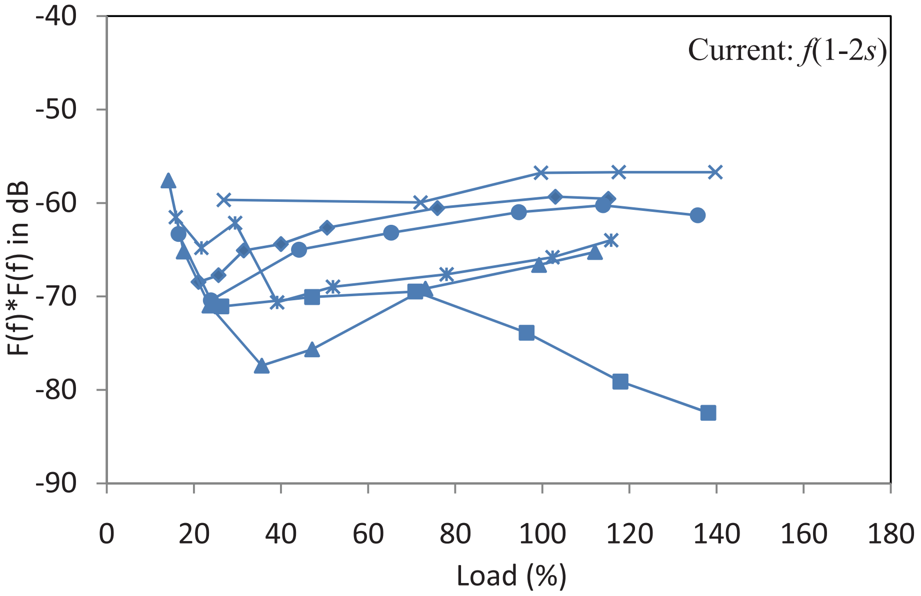

Figure 4.10 – Example of the lower BRB sidebands in the current signals from the six identical motors.

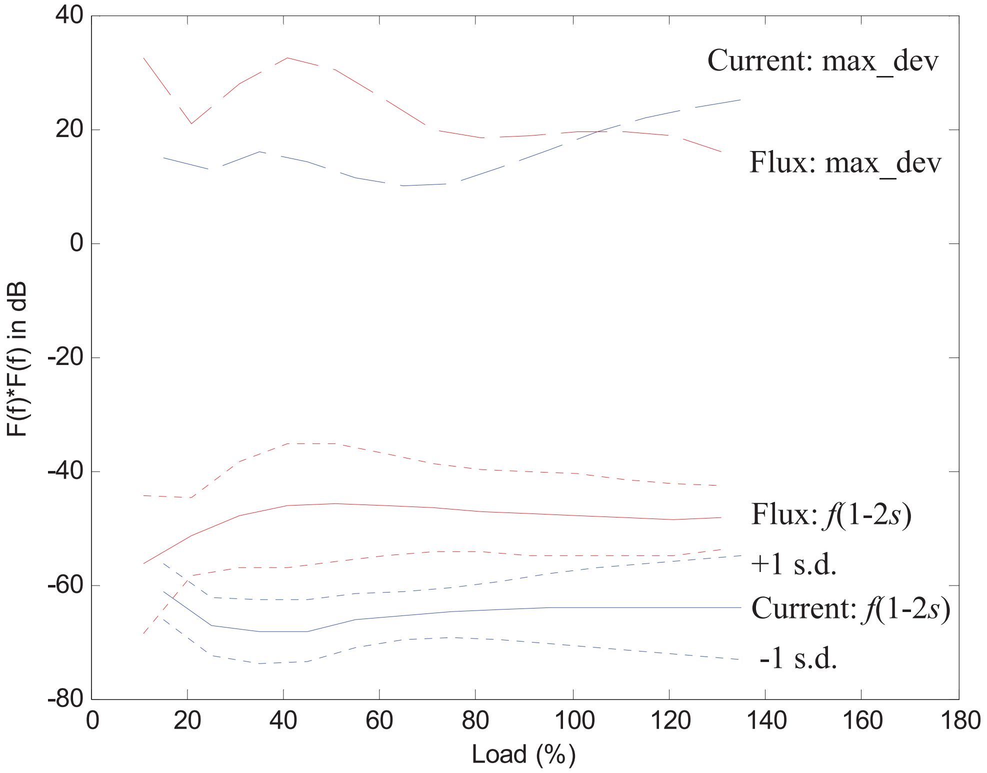

Figure 4.11 – Motor variation test of the lower BRB sidebands.

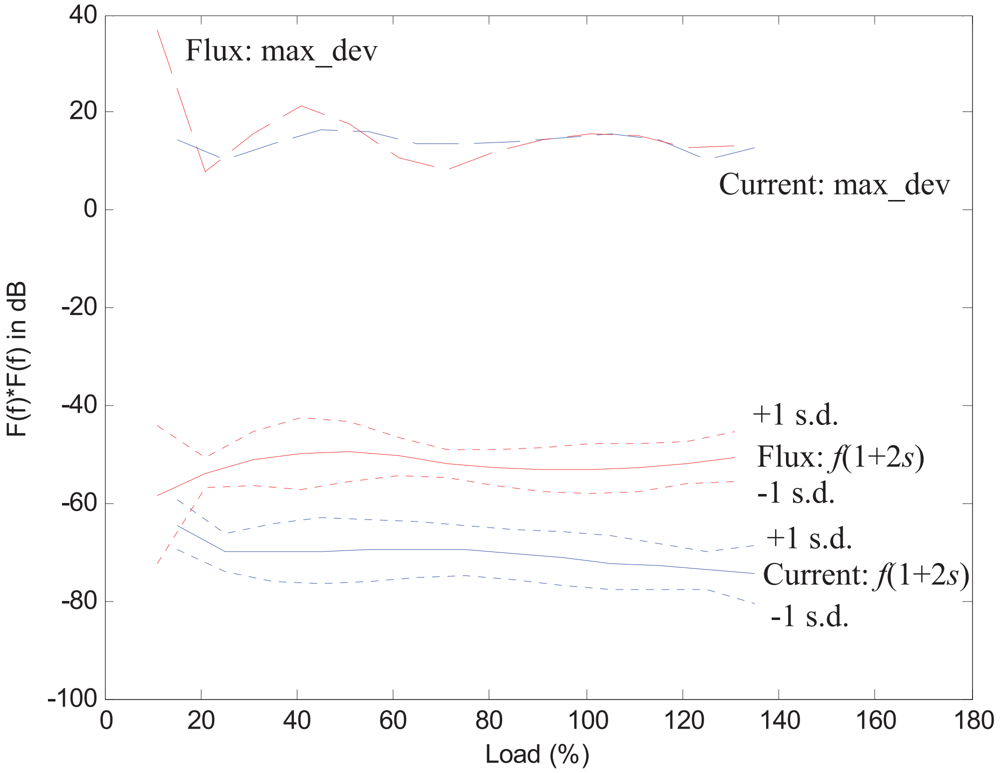

Figure 4.12 – Motor variation test of the upper BRB sidebands.

4.5. Eccentricity Fault Frequencies

The eccentricity fault frequencies, given in (Eq. 1.2) - (Eq. 1.4), are commonly used to detect eccentricity faults in induction motors. However, these frequency components are also present in healthy motors. Thus, this baseline study will investigate the characteristics of the rotor slot harmonics (Eq. 1.2) from the current and flux signals, the rotor frequency sidebands of the fundamental (Eq. 1.3) from the current and flux signals, and the rotor frequency (Eq. 1.4) from the vibration signals in the healthy motors. Furthermore, the baseline study will only consider the first harmonic of the rotor slot frequencies in (Eq. 1.2) because the first harmonic is usually the strongest and the most detectable harmonic based on the experimental study, as will be given later in Chapter 5 and Chapter 6. The experimental study also found that the first few harmonics are usually better in detecting faults. The first harmonic of the rotor slot frequencies in (Eq. 1.2) can be obtained by setting $k = 1$, $n_d = 0$, and $v = 1$, which is expressed in (Eq. 4.3).

$$f_{sede1} = f\left[(R \pm 0)\frac{(1-s)}{p} \pm 1\right] = Rf_r \pm f \qquad \text{(Eq. 4.3)}$$

4.5.1. Rotor slot harmonics

4.5.1.1. Phase Variation Test

Figure 4.13 shows that the magnitudes of the upper rotor slot harmonics do not vary between the different phases but the magnitudes of the lower rotor slot harmonics do vary slightly under the different loading conditions. This slight variation on the lower harmonic may be a result of the weaker signal component, which makes it more susceptible to noise interference. However, the phase variation is observed to be less than 3 dB in most cases. Hence, it is concluded that the examination of one of the current phases is sufficient when investigating the rotor slot harmonics.

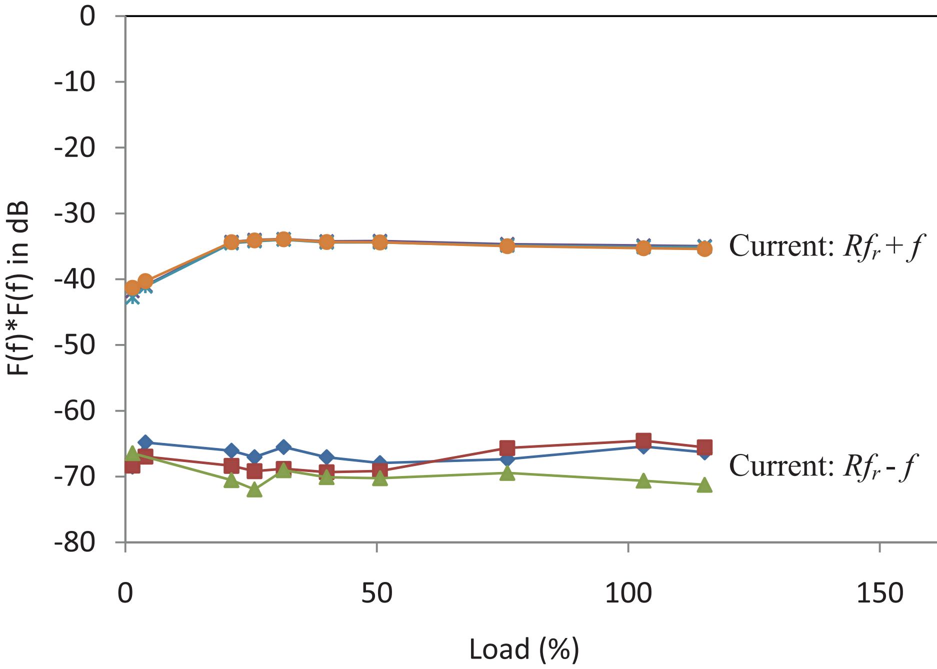

Figure 4.13 – Phase variation test of the rotor slot harmonics.

4.5.1.2. Repeatability Test

Figure 4.14 and Figure 4.15 show that the magnitude of the rotor slot harmonics in (Eq. 4.3) from both the current and the leakage flux signals is very consistent among the 3 repeated measurements. The magnitude variation around a particular load is on average less than 2 dB and the maximum magnitude variation is about 4 dB. These findings suggest that trending of the feature is possible.

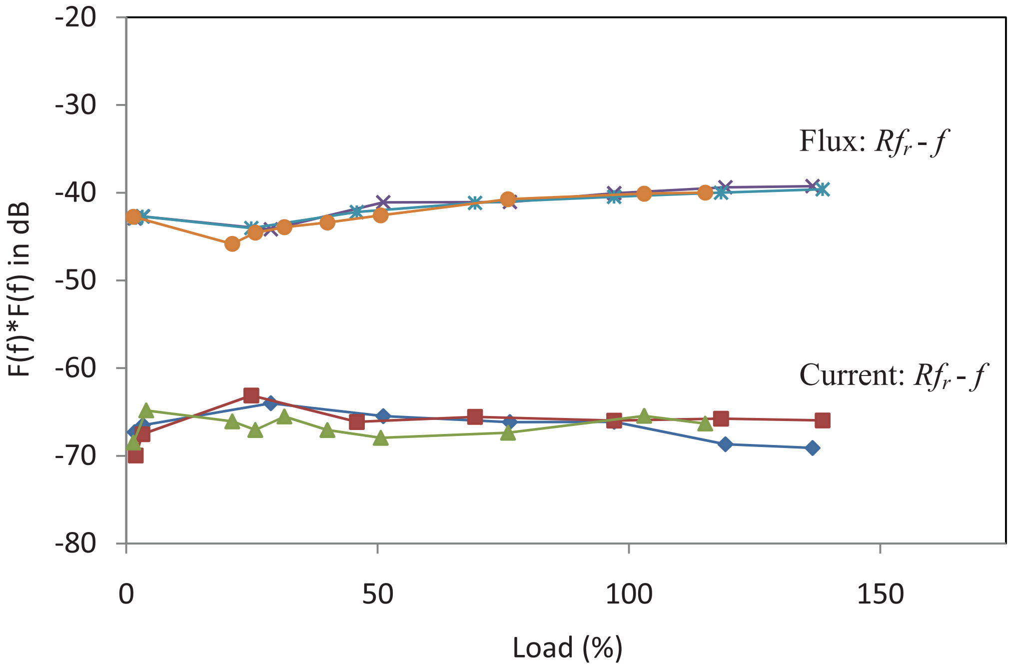

Figure 4.14 – Repeatability test of the lower sideband of the fault frequencies in (Eq. 4.3).

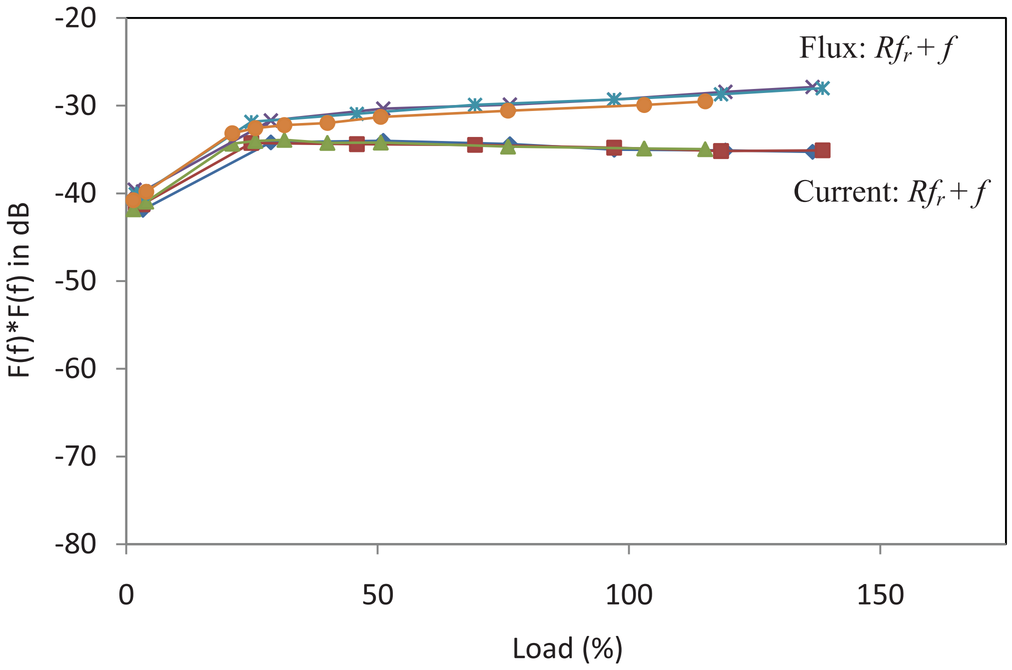

Figure 4.15 - Repeatability test of the upper sideband of the fault frequencies in (Eq. 4.3).

4.5.1.3. Motor Variation Test

The results in Figure 4.16 and Figure 4.17 show that the average magnitude of the lower sideband seems to be fairly constant at around -67 dB for the stator current signal and at around -35 dB for the axial leakage flux signal. The average magnitude of the upper sideband increases as the load is increased from no load to 40% load, and then levels off at around -33 dB for the current signal and around -26 dB for the leakage flux signal.

The standard deviation plots of the lower sideband reveal that the magnitude for two-thirds of the motor population lies within about 5 dB of the average magnitude for the current signal and within about 10 dB of the average magnitude for the leakage flux signal. The standard deviation plots of the upper sideband seem to be similar, where the magnitude for two-thirds of the motor population lies within about 7 dB of the average magnitude for the current signal and within about 10 dB of the average magnitude for the leakage flux signal.

The maximum deviation plots of the lower sideband show that the maximum magnitude variation among the 6 motors seems to decrease as the load increases, where the magnitude variation tends to level off at around 10 dB for the current signal and around 20 dB for the leakage flux signal. The maximum deviation plot of the upper sideband from the current signal seems to be steady at around 20 dB. The maximum deviation plot of the upper sideband from the leakage flux signal seems to increase from 15 dB to 25 dB at light loads (less than 60%) then it decreases again to 15 dB at high loads (greater than 60%).

These findings suggest that the rotor slot harmonics in (Eq. 4.3) are more consistent (i.e. less magnitude variation) in the stator current signal than in the axial leakage flux signal. However, in both signals these harmonics show significant magnitude variation among the 6 healthy motors, which means that setting a threshold for this feature could be difficult.

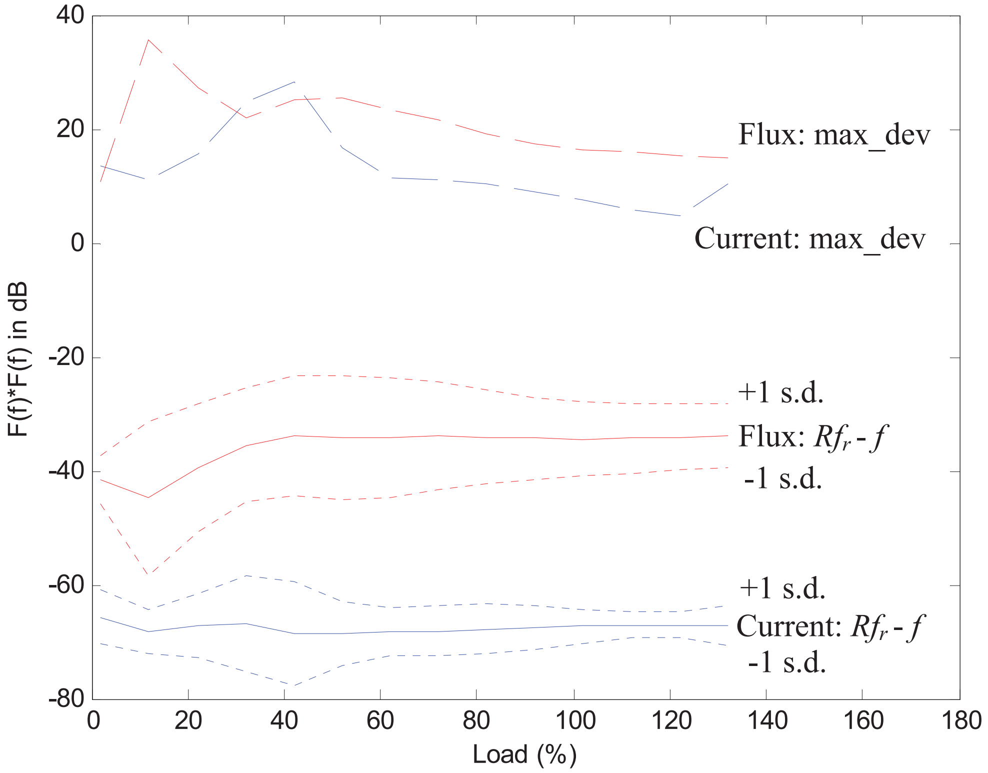

Figure 4.16 – Motor variation test of the lower sideband of the fault frequencies in (Eq. 4.3).

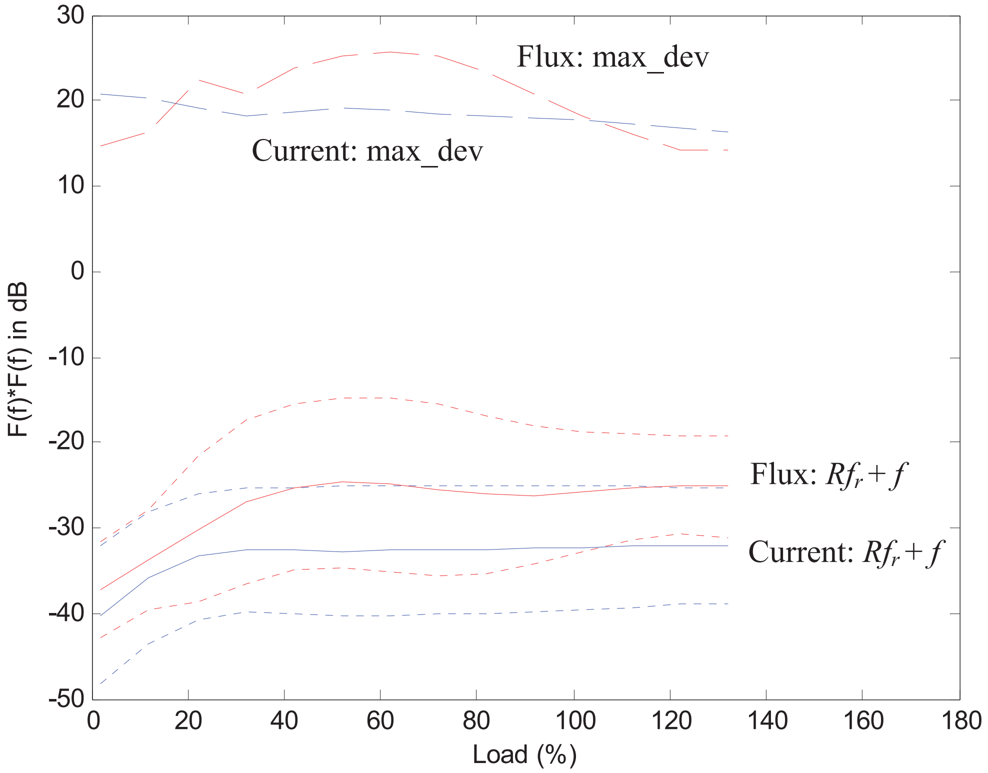

Figure 4.17 - Motor variation test of the upper sideband of the fault frequencies in (Eq. 4.3).

4.5.2. Rotor Frequency Sidebands of the Fundamental

4.5.2.1. Phase Variation Test

Figure 4.18 shows that the magnitudes of the rotor frequency sidebands of the fundamental do not vary much among the different current phases for all tested loading conditions. The phase variation is observed to be always less than 3 dB. Therefore, it is only necessary to examine one of the current phases when investigating the rotor frequency sidebands of the fundamental.

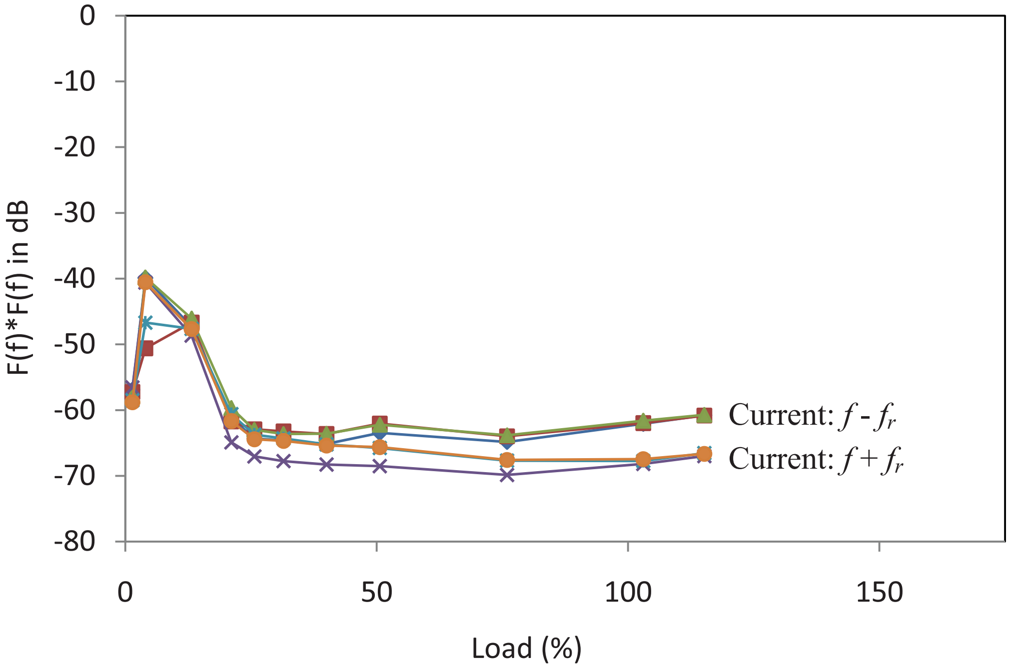

Figure 4.18 – Phase variation test of the rotor frequency sidebands of the fundamental.

4.5.2.2. Repeatability Test

Figure 4.19 and Figure 4.20 show that the magnitude of the rotor frequency sidebands of the fundamental (Eq. 1.3) from the leakage flux signal is very consistent among the 3 repeated measurements but the magnitude from the current signal is found to show significant variation. The magnitude variation from the leakage flux signal is on average less than 1 dB but the magnitude variation from the current signal can be up to 20 dB. These findings suggest that trending of the feature from the leakage flux signal is possible but trending of the feature from the current signal could be difficult.

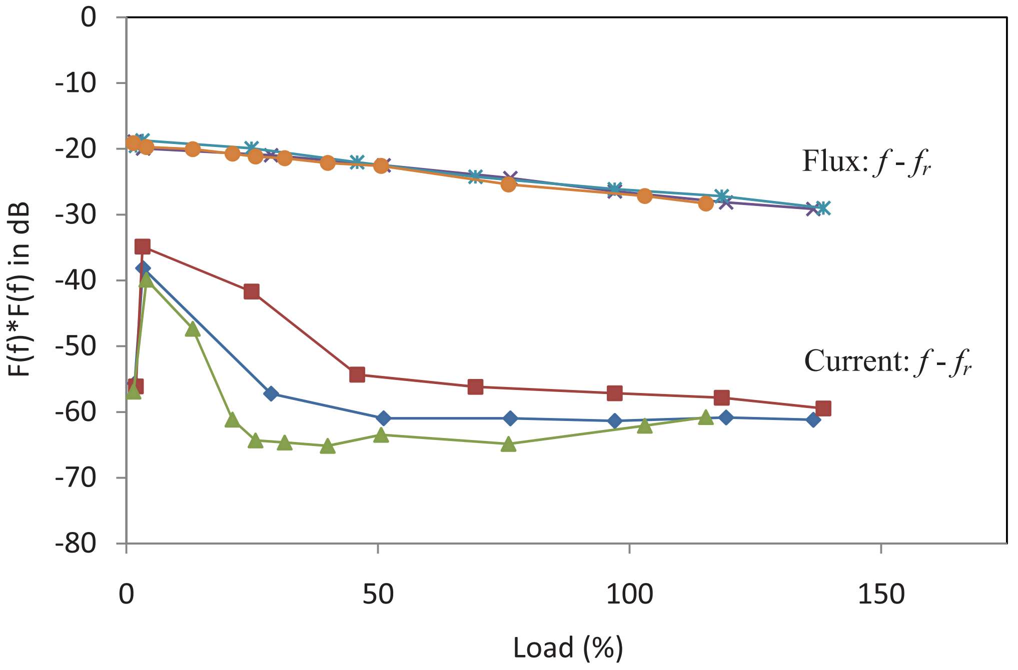

Figure 4.19 – Repeatability test of the lower sideband of the fault frequencies in (Eq. 1.3).

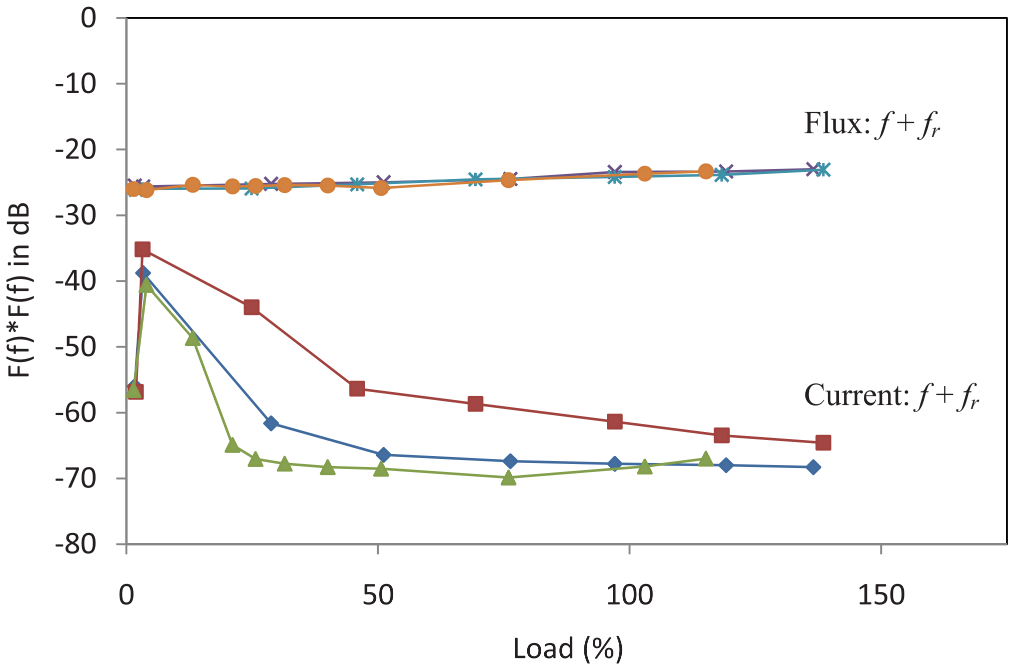

Figure 4.20 - Repeatability test of the upper sideband of the fault frequencies in (Eq. 1.3).

4.5.2.3. Motor Variation Test

The analysis of Figure 4.21 and Figure 4.22 shows that the average magnitude of the lower and upper sidebands from the axial leakage flux seems to be fairly consistent at around -25 to -30 dB. The average magnitude of the lower and upper sidebands from the stator current signal generally falls with increasing load, up to 50% load, then levels off at around -70 dB.

The standard deviation plots of the lower and upper sidebands from both the current and the leakage flux signals reveal that the magnitude for two-thirds of the motor population lies within about 5 - 10 dB of the average magnitude.

The maximum deviation plots of the lower sideband show that the maximum magnitude variation among the 6 motors fluctuates around 15 - 35 dB for both the current and the leakage flux signals. The maximum deviation plots of the upper sideband seem to be steadier at around 20 dB for the current signal and at around 25 dB for the flux signal.

These findings suggest that the fault frequencies in (Eq. 1.3) from the current and the leakage flux signals show similar magnitude variations. However, the feature in both signals shows significant magnitude variation among the 6 healthy motors which may cause setting a threshold for the feature to be difficult.

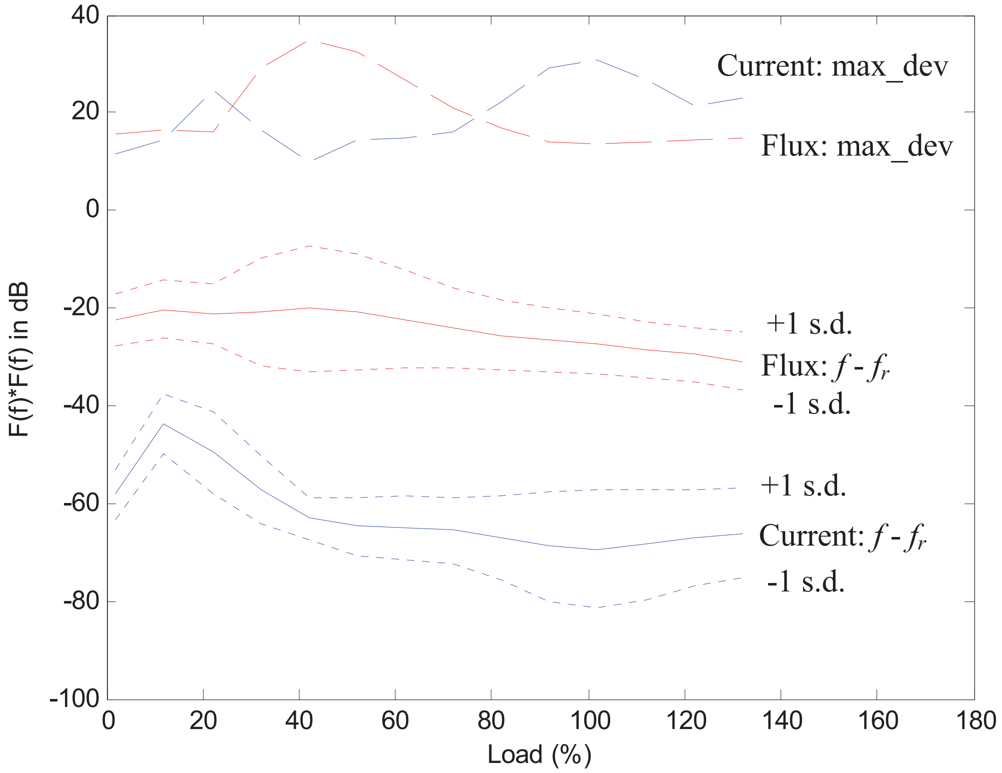

Figure 4.21 – Motor variation test of the lower sideband of the fault frequencies in (Eq. 1.3).

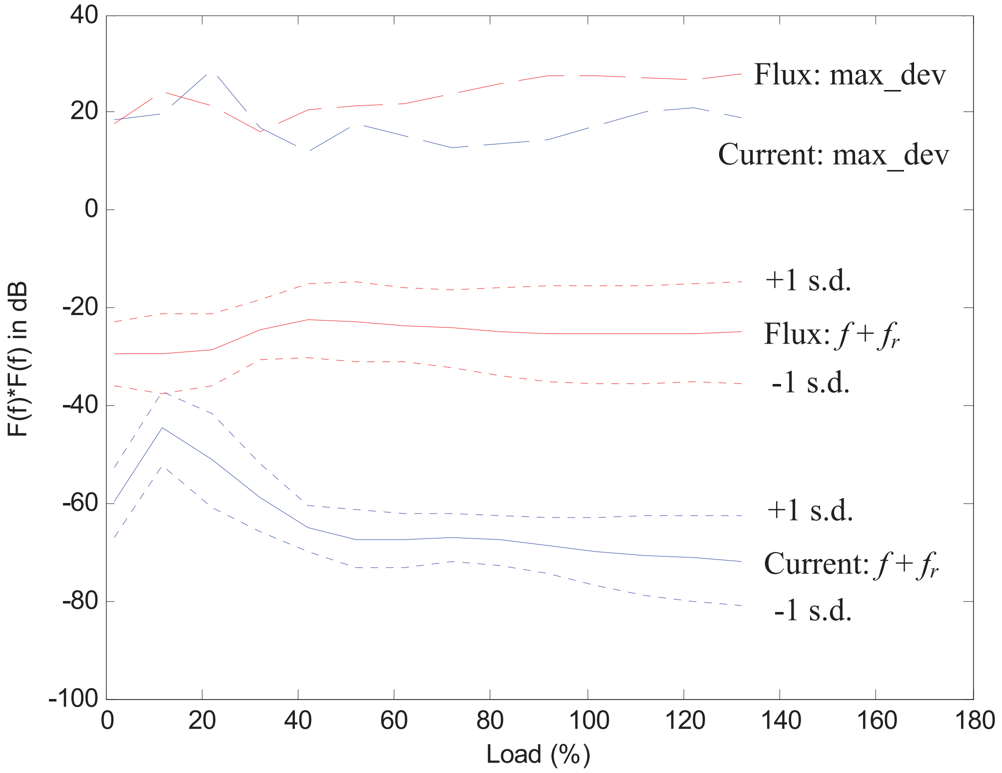

Figure 4.22 - Motor variation test of the upper sideband of the fault frequencies in (Eq. 1.3).

4.5.3. Rotor Frequency

4.5.3.1. Repeatability Test

Figure 4.23 - Figure 4.25 show that the magnitude of the rotor frequency component (Eq. 1.4) from all three motor vibration sensors; driving end horizontal (DEH), non-driving end horizontal (NDEH), and driving end vertical (DEV) sensors; is fairly consistent among the 3 repeated measurements. The magnitude variation around a particular load is less than 4 dB for the three vibration sensors at loads above 25%. These findings suggest that trending of the feature from all three vibration sensors is possible, except for the anomaly at 3% load from the DEH and NDEH signals, which is believed to be due to measurement errors.

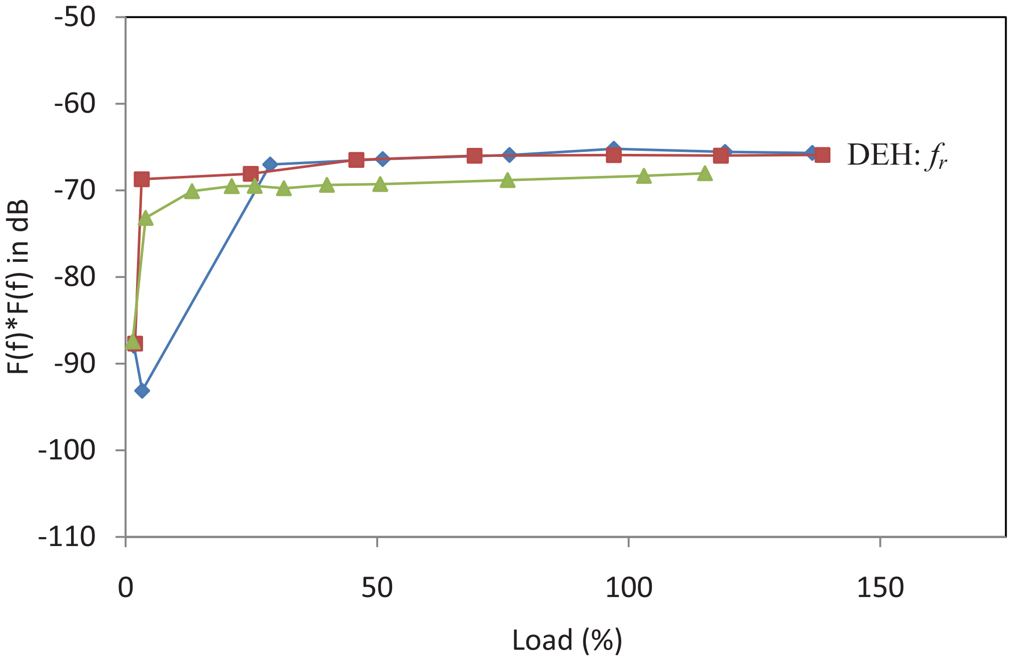

Figure 4.23 - Repeatability test of the fault frequencies in (Eq. 1.4) from the DEH vibration signal.

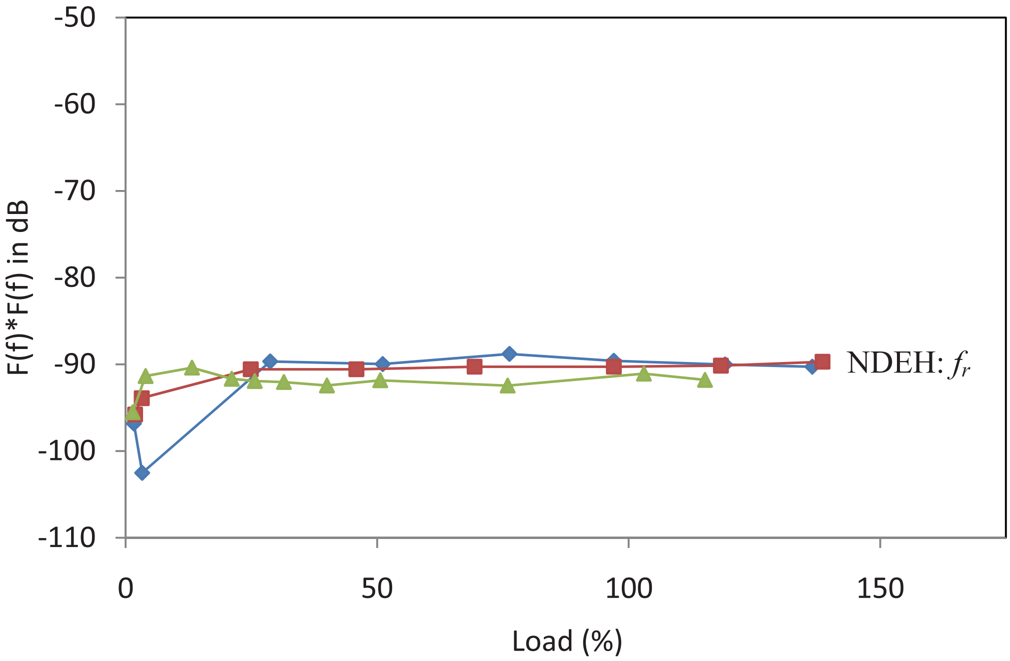

Figure 4.24 - Repeatability test of the fault frequencies in (Eq. 1.4) from the NDEH vibration signal.

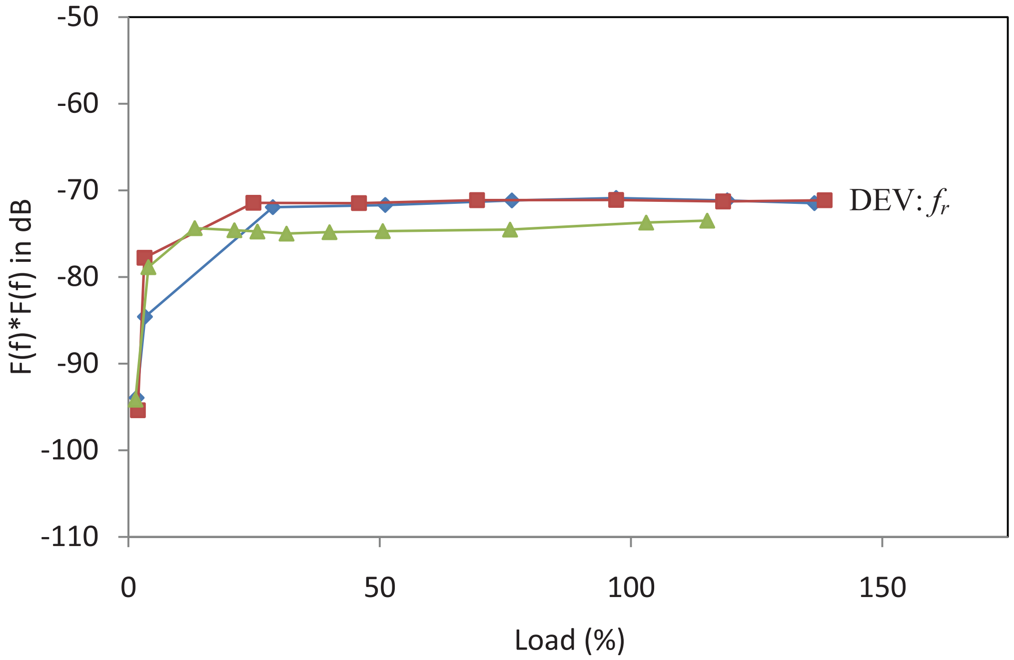

Figure 4.25 - Repeatability test of the fault frequencies in (Eq. 1.4) from the DEV vibration signal.

4.5.3.2. Motor Variation Test

The analysis of Figure 4.26 shows that the average magnitude of the rotor frequency seems to be fairly constant at around -78 dB for the DEH vibration signal, -97 dB for the NDEH vibration signal, and -82 dB for the DEV vibration signal. The difference in the magnitude of the rotor frequency seems to be affected by the location and the orientation of the vibration sensors.

The standard deviation plots of the rotor frequency reveal that the magnitude for two-thirds of the motor population lies within about 10 dB of the average magnitude for the DEH and DEV vibration sensor signals. The standard deviation plot for the NDEH vibration sensor signal seems to be better, where the magnitude for two-thirds of the motor population lies within about 5 dB of the average magnitude.

The maximum deviation plots of the rotor frequency show that the maximum magnitude variation among the 6 motors under each load is about 18 dB for the DEH and DEV vibration signals. The maximum deviation plot from the NDEH vibration sensor seems to be better, where the maximum magnitude variation under each load is about 10 dB.

These findings suggest that the rotor frequency (Eq. 1.4) is most consistent (i.e. least magnitude variation) in the NDEH vibration signal because of the minimal magnitude variation between the 6 motors. As a result, it is possible to set a threshold for the feature in the NDEH vibration signal.

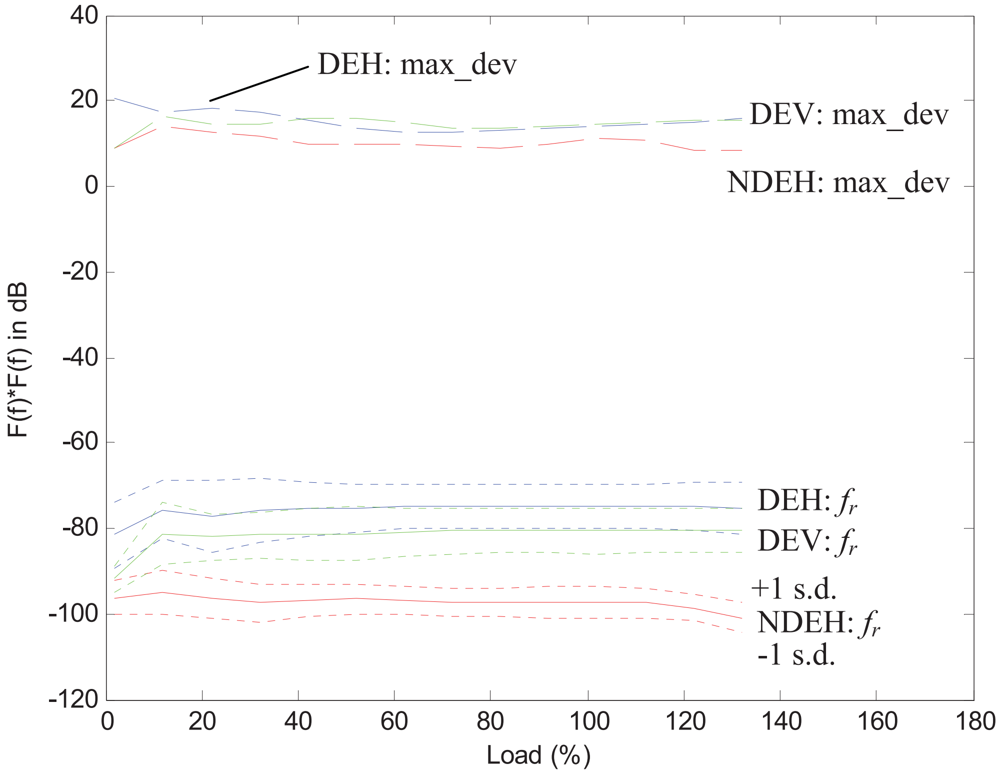

Figure 4.26 – Motor variation test of the fault frequencies in (Eq. 1.4) from the three vibration signals.

4.6. Shorted Turn Fault Frequencies

Harmonics of the fundamental sidebands of the rotor frequency and twice the supply frequency, given in (Eq. 1.5) and (Eq. 1.6) respectively, are commonly used to detect shorted turn faults. However, as demonstrated for the other faults, these frequency components are also present in healthy motors. Thus, this baseline study will investigate the characteristics of the frequency components in (Eq. 1.5) from the current and flux signals and the frequency component in (Eq. 1.6) from the vibration signals in the healthy motors. The baseline study will consider the harmonic of the fault frequencies in (Eq. 1.5) when $k = 1$ and $v = 3$ (Eq. 4.4). This harmonic is chosen because the first harmonic ($k = 1$, $v = 1$) of the fault frequencies in (Eq. 1.5) is the same as the fault frequencies in (Eq. 1.3), see *section 4.5.2*. Note that the first harmonic of the fault frequencies in (Eq. 1.5) can be used to detect both shorted turn faults and eccentricity faults but this harmonic cannot distinguish between the two types of faults.

$$f_{st1} = f\left[\frac{(1-s)}{p} \pm 3\right] = f_r \pm 3f \qquad \text{(Eq. 4.4)}$$

4.6.1. Harmonics of Fundamental Sidebands of Rotor Frequency

4.6.1.1. Phase Variation Test

Figure 4.27 and Figure 4.28 show how the magnitudes of the different phases of the frequency components in (Eq. 4.4) vary under different loading conditions. Figure 4.27 shows that the lower frequency sideband can vary rather significantly, up to 10 dB, between the three phases and Figure 4.28 shows that the upper frequency sideband can vary up to 15 dB between the three phases. This large phase variation can be attributed to this frequency component being rather weak and hence susceptible to noise interference from the testing equipment as well as the testing environment. Because the third harmonic of the fundamental sidebands of the rotor frequency shows quite a significant variation between phases, it will be useful to investigate all three current phases when investigating this frequency component.

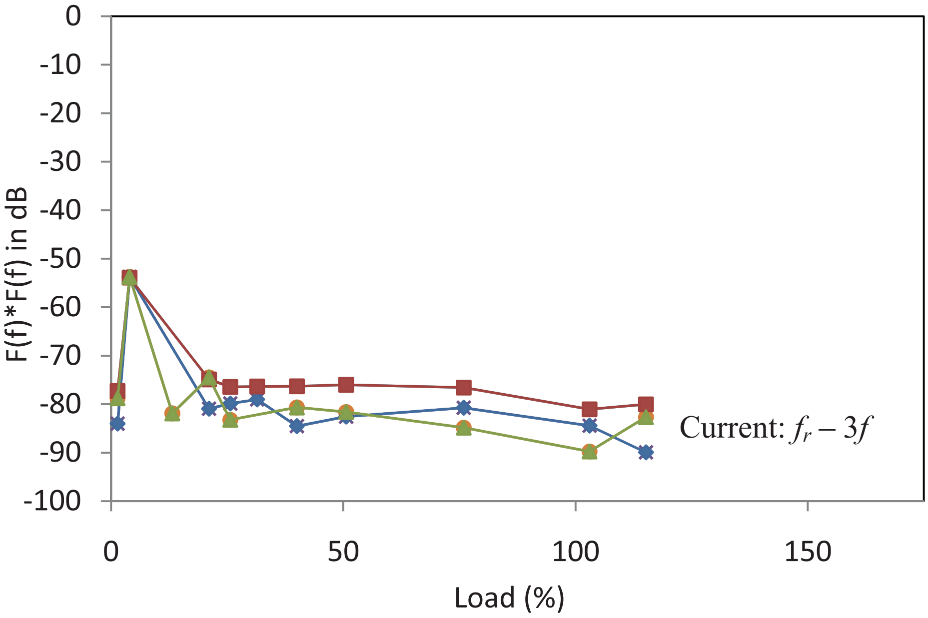

Figure 4.27 – Phase variation test of the lower rotor frequency sideband harmonic.

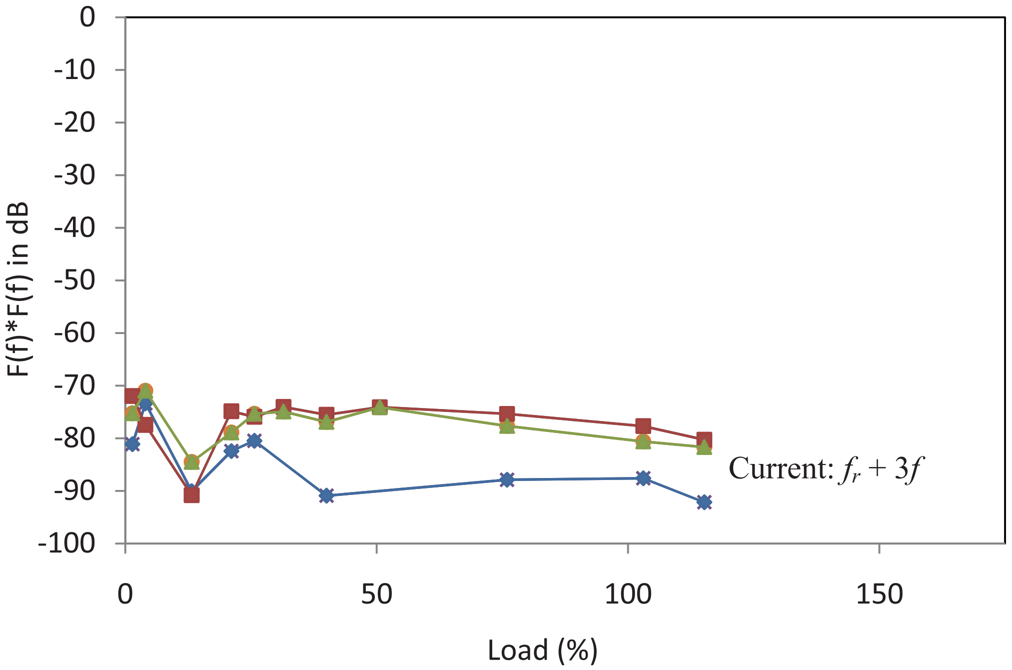

Figure 4.28 - Phase variation test of the upper rotor frequency sideband harmonic.

4.6.1.2. Repeatability Test

Figure 4.29 and Figure 4.30 show that the magnitude of the fault frequency components in (Eq. 4.4) from the leakage flux signal is consistent among the 3 repeated measurements, except for the anomaly for one measurement at around 13% load. On the other hand, the magnitude of the fault frequency components from the current signal is not consistent. Significant magnitude variation can be observed when the load is less than 70%. The magnitude variation in the current signal around a particular load can go as high as 20 dB while the magnitude variation in the leakage flux signal is on average less than 2 dB. These findings suggest that trending of the feature from the leakage flux signal is possible while trending of the feature from the current signal could be difficult unless measurements were only taken when the motor was loaded at greater than 70% of full load.

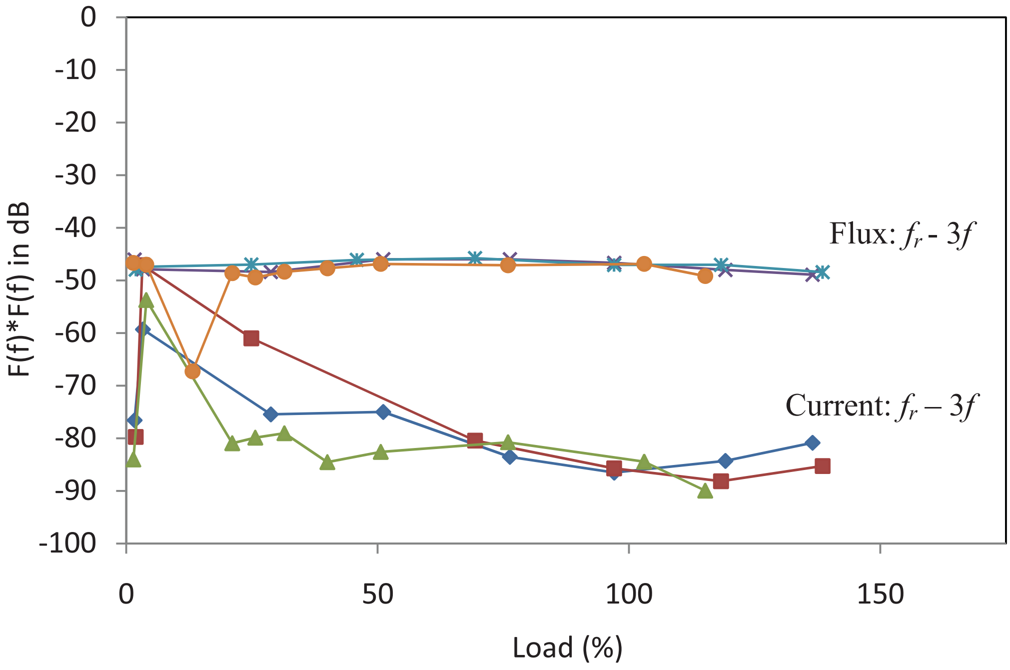

Figure 4.29 - Repeatability test of the lower sideband of the fault frequencies in (Eq. 4.4).

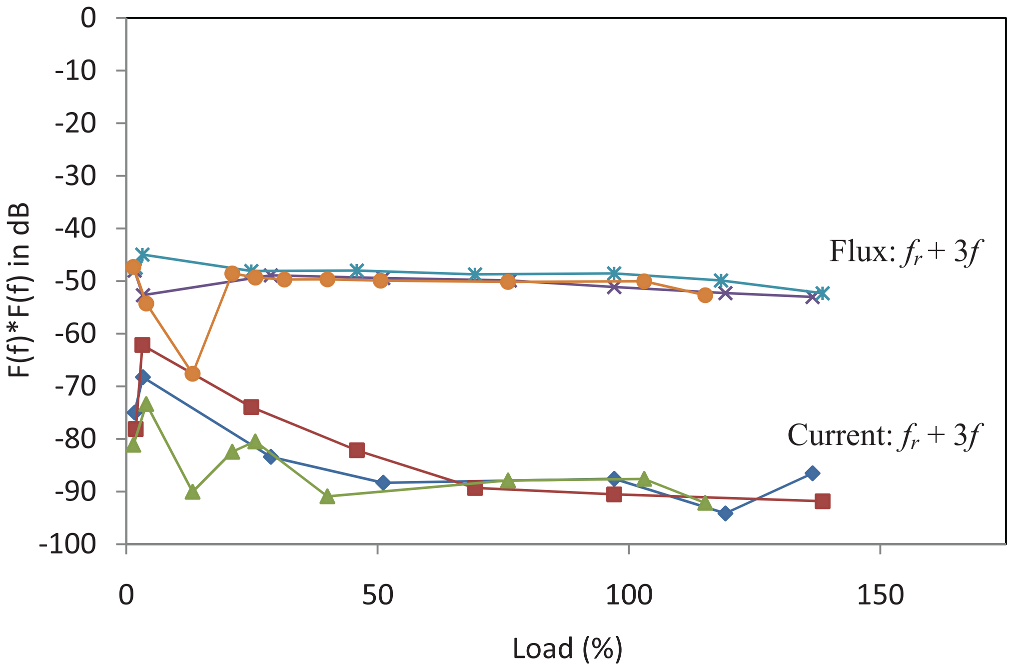

Figure 4.30 - Repeatability test of the upper sideband of the fault frequencies in (Eq. 4.4).

4.6.1.3. Motor Variation Test

It should be noted here that the peaks of the frequency components from the current signal are very weak and many of them are undetectable. As a consequence, the frequency components from the current signal shown in Figure 4.31 and Figure 4.32 are the result of significant interpolation between the available points. The analysis of Figure 4.31 and Figure 4.32 shows that the average magnitude from the leakage flux signal seems to be consistent at around -45 dB for the lower sideband and at around -50 dB for the upper sideband. The average magnitude of both the lower and upper sidebands from the current signal decreases as the load increases. It decreases from around -65 dB (light loads) to -90 dB (high loads) for the lower sideband and from -80 dB (light loads) to -90 dB (high loads) for the upper sideband.

The standard deviation plots of both the lower and upper sidebands from the leakage flux signal are within about 5 - 10 dB of the average magnitude. This means that the magnitude of the fault frequency components for two-thirds of the motor population lies within about 5 - 10 dB of the average magnitude. The standard deviation plots of both the lower and upper sidebands from the current signal show similar characteristics, where the magnitude for two-thirds of the motor population lies within about 5 - 10 dB of the average magnitude.

The maximum deviation plots of both the lower and upper sidebands from the leakage flux signal show that the maximum magnitude variation among the 6 motors fluctuates between 10 and 30 dB. The maximum deviation plots from the current signal show similar characteristics for the lower sideband but the maximum deviation plot of the upper sideband is more consistent at around 17 dB.

These findings suggest that the fault frequencies in (Eq. 4.4) are more reliable in the leakage flux signal than in the current signal because the fault frequency components in the current signal can be difficult to identify. However, this feature in both signals shows significant magnitude variation among the 6 healthy motors which may prove setting a threshold for the feature to be difficult.

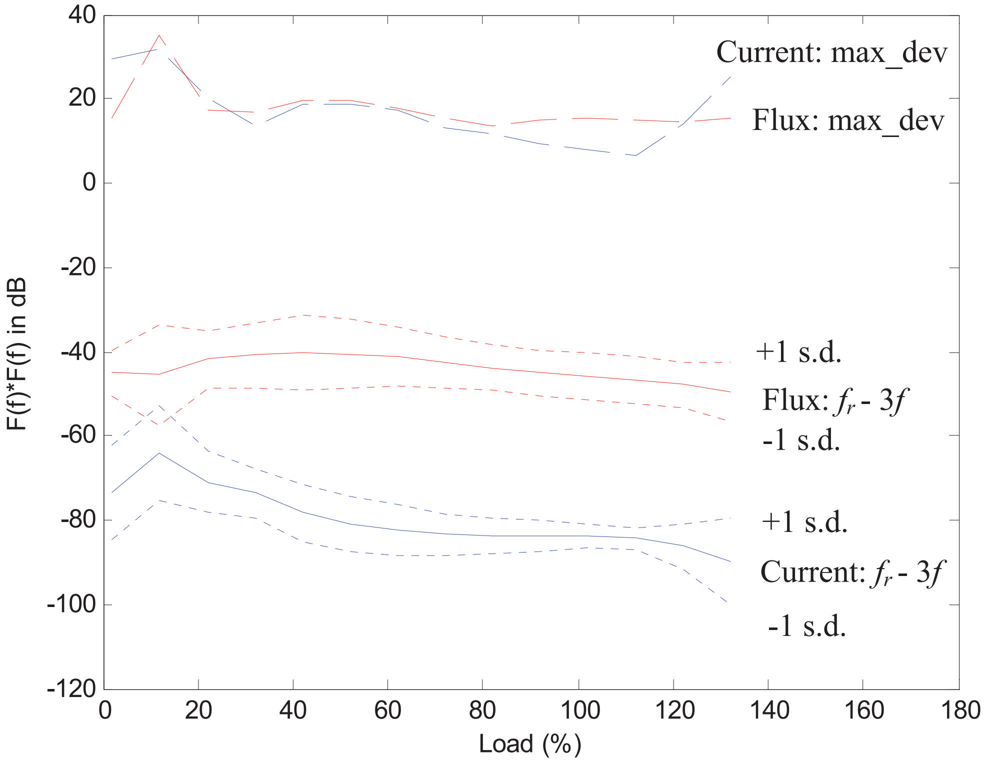

Figure 4.31 – Motor variation test of the lower sideband of the fault frequencies in (Eq. 4.4).

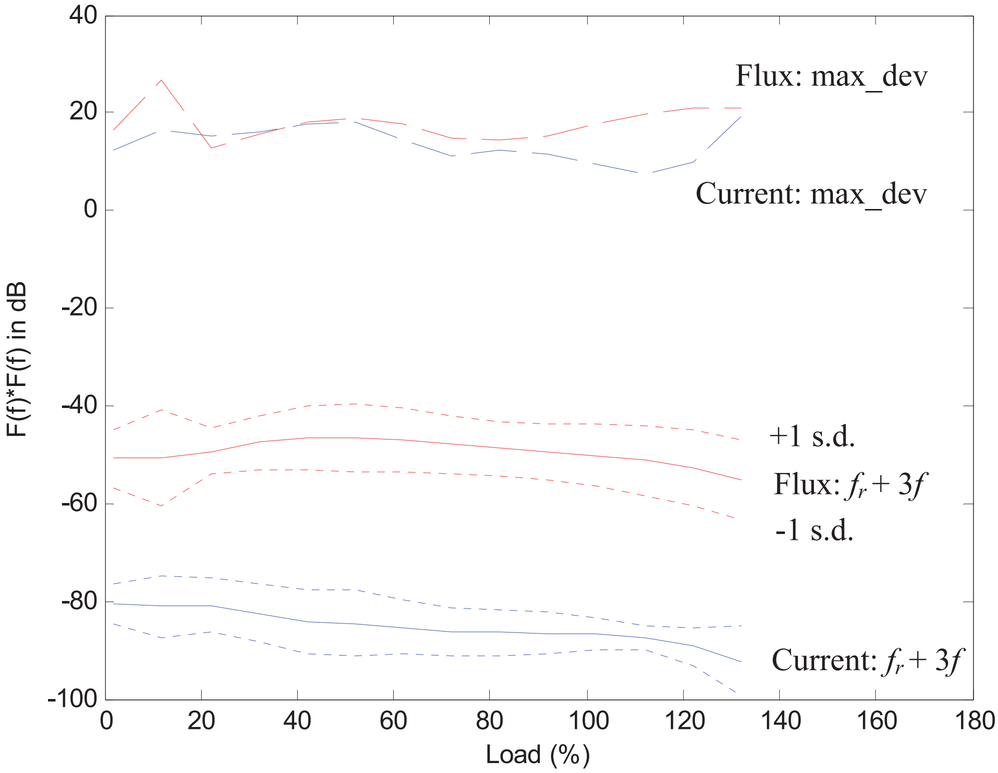

Figure 4.32 - Motor variation test of the upper sideband of the fault frequencies in (Eq. 4.4).

4.6.2. Twice Supply Frequency

4.6.2.1. Repeatability Test

Figure 4.33 - Figure 4.35 show that the magnitude of the twice supply frequency component (Eq. 1.6) from the DEV vibration sensor is fairly consistent among the 3 repeated measurements. The magnitude variation around a particular load is less than 5 dB for most cases, except when the load is at around 3%. However, the magnitudes from the DEH and NDEH vibration sensors show significant variations, which can be as high as 10 dB. These findings suggest that trending of the feature from the DEV vibration sensor is possible but trending of the feature from the DEH and NDEH vibration sensors could be difficult.

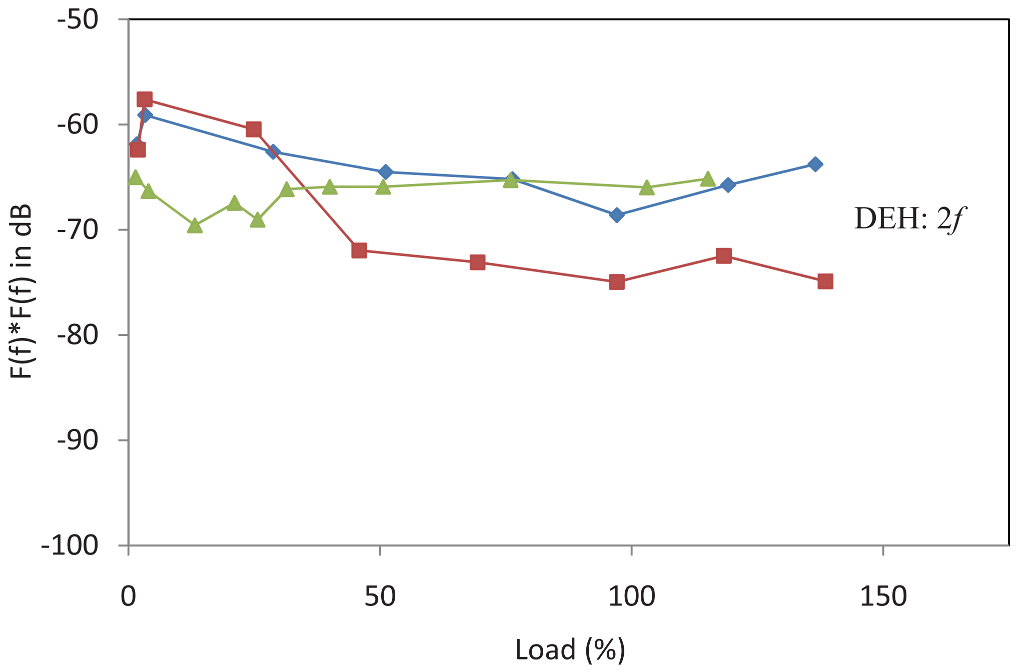

Figure 4.33 - Repeatability test of the fault frequencies in (Eq. 1.6) from the DEH vibration signal.

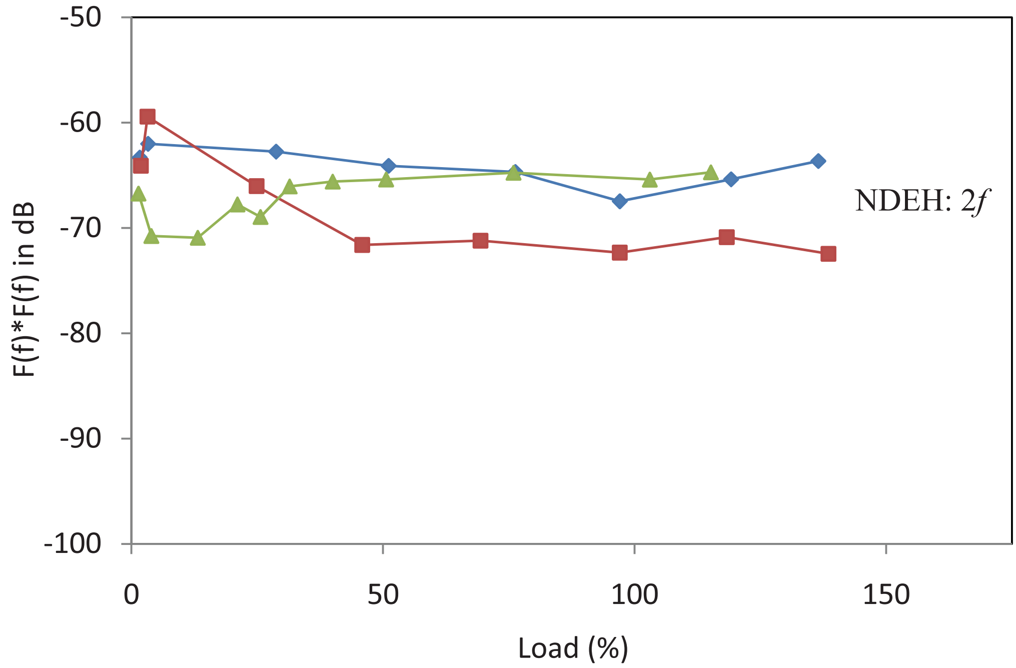

Figure 4.34 - Repeatability test of the fault frequencies in (Eq. 1.6) from the NDEH vibration signal.

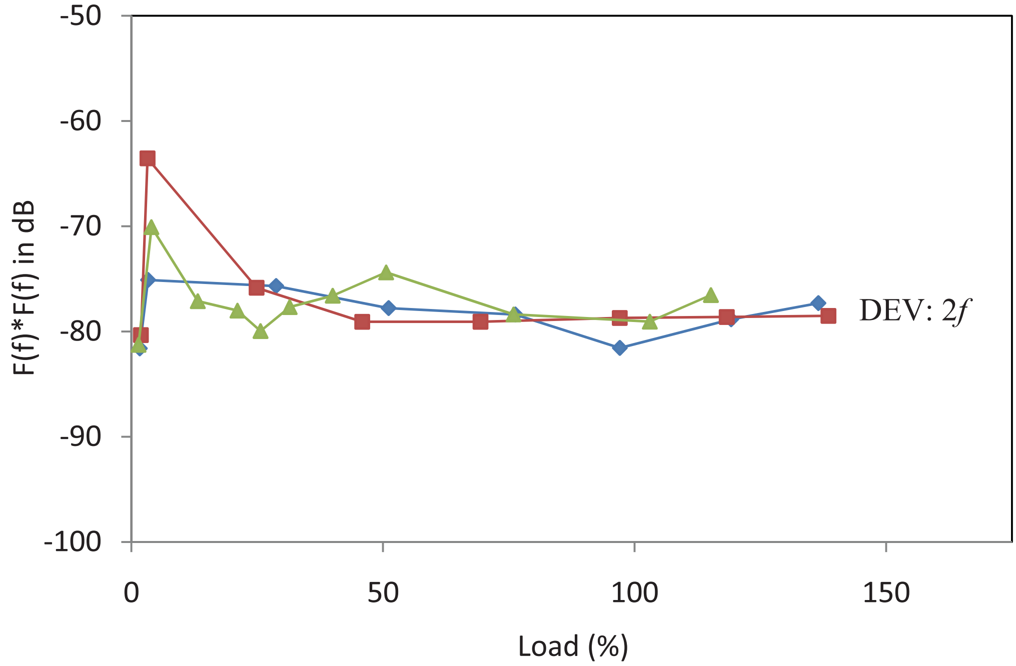

Figure 4.35 - Repeatability test of the fault frequencies in (Eq. 1.6) from the DEV vibration signal.

4.6.2.2. Motor Variation Test

The analysis of Figure 4.36 shows that the average magnitude of the twice supply frequency (Eq. 1.6) seems to be fairly constant at around -70 dB for the DEH and NDEH vibration signals and at around -77 dB for the DEV vibration signal. The difference in the magnitude seems to be affected by the orientation of the vibration sensors.

The standard deviation plots of the twice supply frequency component from the three vibration signals reveal that the magnitude for two-thirds of the motor population lies within about 5 - 10 dB of the average magnitude. However, the standard deviation plot from the DEH vibration sensor seems to be the worst, where the standard deviation increases rapidly when the load is greater than 100%.

The maximum deviation plots of the frequency components show that the maximum magnitude variation among the 6 motors under each load is about 18 dB for the NDEH and DEV vibration signals. The maximum deviation plot from the DEH vibration sensor seems to be worse, where the maximum magnitude variation under each load is about 20 dB and it increases rapidly when the load is greater than 100%.

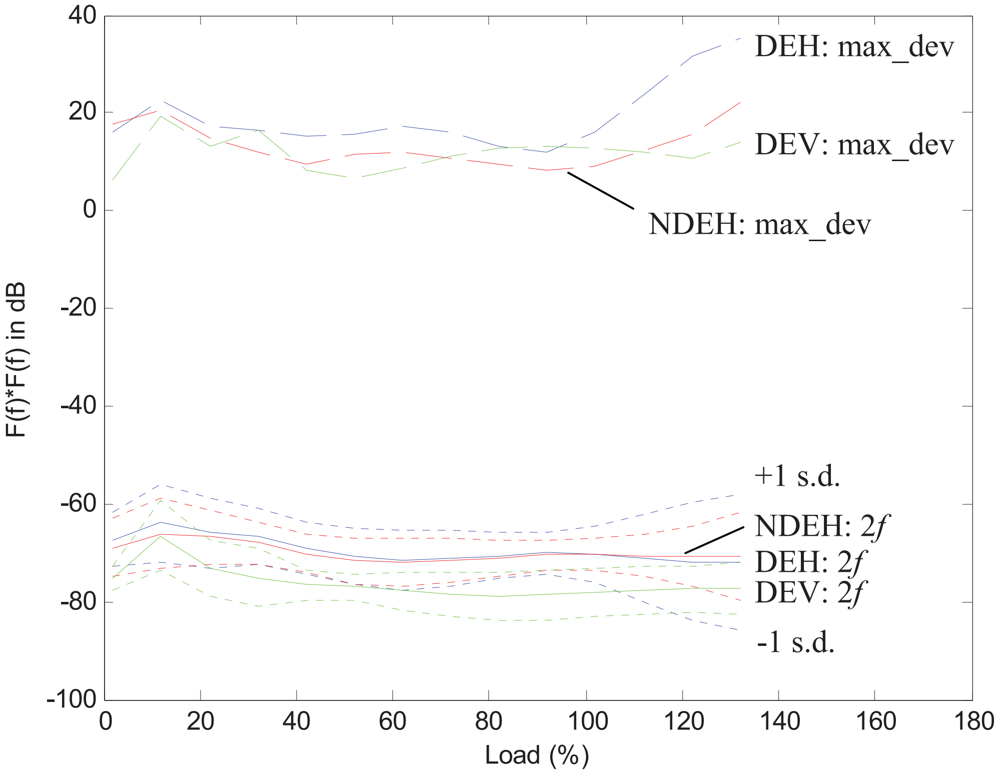

Figure 4.36 – Motor variation test of the fault frequencies in (Eq. 1.6) from the three vibration signals.

These findings suggest that the twice supply frequency is most consistent (i.e. least magnitude variation) in the NDEH and DEV vibration signals. However, the feature from both signals shows significant magnitude variation among the 6 healthy motors which may cause setting a threshold for the feature to be difficult.

4.7. Summary

In this chapter, extensive tests and analysis were carried out on six new healthy induction motors to investigate the phase variation, the repeatability, and the variability of the fault frequency components as a function of motor load. A number of results were presented to provide a baseline for further investigations into on-line multiple-sensor based condition monitoring.

Most of the features (fault frequency components) show a good degree of repeatability. The magnitude variation of the features for a particular load between the repeated measurements is likely to be less than 5 dB. These findings suggest that trending of the features is possible. On the other hand, most of the features show a significant degree of variability between the nominally identical healthy motors. The magnitude variation of the features for a particular load among the six healthy motors is likely to be between 10 - 15 dB. These findings suggest that setting thresholds for the features could be difficult. In addition, the phase variation tests show that there is not much magnitude variation between the three current phases of the fault frequency components, especially when the components are found to be strong and reliable. These suggest that it is only necessary to examine one of the current phases when investigating the fault frequency components.

Chapter 5. Shorted Turn Fault Detection

5.1. Introduction

The shorted turn investigation in this chapter will examine two types of shorted turn faults, which are turn to turn faults and phase to phase turn faults. The investigation focuses on these two types of shorted turn faults because they are common faults which constitute to about 38% of the total induction machine failures. In small motors such faults are not obvious from the motor operation but they reduce the efficiency of the motor and may eventually lead to catastrophic failures. There has been significant research work done in the past on steady-state condition monitoring techniques for detecting shorted turn faults in induction machines using characteristic fault frequencies in the stator current and leakage flux signals [19, 36, 37, 66, 67].

The work in [37] demonstrated an investigation of the turn to turn fault on two different motors, which were a ten pole 3-phase slip ring 150 kW induction motor and a 4 pole squirrel cage 30 kW induction motor, under one particular load (1/3 full load). The investigation examined the use of the characteristic fault frequencies in (Eq. 1.2) and (Eq. 1.5) in order to distinguish between healthy and faulty conditions. The investigation found that the lower sideband of the field rotational frequency with respect to the fundamental (i.e. $k = 1$, $v = 1$ in (Eq. 1.5)) and some components that are related to the slotting harmonics (i.e. $k = 1$, $n_d = 0$, $v = 3$ and $k = 1$, $n_d = 0$, $v = 5$ in (Eq. 1.2)) were good indicators for detecting turn to turn faults. Some of these indicators were found to increase (between 0 - 10%) with the fault severity while other indicators decreased (between 0 - 12%) with the fault severity. However, these indicators may not work on all motors, as stated in the paper, and hence further investigation on other motor types is required.

In [19], a three-phase squirrel cage 11 kW motor was examined under three different loading conditions (no load, full load, and standstill or maximum over load) in order to distinguish between a healthy state and a faulty (6% of turn to turn shorted) condition by using the axial leakage flux and the stator current signals. The paper reported several turn to turn features from the fault frequency components in (Eq. 1.5). It was found that the magnitude of the features in the flux signal tended to increase by about 10 dB when the turn to turn faults were introduced. However, it was not conclusive in the ability of the features to distinguish different fault severities. In addition, the features were found to be less reliable when the motor was under loaded conditions.

A similar investigation on a three-phase six pole 3 kW induction motor was reported in [36]. The paper showed that the magnitudes of the fault frequency components in (Eq. 1.5) and the magnitude of the third fundamental harmonic from the stator current signal were increased by about 5 - 10 dB between a healthy and a faulty motor under a 56% load. The use of the third fundamental harmonic to detect a turn to turn fault was also supported in [67]. These shorted turn investigations were further developed in [66], which enabled the estimation of the turn to turn fault location within a stator winding.

Other shorted turn fault investigations which did not utilise fault frequency components are also reported in the literature [34, 68-73]. In [68], a phase to ground turn fault was investigated on a squirrel cage 4 kW induction motor by utilising the hybrid of the Park's vector and the neural network approach. The investigation showed that the technique was able to distinguish between the healthy condition and the faulty condition with a success rate of greater than 97% after the neural network system had been properly trained. The idea of the Park's vector approach was further developed in [69, 70] which enabled the quantification of the graphical representation of the classical Park's vector approach. This technique was also known as the extended Park's vector approach (EPVA).

The EPVA feature was found to be sensitive to different turn to turn fault severities and also to different loading conditions. The magnitude of the EPVA feature increased between 0 and 20% when 0 to 15% of the stator windings were shorted under no load operation. The EPVA magnitude was also found to decrease with increasing load. In [34, 71-73], turn to turn fault detection based on the negative sequence current and neural network were also investigated.

In summary, the majority of the previous work has focussed only on turn to turn faults under limited fault severities and limited loading conditions, examined only a few shorted turn features in one of the sensor signal types, and made no correlation between the loads and the fault severities at which the features can be reliably used for fault detection. However, it is critical to understand how fault severities and loading conditions affect the fault detection and to identify the most relevant features for detecting turn to turn faults and also phase to phase turn faults.

The work in this chapter will examine many prospective shorted turn features from three different types of sensors (stator current, axial leakage flux, and motor vibration sensors) under five different fault severities and ten different loading conditions, ranging from no load to over load. The work will start by identifying all the useful shorted turn features. Then, they will be compared against the variations between the nominally identical healthy machines in order to determine the loads and the fault severities in which the features can be reliably used to detect the faults. Finally, the possibility of estimating the fault severity will be examined.

The shorted turn investigation in this study will be based on an extensive series of sensor measurements taken using a specially modified 2.2 kW induction machine with adjustable shorted turn settings. Both turn to turn and phase to phase turn faults will be investigated with 5, 10, 15, and 20 turns being shorted (which correspond to 1.7%, 3.5%, 5.3%, and 7.1% of shorted turn faults in a phase winding and 1.7%, 3.5%, 5.3%, and 7.1% of shorted turn faults between adjacent phase windings) (see *section 1.5.3*).

5.2. Shorted Turn Fault Detection Techniques

Table 5.1 shows the shorted turn features that were utilised in the earlier research studies. These previous studies primarily utilised only one of these features and a single sensor type, and found that a significant increase or decrease in the magnitude of a feature can indicate a shorted turn fault. However, neither the relationship between the severity of shorted turn faults and the magnitude of the feature nor the sensitivity of these features to changes in motor loading has been reported sufficiently in the literature.

Table 5.1 – Shorted Turn Features Used in the Literature

Shorted Turn Features	**Sensor Types**	**Shorted Turn Types**	**References**	**Eqn. No.**
Fundamental sidebands of rotor frequency harmonics, f_{st1}	Current, leakage flux	Turn to turn, phase to phase	[19, 36, 37]	(Eq. 5.1)
Twice supply frequency, f_{st2}	Vibration	Turn to turn, phase to phase	[22]	(Eq. 5.2)
Rotor slot harmonics, f_{st3}	Current, leakage flux	Turn to turn, phase to phase	[19, 37]	(Eq. 5.3)
Third harmonic of the fundamental, f_{st4}	Current leakage flux	Turn to turn, phase to phase	[36, 67]	(Eq. 5.4)
EPVA	Current	Turn to turn, phase to phase	[69, 70]	

Where,

$$f_{st1} = f\left[k\frac{(1-s)}{p} \pm v\right] \tag{Eq. 5.1}$$

$$f_{st2} = 2f \tag{Eq. 5.2}$$

$$f_{st3} = f\left[(kR \pm n_d)\frac{(1-s)}{p} \pm v\right] \tag{Eq. 5.3}$$

$$f_{st4} = 3f \tag{Eq. 5.4}$$

Note that (Eq. 5.1) and (Eq. 5.3) are the same as (Eq. 1.5) and (Eq. 1.2) but they are repeated here for convenience.

5.2.1. Fault Frequency Components in Current and Leakage Flux

The third harmonic of the fundamental frequency (Eq. 5.4) is usually strong in the stator current signal. This component was also found to be sensitive to shorted turn faults and hence it has been used to detect shorted turn faults in [36, 67]. Similarly, the frequency components defined by (Eq. 5.1) and (Eq. 5.3) are affected by the presence of shorted turn faults.

In order to understand the existence of the fault frequency components in (Eq. 5.1) and (Eq. 5.3), a detailed analysis of the air-gap flux distribution and its dependence on the fault are described in *Appendix A.1* and *Appendix A.2*. The analysis starts by deriving the flux distributions which are induced by both the stator and rotor currents. From these induced flux distributions, the current harmonics that are affected by the shorted turn faults in both the stator and rotor windings are identified. It is deduced from the analysis that the fault frequency components in (Eq. 5.1) are induced in the rotor winding while the fault frequency components in (Eq. 5.3) are induced in the stator winding.

Furthermore, the frequency components that exist in both the stator and rotor currents should also be present in the leakage flux. This is because the leakage flux of a squirrel cage three-phase induction motor is produced due to the coil-end leakage inductance in the stator windings and the end-ring leakage inductance in the rotor cage (Eq. 5.5) [19]. Therefore, the leakage flux depends on both the stator and rotor currents. As a result, if a fault introduces or varies the frequency components in either rotor or stator currents, it can also be observed in the leakage flux signal.

$$\Phi_{leakage}(t) = k_s i_{sw}(t) + k_r i_{rb}(t) \qquad \text{(Eq. 5.5)}$$

where k_s, k_r are the factors associated with the leakage inductance in the stator windings and the rotor cage, $i_{sw}(t)$ is the stator winding current, and $i_{rb}(t)$ is the rotor bar current.

5.2.2. Fault Frequency Component in Vibration

Another fault frequency component that is commonly related to stator faults is the twice supply frequency component from the motor vibration signal. This frequency component is usually found to be strong and easily detected. In addition, this frequency component can be utilised to detect stator faults without any machine constructional information, unlike the frequency components in (Eq. 5.1) and (Eq. 5.3), which require the number of poles and the number of rotor bars. However, the effectiveness of using the twice supply frequency to detect shorted turn faults has not been thoroughly investigated in previous work.

5.2.3. Extended Park's Vector Approach (EPVA)

The Park's vector components (i_d, i_q) of the three-phase stator current variables (i_a, i_b, i_c) of an induction motor are defined as in (Eq. 5.6) and (Eq. 5.7) [68, 69, 74].

$$i_d = \frac{\sqrt{2}}{\sqrt{3}} i_a - \frac{1}{\sqrt{6}} i_b - \frac{1}{\sqrt{6}} i_c \qquad \text{(Eq. 5.6)}$$

$$i_q = \frac{1}{\sqrt{2}} i_b - \frac{1}{\sqrt{2}} i_c \qquad \text{(Eq. 5.7)}$$

When the motor is operating under ideal conditions (i.e. the motor supply currents only constitute a positive-sequence system), the Park's vector components can be expressed as in (Eq. 5.8) and (Eq. 5.9) [68, 69, 74].

$$i_d = \frac{\sqrt{6}}{2} i_+ \, sin(\omega t) \qquad \text{(Eq. 5.8)}$$

$$i_q = \frac{\sqrt{6}}{2} i_+ \, sin\left(\omega t - \frac{\pi}{2}\right) \qquad \text{(Eq. 5.9)}$$

where i_+ is the magnitude of the current positive-sequence component of symmetrical component systems, defined by (Eq. 5.10) - (Eq. 5.12) [75].

$$i_0 = \frac{1}{3}(i_a + i_b + i_c) \qquad \text{(Eq. 5.10)}$$

$$i_+ = \frac{1}{3}(i_a + 1\angle 120° i_b + 1\angle 240° i_c) \qquad \text{(Eq. 5.11)}$$

$$i_- = \frac{1}{3}(i_a + 1\angle 240° i_b + 1\angle 120° i_c) \qquad \text{(Eq. 5.12)}$$

where i_0 is the magnitude of the current zero-sequence component and i_- is the magnitude of the current negative-sequence component.

The current Park's vector representation of a motor under ideal operating conditions is a perfect circle centred at the origin of the coordinates, as shown in Figure 5.1 (left). From the figure, it is clear that the magnitude (modulus) of the ideal Park's vector is a constant. However, when shorted turn faults are introduced to the stator windings, the three-phase stator currents are no longer balanced and the ideal Park's vector components in (Eq. 5.8) and (Eq. 5.9) are not valid anymore. When there is a shorted turn fault, the resultant imbalance means that the motor supply currents become the sum of positive and negative sequence components, assuming the stator windings have no neutral connection. The presence of these positive and negative sequence components will cause the current Park's vector to become elliptical (Figure 5.1 right). In this condition, it can be shown that the Park's vector magnitude of the major axis is proportional to the sum of the positive and negative sequence components, while the magnitude of the minor axis is proportional to the difference between the positive and negative sequence components [69].

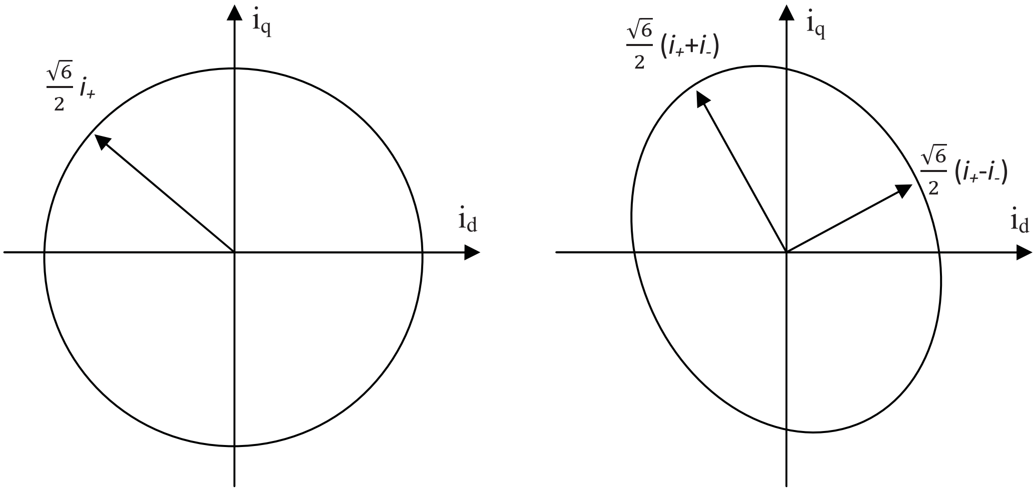

Figure 5.1 – Park's current vector representations of an ideal system (left) and a system with stator asymmetry (right).

Figure 5.1 (right) shows that shorted turn faults cause the magnitude (modulus) of the faulty Park's vector components to contain both a DC component and an AC component. The AC component depends on the negative-sequence component, which relates directly to the asymmetry in the stator windings. As a result, the spectrum of the AC component can be used to analyse the severity of the fault, especially the frequency component at twice the supply frequency, $2f$ [69]. Hence, the EPVA feature is defined as the ratio of the magnitude of the frequency component at $2f$ and the DC level of the Park's vector.

5.3. Analysis of Turn to Turn Faults

In this section, potential turn to turn fault measures (see Table 5.1) will be examined to determine if the measures can be utilised as turn to turn fault features in order to detect and estimate the different fault severities. For a potential fault measure to be considered as a fault feature, it has to satisfy the following requirements:

1. The magnitude of the fault measure must be well above the noise floor, which means the fault measure must be detectable, and
2. There must be significant magnitude variation (generally should be greater than 5 dB, based on the baseline study) between the healthy and the faulty motors.

Furthermore, if the feature is to be considered as a good feature, it should also have:

- its magnitude to consistently increase/decrease with increasing fault severity, and
- a low magnitude variation with the load (or a consistent magnitude variation with the load which is not affected by fault severity).

5.3.1. Using Fundamental Sidebands of Rotor Frequency Harmonics

In this section, several harmonics of the frequency components in (Eq. 5.1), which utilise several values of k (i.e. $k = 1, 2, 3$) and several values of v (i.e. $v = 1, 3, 5$), from both current and leakage flux signals will be investigated. Note that this section will only describe the results for the first harmonic (i.e. $k = 1$ and $v = \pm 1$) in detail. The remaining harmonics and their associated results are given in *Appendix A.3*.

Components at $k = 1$ and $v = \pm 1$

Figure 5.2 displays how the magnitude of the frequency components in the current and leakage flux varies under the different loading and turn to turn fault conditions. The figure shows that the lower sideband ($k = 1$, $v = -1$) in the current signal shows a magnitude variation of about -10 dB between the healthy motor and the 7.1% faulty motor, where the magnitude of the faulty motor is lower than the magnitude of the healthy motor, when the load is greater than 40%. Therefore, the lower sideband can be considered as a turn to turn feature. However, Figure 5.2 also shows that the feature magnitude does not consistently decrease with increasing fault severity. As a consequence, the feature cannot be considered as a good turn to turn feature and it can only be used to distinguish between the healthy and faulty conditions but not to separate the different fault severities. On the other hand, the upper sideband (k = 1, v = +1) in the current signal only shows a small magnitude variation (generally less than 5 dB) between the healthy and faulty conditions. Hence, it cannot be considered as a feature.

The frequency components in the leakage flux signal show useful magnitude variations between the healthy and the faulty conditions, where the magnitude consistently decreases as the severity of the fault increases (i.e. about -10 to -20 dB between the healthy and the 7.1% fault condition). The lower sideband component has the useful pattern when the load is less than 60%, while the upper sideband component has the useful pattern up to 110% load. Therefore, the frequency components at $k = 1$, $v = \pm 1$ in the flux signal can be considered as good turn to turn features.

Out of these four frequency components, the upper sideband of the flux signal is the best feature because it has significant and consistent magnitude variation (greater than 5 dB) between the healthy and the different fault conditions under the greatest range of loading conditions, from no load to 110% of load (10% over load).

Important characteristics of the above fault measures are summarised in Table 5.2. The table shows the minimum/maximum magnitude variation (mag. Δ) due to the 7.1% fault under all tested loading conditions, the maximum magnitude variation of the healthy motor under all tested loading conditions, the useful loads for which the fault measure can be considered as a feature, and the fault severities (levels) that can be distinguished by the fault measure. It should also be noted that the minimum/maximum magnitude variation due to the fault may have a positive value for the minimum and a negative value for the maximum, which means that the magnitude of the healthy motor is higher (positive value) under certain loads but it is lower (negative value) at other loads.

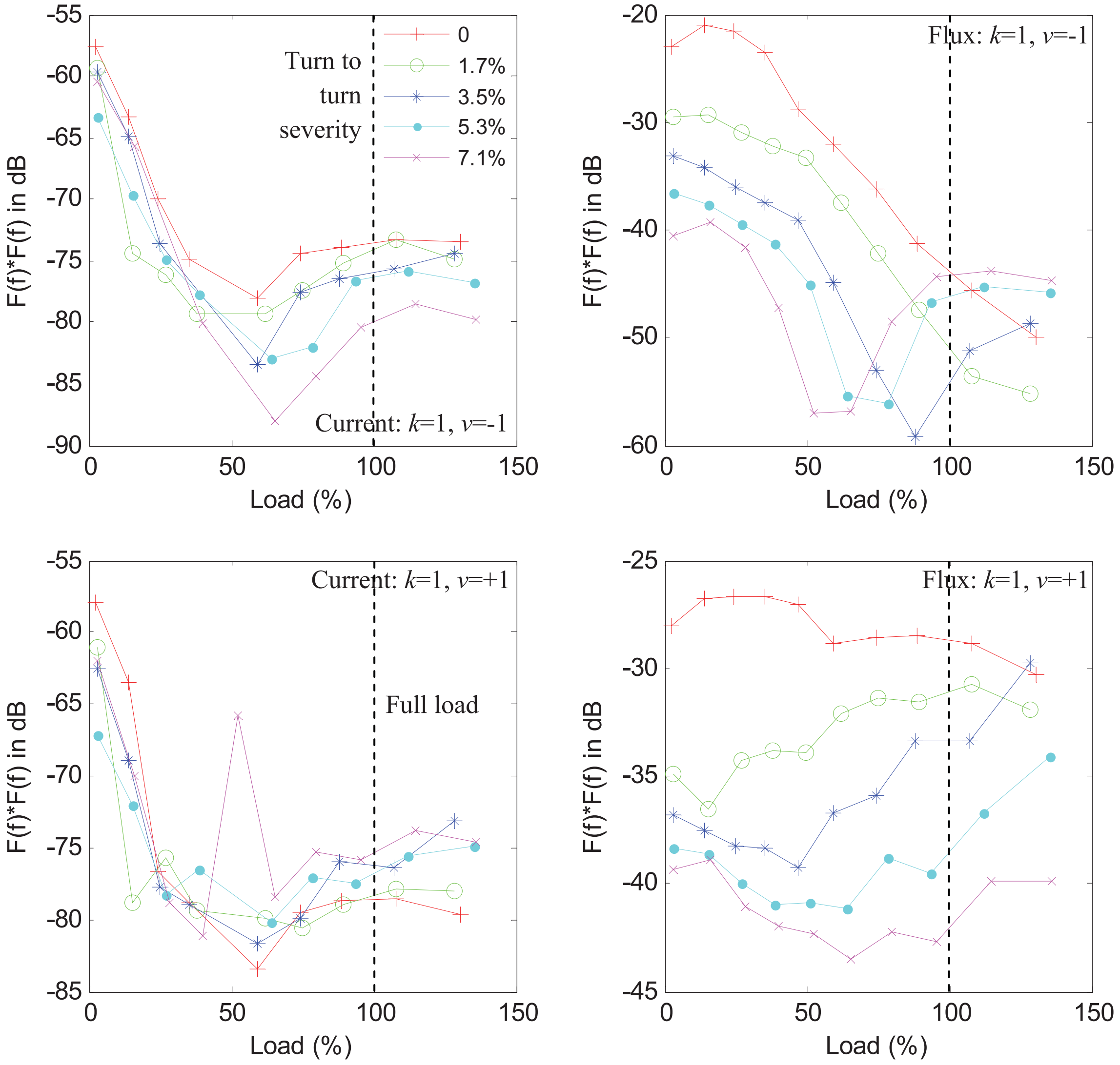

Figure 5.2 – Magnitude of the frequency components in (Eq. 5.1) at $k = 1$, $v = -1$ (top), $k = 1$, $v = +1$ (bottom), from the current (left column) and leakage (right column) flux signals as a function of load.

Table 5.2 – Characteristics of the frequency components in (Eq. 5.1) at $k = 1$, $v = \pm 1$

Frequency component	**Signal**	**(Min,Max) mag. Δ due to 7.1% fault under all loads**	**Max healthy mag. Δ due to all loads**	**Useful loads**	**Fault levels**	**Notes**
(Eq. 5.1) at $k = 1$, $v = -1$	Current	0, -12 dB	20 dB	>40%	≥3.5%	F
(Eq. 5.1) at $k = 1$, $v = -1$	Flux	5, -27 dB	29 dB	<60%	All	F
(Eq. 5.1) at $k = 1$, $v = +1$	Current	-5, 17 dB	26 dB	-	-	NF
(Eq. 5.1) at $k = 1$, $v = +1$	Flux	-10, -15 dB	4 dB	<110%	All	F

where F denotes that the frequency component can be considered as a feature and NF denotes that the frequency component cannot be considered as a feature.

Components at $k = 1, 2, 3$ and $v = \pm 1, \pm 3, \pm 5$

Some important characteristics of these frequency components are summarised in Table 5.3 and the detailed analysis can be found in *Appendix A.3*. In general, the majority of these frequency components are found to either have a low signal to noise ratio (SNR), which makes them difficult to detect, or show inconsistent and insignificant magnitude variation (less than 5 dB) between the healthy and the faulty conditions. However, the components at $k = 1$ and $v = \pm 3, \pm 5$ in the flux signal show more promising results with significant magnitude variations between the healthy and the faulty conditions. As a result, these components can be considered as turn to turn features, with the component at $k = 1$ and $v = -3$ being the best because it is usable under all loading and fault conditions.

Table 5.3 - Characteristics of the frequency components in (Eq. 5.1) at $k = 1, 2, 3$ and $v = \pm 1, \pm 3, \pm 5$

Frequency component	**Signal**	**(Min,Max) mag. Δ due to 7.1% fault under all loads**	**Max healthy mag. Δ due to all loads**	**Useful loads**	**Fault levels**	**Notes**
(Eq. 5.1) at $k = 2$, $v = -1$	Current	-5, 13 dB	17 dB	-	-	NF
(Eq. 5.1) at $k = 2$, $v = -1$	Flux	12, -16 dB	35 dB	-	-	NF
(Eq. 5.1) at $k = 2$, $v = +1$	Current	6, -12 dB	26 dB	-	-	NF
(Eq. 5.1) at $k = 2$, $v = +1$	Flux	-4, -14 dB	18 dB	-	-	NF
(Eq. 5.1) at $k = 3$, $v = -1$	Current	3, -13 dB	36 dB	-	-	NF
(Eq. 5.1) at $k = 3$, $v = -1$	Flux	1, -19 dB	49 dB	-	-	NF
(Eq. 5.1) at $k = 3$, $v = +1$	Current	-5, 10 dB	9 dB	-	-	NF
(Eq. 5.1) at $k = 3$, $v = +1$	Flux	-2, -16 dB	14 dB	-	-	NF
(Eq. 5.1) at $k = 1$, $v = -3$	Current	11, -11 dB	4 dB	-	-	NF
(Eq. 5.1) at $k = 1$, $v = -3$	Flux	-5, -12 dB	9 dB	All	All	F
(Eq. 5.1) at $k = 1$, $v = +3$	Current	1, 6 dB	15 dB	-	-	NF
(Eq. 5.1) at $k = 1$, $v = +3$	Flux	2, -15 dB	18 dB	>20 & <120%	All	F
(Eq. 5.1) at $k = 1$, $v = -5$	Current	11, -11 dB	11 dB	-	-	NF
(Eq. 5.1) at $k = 1$, $v = -5$	Flux	1, -12 dB	11 dB	>20 & <110%	≥5.3%	F
(Eq. 5.1) at $k = 1$, $v = +5$	Current	2, -9 dB	16 dB	-	-	NF
(Eq. 5.1) at $k = 1$, $v = +5$	Flux	4, -13 dB	5 dB	>60%	≥5.3%	F

Discussion

In general, the frequency components in (Eq. 5.1) from the current signal are found to be not reliable in detecting turn to turn faults. These frequency components in the current signal, at best, can only distinguish between the healthy and faulty conditions under certain loading conditions. On the other hand, the frequency components in (Eq. 5.1) from the leakage flux signal are found to be much more reliable in detecting turn to turn faults than their current counterparts. These findings are also supported by the theoretical background in *section 5.2.1* which deduces that shorted turn faults produce frequency components as shown in (Eq. 5.1) in the rotor current but not in the stator current. Since the leakage flux is produced from the combination of rotor and stator currents, the frequency components in the leakage flux signal are more sensitive to the changes in the turn to turn fault conditions. Moreover, the magnitude of the components is mostly found to decrease as the severity of the fault increases.

The analysis of the frequency components in (Eq. 5.1) reveals that the effectiveness of the frequency components to detect turn to turn faults diminishes as the variables k and v are increased. When the variables k and v are increased, the SNR of the frequency components are found to be progressively lower (see *Appendix A.3*). This is to be expected as the strength of a signal component is inversely proportional to its harmonic number. As a consequence, it is recommended to keep the variable k at 1 and the variable v at ±1 and ±3.

5.3.2. Using Twice Supply Frequency

This shorted turn investigation will examine the twice supply frequency component from all three vibration sensors, which are located at the driving end horizontal (DEH) position, the driving end vertical (DEV) position, and the non-driving end horizontal (NDEH) position. The investigation will compare and discuss the effects of the different locations and orientations of the vibration sensors in detecting the turn to turn faults.

The experimental results (see Table 5.4 and *Appendix A.4*) suggest that the effectiveness of the twice supply frequency component in detecting turn to turn faults depends on the orientation of the vibration sensor. The vertical oriented (DEV) vibration sensor signal shows no useful magnitude variation under the different fault severities, while the horizontal oriented (DEH and NDEH) vibration sensor signals show some magnitude variation between the different fault severities, where the magnitude tends to increase as the severity of the fault increases (about 5 dB difference between the healthy and the 7.1% fault conditions). Unfortunately, the horizontal oriented vibration sensor signals only start to become useful in detecting turn to turn faults when the fault severity is 7.1% or greater.

Based on these three frequency components, the component from the NDEH vibration signal is the best feature, especially when the load is greater than 60%, because it can detect the lower fault severity (5.3%) compared to the component from the DEH vibration signal (7.1%).

Table 5.4 - Characteristics of the twice supply frequency components

Frequency component	**Signal**	**(Min,Max) mag. Δ due to 7.1% fault under all loads**	**Max healthy mag. Δ due to all loads**	**Useful loads**	**Fault levels**	**Notes**
(Eq. 5.2)	DEH Vib.	2, 7 dB	8 dB	All	≥7.1%	F
(Eq. 5.2)	NDEH Vib.	5, 7 dB	11 dB	All	≥7.1%	F
(Eq. 5.2)	DEV Vib.	0, 7 dB	8 dB	-	-	NF

5.3.3. Using Rotor Slot Harmonics

The rotor slot harmonics (Eq. 5.3) are commonly known for detecting eccentricity faults but the theoretical derivation in *section 5.2.1* and some previous research suggest that the components in (Eq. 5.3) may also be sensitive to shorted turn faults, especially when the variable n_d is set to 0. As a result, this turn to turn fault investigation will examine several harmonics of the frequency components in (Eq. 5.3) at $n_d = 0$. The investigation will consider several values of k ($k = 1, 2, 3$) and several values of v ($v = 1, 3, 5$) in both the current and leakage flux signals. Some important characteristics of these frequency components are summarised in Table 5.5 and the detailed analysis can be found in *Appendix A.5*.

Table 5.5 - Characteristics of the frequency components in (Eq. 5.3) at $k = 1, 2, 3$ and $v = \pm1, \pm3, \pm5$

Frequency component	**Signal**	**(Min,Max) mag. Δ due to 7.1% fault under all loads**	**Max healthy mag. Δ due to all loads**	**Useful loads**	**Fault levels**	**Notes**
(Eq. 5.3) at $k = 1$, $v = -1$	Current	0, 8 dB	11 dB	>20%	≥5.3%	F
(Eq. 5.3) at $k = 1$, $v = -1$	Flux	-6, -11 dB	4 dB	All	≥3.5%	F
(Eq. 5.3) at $k = 1$, $v = +1$	Current	1, -2 dB	9 dB	-	-	NF
(Eq. 5.3) at $k = 1$, $v = +1$	Flux	-1, -18 dB	8 dB	All	≥5.3%	F
(Eq. 5.3) at $k = 2$, $v = -1$	Current	3, -8 dB	23 dB	-	-	NF
(Eq. 5.3) at $k = 2$, $v = -1$	Flux	6, -14 dB	19 dB	-	-	NF
(Eq. 5.3) at $k = 2$, $v = +1$	Current	-7, 10 dB	12 dB	-	-	NF
(Eq. 5.3) at $k = 2$, $v = +1$	Flux	3, -11 dB	12 dB	-	-	NF
(Eq. 5.3) at $k = 3$, $v = -1$	Current	1, -2 dB	3 dB	-	-	NF
(Eq. 5.3) at $k = 3$, $v = -1$	Flux	4, -21 dB	26 dB	-	-	NF
(Eq. 5.3) at $k = 3$, $v = +1$	Current	0, -1 dB	1 dB	-	-	NF
(Eq. 5.3) at $k = 3$, $v = +1$	Flux	-2, -31 dB	33 dB	-	-	NF
(Eq. 5.3) at $k = 1$, $v = -3$	Current	0, -6 dB	14 dB	-	-	NF
(Eq. 5.3) at $k = 1$, $v = -3$	Flux	0, -15 dB	16 dB	<80%	All	F
(Eq. 5.3) at $k = 1$, $v = +3$	Current	0, -1 dB	4 dB	-	-	NF
(Eq. 5.3) at $k = 1$, $v = +3$	Flux	-1, -14 dB	9 dB	<80%	All	F
(Eq. 5.3) at $k = 1$, $v = -5$	Current	-2, -26 dB	17 dB	-	-	NF
(Eq. 5.3) at $k = 1$, $v = -5$	Flux	2, -28 dB	22 dB	-	-	NF
(Eq. 5.3) at $k = 1$, $v = +5$	Current	-4, 12 dB	23 dB	<80%	≥5.3%	F
(Eq. 5.3) at $k = 1$, $v = +5$	Flux	-3, -12 dB	7 dB	<100%	≥3.5%	F

The majority of these frequency components are found to either have low signal to noise ratio which make them difficult to detect, or show inconsistent and insignificant magnitude variation (less than 5 dB) between the healthy and the faulty conditions. However, the components at $k = 1$ and $v = \pm1, \pm3, +5$ in the flux signal and the components at $k = 1$ and $v = -1, +5$ in the current signal show more promising results where the components can distinguish between the healthy and the faulty conditions (with magnitude variation greater than 5 dB). As a result, these components can be considered as turn to turn features, with the components at $k = 1$ and $v = \pm3$ in the flux being the best because they may be utilised for all tested fault severities under most loads.

The magnitudes of the features are found to either increase or decrease, depending on the values of k and v, as the severity of the fault increases. However, most of the magnitude variations only start to become evident when the fault severity is at 5.3% or greater. Furthermore, most of the magnitude variations among the different fault severities are not consistent or large enough for these frequency components to be considered as good turn to turn features.

The analysis of the frequency components in (Eq. 5.3) also reveals that the effectiveness of the frequency components to detect turn to turn faults diminishes as the variables k and v are increased. When the variables k and v are increased, the SNR of the frequency components are found to be progressively lower (see *Appendix A.5*). As a consequence, it is recommended to keep the variable k at 1 and the variable v at ±1 and ±3.

5.3.4. Using Third Harmonic of the Fundamental

The experimental results of this study (see Table 5.6 and *Appendix A.6*) show that the harmonic from both current and flux signals does not show significant magnitude variation (mostly less than 5 dB) between the healthy and the faulty conditions. As a consequence, these harmonics cannot be used as turn to turn features in this machine. However, the same component was used in [67] and it was observed that there was about 5 dB increase between the healthy motor and the faulty motor with a 4.1% turn to turn fault. Note that the 5 dB difference may come from the variation due to the repeated measurements (see the baseline study in Chapter 4) or from the fact that they used a DTC (direct torque control) inverter instead of direct AC mains feed as in this research.

Table 5.6 - Characteristics of the third fundamental harmonic

Frequency component	**Signal**	**(Min,Max) mag. Δ due to 7.1% fault under all loads**	**Max healthy mag. Δ due to all loads**	**Useful loads**	**Fault levels**	**Notes**
(Eq. 5.4)	Current	-2, 4 dB	10 dB	-	-	NF
(Eq. 5.4)	Flux	-1, -7 dB	7 dB	-	-	NF

5.3.5. Using Extended Park's Vector Approach (EPVA)

A typical Park's current vector locus of a healthy motor running at full load is shown in Figure 5.3 (top). The figure shows that the Park's vector locus of a healthy motor is not a perfect circle. This distortion is partly due to magnetic saturation and partly due to the inherent asymmetry in the motor, which can be caused by manufacturing imperfections and tolerances. Figure 5.3 (bottom) shows the spectrum of the Park's vector magnitude, between 0 Hz up to 2 kHz (cut-off frequency), which highlights the twice supply frequency component. The magnitude of this component, which is normalised to the DC component, is the EPVA feature for detecting shorted turn faults.

Figure 5.4 shows that the magnitude of the EPVA component does not vary significantly with the load (less than 5 dB from no load to over load for the faulty conditions). The EPVA component is found to have a high signal to noise ratio and can be easily identified. In addition, the magnitude variation among the different fault severities shows a useful pattern, where the magnitude consistently increases with increasing fault severity, when the load is greater than 20%. Although the magnitude separation between the different fault severities is quite small (about 1 dB), the magnitude separation between the healthy and faulty conditions is quite significant (greater than 10 dB). This suggests that the component can be easily utilised to distinguish between the healthy and faulty conditions but it may be difficult to estimate the fault severities. The important characteristics of the EPVA components are summarised in Table 5.7.

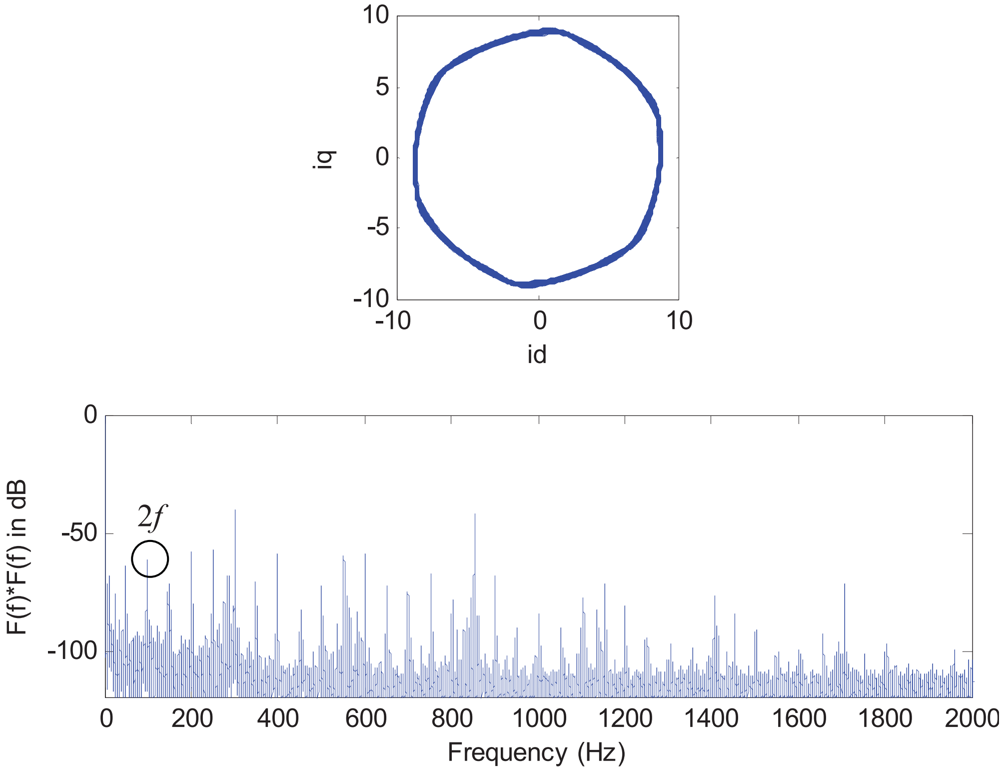

Figure 5.3 – Typical Park's vector locus of the three phase stator currents (top) and spectrum of the magnitude of the Park's vector components (bottom).

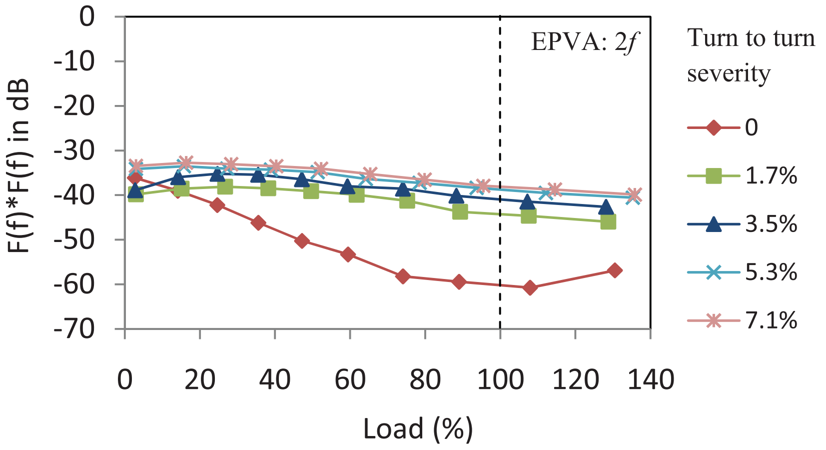

Figure 5.4 – Magnitude of the EPVA feature as a function of load.

Table 5.7 - Characteristics of the EPVA feature

Frequency component	**Signal**	**(Min,Max) mag. Δ due to 7.1% fault under all loads**	**Max healthy mag. Δ due to all loads**	**Useful loads**	**Fault levels**	**Notes**
EPVA	Current	3, 22 dB	25 dB	>20%	All	F

5.3.6. Summary of Effective Turn to Turn Features

It should be emphasised that the analysis performed in this chapter is much more comprehensive than the analysis performed in the previous work described in *section 5.1*. For example, the previous work usually investigated two fault severities under one or more loading conditions (equivalent to about 2 - 10 data points in our graphical representation), whereas the current investigation examines 5 different fault severities and for each fault severity ten different loading conditions are analysed (hence 50 data points in the figures). Based on this comprehensive analysis, the utilised turn to turn fault frequency components can be divided into 2 different categories, which are ideal turn to turn features and non-ideal turn to turn features.

In an ideal turn to turn feature, the magnitude of the feature either consistently increases or consistently decreases as the severity of the fault increases and the magnitude separation among all tested fault severities is distinct. The turn to turn features that are found to be ideal are listed in Table 5.8. In addition, the table also shows the sensor signal type of the feature, the load range in which the feature is considered ideal, the minimum/maximum magnitude variation between the healthy and the 7.1% fault severity condition under the useful loads, and the maximum magnitude variation of the healthy motor under the useful loads. These parameters should give an indication of the performance of the feature. The features' performance will be explored with greater detail in the following sub-section.

Preferably, the ideal features should have a magnitude variation due to the fault as high as possible and a magnitude variation due to the load as low as possible (i.e. 0 dB). However, Table 5.8 shows that the magnitude of the ideal features and their magnitude variations between the healthy and faulty conditions change with loading. Hence, the load of a motor plays an important part in the performance of these ideal features to detect the turn to turn faults.

Table 5.8 – Ideal Turn to Turn Features

Frequency component	**Signal**	**Useful loads**	**(Min,Max) mag. Δ due to 7.1% fault**	**Max healthy mag. Δ due to load**
(Eq. 5.1) at $k = 1$, $v = -1$	Flux	<60%	-18, -28 dB	11 dB
(Eq. 5.1) at $k = 1$, $v = +1$	Flux	<110%	-11, -15 dB	2 dB
(Eq. 5.1) at $k = 1$, $v = -3$	Flux	All	-5, -12 dB	9 dB
(Eq. 5.1) at $k = 1$, $v = +3$	Flux	>20% & <120%	-5, -15 dB	17 dB
EPVA	Current	>20%	9, 22 dB	19 dB

A non-ideal turn to turn feature is where the magnitude of the feature allows either (a) a distinction between the healthy and some faulty conditions but the feature may not distinguish the different levels of the fault, or (b) a distinction between a few fault severities but not all tested fault severities. The turn to turn features that are found to be non-ideal are listed in Table 5.9. The table, as in the ideal feature cases, shows more evidence that the magnitude of the features varies significantly with the load, which supports the argument that loading conditions have a significant impact on the performance of the fault detection.

Table 5.9 – Non-Ideal Turn to Turn Features

Frequency component	**Signal**	**Useful loads**	**Fault levels**	**(Min,Max) mag. Δ due to 7.1% fault**	**Max healthy mag. Δ due to load**	**Notes**
(Eq. 5.1) at $k = 1$, $v = -1$	Current	>40%	≥3.5%	-5, -10 dB	5 dB	D
(Eq. 5.1) at $k = 1$, $v = -5$	Flux	>20% & <110%	≥5.3%	-3, -13 dB	9 dB	S
(Eq. 5.1) at $k = 1$, $v = +5$	Flux	>60%	≥5.3%	-5, -13 dB	2 dB	S
(Eq. 5.2)	DEH Vib.	All	≥7.1%	2, 7 dB	8 dB	D
(Eq. 5.2)	NDEH Vib.	All	≥7.1%	5, 7 dB	11 dB	S
(Eq. 5.3) at $k = 1$, $v = -1$	Current	>20%	≥5.3%	2, 6 dB	6 dB	S
(Eq. 5.3) at $k = 1$, $v = -1$	Flux	All	≥3.5%	-6, -11 dB	4 dB	D
(Eq. 5.3) at $k = 1$, $v = +1$	Flux	All	≥5.3%	-1, -18 dB	8 dB	D
(Eq. 5.3) at $k = 1$, $v = -3$	Flux	<80%	All	-9, -16 dB	6 dB	D
(Eq. 5.3) at $k = 1$, $v = +3$	Flux	<80%	All	-4, -13 dB	9 dB	D
(Eq. 5.3) at $k = 1$, $v = +5$	Current	<80%	≥5.3%	1, 10 dB	23 dB	D
(Eq. 5.3) at $k = 1$, $v = +5$	Flux	<100%	≥3.5%	-3, -12 dB	6 dB	D

where D denotes that the feature can distinguish the healthy and the faulty conditions but not separating the different fault severities; and S denotes that the feature can separate the different fault severities within the usable faults.

5.3.6.1. Usability of the Ideal Turn to Turn Features

This section examines all of the ideal turn to turn features in greater detail by considering the magnitude variation due to the nominally identical healthy machines and their standard deviations in order to determine the loads and the fault severities in which the features can reliably be used to detect the faults and to examine the possibility of estimating the fault severity.

Figure 5.5 shows how the first ideal turn to turn feature (i.e. (Eq. 5.1) at $k = 1$, $v = -1$) varies under the different loading and turn to turn fault severity conditions while illustrating the useful loading conditions (non grey shaded area) and the result of the six healthy motor variation tests (red shaded area, refer to the baseline study in Chapter 4). The figure shows that there is a clear magnitude separation between the healthy motor variation test and the magnitude of the faulty conditions, especially when the fault is at 3.5% or greater, under the useful loading conditions. However, when the fault is at 1.7%, the magnitude of the faulty condition may intersect with the magnitude of the healthy motor variation test. If the fault is at 1.7% and a threshold is set for the feature, the possibility of false alarm may increase dramatically. As a result, setting a threshold for the feature can only be considered if the feature only needs to identify faults with severity greater than 1.7%. This finding shows that detecting turn to turn faults is possible but estimating the fault severity is much more difficult.

Fault severity estimation is possible if the magnitude difference between one fault severity to the next severity is greater than 5 dB (note that the repeatability tests in Chapter 4 show that the magnitude variation between the repeated tests can go up to 5 dB). However, Figure 5.5 shows that the magnitude difference between one fault severity to the next (i.e. about 2% fault severity difference) is less than 5 dB. Therefore, estimating the fault severity (with 2% fault severity precision) using this feature (or any of the following features) is difficult.

It should also be noted that the healthy magnitude curve for the motor used in this particular study is slightly different than the average healthy magnitude curve. This may be caused by the fact that the test motor was re-wound in order to have the shorted turn fault settings adjustable, which may have slightly altered the machine characteristics. Therefore, the fault characteristics of the machine used in this study may not perfectly match the fault characteristics of the original production motor, but they are expected to be similar because both motors are structurally similar and they operate under the same motor principles.

Figure 5.6 shows that for the second ideal feature (i.e. (Eq. 5.1) at $k = 1$, $v = +1$), the magnitude variation of the six healthy motors (red shaded area) under the useful loading conditions (non grey shaded area) is only fully separated from the magnitude of the faulty conditions when the fault severity is at 5.3% or greater. The figure also shows that estimating the fault severity is difficult because the magnitude difference between one severity to the next is less than 5 dB.

Figure 5.7 shows that for the third ideal feature (i.e. (Eq. 5.1) at $k = 1$, $v = -3$), the magnitude variation of the six healthy motors under the useful loading conditions is only fully distinguishable from the magnitude of the faulty conditions when the load is greater than 20% but less than 120%. Under these loading conditions, the magnitude of the faulty conditions (all fault severities) never intersects with the magnitude variation of the healthy motors. As a result, setting a threshold for the feature can only be considered if the loading conditions are known to vary between 20% and 120%.

Figure 5.8 shows that for the fourth ideal feature (i.e. (Eq. 5.1) at $k = 1$, $v = +3$), the magnitude variation of the six healthy motors under the useful loading conditions is only fully distinguishable from the magnitude of the faulty conditions when the load is between 60% and 110% or when the fault severity is at 5.3% or greater. As a result, setting a threshold for the feature can only be considered if the feature only needs to identify the faults with severity greater than or equal to 5.3% or if the loading conditions are known to vary between 60% and 110%.

Figure 5.9 shows that for the EPVA feature, the magnitude variation of the six healthy motors under the useful loading conditions is only fully distinguishable from the magnitude of the faulty conditions when the fault severity is at 3.5% or greater. When the fault is at 1.7% or less, the magnitude of the faulty conditions is within the magnitude variation of the healthy motors. As a result, setting a threshold for the feature can only be considered if the feature only needs to identify faults with severity greater than or equal to 3.5%.

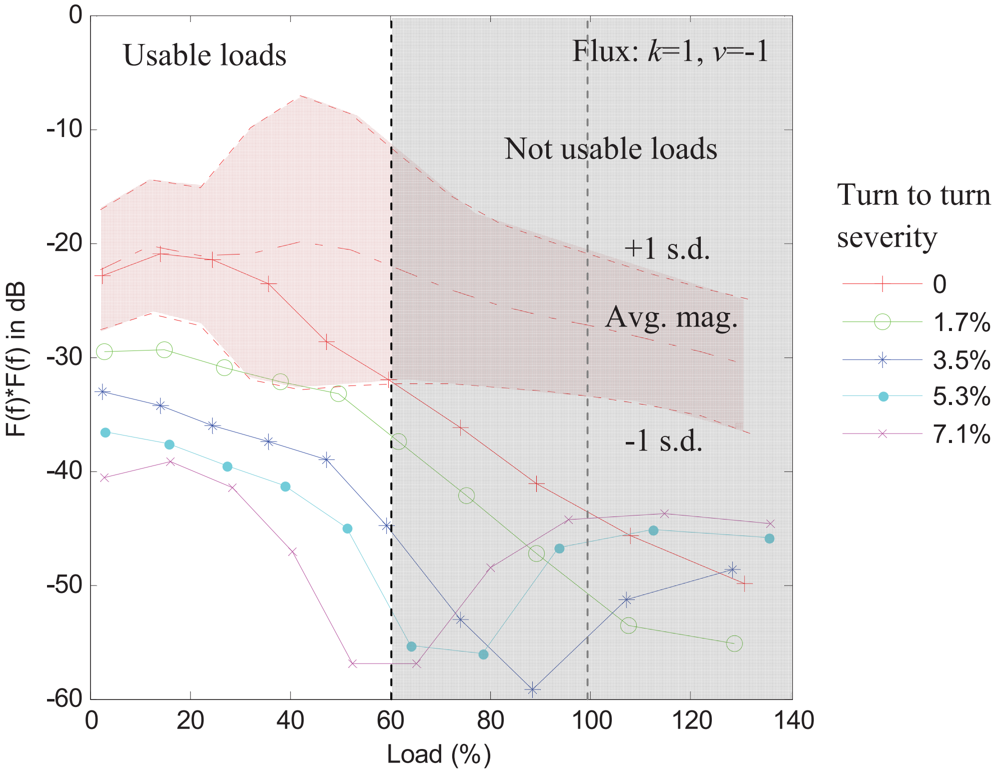

Figure 5.5 – Magnitude of the frequency components in (Eq. 5.1) at $k = 1$ and $v = -1$ in the leakage flux signal as a function of load.

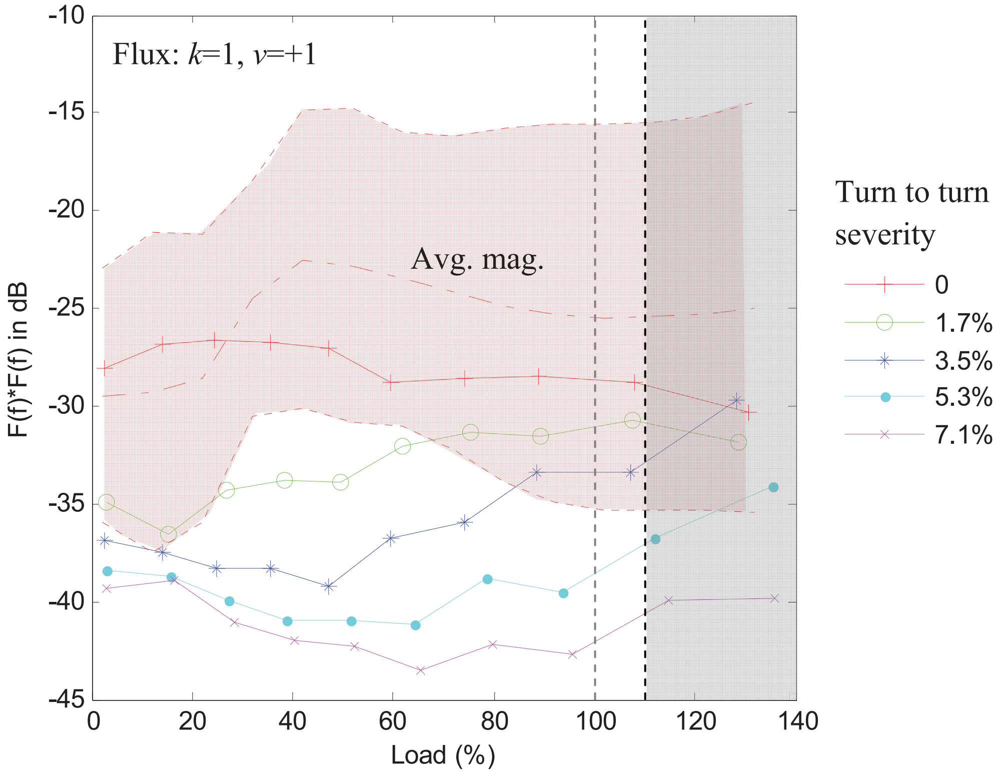

Figure 5.6 – Magnitude of the frequency components in (Eq. 5.1) at $k = 1$ and $v = +1$ in the leakage flux signal as a function of load.

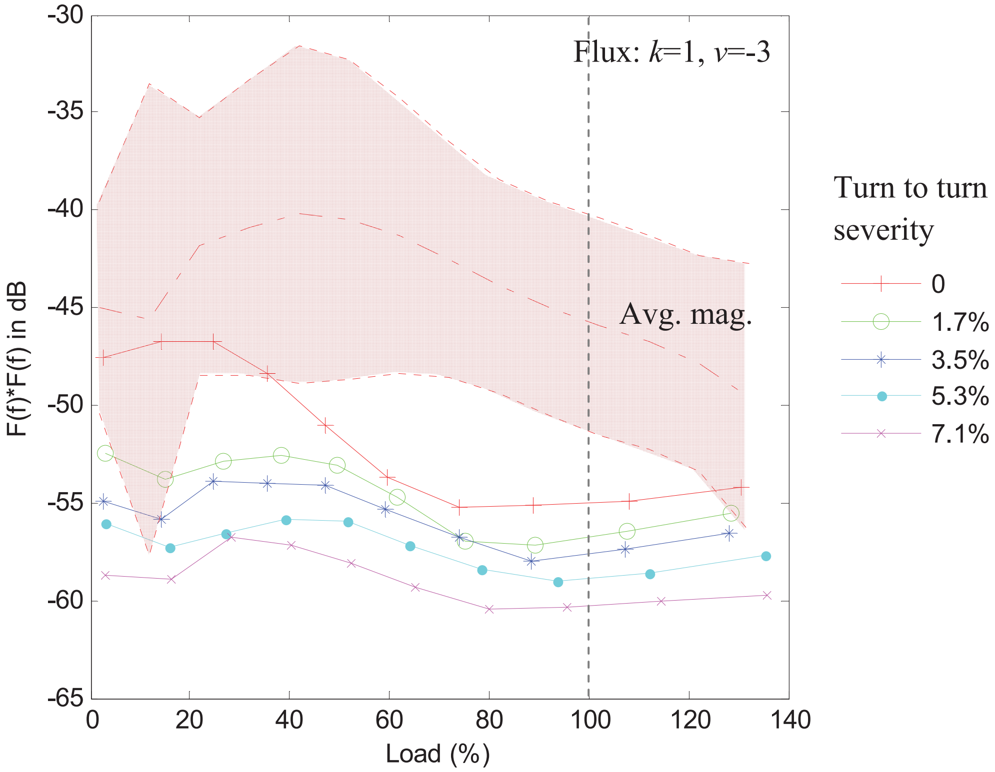

Figure 5.7 – Magnitude of the frequency components in (Eq. 5.1) at *k* = 1 and *v* = -3 in the leakage flux signal as a function of load.

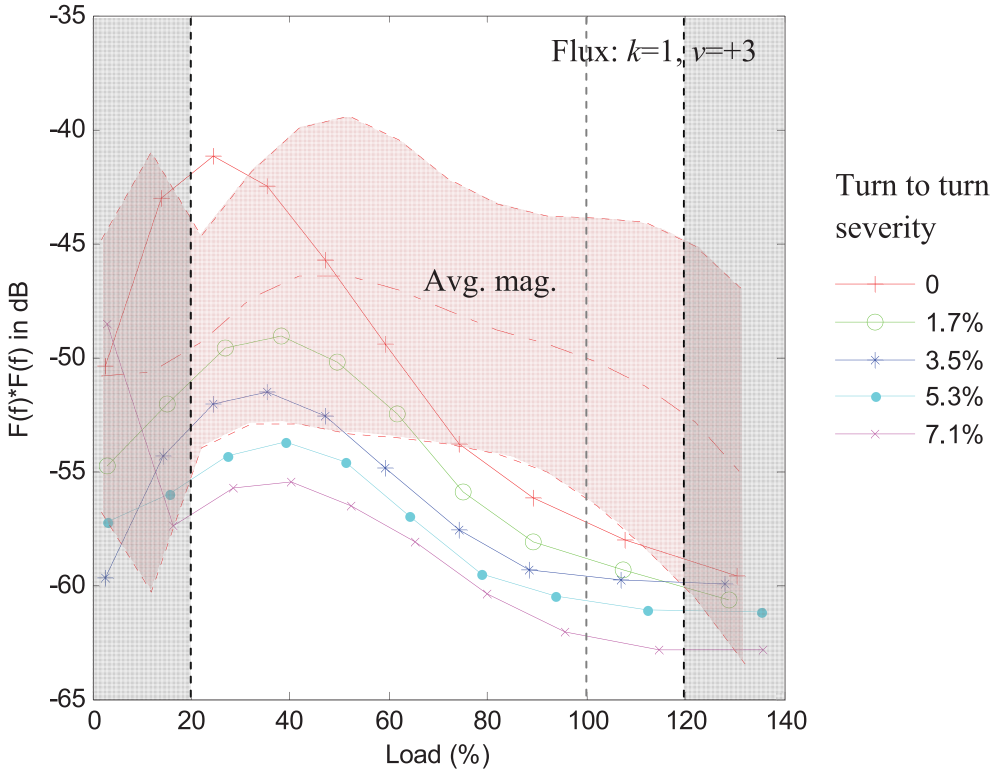

Figure 5.8 – Magnitude of the frequency components in (Eq. 5.1) at *k* = 1 and *v* = +3 in the leakage flux signal as a function of load.

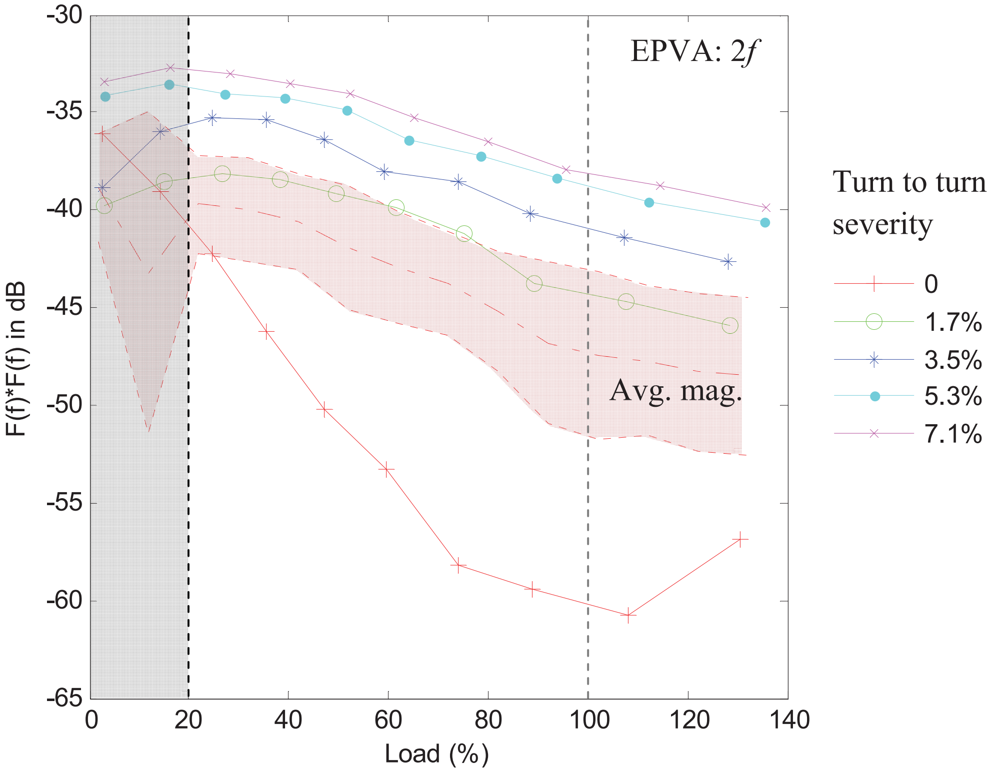

Figure 5.9 – Magnitude of the EPVA feature as a function of load.

5.4. Analysis of Phase to Phase Turn Faults

The phase to phase turn faults are expected to have similar electromagnetic consequences in the stator and rotor MMFs as the turn to turn faults. As such, the features that are found to be useful in detecting turn to turn faults are also expected to be useful in detecting phase to phase turn faults. The following shorted turn investigation will examine all of the ideal turn to turn features and some of the non-ideal turn to turn features in an attempt to detect and estimate the severity of the phase to phase turn faults.

5.4.1. Using Fundamental Sidebands of Rotor Frequency Harmonics

The turn to turn fault investigation has found that the frequency components in (Eq. 5.1) at $k = 1$ and $v = \pm 1, \pm 3$ from the leakage flux signal are very good at detecting the turn to turn faults. Therefore, this shorted turn investigation will utilise these ideal turn to turn features for the detection of phase to phase turn faults.

Components at $k = 1$ and $v = \pm 1$ in the Leakage Flux Signal

Figure 5.10 shows how the magnitude of the components varies under the different loading and phase to phase turn fault conditions, while Table 5.10 summarised the important characteristics of the frequency components. The figure shows that the magnitude of the lower sideband component ($k = 1$, $v = -1$) consistently increases with increasing fault severity when the load is greater than 70%. Under these loads, the magnitude variation between the healthy and the 7.1% fault condition is observed to be about 10 to 15 dB. This finding suggests that the lower sideband can be considered as a good phase to phase turn feature. In contrast, the same feature was also considered as a good turn to turn feature but its magnitude was found to consistently decrease, instead of increase, with increasing fault severity at loads less than 60%. This shows that the two types of shorted turn faults may show different characteristics for the fault features.

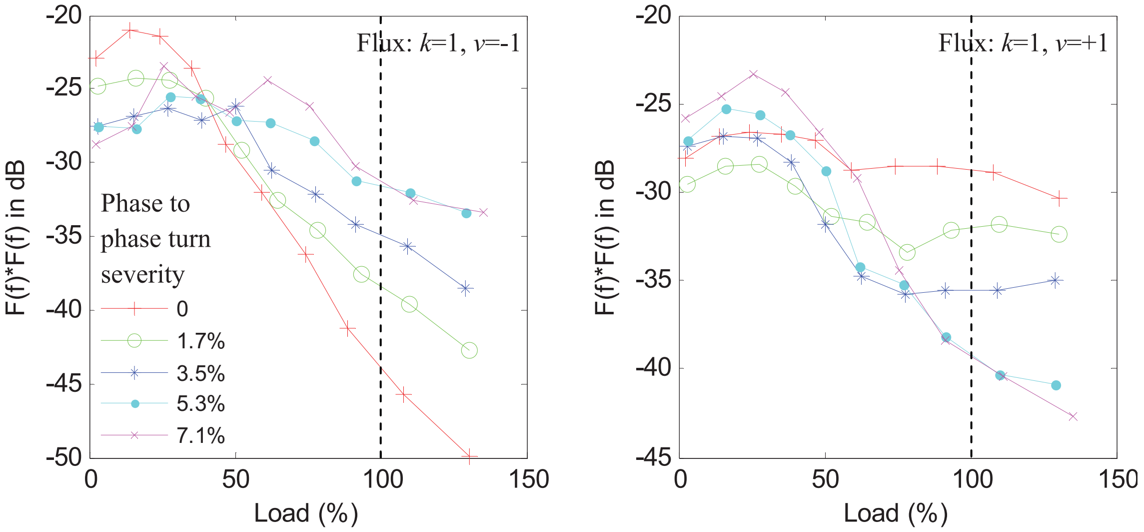

Figure 5.10 – Magnitude of the frequency components in (Eq. 5.1) at $k = 1$, $v = \pm 1$ from the leakage flux signal as a function of load.

Figure 5.10 also shows that the magnitude of the upper sideband component ($k = 1$, $v = +1$) tends to decrease as the severity of the fault increases when the load is greater than 70%. However, the magnitudes of the 5.3% fault and the 7.1% fault are indistinguishable in this case. As a result, the upper sideband can only be used to distinguish between the healthy and the faulty conditions but not to separate the fault severity. In contrast, the same feature was considered as a good turn to turn feature, where its magnitude can separate the different fault severities, although the magnitude difference between the healthy and the

7.1% fault in the two types of shorted turn faults was found to be about the same (10 – 15 dB).

Table 5.10 - Characteristics of the frequency components in (Eq. 5.1) at $k = 1$, $v = \pm 1$

Frequency component	**Signal**	**(Min,Max) mag. Δ due to 7.1% fault under all loads**	**Max healthy mag. Δ due to all loads**	**Useful loads**	**Fault levels**	**Notes**
(Eq. 5.1) at $k = 1$, $v = -1$	Flux	-7, 16 dB	29 dB	>70%	All	F
(Eq. 5.1) at $k = 1$, $v = +1$	Flux	3, -12 dB	4 dB	>70%	All	F

Components at $k = 1$ and $v = \pm 3$ in the Leakage Flux Signal

The experimental results of this study (see Table 5.11 and *Appendix A.7*) show that the magnitude of the frequency components tends to increase (consistently for the upper sideband) with increasing fault severity. The results also show that the magnitude variation is more significant in the upper sideband (5 – 10 dB between the healthy and the 7.1% fault) than in the lower sideband (about 5 dB between the healthy and the 7.1% fault), which makes the upper sideband the better feature.

As a comparison, the same features were also considered as turn to turn features but their magnitudes were found to decrease, instead of increase, with increasing fault severity. This provides more supports that the two types of shorted turn faults may show different characteristics on the fault features. These findings suggest that the phase to phase turn faults have similar, but not the same, electromagnetic consequences to the stator and rotor MMFs as the turn to turn faults.

Table 5.11 - Characteristics of the frequency components in (Eq. 5.1) at $k = 1$, $v = \pm 3$

Frequency component	**Signal**	**(Min,Max) mag. Δ due to 7.1% fault under all loads**	**Max healthy mag. Δ due to all loads**	**Useful loads**	**Fault levels**	**Notes**
(Eq. 5.1) at $k = 1$, $v = -3$	Flux	0, 6 dB	9 dB	>30%	All	F
(Eq. 5.1) at $k = 1$, $v = +3$	Flux	5, 10 dB	18 dB	All	All	F

5.4.2. Using Twice Supply Frequency

The twice supply frequency components from the DEH and NDEH vibration sensors are found to be better than the DEV vibration sensor in detecting the turn to turn faults. Hence, these two vibration sensors are used to investigate the phase to phase turn faults.

The experimental results given in Table 5.12 and *Appendix A.8* show that the frequency component from the DEH vibration sensor can only be used to distinguish between the healthy and the 7.1% fault condition when the load is greater than 70%. Similarly, the frequency component from the NDEH vibration sensor can only be used to distinguish the healthy and the 7.1% fault but under all tested loading conditions. This analysis shows very similar results to the analysis of the turn to turn faults.

Table 5.12 – Characteristics of the twice supply frequency components

Frequency component	**Signal**	**(Min,Max) mag. Δ due to 7.1% fault under all loads**	**Max healthy mag. Δ due to all loads**	**Useful loads**	**Fault levels**	**Notes**
(Eq. 5.2)	DEH Vib.	-1, 5 dB	8 dB	>70%	≥7.1%	F
(Eq. 5.2)	NDEH Vib.	2, 9 dB	11 dB	All	≥7.1%	F

5.4.3. Using Rotor Slot Harmonics

The turn to turn fault investigation has found that the frequency components in (Eq. 5.3) at $n_d = 0$, $k = 1$, and $v = \pm 1, \pm 3$ from the leakage flux signal can be used to distinguish between the healthy and faulty conditions. Although the frequency components may not be able to separate the different fault severities, the frequency components can still be considered as turn to turn features (the non-ideal features). Therefore, these non-ideal turn to turn features will be utilised for analysing the phase to phase turn faults.

The experimental results given in Table 5.13 and *Appendix A.9* show that most of these frequency components are not useful because they do not show significant magnitude variation (i.e. mostly less than 5 dB) between the healthy and the faulty conditions. However, the frequency component at $n_d = 0$, $k = 1$, and $v = +1$ in the flux signal show a useful pattern, where the magnitude consistently increases as the severity of the fault increases (with 5 – 10 dB variation between the healthy and the 7.1% fault), when the load is greater than 30%. As a result, this upper sideband can be considered as a good phase to phase turn feature. As a comparison, the upper sideband was also considered as a turn to turn feature but its magnitude was found to decrease, instead of increase, with increasing fault severity.

Table 5.13 - Characteristics of the frequency components in (Eq. 5.3) at $k = 1$ and $v = \pm1, \pm3$

Frequency component	**Signal**	**(Min,Max) mag. Δ due to 7.1% fault under all loads**	**Max healthy mag. Δ due to all loads**	**Useful loads**	**Fault levels**	**Notes**
(Eq. 5.3) at $k = 1$, $v = -1$	Flux	0, 8 dB	4 dB	-	-	NF
(Eq. 5.3) at $k = 1$, $v = +1$	Flux	5, 11 dB	8 dB	>30%	All	F
(Eq. 5.3) at $k = 1$, $v = -3$	Flux	-9, 9 dB	16 dB	-	-	NF
(Eq. 5.3) at $k = 1$, $v = +3$	Flux	1, 4 dB	9 dB	-	-	NF

5.4.4. Using Third Harmonic of the Fundamental

The experimental results given in Table 5.14 and *Appendix A.10* show that the frequency component at $3f$ in both the current and flux signals are insensitive to the phase to phase turn faults and show insignificant magnitude variation among the different fault severities. As a consequence, these components cannot be considered as phase to phase turn features.

Table 5.14 – Characteristics of the third supply harmonics

Frequency component	**Signal**	**(Min,Max) mag. Δ due to 7.1% fault under all loads**	**Max healthy mag. Δ due to all loads**	**Useful loads**	**Fault levels**	**Notes**
(Eq. 5.4)	Current	4, -5 dB	10 dB	-	-	NF
(Eq. 5.4)	Flux	0, -3 dB	7 dB	-	-	NF

5.4.5. Using Extended Park's Vector Approach (EPVA)

The important characteristics of the EPVA component are summarised in Table 5.15. The magnitude of the EPVA component seems to be rather steady at –25 to -35 dB for the faulty conditions (i.e. only small magnitude variation, less than 5 dB, with the load) and decreasing with the load for the healthy condition, as shown in Figure 5.11. The magnitude variation among the different fault severities also shows a very good pattern, where the magnitude consistently increases with increasing fault severity, under all loading conditions. Although the magnitude separation between the different fault severities is quite small (less than 5 dB), the magnitude separation between the healthy and faulty conditions is quite significant (about 10 – 25 dB). Therefore, this EPVA component can be considered as a good phase to phase turn feature, although it may not be able to estimate the fault severity. These findings are similar to the findings when using the same feature to analyse the turn to turn faults.

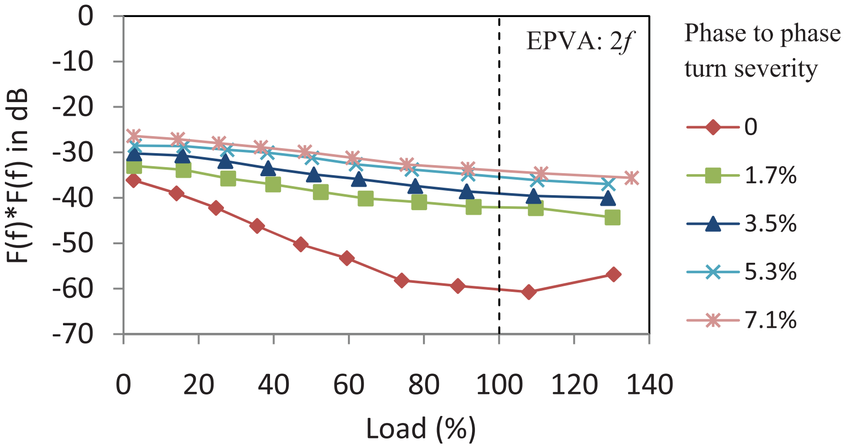

Figure 5.11 - Magnitude of the EPVA feature as a function of load.

Table 5.15 – Characteristics of the EPVA feature

Frequency component	**Signal**	**(Min,Max) mag. Δ due to 7.1% fault under all loads**	**Max healthy mag. Δ due to all loads**	**Useful loads**	**Fault levels**	**Notes**
EPVA	Current	10, 26 dB	25	All	All	F

5.4.6. Summary of Effective Phase to Phase Turn Features

The analysis of the phase to phase turn faults reveals that the frequency components which are sensitive to the turn to turn faults are also generally sensitive to the phase to phase turn faults and the frequency components which are not sensitive to the turn to turn faults are also generally insensitive to the phase to phase turn faults. These findings support the proposition that the phase to phase turn faults exhibit similar (but not the same) electromagnetic consequences to the stator and rotor MMFs as the turn to turn faults.

As in the turn to turn features, the phase to phase turn features can be divided into 2 categories, which are ideal and non-ideal features. The phase to phase turn features that are found to be ideal are listed in Table 5.16 and the non-ideal features are listed in Table 5.17. A comparison between the phase to phase turn features and the turn to turn features (Table 5.8 and Table 5.9) shows that the ideal turn to turn features are not necessarily ideal features for the phase to phase turn faults and their characteristics (i.e. magnitude variation due to fault and magnitude variation due to load) are not the same and can even be the opposite (e.g. the magnitude of the feature in (Eq. 5.1) at $k = 1$, $v = -1$ is found to decrease with fault severity in the turn to turn faults but it increases with fault severity in the phase to phase turn faults).

Table 5.16 – Ideal Phase to Phase Turn Features

Frequency component	Signal	Useful loads	(Min,Max) mag. Δ due to 7.1% fault	Max healthy mag. Δ due to load
(Eq. 5.1) at $k = 1$, $v = -1$	Flux	>70%	10.1, 16.6 dB	13.7 dB
(Eq. 5.1) at $k = 1$, $v = +3$	Flux	All	5, 9.8 dB	18.4 dB
(Eq. 5.3) at $k = 1$, $v = +1$	Flux	>30%	7.5, 10.7 dB	5.4 dB
EPVA	Current	All	9.7, 26.1 dB	24.6 dB

Table 5.17 – Non-Ideal Phase to Phase Turn Features

Frequency component	**Signal**	**Useful loads**	**Fault levels**	**(Min,Max) mag. Δ due to 7.1% fault**	**Max healthy mag. Δ due to load**	**Notes**
(Eq. 5.1) at $k = 1$, $v = +1$	Flux	>70%	All	-5.8, -12.4 dB	1.8 dB	D
(Eq. 5.1) at $k = 1$, $v = -3$	Flux	>30%	All	1.5, 5.6 dB	6.9 dB	D
(Eq. 5.2)	DEH Vib.	>70%	≥7.1%	2.3, 4.8 dB	2 dB	D
(Eq. 5.2)	NDEH Vib.	All	≥7.1%	2.2, 8.7 dB	11.4 dB	D

where D denotes that the feature can distinguish between the healthy and the faulty conditions but it may not separate all the fault severities.

5.4.6.1. Usability of the Ideal Phase to Phase Turn Features

This section examines all of the ideal phase to phase turn features in greater detail by considering the magnitude variation due to the nominally identical healthy machines and their standard deviations, in order to determine the loads and the fault severities in which the features can reliably be used to detect the faults and to examine the possibility of estimating the fault severity.

Figure 5.12 shows how the first ideal feature (i.e. (Eq. 5.1) at $k = 1$, $v = -1$) varies under the different loading and fault conditions while illustrating the useful loading conditions (non grey shaded area) and the result of the six healthy motor variation tests (red shaded area). The figure shows that the magnitude tends to increase as the severity of the fault increases. However, the magnitude of the faulty conditions is either within or below the magnitude variation of the six healthy motors, while the magnitude of the healthy condition is significantly below the magnitude variation of the six healthy motors. This observation suggests that setting a threshold for the feature would be very difficult. This is because the magnitude of the faulty conditions, which is within or below the magnitude variation of the six healthy motors, would dramatically increase the probability of false alarm. As a consequence, trending of the feature, which is a process to measure the feature continuously or regularly so as to detect any changes to the feature, is the only possible alternative.

As a comparison, the same feature was found to be able to detect turn to turn faults with severities greater than 1.7% under loads less than 60% (Figure 5.5). This comparison again shows that there may be fault characteristic differences between the turn to turn faults and the phase to phase turn faults.

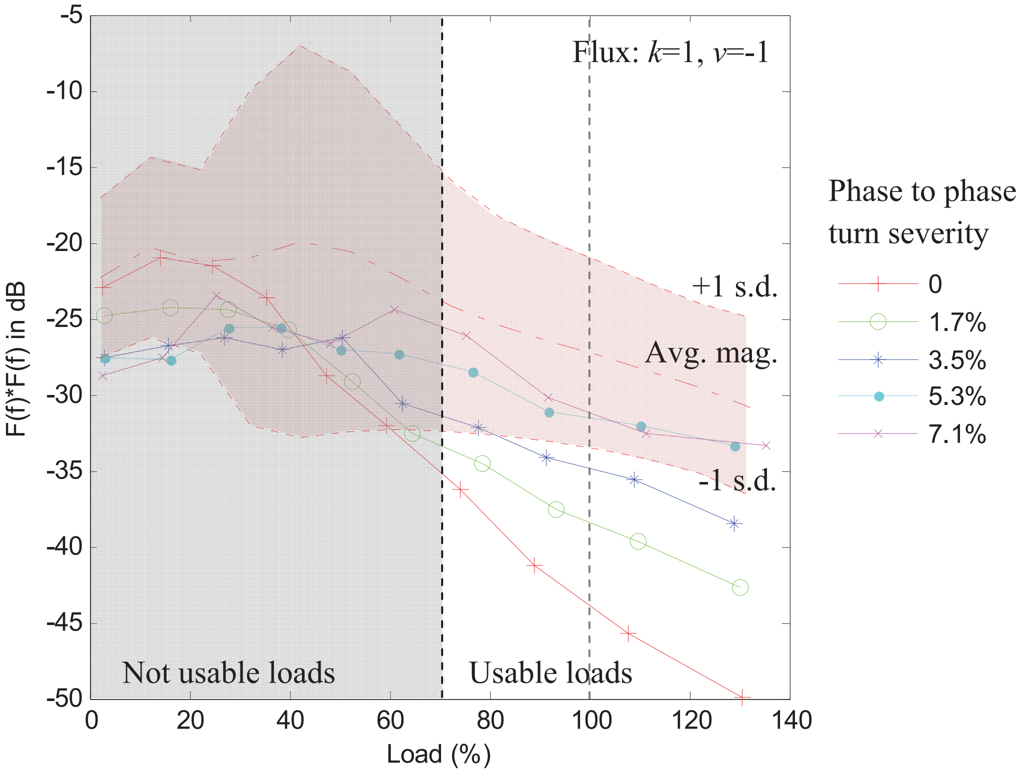

Figure 5.12 – Magnitude of the frequency component in (Eq. 5.1) at $k = 1$ and $v = -1$ from the leakage flux signal as a function of load.

Figure 5.13 shows that for the second ideal feature (i.e. (Eq. 5.1) at $k = 1$, $v = +3$), the magnitude variation of the six healthy motors (red shaded area) is only fully distinguishable to the magnitude of the faulty conditions when the fault severity is at 3.5% or greater and the load is less than 50%. As a result, setting a threshold for the feature can only be considered if the feature only needs to identify faults with severity greater than or equal to 3.5% and loads less than 50%. As a comparison, the same feature was also identified as an ideal turn to turn feature, where it could either detect all fault severities when the loads were between 60% and 110% or detect faults with severity greater than 5.3% under all tested loads. Based on these findings, it is difficult to make any correlations between the phase to phase turn faults and the turn to turn faults.

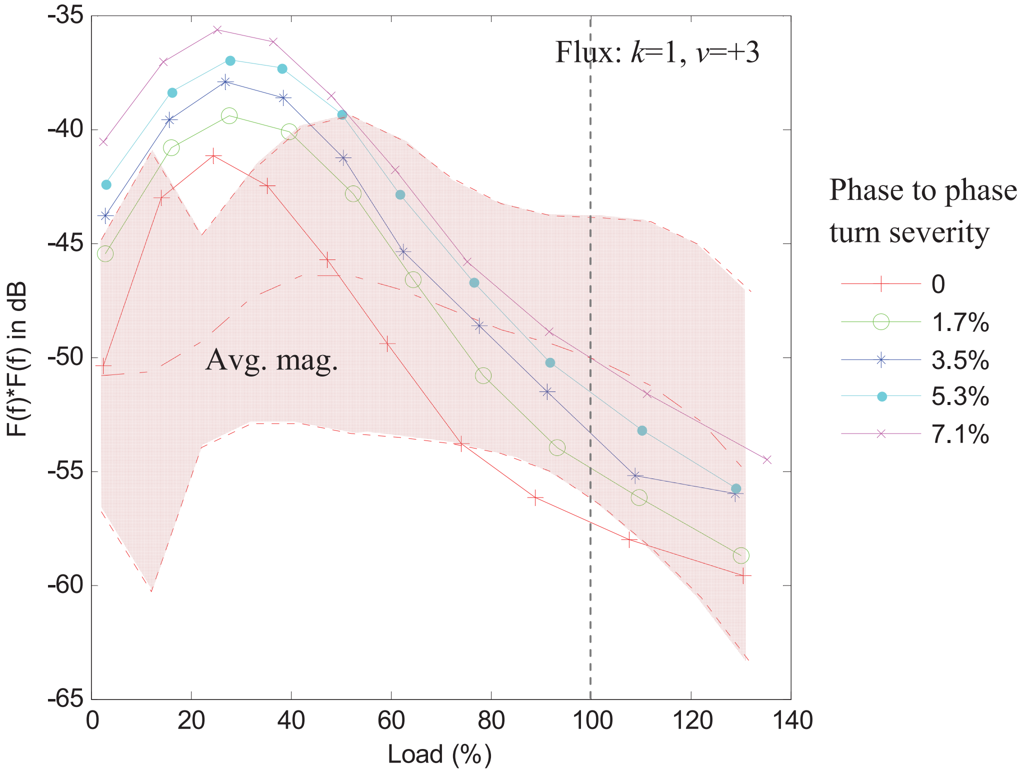

Figure 5.13 – Magnitude of the frequency component in (Eq. 5.1) at $k = 1$ and $v = +3$ from the leakage flux signal as a function of load.

Figure 5.14 shows that the magnitude of the third ideal feature (i.e. (Eq. 5.3) at $k = 1$ and $v = +1$) tends to increase as the severity of the fault increases. However, the magnitude of the faulty conditions under the useful loading conditions (non grey shaded area) is either within or below the magnitude variation of the six healthy motors (red shaded area). Furthermore, the magnitude of the healthy condition is significantly below the magnitude variation of the six healthy motors. This observation suggests that setting a threshold for the feature would be very difficult. As a consequence, trending of the feature is the only possibility. In contrast, the same feature was not found to be an ideal turn to turn fault feature because its magnitude did not consistently increase/decrease with the fault severity.

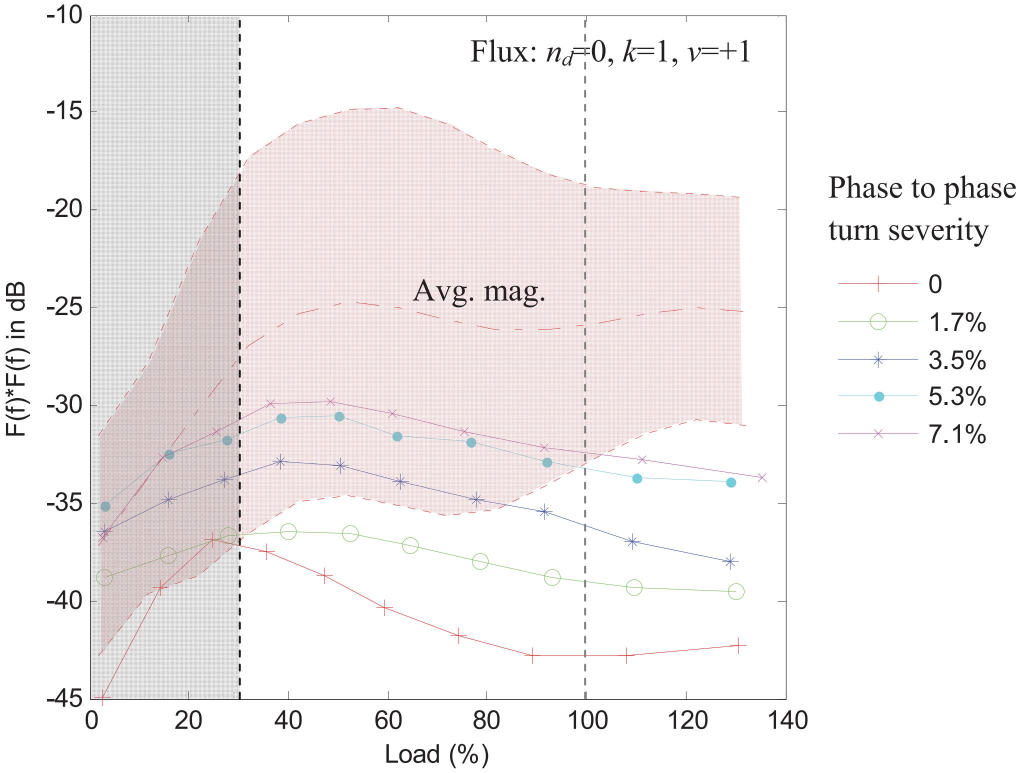

Figure 5.14 – Magnitude of the frequency component in (Eq. 5.3) at $n_d = 0$, $k = 1$ and $v = +1$ from the leakage flux signal as a function of load.

Figure 5.15 shows that for the EPVA feature, the magnitude variation of the six healthy motors (red shaded area) is fully distinguishable to the magnitude of the faulty conditions under all tested loading and phase to phase turn conditions. Therefore, setting a threshold for the feature can be considered for all loading and fault conditions. These results show that detecting the phase to phase turn faults is possible with the EPVA feature. However, estimating the fault severity with 2% accuracy may not be possible because the magnitude difference between one fault severity to the next is less than 5 dB. Note that the baseline study (Chapter 4) shows that the magnitude variation due to repeated measurements can vary up to 5 dB.

As a comparison, the same feature was also found to be an ideal turn to turn feature with similar characteristics, where it could detect the faults with severity greater or equal to 3.5% when the loads were greater than 20% (Figure 5.9). The comparison suggests that detecting the phase to phase turn faults with this feature is slightly more feasible than detecting the turn to turn faults.

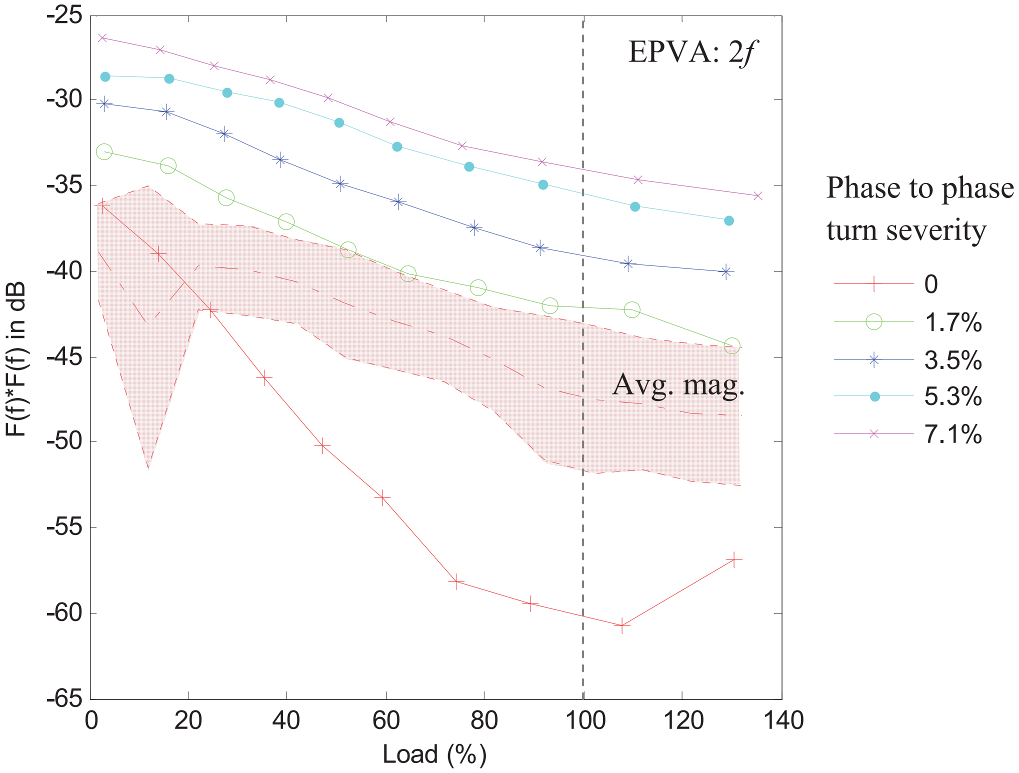

Figure 5.15 – Magnitude of the EPVA feature as a function of load.

5.5. Summary

Previous research has investigated turn to turn faults using fault frequency components and Park's vector approach under limited fault severities and under a few loading conditions. The research generally identified that there is an increase or decrease in the magnitude of the fault features but did not make a comprehensive correlation between the feature magnitude and the load or between the feature magnitude and the fault severity. As a consequence, previous work was unable to make a clear conclusion regarding for what loads can the feature be effective or what fault severities can the feature detect reliably.

The shorted turn investigation in this chapter expanded previous work by investigating not only turn to turn faults but also phase to phase turn faults using the shorted turn fault frequency components and the Park's vector approach in the current, leakage flux, and vibration sensor signals. The investigation examined each of the fault features under a wide range of fault severities (0% - 7.1% in five steps) and each fault severity was tested under a range of loading conditions (no load – over load in ten steps). The investigation also compared the different shorted turn fault detection methods and identified the most relevant features for detecting the turn to turn faults and the phase to phase turn faults. Furthermore, these most relevant features were compared with the magnitude variation due to nominally identical healthy motors and its standard deviations (using the baseline study in Chapter 4) in order to determine the usability of the features (i.e. the loads and the fault severities over which the feature can be effective).

The key results of this investigation are:

- Fault frequency components are identified whose magnitudes vary (increase or decrease) with increasing levels of shorted turn fault, however these components are also found to be sensitive to the level of loading;
- The features obtained from the leakage flux signal seem to be generally better (i.e. show larger and more consistent magnitude variations between the healthy and faulty motors) than the features obtained from the stator current;
- The EPVA feature in the current signal gives the best results in detecting both types of shorted turn faults (turn to turn and phase to phase turn faults), followed closely by the frequency components in (Eq. 5.1) at $k = 1$ and $v = \pm 1, \pm 3$ from the leakage flux signal.
- Turn to turn faults can be detected effectively using the EPVA feature when the load is greater than 20% and the fault severity is greater than or equal to 3.5%; and phase to phase turn faults can be detected effectively using the EPVA feature under all loading conditions when the fault severity is greater than or equal to 1.7%.
- Detecting the turn to turn faults and the phase to phase turn faults is possible, however estimating the fault severity with 2% accuracy is very difficult.

Chapter 6. Static Eccentricity Fault Detection

6.1. Introduction

There has been significant research already undertaken on steady-state condition monitoring techniques for detecting static and dynamic eccentricity faults in induction machines using characteristic fault frequencies in the current and vibration signals [13, 27-29, 76-79]. Static eccentricity (SE) is where the air gap difference between the stator and the rotor varies but the position of the minimum air gap is fixed, while dynamic eccentricity (DE) is where the position of the minimum air gap rotates with the rotor.

In [13], a 11 kW machine was studied to detect and distinguish different severities of both static (SE = 0 to 50% in 6 equal steps) and dynamic eccentricity (DE = 0%, 20%, 40%) using the fault frequency components in (Eq. 1.3) from the current spectrum, under 3 different loading conditions (0%, 50% and 100%). It was demonstrated in the paper that when both static and dynamic eccentricity faults were present, the magnitude of the sideband components increased as the severity of the faults increased. For example, the sideband magnitude was less than -65 dB for the healthy motor and it was about -45 dB for the faulty motor with 33% SE and 20% DE under full load condition. However, when only static eccentricity was present, the sideband magnitude variation between the healthy and the faulty motors was relatively small and hence the faults were harder to detect. For example, the sideband magnitude was less than -65 dB for the healthy motor and it was about -60 dB for the faulty motor with 50% SE under full load condition. This finding was confirmed by the work in [79].

The work in [29] investigated possible eccentricity faults of unknown severity in a 1.45 MW motor at an industrial site by utilising the fault frequency components in (Eq. 1.2) and (Eq. 1.3) from the current signal. It was observed that the magnitude of the frequency components increased by about 5 dB for the faulty motor compared to the healthy motor. The work was improved in [78] by investigating prediction curves for the stator current versus the frequency component in (Eq. 1.2) as a function of eccentricity under two different loading conditions. The investigation found that the magnitude of the frequency component was sensitive to both the fault severity and the loading conditions.

Eccentricity fault detection on a simulated 2.24 kW machine, using the modified winding function approach, was reported in [76]. The paper investigated different levels of both static and dynamic eccentricity using (Eq. 1.2) and (Eq. 1.3) in the current spectrum under two loading conditions (no load and full load). In the study, the simulation results were verified using a practical motor. It was concluded that the fault frequency components given by (Eq. 1.3) are present in both the healthy and the faulty motors and the magnitude difference between them was marginal (i.e. less than 5 dB) when dynamic eccentricity was not present (e.g. SE = 38% and DE = 0%). However, the magnitude difference between the healthy and faulty motors became more evident (up to 30 dB) when dynamic eccentricity was also introduced to the motor (e.g. SE = 41% and DE = 21%).

Other eccentricity fault detection techniques were investigated in [80-82]. The work in [80] utilised multiple reference frame (MRF) theory in order to synchronise a different reference frame to the fault frequency components in (Eq. 1.3) so that their amplitudes were less dependent on the characteristics and operating conditions of the motor. The work reported a significant increase in the severity factor of the faulty motor compared to the healthy motor. The investigation in [81] used the Park's vector approach, which was then quantified by means of the normalised splitting severity factor, in order to distinguish the different levels of static eccentricity fault. It was found that the normalised splitting severity factor tends to increase as the fault severity increases. The work in [82] utilised a time stepping finite element (FE) method in order to predict the amplitude of the fault frequency components in (Eq. 1.2) as a function of static eccentricity. The results showed that the predicted amplitude lies between 0 – 5 dB of the actual amplitude.

In summary, the majority of the previous work only utilised the fault frequency components in (Eq. 1.2) and (Eq. 1.3) to detect eccentricity faults. It was observed that static eccentricity faults showed less magnitude variation on the fault frequency components than the combined faults of static and dynamic eccentricity. In most cases, static eccentricity faults increased the magnitude of the fault frequency components by about 5 dB. Furthermore, the previous work examined the eccentricity faults using only one type of sensor signal under limited fault severities and limited loading conditions. As a consequence, the authors did not investigate the effect of load on the eccentricity features and they made no correlation between the loads and the fault severities at which the features can be reliably used for fault detection. However, it is critical to understand how fault severities and loading conditions affect the fault detection and to identify the most relevant features for detecting eccentricity faults.

The work in this chapter examines and compares potential static eccentricity measures from the current, leakage flux, and vibration sensor signals in order to identify the useful features. Then, the useful features are combined in order to produce a better fault indicator, in which case the feasibility of fault detection and fault estimation is examined. Note that this work focuses only on static eccentricity faults because they are found to be more difficult to detect than dynamic eccentricity faults. Furthermore, if a feature can detect static eccentricity faults, it is very likely that the same feature can also detect mixed eccentricity faults (i.e. both static and dynamic eccentricity).

This eccentricity investigation is based on an extensive series of sensor measurements taken using a specially modified 2.2 kW induction machine under varying conditions of static eccentricity and loading (see *section 1.5.2*). The static eccentricity tests are performed from –50% to +50% (of the total airgap of the test motor) in nine equal steps (that is, from –0.2 mm to +0.2 mm, where the nominal airgap is 0.4 mm). At each eccentricity level, the load is varied from 5% to 100% of rated load in ten steps. In addition, the test motor is also re-aligned every time the eccentricity level is changed in order to maintain the consistency of the measurement data.

6.2. Eccentricity Fault Detection Techniques

As it is well known, an induction motor is a highly symmetrical machine, whose symmetry is distorted by the presence of a fault. The eccentricity related distortion in induction motors produces characteristic fault frequencies in the stator current, axial leakage flux, and motor vibration signals as given in the (Eq. 6.1) - (Eq. 6.7) in Table 6.1.

Table 6.1 – Eccentricity Features

Eccentricity Features	**Sensor Types**	**Eccentricity Types**	**References**	**Eqn. No.**
Rotor slot harmonics, f_{sede1}	Current, leakage flux	Static, dynamic	[27-29, 76-78]	(Eq. 6.1)
Rotor frequency sidebands of the fundamental, f_{sede2}	Current, leakage flux	Static, dynamic	[13, 27-29, 76, 79]	(Eq. 6.2)
Rotor frequency sidebands of twice the fundamental, f_{sede3}	Vibration	Static, dynamic	[13]	(Eq. 6.3)
Third harmonic of rotor frequency, f_{se1}	Vibration	Static		(Eq. 6.4)
Twice supply frequency, f_{se2}	Vibration	Static	[13]	(Eq. 6.5)
Rotor frequency, f_{de1}	Vibration	Dynamic	[13]	(Eq. 6.6)
Second harmonic of rotor frequency sidebands of the fundamental, f_{de2}	Vibration	Dynamic	[13]	(Eq. 6.7)
RMS vibration	Vibration	Static, dynamic		

where,

$$f_{sede1} = f\left[(kR \pm n_d)\frac{(1-s)}{p} \pm v\right] \tag{Eq. 6.1}$$

$$f_{sede2} = f \pm f_r \tag{Eq. 6.2}$$

$$f_{sede3} = 2f \pm f_r \tag{Eq. 6.3}$$

$$f_{se1} = 3f_r \tag{Eq. 6.4}$$

$$f_{se2} = 2f \tag{Eq. 6.5}$$

$$f_{de1} = f_r \tag{Eq. 6.6}$$

$$f_{de2} = 2(f \pm f_r) \tag{Eq. 6.7}$$

Note that (Eq. 6.1) and (Eq. 6.2) are the same as (Eq. 1.2) and (Eq. 1.3) but they are repeated here for convenience.

The previous studies primarily utilised only one of these equations and a single sensor type, and found that a significant increase in the magnitude of a characteristic fault frequency can indicate an eccentricity fault. However, neither the relationship between the degree of eccentricity and the magnitude of the fault frequency component nor the sensitivity of these fault frequencies to changes in loading and misalignment has been reported in detail in the literature. This chapter of the thesis will address these issues.

6.2.1. Current and Flux Monitoring

Stator current and axial leakage flux measurements can be used for eccentricity fault detection. Eccentricity faults disturb the symmetry of an induction motor, which results in an unbalanced magnetic pull (UMP) which in turn produces known characteristic fault frequencies in the current and flux spectra.

As given in Table 6.1, (Eq. 6.1) can be used to detect static eccentricity when n_d is set to 0. When $n_d = 0$, the equation can be reduced to the combination of rotor frequency, f_r, and fundamental frequency, f, as given below in (Eq. 6.8).

$$f_{sede1} = f\left[(kR \pm 0)\frac{(1-s)}{p} \pm v\right] = kRf_r \pm vf \qquad \text{(Eq. 6.8)}$$

It has been reported in [13, 76, 79] that the presence of static eccentricity faults may also produce dynamic eccentricity components. Therefore, monitoring both the dynamic and static eccentricity fault frequencies even in the presence of only one type of eccentricity fault may be beneficial. Dynamic eccentricity faults can also be detected using (Eq. 6.1) by setting n_d to 1, 2, 3 …

A limitation of the eccentricity fault frequency components in (Eq. 6.1) is that they may not be present in all types of motors. It was shown in [27, 83] that these frequency components are present in motors which do not generate the principal slot harmonic (PSH), Rf_r, in the current spectrum if their number of rotor bars satisfies (Eq. 6.9) and in motors which generate the PSH in the current spectrum if their number of rotor bars satisfies (Eq. 6.10). This difference comes from the differences in the additional pole pair rotor MMF harmonics, which are produced by the MMF acting on the permeance between the stator and the rotor [76].

$$R = 2p(3(m \pm q) \pm r) \qquad \text{(Eq. 6.9)}$$

$$R = 2p(3(m \pm q) \pm r) \pm z \qquad \text{(Eq. 6.10)}$$

where r, z, m, and q are real variables governed by the following relationships; $r = 0$ or 1, $z = 1$ or 2, $m \pm q = 0,1,2,3,\ldots$

Another feature commonly utilised for eccentricity fault detection in the current and flux spectra is associated with the fault frequency components in (Eq. 6.2). These fault frequency components are usually found to be relatively strong and easy to detect. In addition, unlike (Eq. 6.1), machine construction information, such as the number of rotor slots, is not required in (Eq. 6.2). However, the fault frequency components in (Eq. 6.2) are affected by the presence of both static and dynamic eccentricity [13, 29]. Therefore the feature from (Eq. 6.2) cannot distinguish the type of eccentricity fault but it is still considered reliable in detecting the general level of eccentricity.

6.2.2. Vibration Monitoring

As listed in Table 6.1, the characteristic eccentricity fault frequency components in (Eq. 6.3) - (Eq. 6.7) are present in the motor vibration signal and these frequency components can be used to detect eccentricity faults. Although a detailed derivation of the origin of these fault frequency components is given in [13], there is a lack of detailed investigation and experimentation in the literature using these frequency components.

In this chapter, the effect of eccentricity on the RMS vibration level is also investigated since eccentricity faults are expected to cause unbalanced magnetic pull (UMP) which is likely to increase the overall vibration level of the machine. However, an increase in vibration level can also be caused by many other factors such as misalignment, load faults, and supply faults (e.g. supply imbalance). Therefore, the RMS vibration feature cannot be used as a single eccentricity feature but it can be used as a support eccentricity feature for confirming the existence and the degree of the eccentricity faults.

6.3. Analysis of Static Eccentricity Faults

The aim of this section is to identify useful eccentricity fault features from potential eccentricity fault measures (see Table 6.1). For a fault measure to be considered useful in this case, it has to satisfy the following requirements:

1. The magnitude of a fault measure must be well above the noise floor (i.e. a fault measure must be detectable), and
2. There must be consistent and observable magnitude variation between healthy and faulty motors (i.e. the magnitude of a fault measure must increase with increasing fault severity).

Note that the useful feature in this investigation doesn't need to have a significant magnitude variation (i.e. greater than 5 dB) between the healthy and the faulty motors, unlike the shorted turn investigation in Chapter 5, because the useful features in this study will be combined in the next process in order to produce a better fault indicator. The process of combining the useful features, utilised in this chapter, can also be used for combining the useful shorted turn features, which can be studied in future investigations.

6.3.1. Using Rotor Slot Harmonics

In this eccentricity investigation, only the first sideband (harmonic) of the rotor slot harmonics (Eq. 6.1) is investigated. This is because preliminary analysis shows that the first sideband is usually the sideband with the highest signal to noise ratio (SNR) and it usually shows more magnitude variation between healthy and faulty motors than the other harmonics. As such, the investigation only considers (Eq. 6.1) with $k = 1$, $n_d = 0$, $v = \pm 1$ when examining static eccentricity components, and $k = 1$, $n_d = 1$, $v = \pm 1$ when examining dynamic eccentricity components.

6.3.1.1. Static Eccentricity Components

The static eccentricity components of the fault frequencies in (Eq. 6.1) can be divided into 2 components, which are the lower sideband ($v = -1$) and the upper sideband ($v = +1$).

Lower Sideband

Figure 6.1 shows how the magnitude of the lower sideband from both the current and the leakage flux signals varies as a function of load (top row) and as a function of eccentricity severity (bottom row). The figure shows that the magnitude from the current signal tends to fluctuate between -60 to -70 dB across the different loading conditions, which is above the noise floor (about -90 dB). However, the magnitude variation between the healthy and the faulty motors shows no useful pattern (i.e. the magnitude does not increase with increasing fault severity). As a consequence, the lower sideband of the static eccentricity components in (Eq. 6.1) from the current signal cannot be considered as an eccentricity feature.

As a comparison, the previous work in [29, 76] found that the magnitude of the current components in (Eq. 6.1) could increase by up to 5 dB from healthy to faulty conditions. However, these previous studies did not consider the magnitude pattern with different loads or different fault severities. For example, Figure 6.1 also shows that the magnitude of the current component at 25% load can vary by up to 8 dB between healthy and faulty conditions but the magnitude pattern (behaviour) with different loads and different fault severities shows no consistency.

The fault frequency components in (Eq. 6.1) are commonly investigated using the stator current signal but this eccentricity investigation also utilises the leakage flux signal. Using the flux components to detect eccentricity faults has not been examined previously. Figure 6.1 shows that the lower sideband in the leakage flux signal is detectable and its magnitude tends to increase as the load increases and levels off at around -40 dB. In addition, the magnitude variation between the different levels of eccentricity shows a useful pattern, where the magnitude tends to increase as the severity of the fault increases, especially at higher loads (>78%). However, the magnitude only increases by about 3 - 5 dB when going from the healthy to the 50% eccentricity, which suggests that setting a threshold for the feature can be difficult but trending of the feature is possible, as investigated in the baseline study (see Chapter 4).

Important characteristics of the above fault measures are summarised in Table 6.2. The table shows the minimum/maximum magnitude variation (mag. Δ) due to the -50% and +50% static eccentricity faults (i.e. -0.2 mm and 0.2 mm faults) under all tested loading conditions, the maximum magnitude variation of the healthy motor under all tested loading conditions, and the useful loads in which the fault measure can be considered as a feature. It should be noted that the minimum/maximum magnitude variation due to the fault may have a positive value for the minimum and a negative value for the maximum which means that the magnitude of the healthy motor is higher (positive value) under certain loads but it is lower (negative value) at other loads.

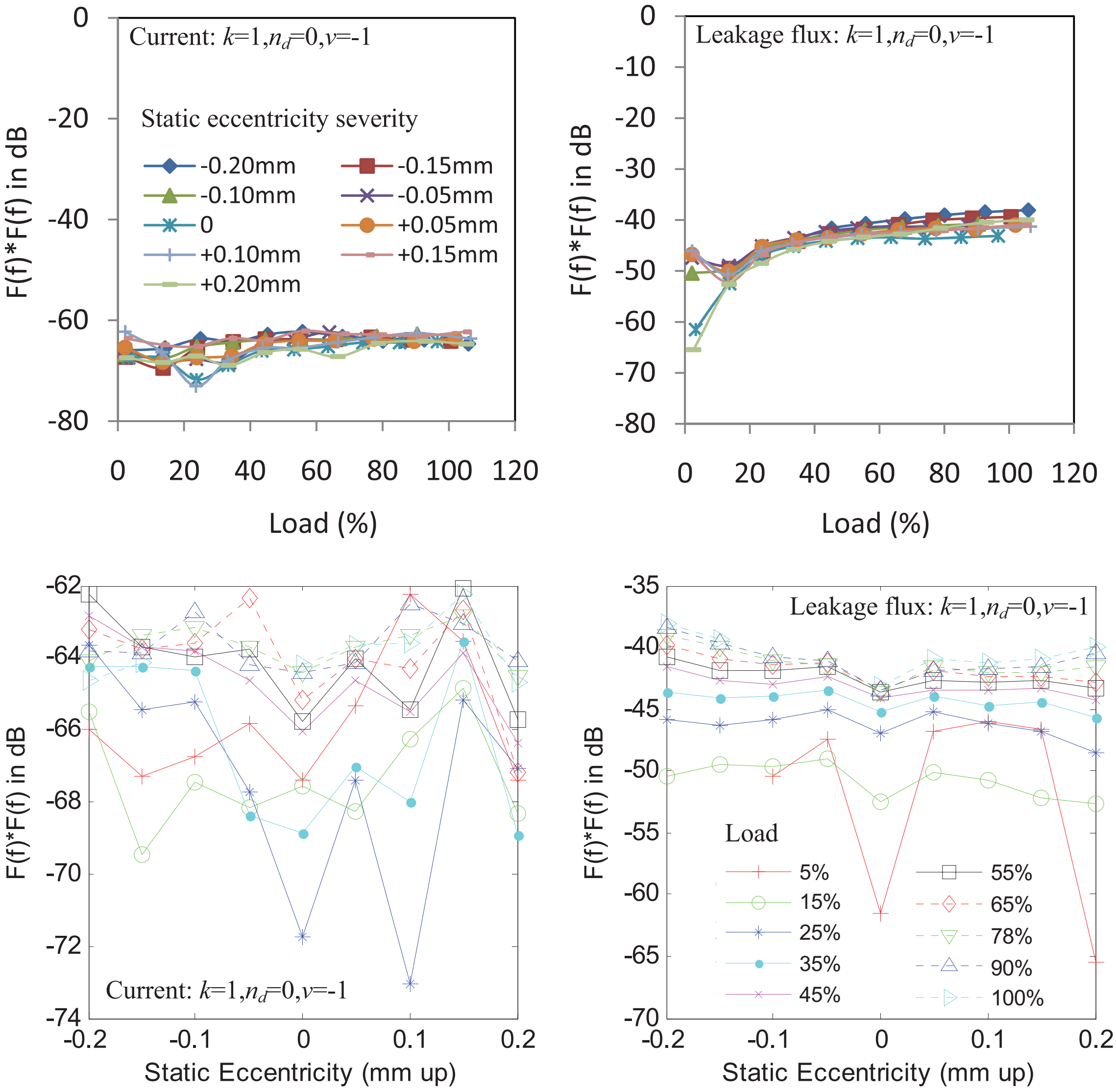

Figure 6.1 - Magnitude of the lower sideband of the static eccentricity components in (Eq. 6.1) from the current and the leakage flux signals as a function of load (top) and as a function of static eccentricity level (bottom).

Table 6.2 - Characteristics of the static eccentricity components in (Eq. 6.1) with $k = 1$ and $v = -1$

Frequency component	**Signal**	**(Min,Max) mag. Δ due to -50%/+50% fault under all loads**	**Max healthy mag. Δ due to all loads**	**Useful loads**	**Notes**
(Eq. 6.1) with k=1, n_d=0, v=-1	Current	(-1,8)/(-2,4) dB	7 dB	-	NF
(Eq. 6.1) with k=1, n_d=0, v=-1	Flux	(1,5)/(3,-4) dB	20 dB	>78%	F

where F denotes that the fault measure can be considered as a useful feature and NF denotes that the fault measure is not a feature.

Upper Sideband

Figure 6.2 and Table 6.3 show that the upper sideband in the current signal doesn't show a useful magnitude variation between the healthy motor and the faulty motors. On the other hand, the upper sideband in the flux signal shows a consistent and observable magnitude variation between the healthy and the faulty conditions, where the magnitude increases as the severity of the fault increases, when the load is greater than 15%. Although the magnitude variation between the different levels of eccentricity is not large (about 5 dB between the healthy and the 50% fault), the sideband can still be considered as a useful feature.

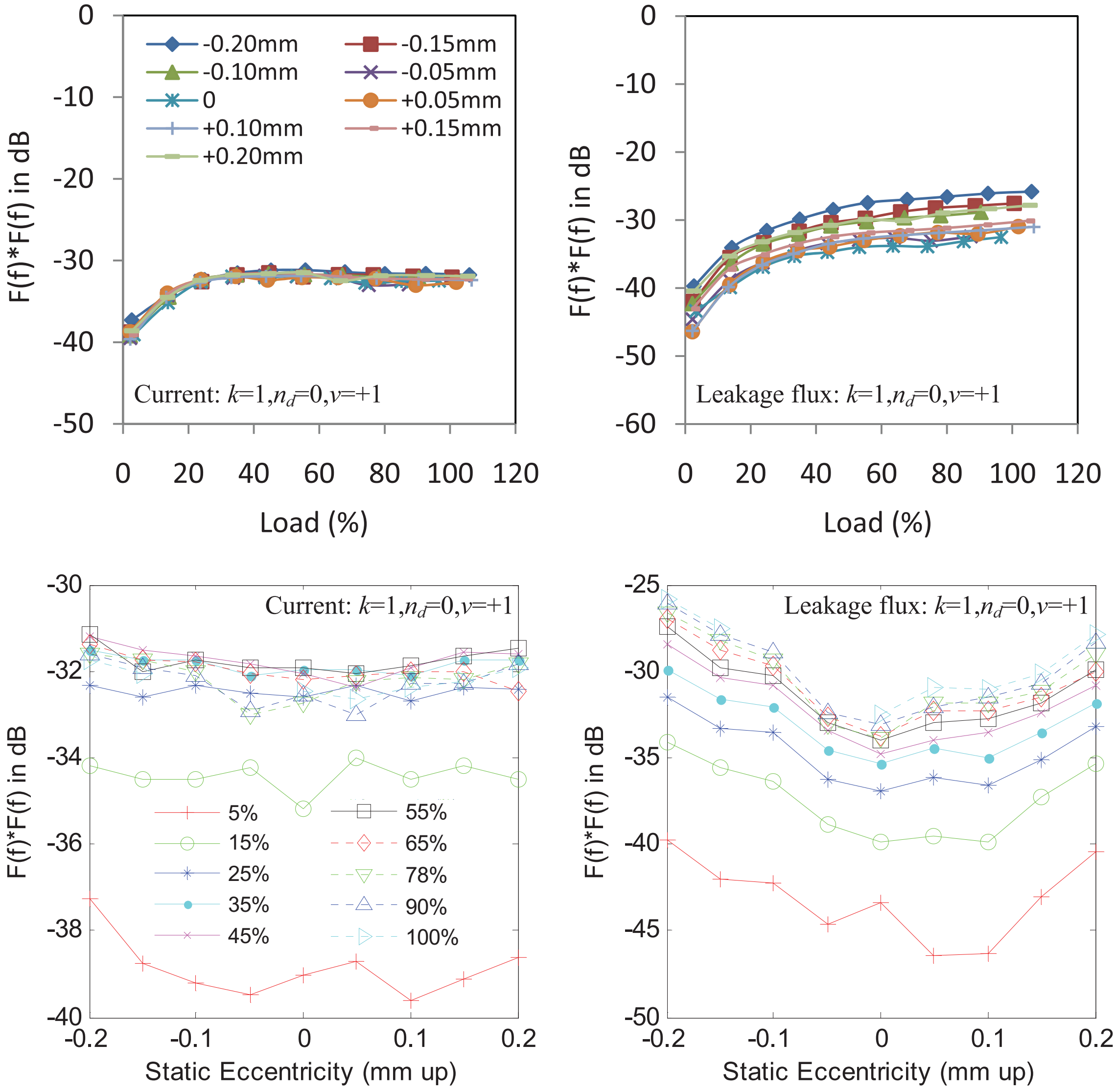

Figure 6.2 – Magnitude of the upper sideband of the static eccentricity components in (Eq. 6.1) from the current and the leakage flux signals as a function of load (top) and as a function of static eccentricity level (bottom).

Table 6.3 - Characteristics of the static eccentricity components in (Eq. 6.1) with $k = 1$ and $v = +1$

Frequency component	Signal	(Min,Max) mag. Δ due to -50%/+50% fault under all loads	Max healthy mag. Δ due to all loads	Useful loads	Notes
(Eq. 6.1) with k=1, n_d=0, v=+1	Current	(0,2)/(0,1) dB	8 dB	-	NF
(Eq. 6.1) with k=1, n_d=0, v=+1	Flux	(4,7)/(3,5) dB	12 dB	>15%	F

It should also be noted that the rate of the magnitude variation due to the different fault severities is not symmetrical about the concentric rotor position (zero eccentricity). The magnitude tends to increase more rapidly with the negative eccentricity (i.e. rotor position is below the concentric position) than the positive eccentricity (i.e. rotor position is above the concentric position). This suggests that the test motor may have a degree of inherent eccentricity faults due to the manufacturing tolerances and imperfections.

6.3.1.2. Dynamic Eccentricity Components (Under Static Eccentricity Faults)

The dynamic eccentricity components of the fault frequencies in (Eq. 6.1) can be divided into 2 components, which are the lower sideband ($v = -1$) and the upper sideband ($v = +1$).

Lower Sideband

The experimental results given in Table 6.4 and *Appendix B.1* show that the lower sideband in the current and the flux signals cannot be considered as useful features because they have low SNRs (difficult to detect as they are close to the noise floor) and their magnitudes show no useful (consistent) variation between the healthy and the faulty motors.

Table 6.4 - Characteristics of the dynamic eccentricity components in (Eq. 6.1) with $k = 1$ and $v = -1$

Frequency component	Signal	(Min,Max) mag. Δ due to -50%/+50% fault under all loads	Max healthy mag. Δ due to all loads	Useful loads	Notes
(Eq. 6.1) with k=1, n_d=1, v=-1	Current	(0,-4)/(-6,-13) dB	10 dB	-	NF
(Eq. 6.1) with k=1, n_d=1, v=-1	Flux	(-4,16)/(-1,6) dB	37 dB	-	NF

Upper Sideband

The experimental results given in Table 6.5 and *Appendix B.1* demonstrate that the magnitude of the upper sideband in the current signal tends to increase with increasing fault severity, especially when the motor load is greater than 25%. Under these loads, the magnitude is found to increase by about 15 dB from the healthy to the 50% eccentricity. Therefore, this sideband in the current signal can be used as a static eccentricity feature, even though it is known to be sensitive to dynamic eccentricity faults. Furthermore, either trending of the feature or setting a threshold for the feature can be considered because the magnitude variation between the different fault severities is significant. This finding also confirms that the static eccentricity faults exhibit dynamic eccentricity characteristics in the frequency spectrum.

On the other hand, the magnitude of the upper sideband from the leakage flux signal displays no consistent variation between the fault severities. As a consequence, the upper sideband in the leakage flux signal cannot be considered as a feature.

Table 6.5 – Characteristics of the dynamic eccentricity components in (Eq. 6.1) with $k = 1$ and $v = +1$

Frequency component	Signal	(Min,Max) mag. Δ due to -50%/+50% fault under all loads	Max healthy mag. Δ due to all loads	Useful loads	Notes
(Eq. 6.1) with k=1, n_d=1, v=+1	Current	(-12,17)/(-13,15) dB	36 dB	>25%	F
(Eq. 6.1) with k=1, n_d=1, v=+1	Flux	(3,-14)/(1,11) dB	10 dB	-	NF

6.3.2. Using Rotor Frequency Sidebands of the Fundamental

The rotor frequency sidebands of the fundamental (Eq. 6.2) can be divided into 2 components, which are the lower sideband, $f - f_r$, and the upper sideband, $f + f_r$.

Lower Sideband

The experimental results (see Table 6.6 and *Appendix B.2*) show that the magnitude of the lower sideband in the current signal reveals a useful pattern, where the magnitude tends to increase as the severity of the fault increases, when the load is greater than 25%. Under these loads, the magnitude variation is also found to be significant, where the magnitude increases by about 15 dB from the healthy to the 50% eccentricity. Since the magnitude variation is significant, this component can be considered as an eccentricity feature. As a comparison, similar findings were observed in [13, 29, 76] where the current components in (Eq. 6.2) can vary up to 5 dB between the healthy and about the 35% static eccentricity fault.

Further inspection on the experimental results (see *Appendix B.2*) shows that the magnitude variation is not symmetrical about the concentric rotor position (zero eccentricity) but it is symmetrical about the 12.5% eccentricity. This can be caused by inherent eccentricity or unbalances in the electromagnetic characteristics of the motor.

The fault frequency components in (Eq. 6.2) are commonly investigated using the stator current signal but this eccentricity investigation also considers the use of the leakage flux signal. Using the flux components to detect eccentricity faults has not been examined previously. Unfortunately, the experimental results show that the magnitude of the lower sideband from the leakage flux signal doesn't show any useful pattern, where the magnitude does not increase with increasing fault severity. Instead, the magnitude shows a rather linear variation with eccentricity, and the load variation changes both offset and slope (eg. the slope is almost flat at 50% load).

Table 6.6 - Characteristics of the lower sideband of the rotor frequency sidebands of fundamental component

Frequency component	**Signal**	**(Min,Max) mag. Δ due to -50%/+50% fault under all loads**	**Max healthy mag. Δ due to all loads**	**Useful loads**	**Notes**
$f\text{-}f_r$	Current	(-10,14)/(-10,13) dB	35 dB	>25%	F
$f\text{-}f_r$	Flux	(-1,4)/(-2,4) dB	8 dB	-	NF

Upper Sideband

The experimental results in Table 6.7 and *Appendix B.2* demonstrate that the magnitude of the upper sideband in the current signal is detectable and shows significant magnitude variation among the different levels of static eccentricity, where the magnitude increases by about 20 dB from the healthy to the 50% eccentricity, when the load is greater than 25%. However, the magnitude variation is not symmetrical about the concentric rotor position but it is symmetrical about the -12.5% eccentricity. Note that this is opposite to the trend associated with the lower sideband, which is symmetrical about +12.5% eccentricity. These findings show that detecting eccentricity faults below 12.5% using these frequency components is difficult.

Similarly, the magnitude of the upper sideband in the leakage flux signal can be used to distinguish between the healthy and the faulty conditions under all loads. However, its magnitude cannot be used to separate the different fault severities.

Table 6.7 – Characteristics of the upper sideband of the rotor frequency sidebands of fundamental component

Frequency component	Signal	(Min,Max) mag. Δ due to -50%/+50% fault under all loads	Max healthy mag. Δ due to all loads	Useful loads	Notes
$f+f_r$	Current	(18,-21)/(-10,20) dB	46 dB	>25%	F
$f+f_r$	Flux	(2,6)/(2,6) dB	5 dB	All	F

6.3.3. Using Rotor Frequency Sidebands of Twice the Fundamental

The rotor frequency sidebands at twice the fundamental in (Eq. 6.3) are detected from the vibration signal and are not as commonly used as the previous frequency components in (Eq. 6.1) and (Eq. 6.2) [13]. The frequency components in (Eq. 6.3) can be divided into 2 components, which are the lower sideband, $2f - f_r$, and the upper sideband, $2f + f_r$. Unfortunately, both sidebands cannot be considered as useful features because they do not show consistent (useful) magnitude variations between the healthy and the faulty motors (see Table 6.8 and *Appendix B.3*).

Table 6.8 – Characteristics of the rotor frequency sidebands of twice fundamental component

Frequency component	Signal	(Min,Max) mag. Δ due to -50%/+50% fault under all loads	Max healthy mag. Δ due to all loads	Useful loads	Notes
$2f-f_r$	Vib.	(7,-21)/(-13,11) dB	40 dB	-	NF
$2f+f_r$	Vib.	(-6,15)/(-5,7) dB	18 dB	-	NF

6.3.4. Using Third Harmonic of Rotor Frequency

The harmonics of the rotor frequency component in the motor vibration are commonly used for detecting eccentricity and misalignment faults. The third harmonic, $3f_r$, shows a slight magnitude variation between the different levels of eccentricity when the load is greater than 25% (see Table 6.9 and *Appendix B.4*). However, the magnitude variation is inconsistent (i.e. does not consistently increase with increasing fault severity) for the frequency component to be considered as a useful feature.

Table 6.9 – Characteristics of the third harmonic of the rotor frequency component

Frequency component	**Signal**	**(Min,Max) mag. Δ due to -50%/+50% fault under all loads**	**Max healthy mag. Δ due to all loads**	**Useful loads**	**Notes**
$3f_r$	Vib.	(-10,14)/(-10,13) dB	27 dB	-	NF

6.3.5. Using Twice Supply Frequency

Table 6.10 and *Appendix B.5* present the experimental results of analysing the magnitude of the twice supply frequency component in the motor vibration signal. As can be seen in the results, the magnitude of this component does not show a consistent (useful) variation pattern between the healthy and the faulty motors.

Table 6.10 – Characteristics of the twice supply frequency component

Frequency component	**Signal**	**(Min,Max) mag. Δ due to -50%/+50% fault under all loads**	**Max healthy mag. Δ due to all loads**	**Useful loads**	**Notes**
$2f$	Vib.	(-8,13)/(-3,-20) dB	28 dB	-	NF

6.3.6. Using Rotor Frequency

The experimental results given in Table 6.11 and *Appendix B.6* indicate that the magnitude of the rotor frequency component, f_r, in the vibration signal shows a slight variation in pattern between the different levels of eccentricity when the load is greater than 15%.

However, the magnitude variation is inconsistent for the frequency component to be considered as a useful feature.

Table 6.11 – Characteristics of the rotor frequency component

Frequency component	**Signal**	**(Min,Max) mag. Δ due to -50%/+50% fault under all loads**	**Max healthy mag. Δ due to all loads**	**Useful loads**	**Notes**
f_r	Vib.	(0,3)/(2,-8) dB	8 dB	-	NF

6.3.7. Using Second Harmonic of Rotor Frequency Sidebands of the Fundamental

The second harmonic of the rotor frequency sidebands of the fundamental in (Eq. 6.7) are one of the less commonly investigated components. These frequency components can be divided into 2 components, which are the lower sideband, $2(f - f_r)$, and the upper sideband, $2(f + f_r)$. Unfortunately, both sidebands in the vibration signal cannot be considered as useful features because they have low SNRs (i.e. difficult to detect) and their magnitude shows no consistent variation between the healthy and the faulty motors (see Table 6.12 and *Appendix B.7*).

Table 6.12 - Characteristics of the second harmonic of the rotor frequency sidebands of fundamental

Frequency component	**Signal**	**(Min,Max) mag. Δ due to -50%/+50% fault under all loads**	**Max healthy mag. Δ due to all loads**	**Useful loads**	**Notes**
$2(f - f_r)$	Vib.	(4,-9)/(0,1) dB	36 dB	-	NF
$2(f + f_r)$	Vib.	(9,-10)/(6,-21) dB	34 dB	-	NF

6.3.8. Using RMS Vibration

The experimental results given in Table 6.13 and *Appendix B.8* show that the RMS vibration tends to decrease at light load (0 - 20%) then increase again at higher loads as the higher torque in the motor generates more vibration. In the results, the magnitude variation between the different levels of eccentricity is clearly observable and shows a consistent (useful) pattern, where the vibration level increases as the severity of the fault increases (i.e. about 0.05 g for the healthy conditions and about 0.15 - 0.2 g for the -50% fault). As a result, the RMS vibration can be considered as a support feature for detecting eccentricity faults (see *section 6.2.2*).

It should also be noted that the shape of the RMS vibration curve is not symmetrical about the zero eccentricity position. The RMS vibration increases more rapidly when the motor bearing is moved down (negative static eccentricity) than when it is moved up (positive static eccentricity). A possible explanation is that the original rotor position may not be perfectly centred or as mentioned previously the magnetic and flux field distribution of the original rotor position may not be perfectly symmetrical, as would be expected in practical motors.

Table 6.13 – Characteristics of the RMS vibration

Feature	Signal	(Min,Max) mag. Δ due to -50%/+50% fault under all loads	Max healthy mag. Δ due to all loads	Useful loads	Notes
RMS	Vib.	(0.1,0.2)/(0,0.1) g	0.1 g	>25%	F

6.3.9. Summary of Effective Static Eccentricity Features

The analysis of the eccentricity features reveals that the features can be divided into 3 different categories, which are ideal eccentricity features, non-concentric eccentricity features, and eccentricity detection features. With ideal eccentricity features, the magnitude of the feature increases as the severity of the fault increases and the magnitude variation between the different levels of eccentricity is centred about the concentric rotor (zero eccentricity) position. The eccentricity features that are found to be ideal are listed in Table 6.14. Out of these four ideal features, the feature based on the current component of (Eq. 6.1) with $k = 1$, $n_d = 1$, $v = +1$ is the best because it shows the most significant magnitude variation between the healthy and the faulty motors (i.e. about 15 - 17 dB variation between the healthy and the 50% fault) and it works under most loading conditions (i.e. >25%). Similarly, the feature based on the RMS vibration gives a good eccentricity indicator (i.e. the RMS increased by about 2 - 4 times from the healthy to the 50% fault) but it is known to be a non-unique eccentricity feature (see *section 6.2.2*).

In non-concentric eccentricity features, the magnitude of the feature increases as the severity of the fault increases but the magnitude variation among the different levels of eccentricity is not centred about the concentric rotor (zero eccentricity) position. The eccentricity features that are found to be non-concentric are listed in Table 6.15.

For eccentricity detection features, the magnitude of the feature allows a distinction between the healthy and the faulty motors but the feature cannot be used to separate the different levels of eccentricity fault. The eccentricity feature that is found to fall into this category is listed in Table 6.16.

The analysis of the useful eccentricity features (Table 6.14 - Table 6.16) shows that none of the features are effective under all loading conditions. The analysis found that some features are better in detecting eccentricity faults at certain loading conditions, while other features are better at other loads. In general, most features are useful only when the load is greater than 25%. In addition, the useful features display significant magnitude variation due to loading conditions, which can be in excess of 10 dB. As a consequence, it is critical to know the load of a motor when attempting to detect its eccentricity condition.

Table 6.14 – Ideal eccentricity features

Feature	**Signal**	**Max mag. Δ due to -50%/+50% fault under all loads**	**Max healthy mag. Δ due to all loads**	**Useful loads**
(Eq. 6.1) with k=1, n_d=0, v=-1	Flux	5 / 3 dB	20 dB	>78%
(Eq. 6.1) with k=1, n_d=0, v=+1	Flux	7 / 5 dB	12 dB	>15%
(Eq. 6.1) with k=1, n_d=1, v=+1	Current	17 / 15 dB	36 dB	>25%
RMS	Vib.	0.2 / 0.1 g	0.1 g	>25%

Table 6.15 – Non-concentric eccentricity features

Feature	**Signal**	**Max mag. Δ due to -50%/+50% fault under all loads**	**Max healthy mag. Δ due to all loads**	**Useful loads**	**Symmetry**
f-f_r	Current	14 / 13 dB	35 dB	>25%	at +12.5% fault
f+f_r	Current	18 / 20 dB	46 dB	>25%	at -12.5% fault

Table 6.16 – Detection eccentricity feature

Feature	Signal	Max mag. Δ due to -50%/+50% fault under all loads	Max healthy mag. Δ due to all loads	Useful loads
$f+f_r$	Flux	6 / 6 dB	5 dB	All

6.4. Combining Static Eccentricity Features

In order to improve the detection of eccentricity, this work proposes a method to combine the ideal and the non-concentric eccentricity features, except for the feature based on the RMS vibration because this feature is not a unique eccentricity feature, depending on the motor load. This method will be referred as weighted linear combination (WLC). In the WLC method, each feature is associated with a weight, which can be either 0 or 1, depending on the motor load (the possibility of using other weight values is discussed later). This weight determines whether a particular feature is active (1) or inactive (0) at a specific loading condition. The weighted combination of eccentricity features is mathematically expressed in (Eq. 6.11) and the list of used features at different loads is shown in Table 6.17. As an example, the feature to be activated at 20% load is only the flux component in (Eq. 6.1) with k = 1, n_d = 0, v = +1. Therefore, under this loading condition the weight of this feature is set to 1 (active) while the weights of the other features are set to 0 (inactive).

$$WLC(l) = \frac{1}{N_{ft}(l)}\left(\widetilde{w}(l) \times \widetilde{ft}^{t}(l)\right) \qquad \text{(Eq. 6.11)}$$

where

$$\widetilde{w}(l) = [w_1(l) \;\; w_2(l) \;\; w_3(l) \;\; \dots] \qquad \text{(Eq. 6.12)}$$

$$\widetilde{ft}^{t}(l) = [ft_1(l) \;\; ft_2(l) \;\; ft_3(l) \;\; \dots]^{t} \qquad \text{(Eq. 6.13)}$$

where N_{ft} is the number of features selected for that particular load, w is the weight of each feature, ft is the feature, and l is the loading conditions.

Table 6.17 – List of active features for WLC

Loads	**Active Features**	**Signal**
<15%	-	-
15%<x<25%	(Eq. 6.1) with k=1, n_d=0, v=+1	Flux
25%<x<78%	(Eq. 6.1) with k=1, n_d=0, v=+1 (Eq. 6.1) with k=1, n_d=1, v=+1 f-f_r f+f_r	Flux Current Current Current
>78%	(Eq. 6.1) with k=1, n_d=0, v=-1 (Eq. 6.1) with k=1, n_d=0, v=+1 (Eq. 6.1) with k=1, n_d=1, v=+1 f-f_r f+f_r	Flux Flux Current Current Current

Figure 6.3 displays the results of combining the eccentricity features (i.e. the ideal and non-concentric features) by means of the WLC while utilising Table 6.17 to determine the weights of the features (i.e. 0 or 1) under the different loads. In the results, the WLC technique shows significant magnitude variation between the healthy and the faulty motors (i.e. up to 15 dB difference between the healthy and the 50% fault) and the magnitude consistently increases with the fault severity. In general, the WLC technique is useful when the fault severity is greater than 50% for loads between 15% and 25% and when the fault severity is greater than 25% for loads greater than 25%. Under these conditions, the magnitude separation between the healthy and the faulty motors is greater than 5 dB, which is the minimum magnitude separation for the possibility of fault detection. Note that the baseline study in Chapter 4 indicates that the magnitude variation due to repeated measurements can be up to 5 dB. On the other hand, estimating the fault severity may be difficult because the magnitude separation between one fault severity (eg. 12.5%) to the next (eg. 25%) is generally less than 5 dB.

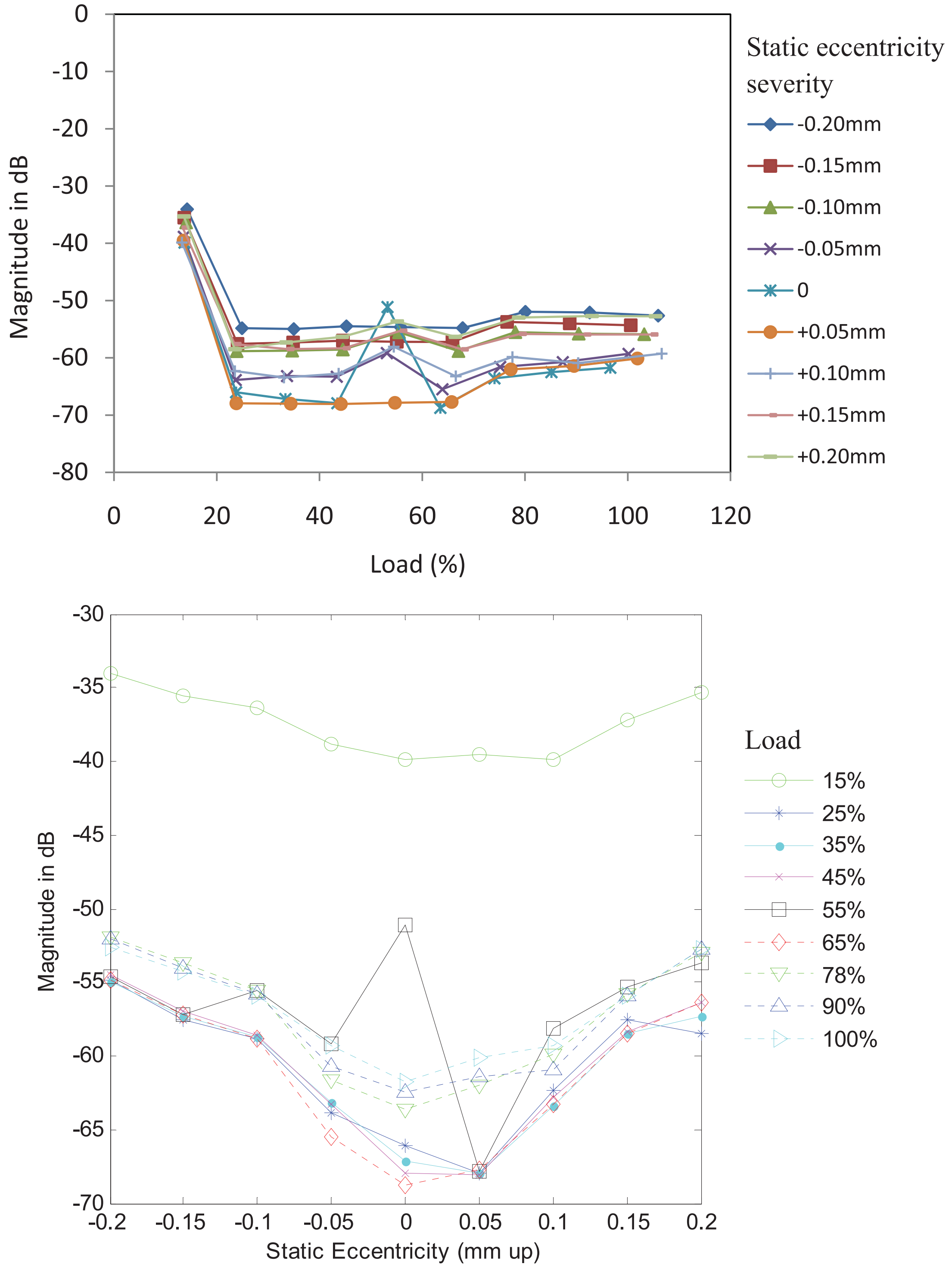

Figure 6.3 - WLC of the eccentricity features as a function of load (top) and as a function of static eccentricity level (bottom).

Comparisons between the WLC technique and the feature based on the current component of (Eq. 6.1) with $k = 1$, $n_d = 1$, $v = +1$ (see Figure B.2 in *Appendix B.1*) show that the WLC technique may have less magnitude separation between the healthy and the

50% fault conditions (i.e. about 10 - 15 dB separation for the WLC technique and about 15 dB separation for the current feature). However, the WLC technique shows more consistent magnitude separation between the different fault severities (i.e. the magnitude consistently increases with increasing fault severity) and it is useful under more loading conditions (i.e. useful for loads greater than 15% for the WLC technique instead of loads greater than 25% for the current feature). These improvements (and drawbacks) come from the fact that the WLC technique combines and averages the results of several eccentricity features. If more useful features are obtained, the WLC technique should work more effectively and the overall eccentricity fault detection could be improved. Another way to improve the WLC technique is to use a variable feature weight (eg. 1, 2, 3, …) such that better features have higher weight values. However, deciding the weight value in this case is more difficult and requires more data from different motors to better understand the characteristics of each feature.

It should also be noted here that there is an anomaly in the WLC plots for the healthy motor (zero eccentricity) when the load is at 55%. In this case, the magnitude of the WLC seems to be uncharacteristically high. A possible explanation for this is that there was a supply issue when the measurements were taken.

6.5. Analysis of Mixed Static Eccentricity and Misalignment Faults

If a motor is originally aligned, the introduction of static eccentricity faults will change the relative position between the rotor and the stator airgap, and hence the position of the shaft to the coupling (i.e. displacement misalignment). Therefore, it is common to have a misalignment fault when a static eccentricity fault occurs [84].

Eccentricity and misalignment faults are commonly related to the harmonics of rotor frequency [13]. In this investigation, the first (Eq. 6.6) and the third (Eq. 6.4) harmonics of the rotor frequency will be examined. Furthermore, the investigation will also analyse the effects of the mixed faults on the eccentricity features. This analysis has not been done thoroughly in previous studies.

The mixed static eccentricity and misalignment faults were simulated by introducing a static eccentricity to the motor first, as in the previous sections, but then the test motor was not re-aligned to the load after the eccentricity fault was introduced. This process produced a combination of static eccentricity and misalignment faults.

6.5.1. Using Rotor Frequency

The results for the mixed faults in Figure 6.4 show that the rotor frequency component, f_r, tends to increase at light loads (less than 20%) then levels off at higher loads. The figure also shows that the component magnitude can be used to distinguish between the healthy and the negative eccentricity conditions with 5 - 10 dB variation when the load is greater than 15% but it cannot separate the different fault severities.

Comparing the results in Figure 6.4 (mixed faults) and the results in *Appendix B.6* (static eccentricity only) shows that the magnitude of the rotor frequency is affected by both the eccentricity and the misalignment faults but the presence of misalignment faults causes a larger magnitude variation on the rotor frequency component, which is 5 - 10 dB variation instead of 0 - 3 dB variation if only eccentricity faults are present.

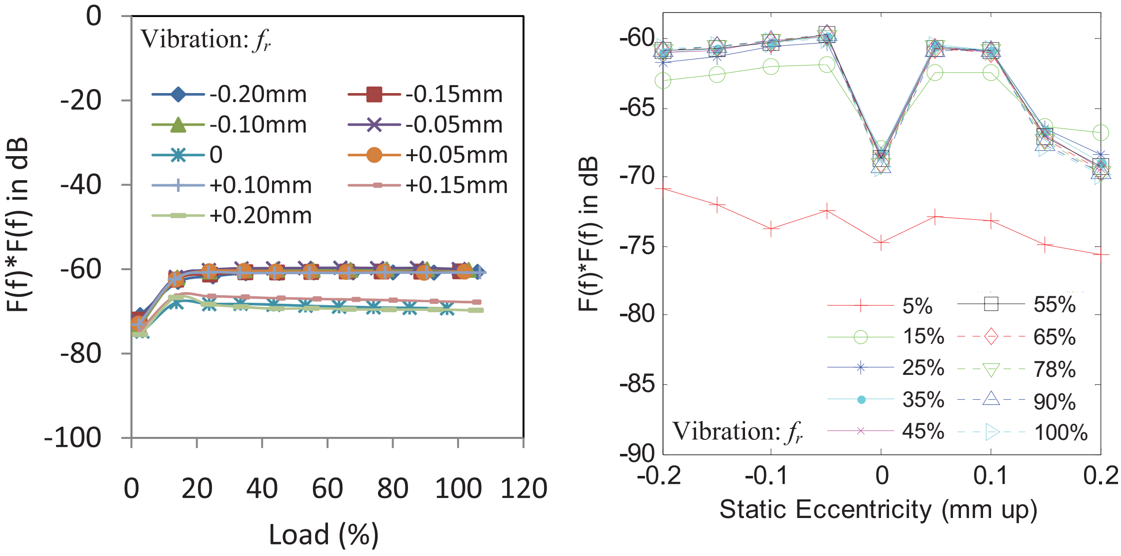

Figure 6.4 – Magnitude of the rotor frequency (Eq. 6.6) in the vibration signal under the mixed static eccentricity and misalignment faults: as a function of load (left) and as a function of static eccentricity level (right).

6.5.2. Using Third Harmonic of Rotor Frequency

Figure 6.5 shows that the magnitude of this frequency component tends to fluctuate between -55 and -90 dB under the different loading and mixed fault conditions. Comparing the results in Figure 6.5 (mixed faults) and the results in *Appendix B.4* (static eccentricity faults) shows that the magnitude of the third rotor frequency harmonic is affected by both the eccentricity and the misalignment faults but the magnitude variation between the fault severities is larger with the mixed faults, where the magnitude varies about 15 - 35 dB between the healthy and the 50% fault instead of 10 - 14 dB when only eccentricity faults are present. When the mixed faults are present, the magnitude variation is also found to be more consistent, where the magnitude tends to increase with increasing fault severity, especially when the load is greater than 25%. As a result, the third rotor frequency harmonic can be considered as a misalignment feature.

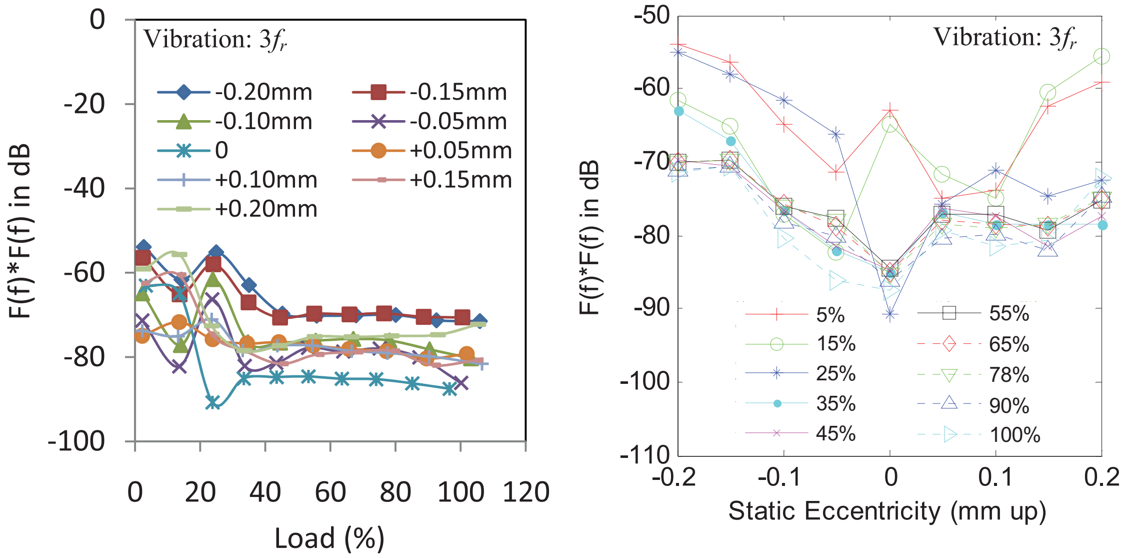

Figure 6.5 – Magnitude of the third harmonic of the rotor frequency (Eq. 6.4) in the vibration signal under the mixed static eccentricity and misalignment faults: as a function of load (left) and as a function of static eccentricity level (right).

6.5.3. Effects of Misalignment on Ideal Eccentricity Features

Comparisons of the mixed fault results in Figure 6.6 and the static eccentricity fault results in Figure 6.1, Figure 6.2, and Figure B.2 (see *Appendix B.1*) show that the presence of misalignment faults may reduce the magnitude variation between the fault severities of these ideal features. For example, when the mixed faults are present, the flux feature based on (Eq. 6.1) with $k = 1$, $n_d = 0$, $v = -1$ shows a magnitude variation of only 0 - 2 dB, instead of 1 - 5 dB when only static eccentricity faults are present, between the healthy and the 50% fault. Furthermore, the presence of the mixed faults reduces the consistency of the magnitude variation pattern between the different fault severities. For example, when the mixed faults are present, the magnitude of the flux feature based on (Eq. 6.1) with k = 1, n_d = 0, v = +1 no longer increases consistently with increasing fault severity.

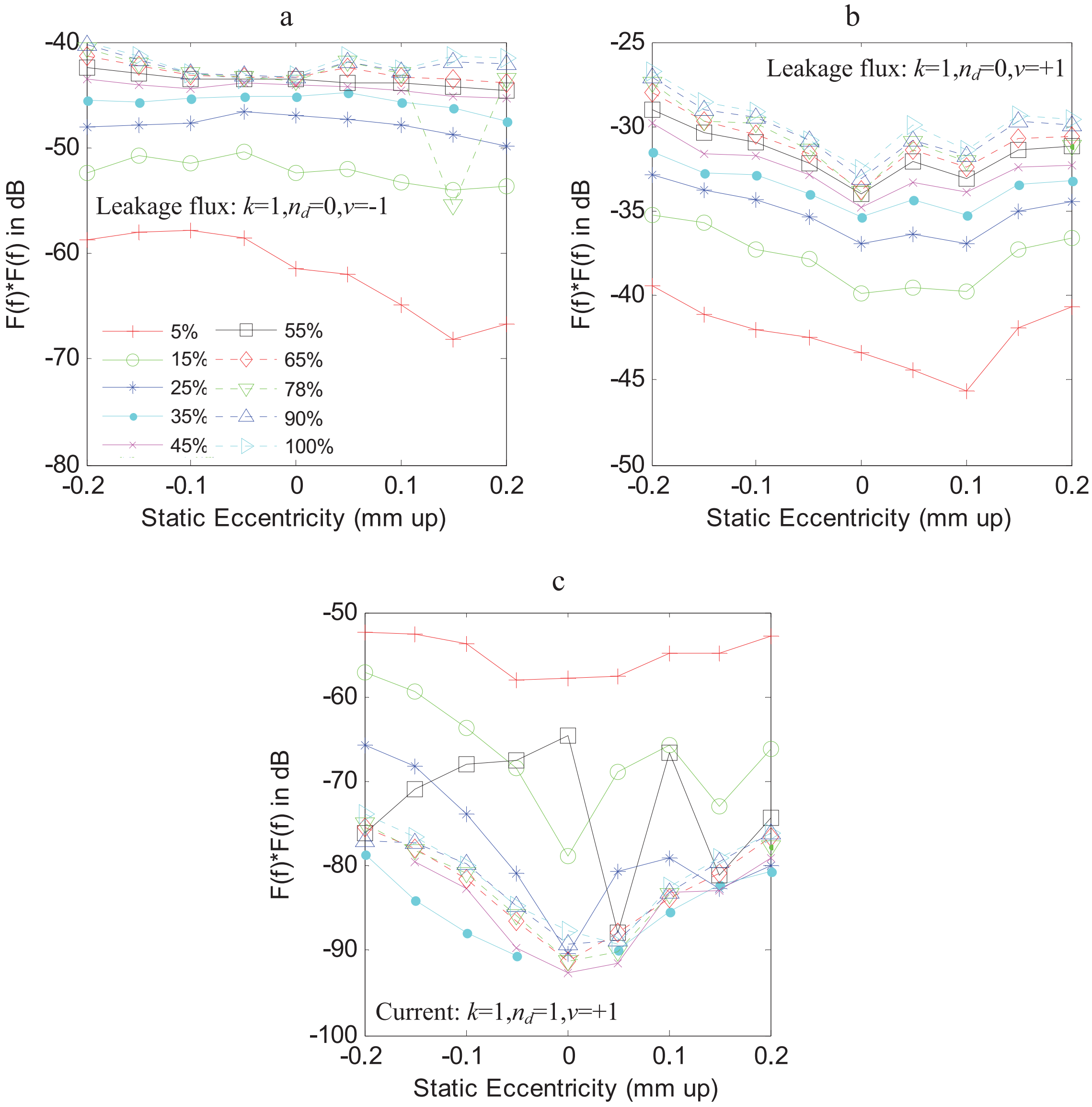

Figure 6.6 – Magnitude of the ideal eccentricity features under the mixed (static eccentricity and misalignment) fault conditions.

6.5.4. Effects of Misalignment on Non-Concentric Eccentricity Features

Comparisons of the mixed fault results in Figure 6.7 and the static eccentricity fault results in *Appendix B.2* show that the presence of misalignment faults has a number of effects on the non-concentric eccentricity features. The first effect is that the features are no longer non-concentric but they are centred about zero eccentricity. The second effect is similar to the effects on the ideal features where the presence of the misalignment faults reduces the magnitude variation between the different fault severities and its consistency, such as for the case shown in Figure 6.7b.

In general, the effects of the misalignment faults on the ideal and the non-concentric eccentricity features seem to be substantial. Hence, these issues need to be addressed (see *section 6.5.5*).

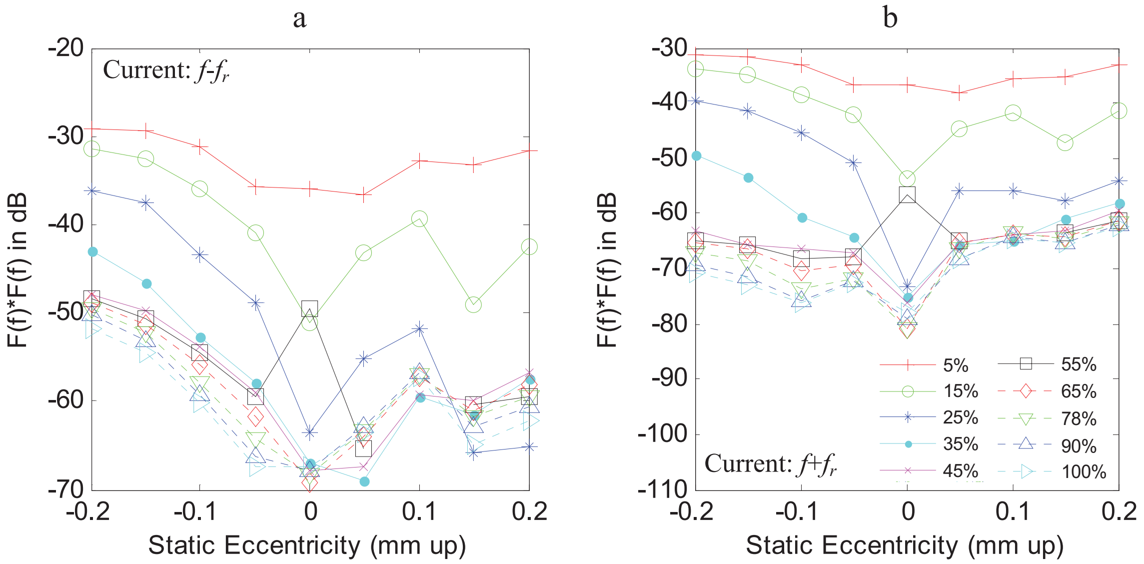

Figure 6.7 – Magnitude of the non-concentric eccentricity features under the mixed (static eccentricity and misalignment) fault conditions.

6.5.5. WLC of Eccentricity Features Under Mixed Faults

The issues that are introduced by the misalignment faults on the eccentricity features can be reduced by utilising the WLC of the eccentricity features because this technique combines the ideal features and the non-concentric features. Figure 6.8 shows that the results of the WLC technique with the mixed faults produce similar characteristics as the results of the WLC technique with the eccentricity faults (Figure 6.3). For example, the magnitude shows similar variation of about 10 - 15 dB between the healthy and the 50% fault in both cases and in both cases the WLC technique is useful when the fault severity is greater than 50% for loads between 15% and 25% and when the fault severity is greater than 25% for loads greater than 25%. This finding suggests that the WLC of the eccentricity features can be utilised to detect the eccentricity faults even in the presence of misalignment faults.

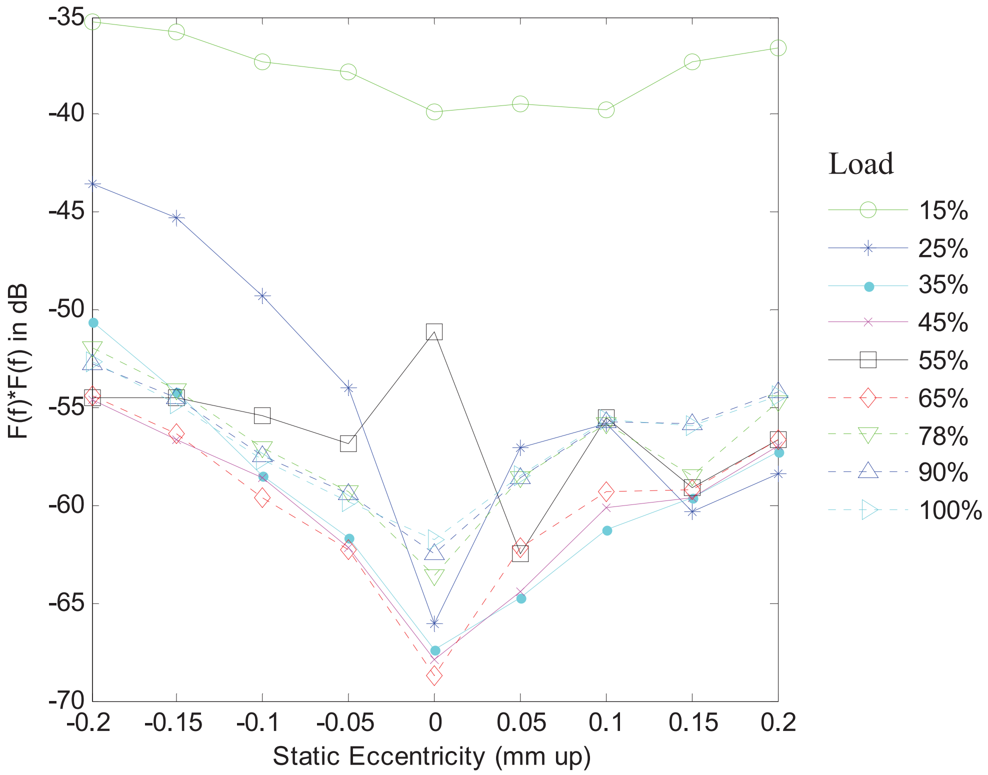

Figure 6.8 - WLC of the eccentricity features as a function of static eccentricity level under the mixed (static eccentricity and misalignment) fault conditions.

6.6. Summary

The investigation reported in this chapter was based on comprehensive experimental results using three different signal types (stator current, axial leakage flux, and motor vibration signals) under 10 different loads and under 9 different fault conditions. The chapter examined the performance of potential fault measures from the current, leakage flux, and vibration sensor signals in detecting static eccentricity faults under different loads and fault severities. Once the most useful features were identified in the chapter, they were combined using the WLC technique in order to produce a better and more consistent fault indicator. In addition, the eccentricity investigation also examined the effects of misalignment faults on the useful eccentricity features, as well as looking at some features that may be affected by the misalignment faults. This was important since the presence of eccentricity faults in a machine would naturally produce misalignment faults as well.

The key results of this investigation are:

- Fault frequency components are identified whose magnitudes increase with increasing levels of eccentricity, however these components are also sensitive to the level of loading;
- Single features based on the current component of the rotor slot harmonics (Eq. 6.1), the current components of the rotor frequency sidebands of the fundamental (Eq. 6.2) and the RMS total vibration give good results because they show significant magnitude variation (>5 dB) between the healthy and the faulty motors;
- It is shown that combining information from multiple frequency components using the WLC technique, and taking into account the loading condition can improve the consistency in detecting static eccentricity faults;
- The WLC technique can be considered useful for the test motor when the fault severity is greater than 50% for loads between 15% and 25% and when the fault severity is greater than 25% for loads greater than 25%.
- Detecting static eccentricity faults is found to be possible but estimating the fault severity can be difficult.
- The rotor frequency component and its third harmonic seem to be affected by both the eccentricity and the misalignment faults but the misalignment faults cause greater magnitude variations of these features between the healthy and the faulty motors;
- The reliability of the useful eccentricity features may be reduced by the presence of misalignment faults but the WLC technique can reduce these issues;

The analysis of the experimental results also suggests that it is possible to distinguish between misalignment faults, eccentricity faults, and both faults together. This can be done by monitoring the magnitudes of the rotor frequency component, the third harmonic of the rotor frequency component, and the WLC feature. If only the magnitudes of the rotor frequency and its third harmonic components are affected by a motor fault, then it is likely to be a misalignment fault. If only the magnitude of the WLC feature is affected by a fault, then it is likely to be an eccentricity fault. However, if the magnitudes of all three features are affected by a fault, then it is likely to be a mixed fault.

Chapter 7. Broken Rotor Bar Fault Detection During Starting

7.1. Introduction

There has been a substantial amount of research over the past 15 years on the development of various steady-state condition monitoring techniques for the detection of broken rotor bar faults. The fault detection techniques are mainly based on the fast Fourier transform (FFT) [3, 18, 22, 23, 27, 85]. FFT analysis is usually applied when the motor is operating in steady-state, where a set of measurements is taken over a period of time. These measurements are then analysed to obtain the signal frequency components, where the frequency resolution is both determined and limited by the measurement period [86].

Broken rotor bars (BRB) are one of the easiest induction motor faults to detect using steady-state stator current condition monitoring techniques. The previous techniques are usually based on monitoring the amplitudes of the double slip frequency sidebands of the fundamental supply frequency in the current spectrum [3]. It has been shown that the greater the rotor bar fault severity, the higher is the amplitude of these sidebands.

However, the sideband amplitudes are also found to be sensitive to motor loading [3, 18, 22, 23, 27, 85]. For example, at no load or at very light loads, these broken rotor bar sidebands are undetectable because the rotor currents generated under this condition are small and the broken rotor bar sidebands are very close to the fundamental frequency, where the fundamental component masks the sidebands (see *section 4.4*). Therefore, there is a need to develop condition monitoring techniques to address these issues and to develop an effective fault detection technique for rotor bar faults at light loads.

This chapter considers the analysis of broken rotor bar fault detection using stator currents during direct-on-line (DOL) starting of the motor. During DOL starting, the rotor current of the induction machine is very high, typically 5 to 6 times the rated current. Therefore, it is expected that rotor faults should be much more evident under this condition than under normal running conditions. Moreover, there is also the advantage that the starting current is less sensitive than the running current to the level of motor load, and so reliable conclusions from the data analysis should be obtainable even with motors with no mechanical load. However, there are two drawbacks in dealing with the starting current. The first drawback is that the motor speed is constantly changing during starting, which means that the fault related signal frequency components are changing in both amplitude and frequency. The second drawback is that the starting current only occurs for a short time. This starting time, which depends upon the total inertia of the motor and the load, may vary from a fraction of a second for small motors, up to several seconds for large motors.

Therefore, due to the transient nature of the starting current signal, conventional FFT techniques are not suitable for analysing the signal. Although the short-time Fourier transform (STFT) can be used for analysing transient signals using a time-frequency representation, it can only analyse the signal with a fixed sized window for all frequencies, which leads to poor frequency resolution. However, wavelet techniques can overcome this problem by using a variable sized window (see *section 2.4*).

Wavelet based techniques for detecting broken rotor bars using the induction motor starting current have been reported previously in [87-89]. The work in [87] used an adaptive signal cancellation technique in order to remove the fundamental component from the starting current, leaving only the residual current. This residual current was then analysed by using a discrete wavelet transform. The resultant wavelet coefficients were then used to differentiate a healthy motor and a faulty motor under varying loading conditions. The work in [88] applied the wavelet transform to the Hilbert transform of the starting current signal. The resultant wavelet coefficients were then used to compute what was called the wavelet ridge. This wavelet ridge was utilised to distinguish a healthy motor from faulty motors with different numbers of broken rotor bars. In [89], a number of time-frequency signal processing techniques, such as spectrograms, Wigner distribution, and wavelet decomposition, were compared. It was found that the wavelet technique was the best method to extract the broken rotor sidebands during the starting operation. The wavelet technique differentiated healthy and faulty motors by monitoring the sideband amplitudes.

Other transient analysis techniques for monitoring of machines are reported in [39, 53, 54, 90, 91]. The study in [39] utilised a bandpass filter in order to track the broken rotor bar sidebands, $(1\pm2s)f$, during the starting phase from standstill up to rated speed. The amplitude ratios of the sidebands were then used to compare faulty and healthy motors, which were 4 pole, 51 rotor bar, 11 kW motors, under the no load condition. In [90], it was demonstrated on a simulated 5.59 kW induction motor, through the winding function approach (WFA), that the starting current waveform of the faulty motor with 4 broken bars and 1 broken end ring was observably different from the starting current waveform of the healthy motor. The work in [91] presented a comparison of several spectral estimation techniques, such as the Welch method, multitaper approach, covariance based approach, and multiple signal classification (MUSIC) algorithm, in extracting the broken rotor bar sidebands and reducing the noise influence during the motor starting operation. It was found that the MUSIC algorithm provided the best result.

The method for detecting broken rotor bar faults during starting can be utilised when a motor is under maintenance, or a new motor is being tested during production, or when a motor is turned on during day to day operation. The broken rotor bar investigation in this chapter proposes a new method for detecting broken rotor bar faults under different loading conditions and varying fault severities. The method utilises a continuous wavelet transform of the envelope of the starting current signal, which is sampled at 8 kHz, in order to distinguish between the healthy and faulty motors (see *section 1.5.1*). The wavelet function used in this investigation is Daubechies-8 (db8) from the Daubechies family [50].

This particular wavelet function is chosen because it produces wavelet characteristics that are suitable for feature extraction of the current sensor signals.

The investigation in this chapter begins by discussing the wavelet technique, where comparisons of a healthy and a faulty motor are shown (*section 7.2*). In *section 7.3*, a detailed analysis of the healthy and faulty motors is described. This section examines the variability tests and compares the varying degrees of broken rotor bar fault. Finally, a summary of the findings is given in *section 7.4*.

7.2. Continuous Wavelet Transform of Starting Current

As mentioned previously, the wavelet transform allows the analysis of a transient signal, such as the starting current of an induction motor, where a normal FFT would not be beneficial. The continuous wavelet transform (CWT) can be utilised to extract and analyse the transient characteristics of the starting current of an induction motor. Typical time domain and CWT plots of the starting current signal obtained from the healthy and faulty motors running at no load are shown in Figure 7.1 and Figure 7.2. The figures show that the CWT plots have successfully extracted the transient characteristics of the starting current waveforms and that there are visible differences between the healthy and faulty motors.

A comparison of Figure 7.1 and Figure 7.2 suggests that there are two evident effects of the broken rotor bar fault on the starting current. The first effect is that the starting current takes a slightly longer time to decay and reach steady-state in comparison to the healthy induction motor. This is because an induction motor with broken rotor bars produces less torque and hence takes longer to reach steady-state [92]. However, this effect by itself cannot be used as a feature for distinguishing the healthy and faulty motors because it can also be caused by changes in the inertia and the loading conditions of the motor. The second effect is apparent in the CWT plots. There are observable differences between the CWT plot of the healthy motor and the CWT plot of the faulty motor with 4 broken rotor bars at shifts around 0 to 375 ms, which correspond to the starting period, and scales around 201 to 301, which corresponds to the lower frequency components, where the wavelet coefficients of the faulty motor is stronger than the wavelet coefficients of the healthy motor. These differences indicate that the wavelet transform is able to detect the changes in signal components between the faulty motor and the healthy motor during the starting period. These differences of the wavelet coefficients are suggested, in this investigation, to be the identifying feature for detecting a broken rotor bar fault. However, the differences are overshadowed by the strong fundamental 50 Hz component in the signal (as highlighted by the region between the dashed lines in the figures), which does not incorporate any useful information about the rotor bar faults. Therefore, this 50 Hz component needs to be removed in order to have a more accurate and reliable analysis.

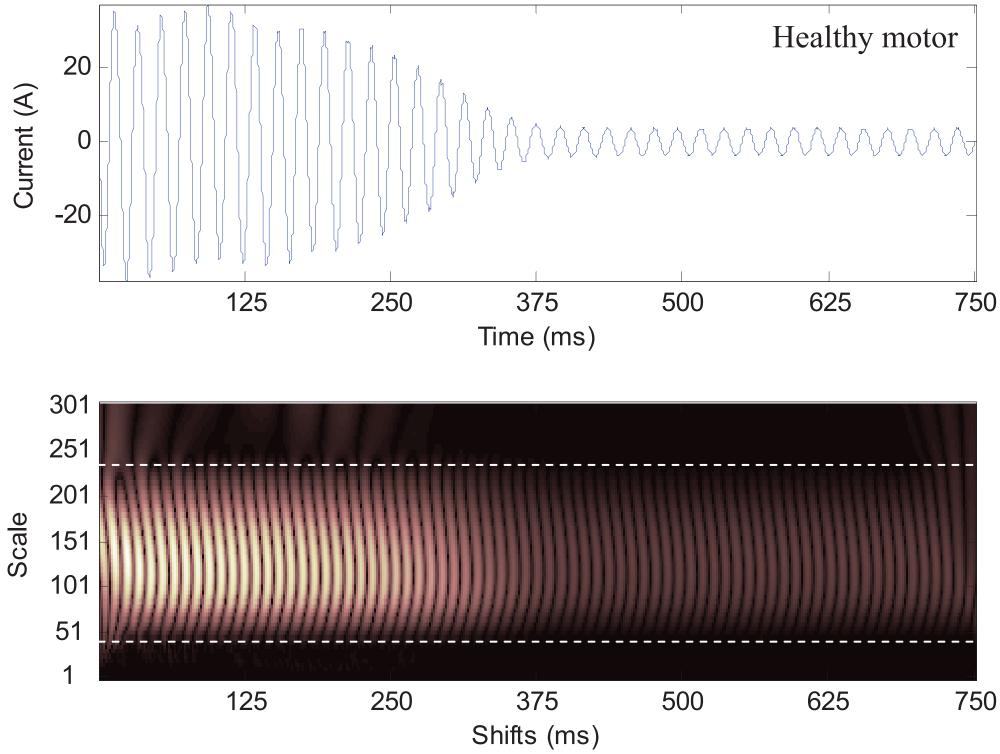

Figure 7.1 - Starting current (phase A) signal (top) and continuous wavelet transform of the starting current signal (bottom) of the healthy motor.

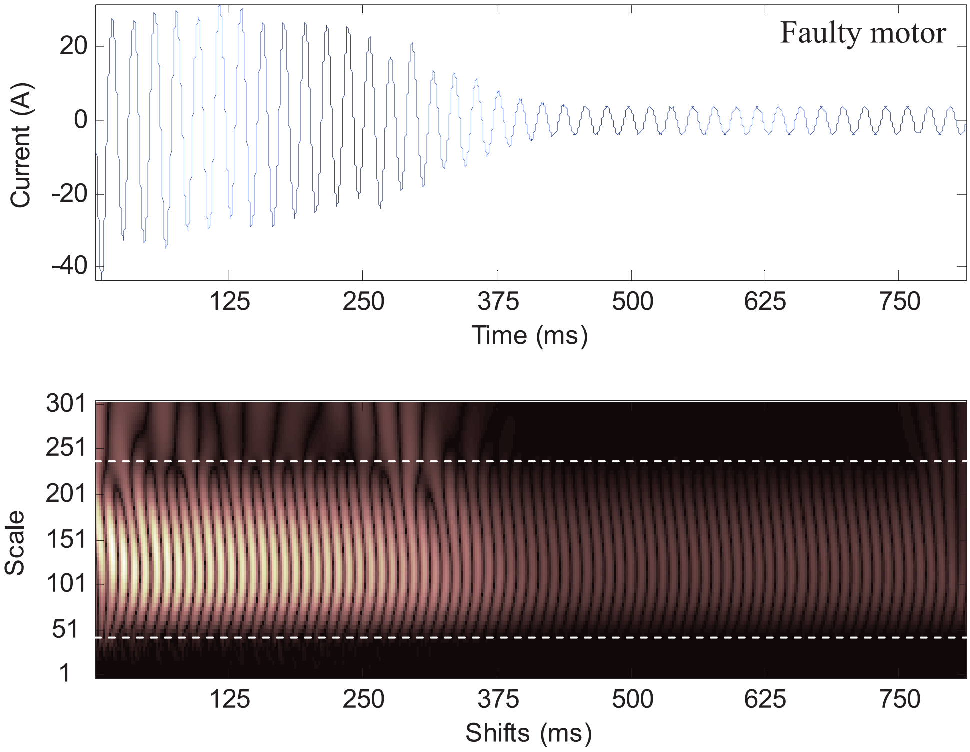

Figure 7.2 - Starting current (phase A) signal (top) and continuous wavelet transform of the starting current signal (bottom) of the faulty motor with 4 BRB.

7.2.1. Continuous Wavelet Transform of the Envelope of Starting Current

In order to remove the fundamental component, a signal model for the stator current is required. Here, it is suggested that the stator current signal is a summation of many modulated signal components and other frequency components, such as the supply frequency, the rotor frequency, and the slip frequency. This assumption is also supported in [3], which indicates that most of the fault frequencies are symmetrical about certain frequencies. For example, the broken rotor bar (BRB) fault frequencies, $f \pm 2sf$, are symmetrical about the fundamental frequency.

Let $i(t)$ denote the steady-state stator current which comprises many modulated signal components.

$$i(t) = i_s(t) + n(t) \qquad \text{(Eq. 7.1)}$$

where $i_s(t)$ is the steady-state signal components and $n(t)$ represents the noise components.

The steady-state signal component, $i_s(t)$, can be divided into simpler signal components by the principle of superposition. In this investigation, the signal components of interest are the BRB sidebands. Therefore the signal component, $i_s(t)$, is defined as in (Eq. 7.2).

$$i_s(t) = i_{s1}(t) + i_{so}(t) \qquad \text{(Eq. 7.2)}$$

where $i_{s1}(t)$ is the steady-state BRB sideband modulated at the fundamental frequency, and $i_{so}(t)$ represents the other steady-state signal components that make up the stator current.

In this case, let the fundamental signal component, i_f, and the BRB component, i_{brb}, be defined as in (Eq. 7.3) and (Eq. 7.4) respectively.

$$i_f(t) = a_f cos\ (\omega_f t) \qquad \text{(Eq. 7.3)}$$

$$i_{brb}(t) = a_{brb} cos\ (\omega_{brb} t) \qquad \text{(Eq. 7.4)}$$

where a_f and a_{brb} are the amplitudes of the fundamental signal component and the BRB component respectively.

From (Eq. 7.3) and (Eq. 7.4), the fundamental frequency modulated at the steady-state BRB sideband can be defined as in $i_{s1}(t)$ (Eq. 7.5) [3, 27, 85]. In this case, the fundamental signal component, i_f, acts as a carrier, which is modulated by the BRB component. In terms of the frequency domain, the BRB component is shifted from the baseband to the carrier signal frequency and is reflected about the carrier signal.

$$\begin{aligned} i_{s1}(t) &= \left[a_f + a_{brb}\, cos(\omega_{brb} t)\right] cos(\omega_f t) \\ &= a_f\, cos(\omega_f t) + \frac{a_{brb}}{2} cos\left[(\omega_f + \omega_{brb})t\right] \\ &\quad + \frac{a_{brb}}{2} cos\left[(\omega_f - \omega_{brb})t\right] \end{aligned} \qquad \text{(Eq. 7.5)}$$

The above equation shows that the sum of a_f and a_{brb} is proportional to the amplitude of the current component. As can be seen in Figure 7.1 and Figure 7.2, this sum is significantly larger during the starting period than the steady-state operation. Therefore, the BRB sidebands should be more detectable during the starting period. In addition, it should be noted here that due to the time varying feature of the starting current, some variables in

(Eq. 7.5) are also time varying, such that $a_f = a_f(t)$, $a_{brb} = a_{brb}(t)$, *and* $\omega_{brb}(t) = 4\pi s(t) f$, where $s(t)$ is the time varying slip.

The method used to remove the fundamental 50 Hz component, $i_f(t)$, in the starting current signal is by extracting the envelope of the starting current signal. This is because a transient signal tends to have multiplicative signal components. For example, consider the transient signal shown in Figure 7.3. The figure shows that the example transient signal is made by a multiplication of two signal components, which are the fundamental signal component and the envelope of the transient signal. Clearly, if the fundamental component is removed, the component left in the transient signal is its envelope.

The envelope of the starting current signal can be extracted through a demodulation process [93]. The demodulation process flow diagram and its mathematical formulation are shown in Figure 7.4 and (Eq. 7.6) - (Eq. 7.9) respectively. The demodulation process shows that the starting current signal (considering only the BRB components), $i_{s1}(t)$, is multiplied by cosine and sine 50 Hz sinusoids. The fundamental frequency can be estimated using the data to allow for variations in the actual frequency. Then, the resulting real and quadrature components, i_{s1a} and i_{s1b} respectively, are filtered separately. Finally the magnitude of the sum of the real and quadrature components, i_{ds1}, gives the envelope of the signal.

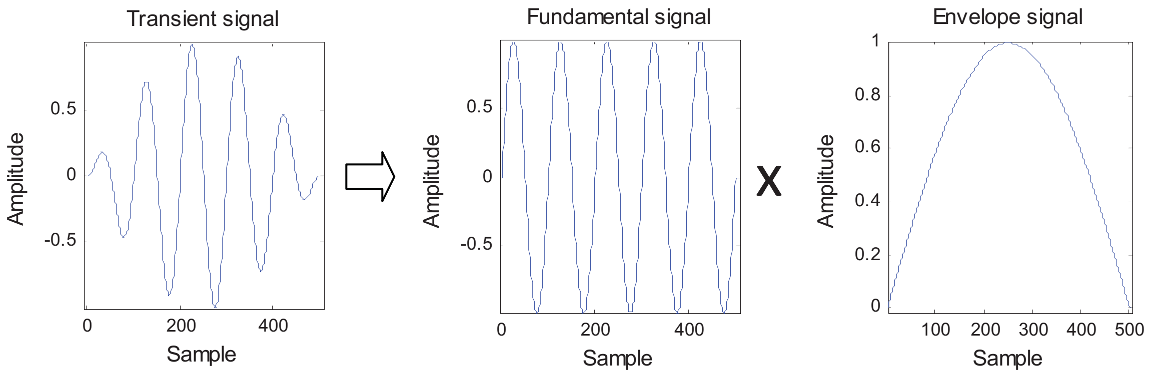

Figure 7.3 – Example of a transient signal and its components.

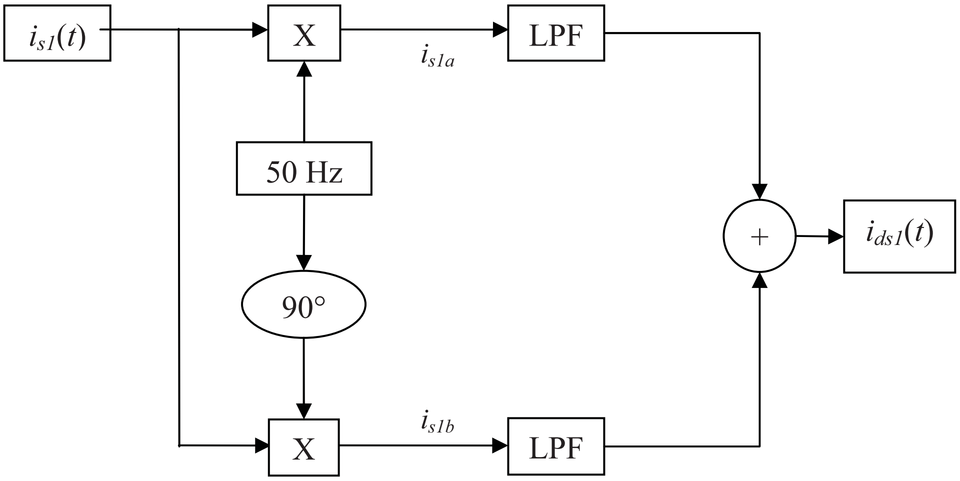

Figure 7.4 - Implementation flow diagram of the envelope extraction.

Let $i_{ds1}(t)$ be the output of the demodulation process and let LPF be the low-pass filtering process. Then,

$$i_{ds1}(t) = LPF(i_{s1a}(t) + ji_{s1b}(t)) \tag{Eq. 7.6}$$

where

$$\begin{aligned} i_{s1a}(t) = \frac{a_f}{2} + \frac{a_f}{2}cos(2\omega_f t) + \frac{a_{brb}}{4}cos[(2\omega_f + \omega_{brb})t] \\ + \frac{a_{brb}}{4}cos(\omega_{brb}t) + \frac{a_{brb}}{4}cos[(2\omega_f - \omega_{brb})t] \\ + \frac{a_{brb}}{4}cos(\omega_{brb}t) \end{aligned} \tag{Eq. 7.7}$$

$$\begin{aligned} i_{s1b}(t) = \frac{a_f}{2}sin(2\omega_f t) + \frac{a_{brb}}{4}sin[(2\omega_f + \omega_{brb})t] \\ + \frac{a_{brb}}{4}sin(\omega_{brb}t) + \frac{a_{brb}}{4}sin[(2\omega_f - \omega_{brb})t] \\ - \frac{a_{brb}}{4}sin(\omega_{brb}t) \end{aligned} \tag{Eq. 7.8}$$

and hence

$$\begin{aligned} i_{ds1}(t) &= \frac{a_f}{2} + \frac{a_{brb}}{2}cos(\omega_{brb}t) \\ &= \frac{1}{2}[a_f + a_{brb}\, cos(\omega_{brb}t)] \end{aligned} \tag{Eq. 7.9}$$

The relation in (Eq. 7.9) clearly shows that the demodulation process has successfully removed the fundamental signal component, $i_f = a_f \cos(\omega_f t)$, leaving a DC component and the BRB component. The sum of these components and the demodulation of the other stator current signal components, $i_{so}(t)$, corresponds to the envelope of the starting current signal.

Figure 7.5 and Figure 7.6 show the improvement obtained by applying the continuous wavelet transform (CWT) on the envelope of the starting current signal compared to applying the CWT on the signal itself (Figure 7.1 and Figure 7.2). Figure 7.5 and Figure 7.6 show that by applying the CWT on the envelope, the fundamental 50 Hz component has been successfully removed. As a result, a more accurate and precise transient analysis can be performed and investigated. Note that this process has also been tested on the other current phases where similar results are obtained (see *section 7.3.2*).

Figure 7.5 and Figure 7.6 reveal another effect of a broken rotor fault. The effect can be seen from the starting current envelope plots, in which the faulty motor draws slightly less current than the healthy motor during starting. This is because there are effectively less rotor bars and hence a greater effective rotor resistance in the faulty motor.

Further examination of the CWT plots in Figure 7.5 and Figure 7.6 reveal the differences between the healthy motor and the faulty motor with broken rotor bars. In order to analyse these differences accurately, the CWT plots are divided into 3 different time regions (Region 1, 2, and 3, separated by the dashed lines) for identifying the different patterns. The regions were initially identified through visual inspection of the starting current waveform and its wavelet transform. However, experiments showed that the lines separating the regions were found to be consistently located with respect to the starting current waveform.

The starting current of a healthy motor exhibits two distinct patterns under the wavelet analysis (Figure 7.5), where the first pattern (in Region 1) corresponds to the initial part of the envelope and the second pattern (in Region 3) corresponds to the end (discontinuity) of the signal. On the other hand, a faulty motor with broken rotor bars exhibits an extra pattern between these two patterns (in Region 2), which occurs just before the transition from the "starting state" to the steady state (Figure 7.6). This third pattern is the distinguishing feature between a healthy and a faulty motor.

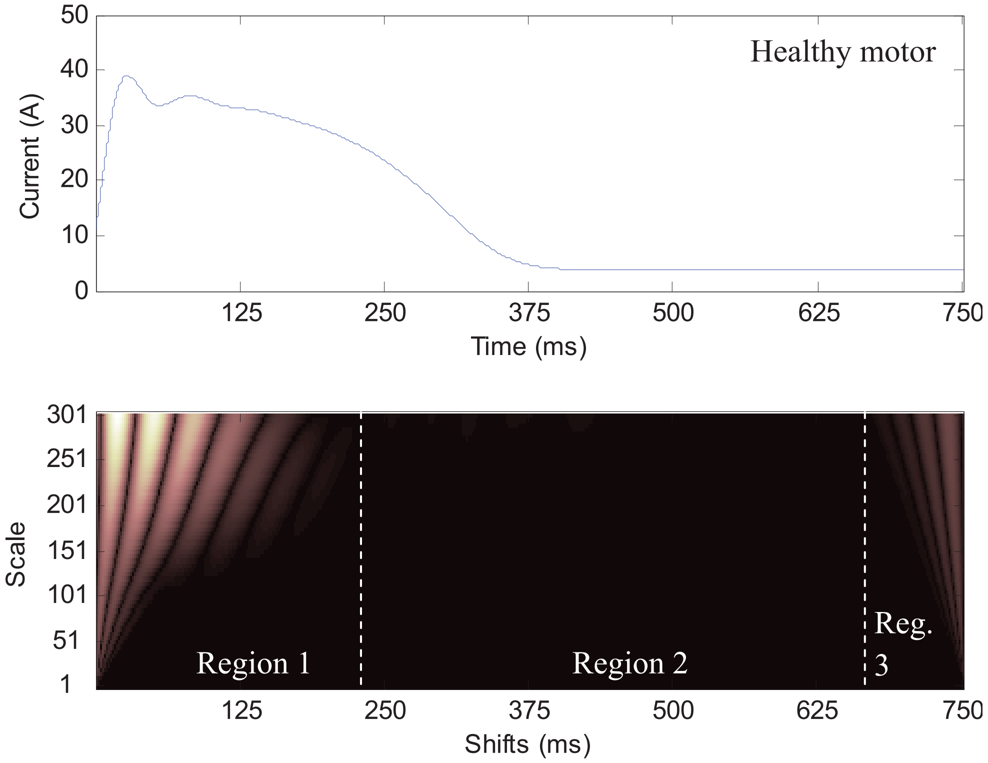

Figure 7.5 - Envelope of the starting current signal (top) and its continuous wavelet transform (bottom) of the healthy motor.

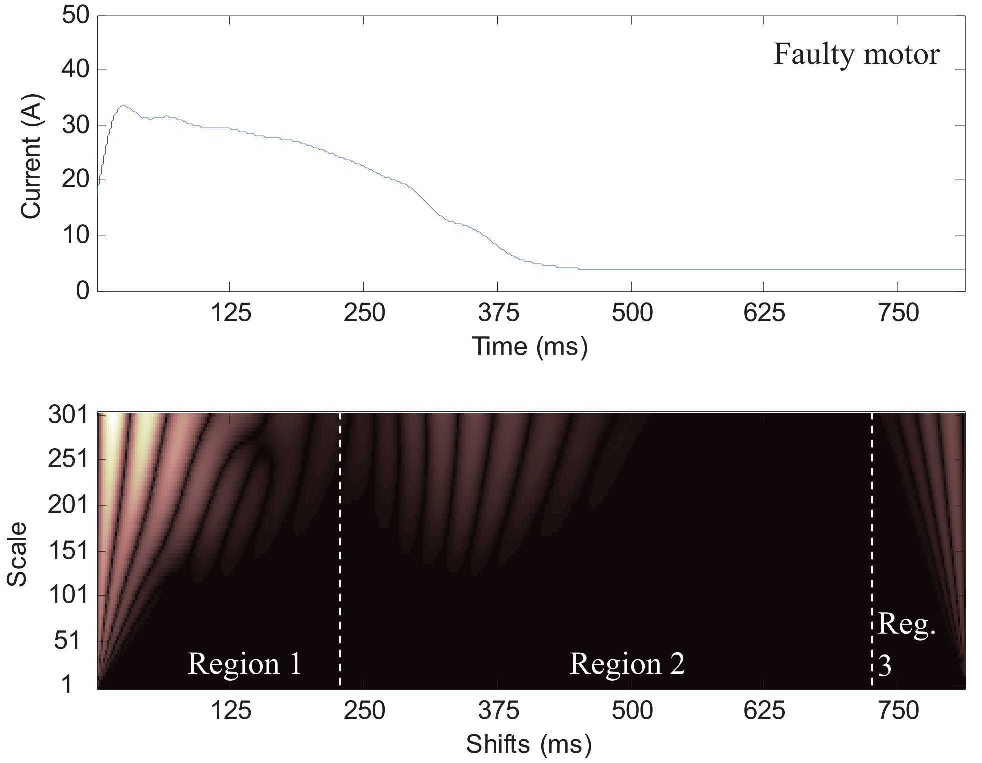

Figure 7.6 - Envelope of the starting current signal (top) and its continuous wavelet transform (bottom) of the faulty motor with 4 BRB.

Furthermore, Figure 7.5 and Figure 7.6 also show that there is a small difference in the first pattern (in Region 1) between the healthy and the faulty motors. However, this difference is found to be difficult to detect and hence is not considered in this investigation.

7.2.2. Wavelet indicator

The differences between the patterns of a healthy motor and the patterns of a faulty motor with broken bars need to be quantified for more convenient identification and possible use in a future automated condition monitoring system. These pattern differences can be quantified by calculating the sum of all the absolute values of the wavelet coefficients of the third pattern (in Region 2). The resultant value is then normalised against the sum of all the wavelet coefficients, the number of samples used, and the scales used. In this broken rotor bar investigation, the power magnitude of the square of this quantification value is named the "wavelet indicator".

Figure 7.7 shows that the wavelet indicator has successfully quantified the pattern differences and hence distinguished a faulty motor with broken rotor bars from a healthy one over a wide range of loads. The wavelet indicator of the faulty motor with 4 broken rotor bars (4 BRB) is consistently higher than the wavelet indicator of the healthy motor under various loading conditions. This finding shows a significant improvement over steady-state analysis methods, such as FFT analysis, where the fault detection is dependent on the loading conditions (i.e. the fault detection is inaccurate at light load).

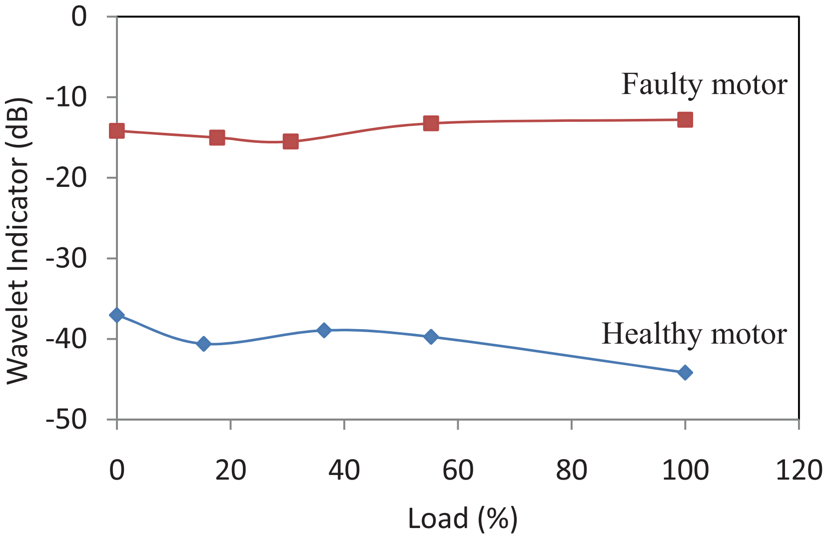

Figure 7.7 - Wavelet indicator plot of the starting current under various loading conditions for the healthy motor and the faulty motor with 4 BRB.

7.3. Experimental Results and Analysis

In order to show that the wavelet technique can be reliably used for detecting broken rotor bar faults, it is necessary to experimentally show that:

- the measurements are repeatable,
- the changes in the wavelet coefficients due to broken rotor bars are not sensitive to other effects such as motor loading, initial rotor position, and supply imbalance, and
- the wavelet technique is able to distinguish between various degrees of broken rotor bar fault.

As indicated earlier, a separately-excited DC machine with a resistive load was used to load the test machine. This produced a load torque which varied approximately linearly with motor speed (refer to *section 1.5*). Figure 7.8 and Figure 7.9 show the starting current variations between the no load case (shown earlier) and the full load case. As expected, the starting time of the motor running at full load is longer than the motor running at no load, by about 100 ms.

As a comparison, the starting current waveform and its envelope of the faulty motor with 4 BRB running at full load are shown in Figure 7.10. It again demonstrates the three effects of a broken rotor bar fault. First, the starting current waveform of the faulty motor takes a slightly longer time to decay than the waveform of the healthy motor. Second, the starting current of the faulty motor draws slightly less current than the healthy motor. Third, the starting current envelope of the faulty motor shows perturbations just before the transition from the starting state to the steady state, which are not present in the healthy motor (note that these perturbations are the components measured by the wavelet indicator).

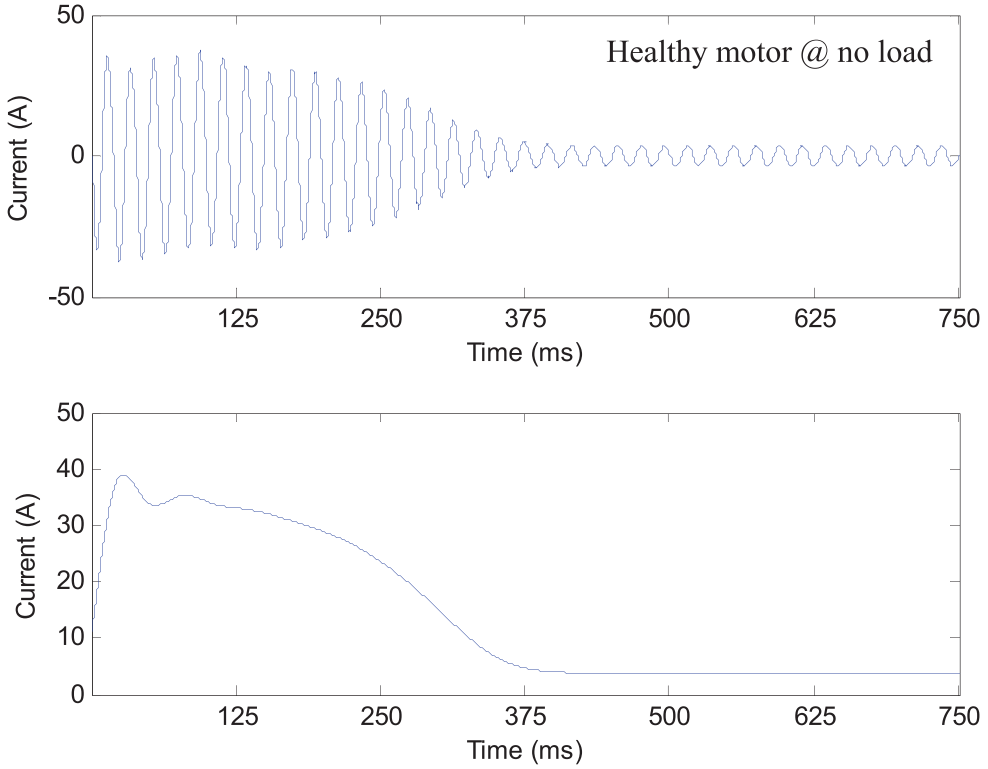

Figure 7.8 - Starting current characteristics of the healthy motor running at no load.

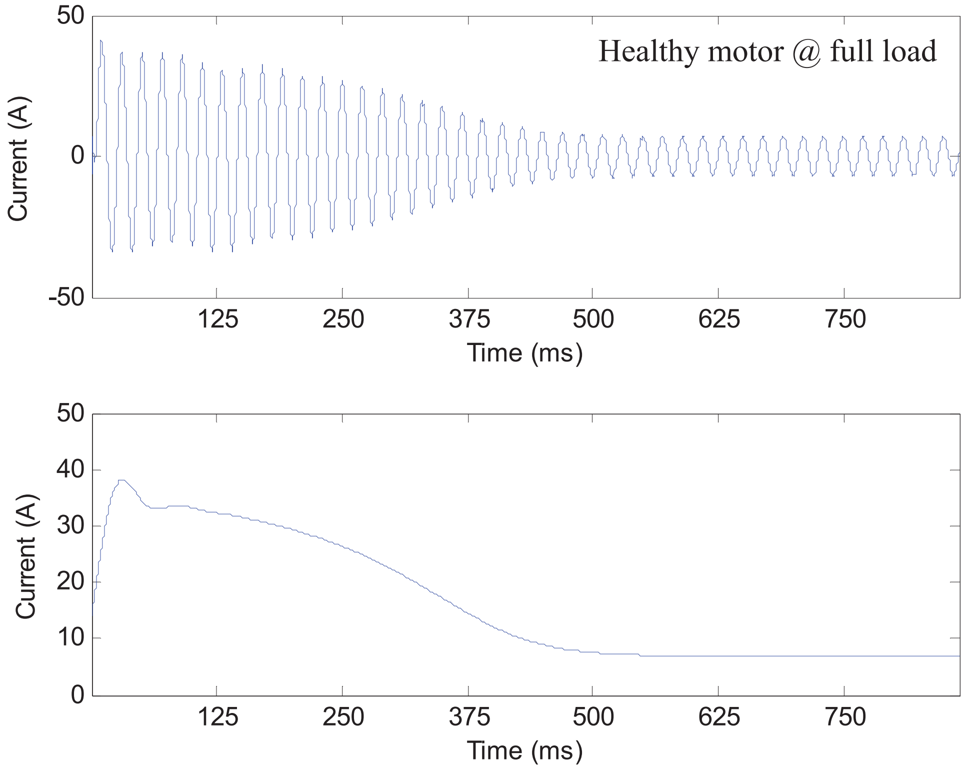

Figure 7.9 - Starting current characteristics of the healthy motor running at full load.

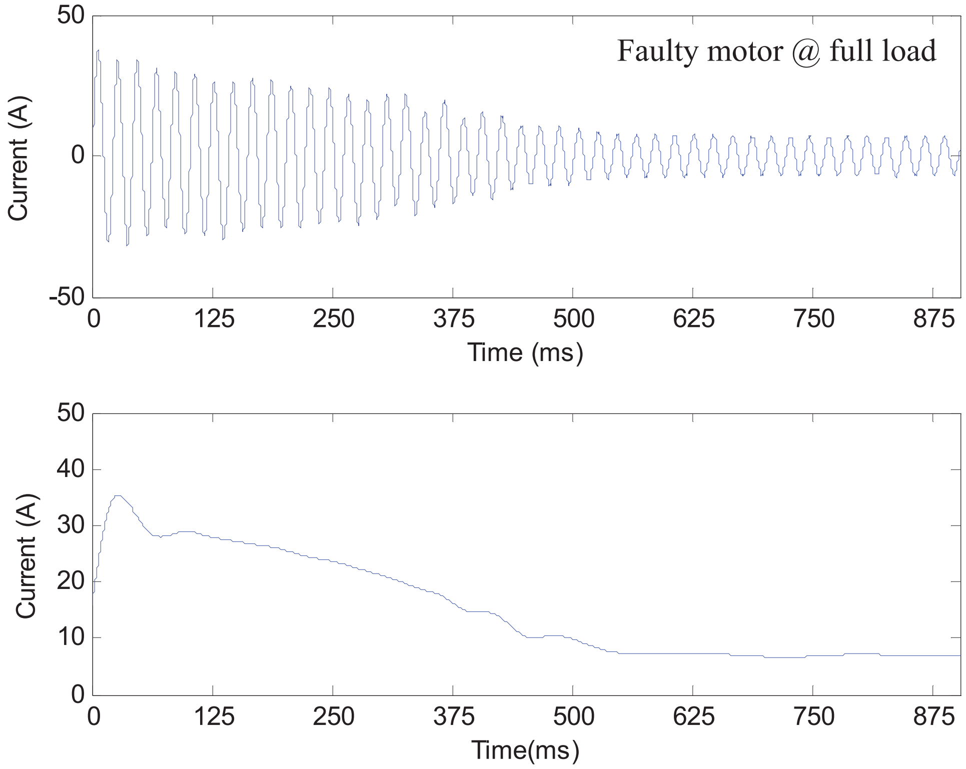

Figure 7.10 - Starting current characteristics of the faulty motor (4 BRB) running at full load.

7.3.1. Variability of Test Setup and Wavelet Technique

There are two types of variability tests considered in this investigation. First the variability of the motor setup, which is performed to ensure that the measurements obtained are repeatable, and second the variability of the wavelet technique under different loading conditions, initial rotor positions, and initial phase angle of the supply. The wavelet technique variability test is required to ensure that the pattern differences between the healthy and faulty motors (with broken rotor bars) are caused by the broken rotor bar fault and are not affected by other factors. For instance, the wavelet technique needs to be able to distinguish between the acceleration characteristic due to broken rotor bars on an unloaded machine and the acceleration characteristic of a healthy machine starting under load.

Figure 7.11 shows the variability of the measurements for 3 different healthy motors of the same type and rating as the faulty motor, namely healthy motor 1, healthy motor 2, and healthy motor 3. As shown by the figure, the three wavelet indicator lines of the healthy motors are very close to each other, which indicate a small degree of variability of the measurement data between the different healthy machines. Also note that the wavelet indicator lines for the healthy motors are well below the lowest level obtained for the faulty machine. Therefore, the slight variability between the healthy motors is insignificant.

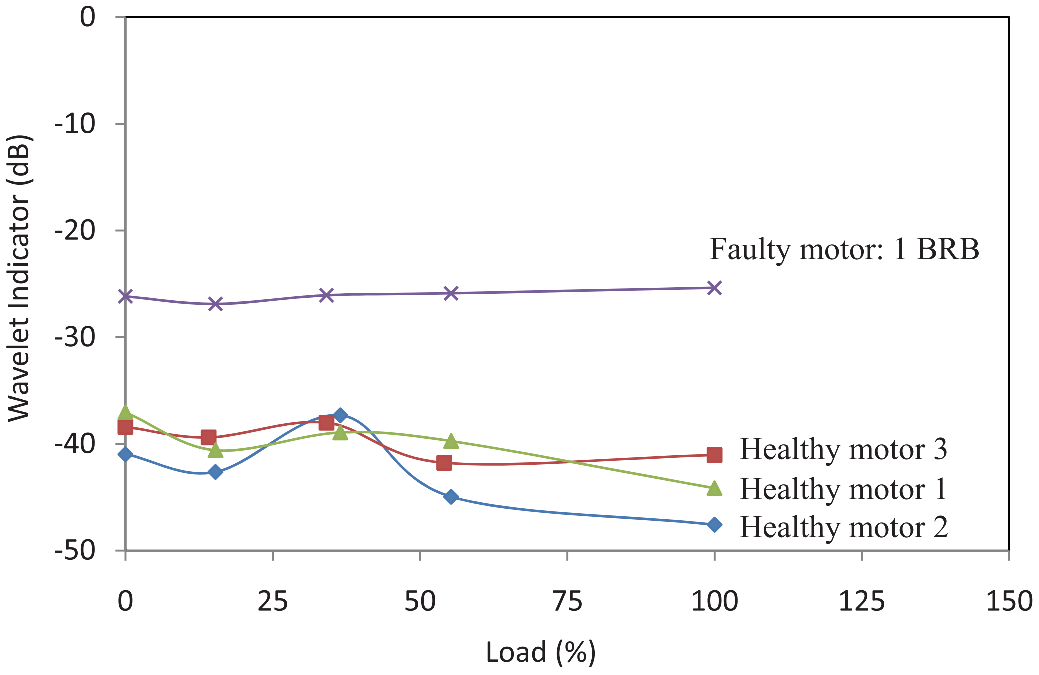

Figure 7.11 - Wavelet indicator plots for the starting current of three healthy motors and one faulty motor with 1 BRB as a function of load.

The wavelet indicator plots in Figure 7.12 indicate how the loading response of the wavelet indicator changes with different initial rotor positions and different phase angles of the supply voltage at starting. This variability test is done on the healthy motor 1 and is repeated three times by choosing random initial rotor positions and random starting phase angles of the supply voltage for every test and every loading condition. As shown in Figure 7.12, the three wavelet indicator lines are close to each other, which indicates that the results from the wavelet technique are not very sensitive to the loading conditions, initial rotor position, and the phase angle of the supply voltage at starting.

Based on the observations from Figure 7.11 and Figure 7.12, the general trend of the wavelet indicator plots for the healthy motors is that they tend to decrease slightly as the load increases.

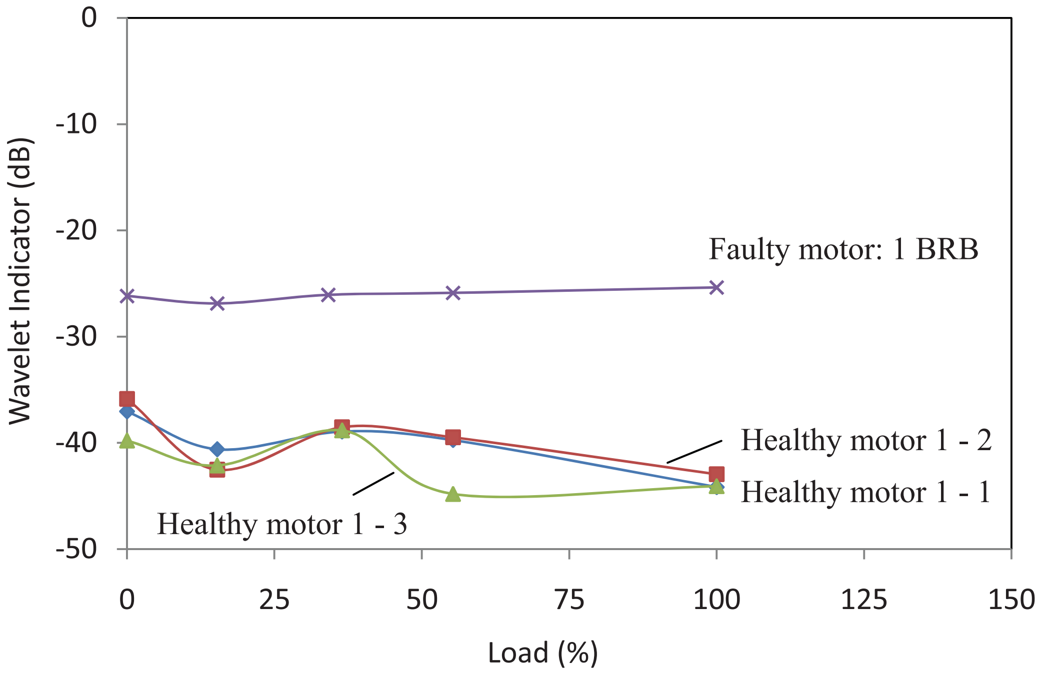

Figure 7.12 - Wavelet indicator plots for the starting current of a healthy motor with different initial rotor positions and supply voltage phase angles as a function of load.

7.3.2. Variability between Different Current Phases

The wavelet indicator plots in Figure 7.13 are given to show the variability between the current signals in each of the three phases of the healthy and faulty motors. The figure shows that the wavelet indicator variability between the different phases is relatively small (less than 5 dB) in comparison to the differences between the wavelet indicators of the healthy motor and the faulty motor with 1 broken rotor bar (approximately 15 dB). This variability test confirms that the wavelet characteristics, which are explained in the previous sections, are consistent in all of the motor phases and the differences between the three phases are insignificant. Therefore, it is justified to consider only one phase of the current for the analysis.

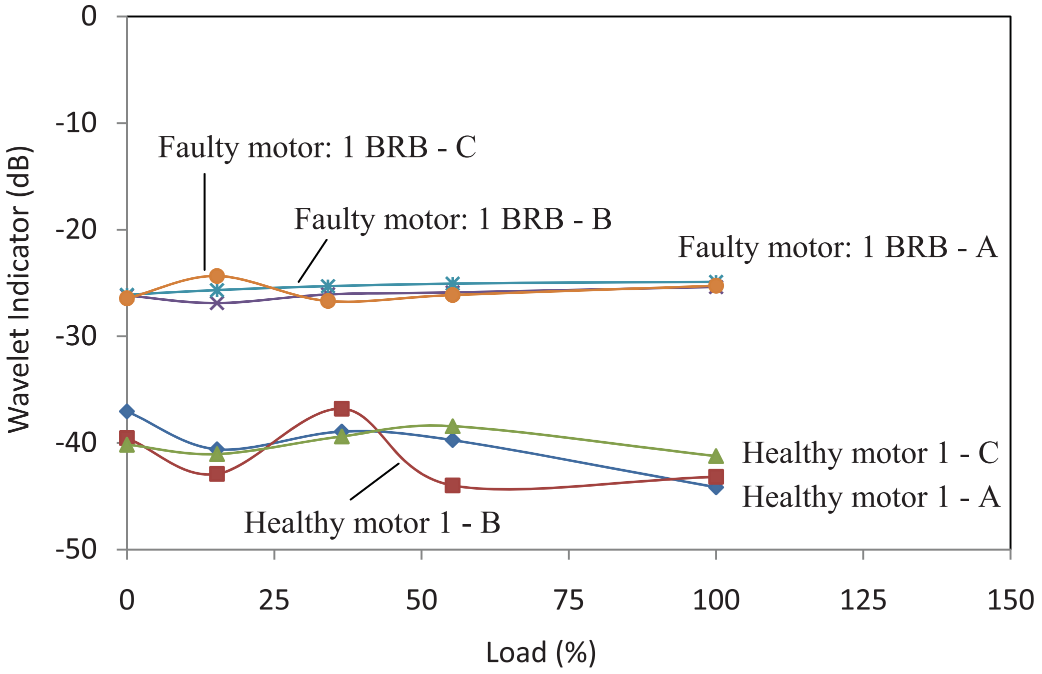

Figure 7.13 - Wavelet indicator plots for the starting current of the three different phases of the healthy motor.

7.3.3. Comparison and Classification of Healthy and Faulty Motors

As stated above, the wavelet indicator is proposed as a means for comparing healthy and faulty motors (with broken rotor bars) and classifying the various degrees of broken rotor bar fault. The comparison and classification is done by measuring the magnitude of the wavelet indicator, and is given in Figure 7.14.

Figure 7.14 clearly shows that the wavelet indicators of the faulty motors with broken rotor bars are consistently higher than the wavelet indicators of the healthy motors. The reason for this increase is due to the broken rotor bar “third pattern” that emerges in the wavelet transform of the envelope of the starting current for the motors with a broken rotor bar fault but not in the healthy motors. It should also be noted that the third wavelet pattern changes its scale and position depending on the loading conditions, such that the higher the load, the higher is the scale and the further is the position, but it always lies between the first and the second wavelet pattern. This behaviour of the third pattern and the fact that the magnitude of the BRB sidebands varies with the load account for the variability between the wavelet indicators of the healthy motors (Figure 7.11 and Figure 7.12).

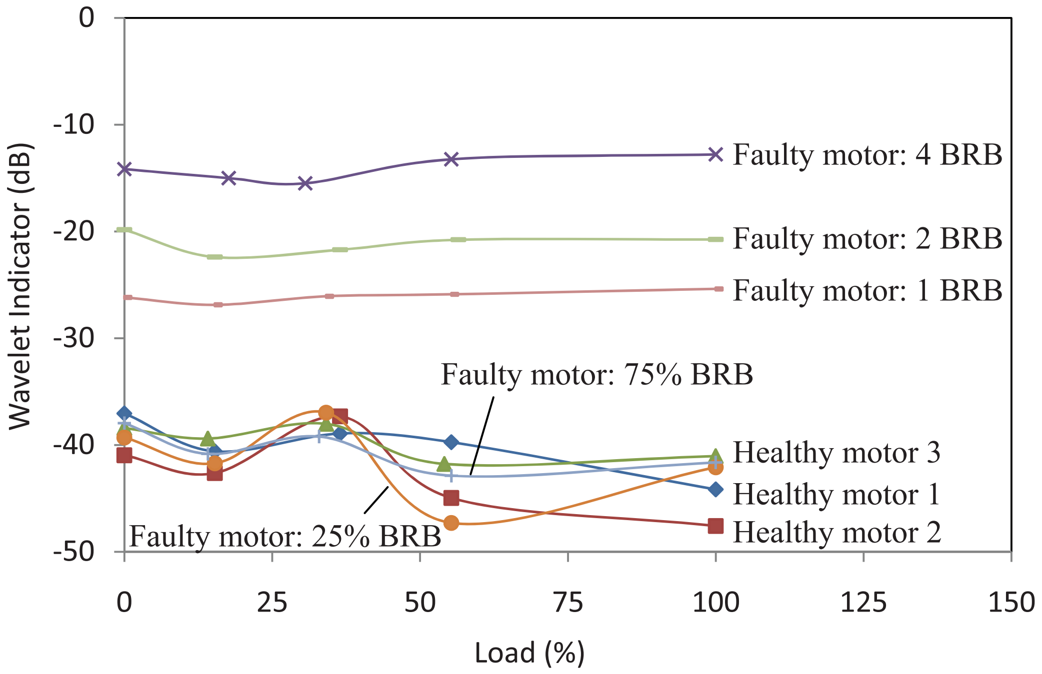

Figure 7.14 - Wavelet indicator plots for the starting current of all tested motors.

A clear trend observable in Figure 7.14 is that the wavelet indicator increases as the severity of the broken rotor bar fault increases. As can be seen from the figure, the faulty motor with 4 broken bars has the highest wavelet indicator. This is then followed by the wavelet indicator of the faulty motor with 2 broken rotor bars, followed by the faulty motor with 1 broken rotor bar. Finally, the healthy motors have the lowest wavelet indicators with about 15 dB difference to the faulty motor with 1 broken bar. In addition, this trend is consistent under different loading conditions. These observations suggest that detecting and classifying different severities of the fault appears simple for fully broken rotor bars. However, the wavelet indicators for the motors with a 25% and 75% partially broken rotor bar are very close to the wavelet indicators of the healthy motors and hence it is difficult to distinguish these two cases from the healthy machines. The reason for this is that a partially broken rotor bar in the test motor is likely to produce only a small change in the overall bar resistance and hence has little effect on the current distribution in the rotor [18].

7.3.4. Motors with Unbalanced Supply

Motors with unbalanced supplies show different wavelet characteristics than motors with broken rotor bar faults. They do not produce an extra wavelet pattern between the first and the second wavelet patterns, like motors with broken rotor bar faults do, but rather slightly alter and extend the first wavelet pattern. This characteristic is shown in Figure 7.15, which displays the plot of a wavelet envelope analysis on a motor, starting at no load, with 33% of current unbalance (CU) and 7.1% of voltage unbalance. Note that any motor should be built to handle 1% of voltage unbalance but it is not recommended to operate a motor with more than 5% of voltage unbalance [94].

The unbalance factor is calculated based on the full-load steady-state signals according to (Eq. 7.10), which is given for the voltage only but can readily be applied to the current.

$$UF = \frac{max\left(\left|V_{a(rms)} - V_{avg}\right|, \left|V_{b(rms)} - V_{avg}\right|, \left|V_{c(rms)} - V_{avg}\right|\right)}{V_{avg}} \qquad \text{(Eq. 7.10)}$$

where UF is the unbalanced factor; $V_{a(rms)}$, $V_{b(rms)}$, $V_{c(rms)}$ are the RMS values of the three phase voltages of the motor; and

$$V_{avg} = \frac{V_{a(rms)} + V_{b(rms)} + V_{c(rms)}}{3} \qquad \text{(Eq. 7.11)}$$

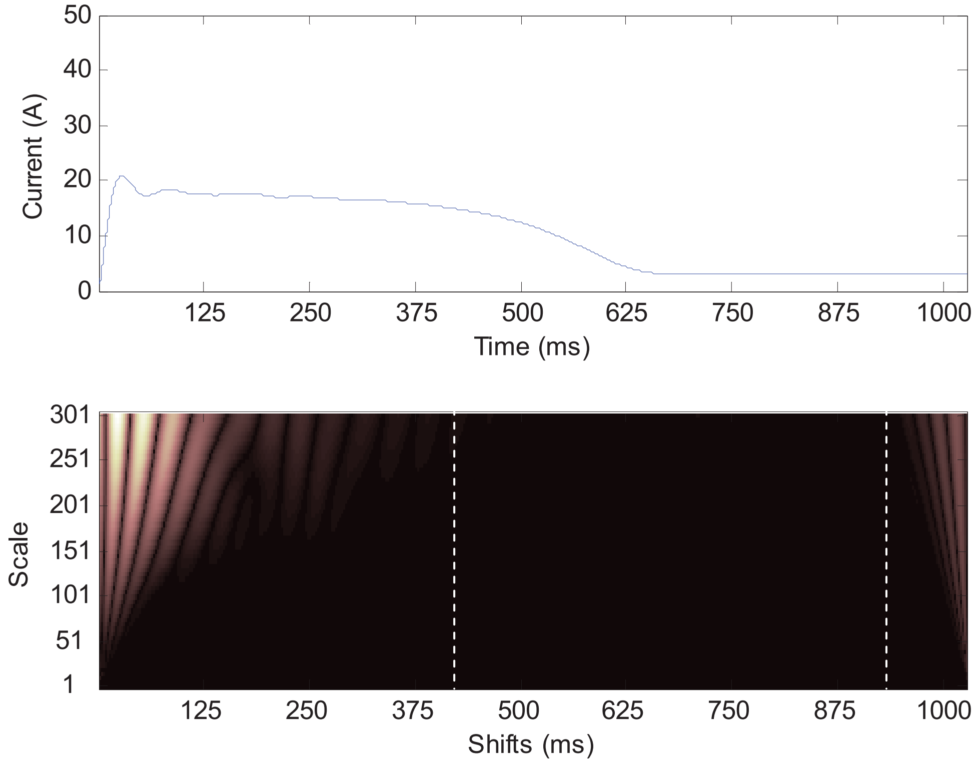

Figure 7.15 - Envelope of the starting current (top) and its continuous wavelet transform (bottom) for a motor with 33% of current unbalance.

In Figure 7.16, the wavelet indicators for the motors with 33% and 20% of current unbalance are found to be about the same level as the healthy motor case. These results show that the wavelet indicator is not affected by an unbalance in the supply. Therefore the proposed wavelet technique is reliable in detecting broken rotor bar faults even if the motor has an unbalanced supply.

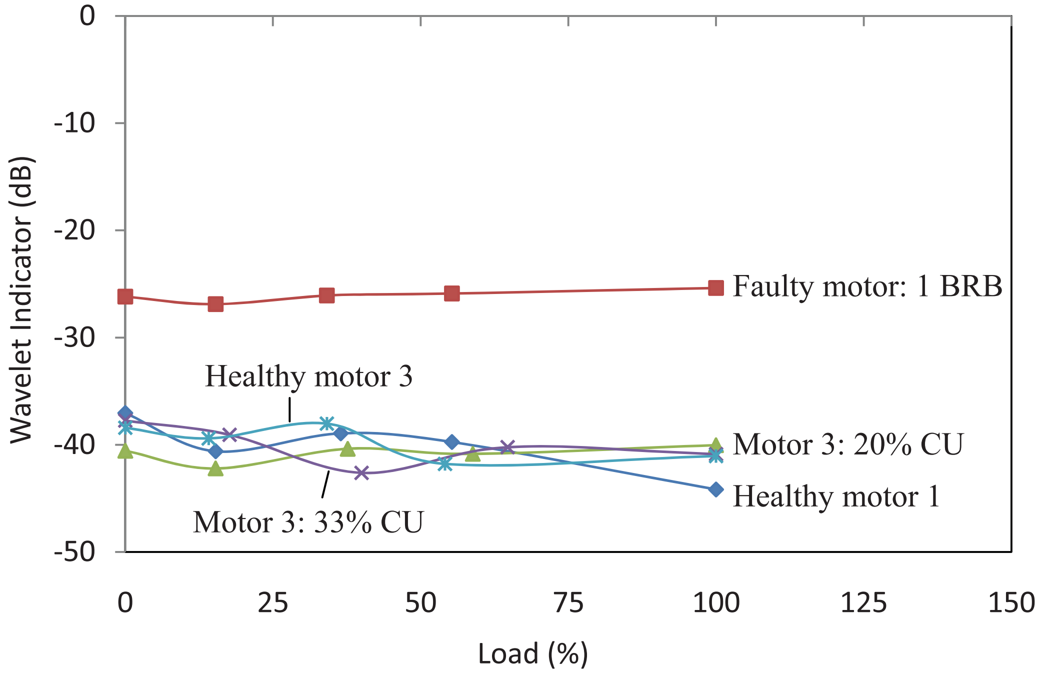

Figure 7.16 - Wavelet indicator plots for the healthy motors and the motors with unbalanced supply.

7.4. Summary

This chapter has investigated the detection of broken rotor bar faults during motor starting operation using a novel measure, the wavelet indicator. The wavelet indicator is obtained by quantifying the wavelet pattern characteristics of the motor starting current envelope. It is found that the magnitude of the wavelet indicator increases as the severity of the broken rotor bar faults increases. Using the wavelet indicator, it is possible to detect broken rotor bar faults, even if a motor only has 1 broken bar, under different loading conditions. This is because the wavelet indicator shows significant magnitude variation between the healthy and the faulty motors (eg. about 15 dB difference between the healthy motor and the faulty motor with 1 broken rotor bar) under all tested loads. However, it is observed that partially broken rotor bars in the test machine cannot be detected using this method. This is likely to be due to the small size of the motor under test and the minimal resistance changes caused by a partially broken rotor bar.

The wavelet indicator can potentially be used to estimate the number of fully broken rotor bars. This is because the magnitude of the wavelet indicator shows significant variation between the different numbers of broken rotor bars (eg. the magnitude increases by greater than 5 dB from 1 broken rotor bar to 2 broken rotor bars). However, this is subject to further investigation.

Chapter 8. Broken Rotor Bar Fault Detection During Rundown

8.1. Introduction

Broken rotor bar fault detection using steady-state condition monitoring techniques, such as the broken rotor bar sidebands, depends on the loading condition of the induction motor, where the fault detection becomes unreliable at light loads (see *sections 4.4* and *7.1*). One method to reduce the effect of load is to utilise the machine starting current waveform. The starting current is much larger than the rated current and is less sensitive to the level of load. In addition, the rotor currents during starting are also high and so the rotor faults should be more evident than under steady-state operation. Broken rotor bar fault detection using the starting current has been thoroughly investigated in Chapter 7.

Another possible method for detecting broken rotor bar faults is to utilise the induced voltage in the stator windings after supply disconnection. When the supply is disconnected, the stator currents drop to zero. As a consequence, the only source of induced stator voltages after supply disconnection is due to the rotor currents. The rotor currents are sensitive to broken rotor bar faults. In particular, a broken rotor bar can cause the rotor current distribution to become distorted, and hence produce characteristic harmonics in the induced voltage.

Broken rotor bar detection using the induced voltage during rundown has been reported previously in [95-97]. The work in [96] was based on 2.24 kW, 3-phase, 4-pole induction motors, one healthy and one faulty with two fully broken rotor bars, under a full load condition (measured during steady-state operation). It was shown that small but significant differences between the amplitudes of the harmonics of the healthy and faulty motors can be observed by applying the Fourier transform (FT) to the first 5 cycles (after disconnecting the supply) of the induced stator voltage. It was reported that the amplitudes of the 35th and 37th harmonics showed the most differences, in which the magnitudes of the faulty motor were 22.5 dB higher for the 35th harmonic and 9.2 dB higher for the 37th harmonic than the magnitudes of the healthy motor.

The work in [95] again investigated the harmonics of the rundown induced voltage but with two differences. Firstly, it used the space vector of the stator induced voltages, instead of monitoring a single stator line voltage, in order to eliminate the line frequency signal component. Secondly, instead of using the FT, it used the MUSIC (multiple signal classification). This estimation algorithm is more effective than the FT for identifying signals with known frequencies amongst noise. The algorithm was tested on a 1.1 kW and a 5.5 kW motor with one, two and three broken bars under no-load conditions. It was observed that the presence of broken rotor bar faults changed the pseudospectrum from a shape with one maximum at the fundamental frequency to a shape with three local maxima at the fundamental frequency, the 5th harmonic, and 7th harmonic.

The study in [97] utilised the short-time discrete Fourier transform (STDFT) method in order to track the harmonics of the rotor frequency component in the induced voltage signal and the leakage flux signal during the motor rundown operation. The study was performed using 18.5 kW, 50 Hz, 230/380 V, 4 poles, 28 rotor bars, three-phase induction machines under no load conditions. It was found that the amplitudes of the 29th, 31st, 47th, and 49th harmonics in the induced voltage signal were higher by about 4 – 11 dB in the faulty motor with 3 BRB than the healthy motor. Similarly, the amplitudes of the fault frequencies at 25 Hz, 75 Hz, 100 Hz, 125 Hz, 175 Hz, 225 Hz, and 275 Hz in the leakage flux signal were higher by about 3 - 18 dB in the faulty motor than in the healthy motor.

In summary, the previous work in detecting broken rotor bar faults during motor rundown operation focused only on using the harmonic components in either the induced voltage or the leakage flux signals under limited loading conditions. As a consequence, the previous work did not investigate the effects of loading on the fault feature. However, the study in this chapter will examine the effects of loading on the fault feature by using a wide range of loading conditions (i.e. no load - full load in ten steps) and a different number of broken rotor bars (i.e. 1, 2, and 4 broken rotor bars).

In addition, this study also investigate the limitations and effectiveness of other techniques for detecting broken rotor bar faults after supply disconnection by utilising both the induced voltage and the stator magnetic flux linkage, which is obtained by integrating the induced voltage. The advantage of using the stator flux linkage compared to the induced voltage is that the flux linkage is independent of the rotor speed and hence the motor load, as motor load is directly proportional to rotor speed (at least in healthy motors). The study in this chapter will examine two features from the rundown induced voltage, which are the harmonic content and the change in the motor output torque for a given value of slip, and three features from the stator flux linkage and its space vector components, which include the step change on disconnection, the rate of decay with time, and its spatially correlated harmonic content.

Broken rotor bar fault detection during motor rundown operation is useful when a motor is in maintenance, a new motor is being tested during production, or a motor is turned off during day to day operation.

8.2. Description of Broken Rotor Bar Detection Techniques During Rundown

When an induction machine is running, the stator currents produce a constant magnitude, sinusoidally distributed magnetic field which rotates at synchronous speed. This rotating magnetic field induces a current distribution in the rotor winding which rotates with respect to the rotor at the slip frequency.

At the instant of supply disconnection, the stator currents drop to zero and a new current distribution is induced in the rotor winding which tries to maintain the instantaneous magnetic field magnitude and spatial orientation in the machine. The new rotor current distribution does not rotate with respect to the rotor and hence the speed of the rotating magnetic field changes from synchronous speed before supply disconnection, to equal to the rotor speed, after disconnection.

After supply disconnection, the induction machine is thus similar to a wound-field synchronous machine with a short-circuited field winding which has a decaying field current. As a result, the induced back-emf in each stator phase winding of the induction machine is a function of three terms (see Figure 8.1):

- the magnitude of the stator flux linkage,
- the rotor speed, and
- the instantaneous rotor position, which is a constant magnitude of sinusoidal function.

The magnitude of the stator flux linkage is produced due to the rotor currents. These rotor bar currents, an instant after disconnecting the supply, have a sinusoidal distribution if all the rotor bars are healthy [96]. When some of the rotor bars are broken, the rotor bar current distribution is no longer sinusoidal and has discontinuities at the locations of the broken bar(s). These rotor bar current discontinuities produce harmonic components in the rundown induced voltage and the rundown flux-linkage. These harmonic fault frequencies are exact harmonics of the frequency of the induced stator voltages.

The stator flux linkage also decays at a rate that depends on the rotor winding inductance and the effective rotor winding resistance. The effective rotor resistance will increase with increasing severity of broken rotor bar faults. As a consequence, the flux-linkage decay time constant is expected to reduce with the increasing fault severity. In addition, the initial value of the stator flux linkage, at the instant of supply disconnection, depends on the degree of coupling between the rotor winding and the air-gap magnetic field at that instant, and so may also be affected by the presence of broken rotor bars. However, the initial value of the flux linkage is also dependent on the level of loading, where it affects the stator current and hence the stator leakage inductance voltage drop.

It should also be noted that after supply disconnection, the magnitude and the signal components of the stator flux linkage depends on the position of the rotor flux distribution, and hence rotor magnetising current distribution, with respect to the broken rotor bars at the instant of disconnection. This is because the position of the rotor magnetising current distribution with respect to the rotor surface does not change after the motor is disconnected from the supply but simply decays exponentially with time. As a consequence, the analysis in this chapter could be made more accurate if a rotor position sensor was utilised to identify the angle of the rotor flux distribution with respect to the rotor at the instant of the supply disconnection.

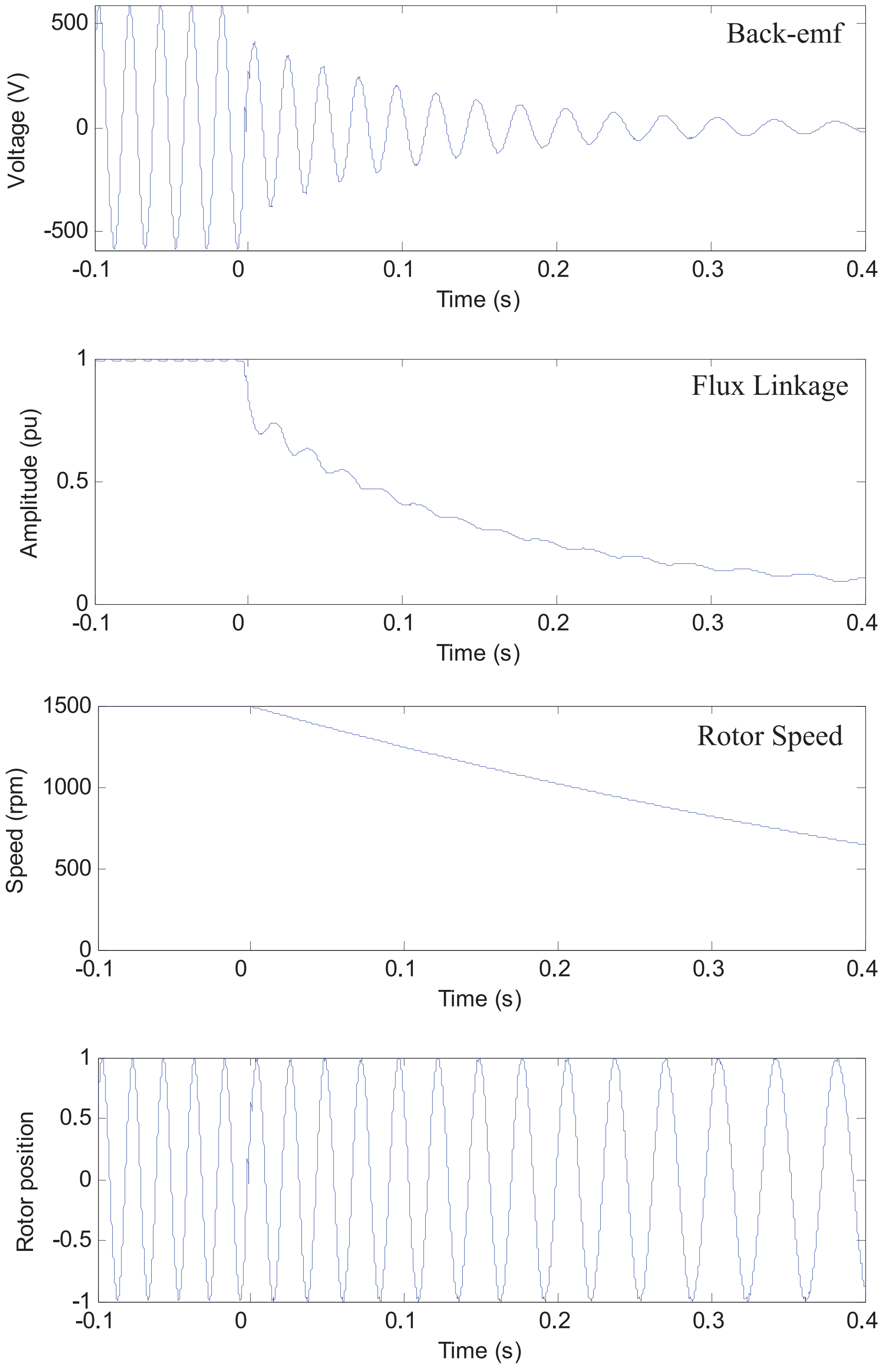

Figure 8.1 - Illustration of the measured components of the induced back-emf before and after supply disconnection.

However, such a technique is considered to be invasive and impractical in an industrial application. Furthermore, this rotor position sensitivity effect would averaged out if a sufficient number of measurements were taken. This slower response due to averaging is acceptable as rotor bar faults normally develop only gradually with time. Therefore, a rotor position sensor is not considered in this thesis.

After disconnecting the supply, the rotor speed falls at a rate dependent on the system inertia and the load torque. The deceleration rate can thus be used to estimate the load torque. It should be noted that the output torque of an induction machine for a given value of slip reduces as the effective rotor resistance (i.e. broken rotor bar fault severity) increases. Hence the severity of broken rotor bar faults can be estimated by analysing the change in slip before and after supply disconnection.

The above discussion has thus highlighted five possible methods for detecting broken rotor bar faults using the back-emf voltage and the stator flux linkage after supply disconnection. These methods are summarised in Table 8.1.

Table 8.1 – Broken rotor bar features for motor rundown operation.

Signal	Features
Induced voltage	Harmonic components Rate of decay of rotor speed for a given operating slip
Flux linkage	Step change in magnitude at supply disconnection
Space vector of flux linkage	Time constant of decay Harmonic components

8.3. Analysis of Rundown Broken Rotor Bar Features Using Induced Voltage

This section investigates the broken rotor bar features obtained from the induced (back-emf) voltage signal during motor rundown operation. Typical measurement results of the back-emf signal for healthy and faulty (4 BRB) motors running at no-load and at full-load are shown in Figure 8.2 and Figure 8.3. It is clear that at full-load, the rotor slows down far more quickly after disconnection and produces a faster back-emf amplitude and frequency change than in the no-load case. Note that the load is calculated based on the percentage of the rated slip when the motor is in the steady-state operation.

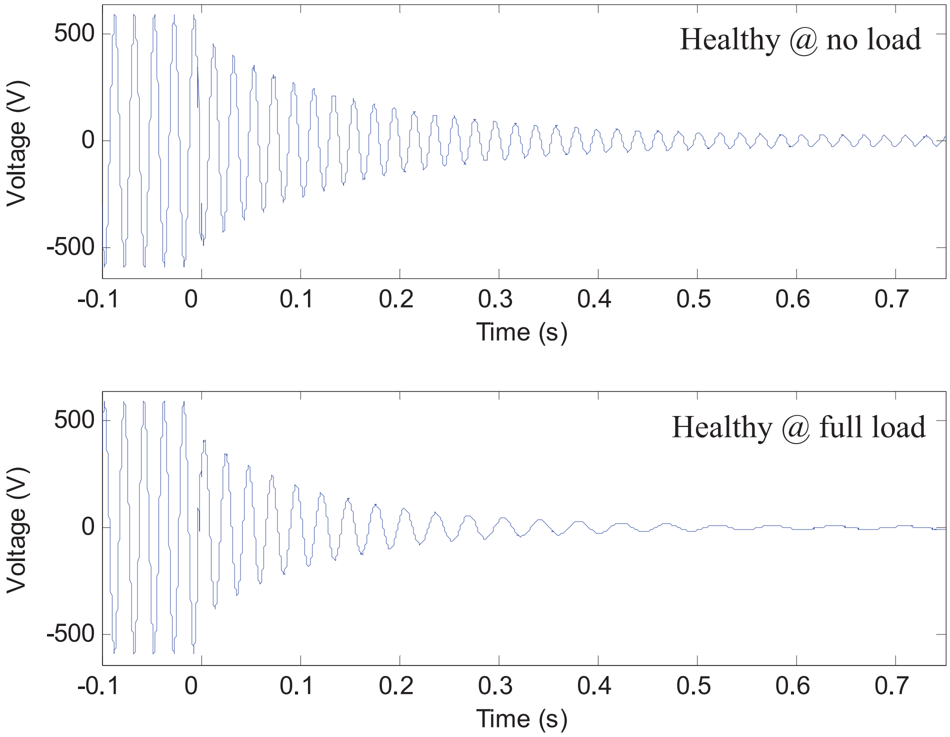

Figure 8.2 - Rundown stator induced voltage on the healthy motor when operating at no-load (top) and full-load (bottom) before and after the supply disconnection (at 0 s).

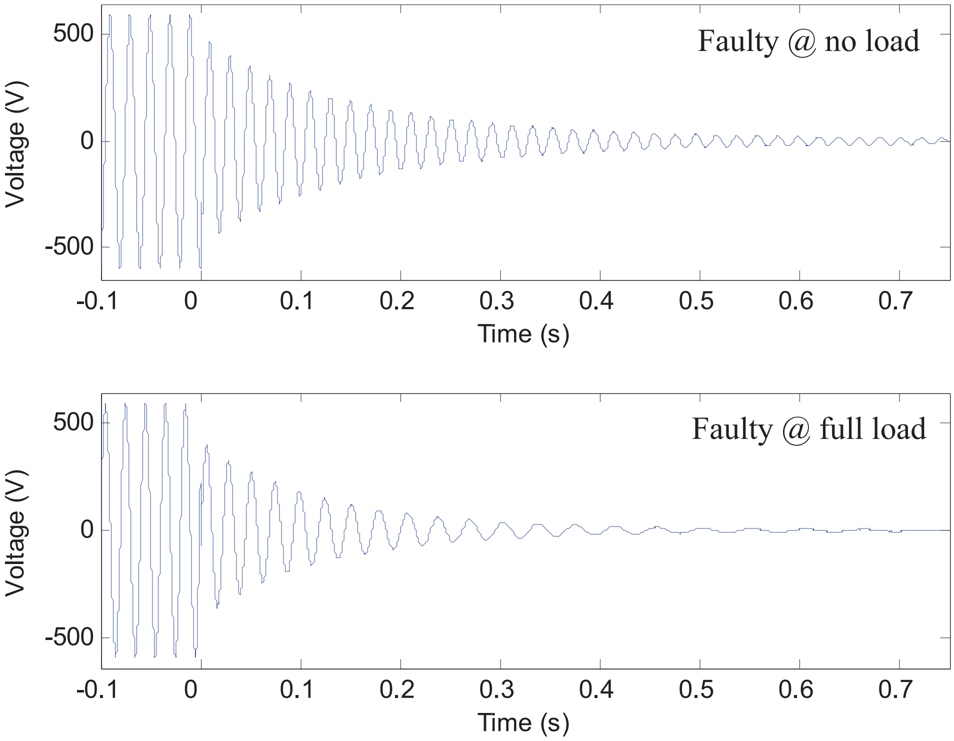

Figure 8.3 - Rundown stator induced voltage on the faulty motor with 4 BRB when operating at no-load (top) and full-load (bottom) before and after the supply disconnection (at 0 s).

A comparison between the back-emf voltages of the healthy and faulty motors reveals that there are no observable differences between them, even though the theoretical analysis presents arguments that there should be characteristic differences between the healthy and faulty motors. This suggests that the characteristic differences may not be significant.

8.3.1. Harmonic Components

The Fourier transform (FT) can extract the frequency information of a signal and monitor its harmonic components. The FT usually requires a signal to be in the steady state for an accurate frequency interpretation and its resolution depends on the observation time, where the longer the observation time is, the higher is the frequency resolution.

The study in this chapter considers the use of FT to analyse the harmonic components in the rundown back-emf waveform. However, the rundown induced voltage is not a steady state signal and so it cannot be observed over a long period of time. As a consequence, the rundown induced voltage needs to be processed to make it more suitable for FT analysis. One solution is to apply the FT to only a limited number of samples of the induced voltage after disconnecting the supply. This process effectively reduces the frequency variation over the observed signal [96]. The number of samples selected in this investigation is equivalent to five cycles of the induced voltage. However, this process also reduces the observation time and hence reduces the frequency resolution. The frequency resolution also gets poorer as the motor load increases because high load causes the back-emf to change its frequency and amplitude faster.

This poor frequency resolution at high loads can be minimised by normalising the magnitude of the decaying back-emf waveform and performing an order tracking technique on the back-emf. The magnitude of the back-emf is normalised by multiplying the signal with the inverse of the exponential decay function of the back-emf waveform. The order tracking technique is the process of re-sampling the back-emf waveform such that each cycle (period) of the waveform contains exactly the same number of samples separated by a fixed spatial (linear) interval rather than a fixed time interval [98]. The order tracking process is effectively the same as synchronously re-sampling the back-emf waveform with constant rotor position intervals. The FT of the resultant signal should show the harmonics of the fundamental more clearly.

8.3.1.1. Analysis of Results

Figure 8.4 and Figure 8.5 show the power spectra of the first five cycles of the rundown induced voltages of the healthy and faulty (4 BRB) motors running at no load and full load. These figures show that the widths of the harmonic peaks are changing with the load. The higher the load, the wider are the harmonic peaks (some examples are highlighted in the figures). This is because the frequency of the harmonics depends on the rotor speed and the rotor speed slows down faster with increasing load. Therefore, when the load is higher, the FT needs to average the harmonic component over a wider range of frequency and hence produces a wider peak width. The fact that the peak width is wider reduces the frequency resolution. As a consequence, the standard FT method is more suitable for light load cases, where the rundown induced voltage has a smaller frequency change with time.

In order to minimise the poor frequency resolution problem, this research utilises the order tracking Fourier transform (OTFT) technique. The results of applying the OTFT technique on the rundown induced voltage signals in Figure 8.4 and Figure 8.5 are shown in Figure 8.6 and Figure 8.7. These figures clearly show the improvements made by the OTFT technique over the standard FT technique, where the width of the harmonic peaks remains constant with changes in the motor load. These results show that the OTFT technique alleviates the poor frequency resolution problems and provides more accurate analysis irrespective of the motor loading conditions. However, it should be noted that the OTFT technique involves interpolation of the input signal, which may introduce errors due to the approximation of the signal. These interpolation errors may introduce frequency components that should not be in the signal. As such, utilising this technique should consider the trade off between the frequency resolution problems and the interpolation errors.

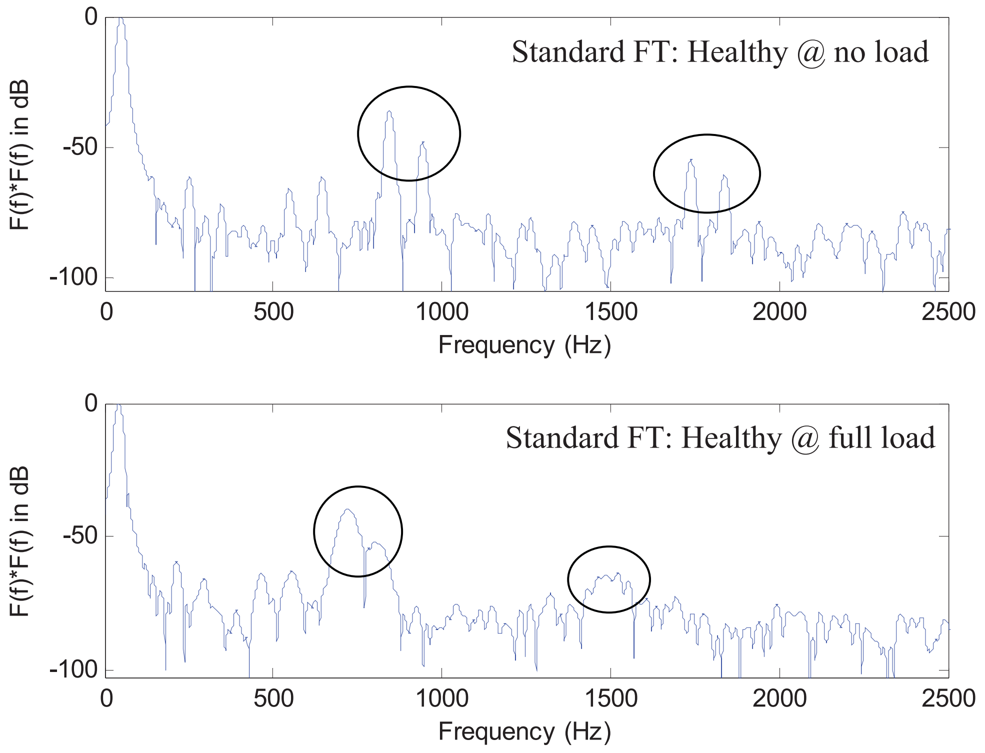

Figure 8.4 - Power spectra of the rundown induced voltages of the healthy motor running at no load (top) and at rated load (bottom).

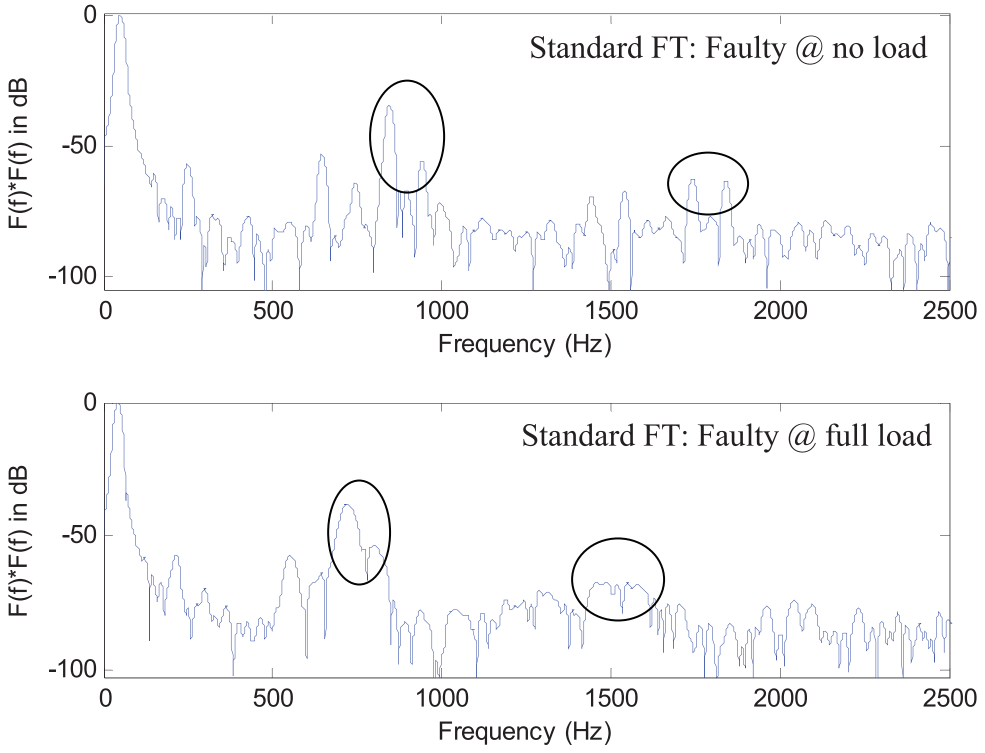

Figure 8.5 - Power spectra of the rundown induced voltages of the faulty motor with 4 BRB running at no load (top) and at rated load (bottom).

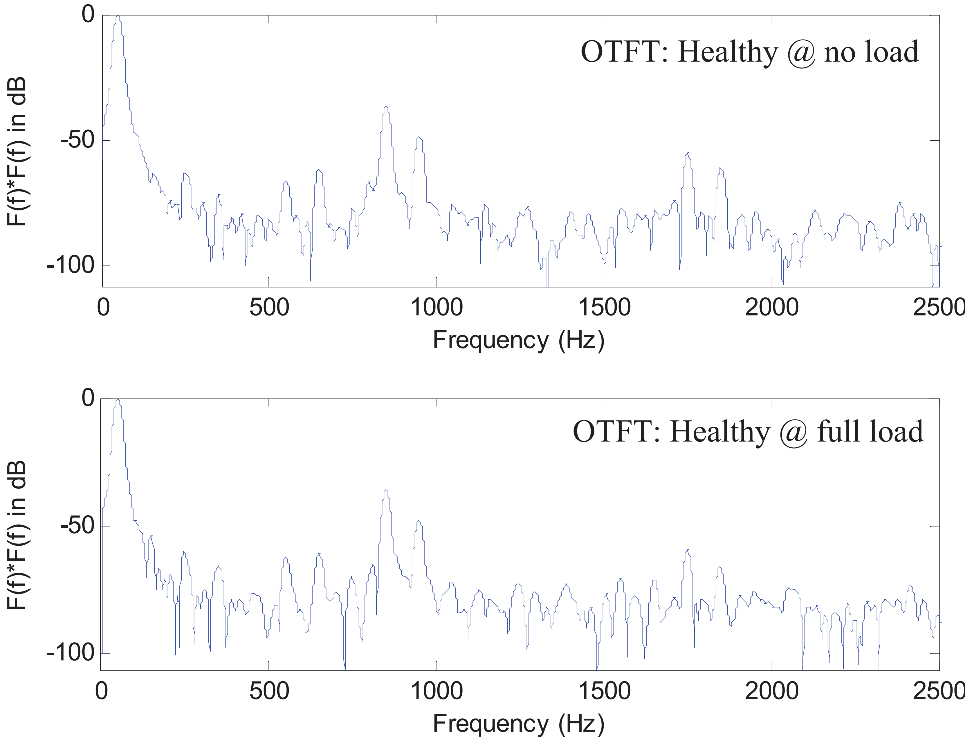

Figure 8.6 - Power spectra (with OT technique) of the rundown induced voltages of the healthy motor running at no load (top) and at rated load (bottom).

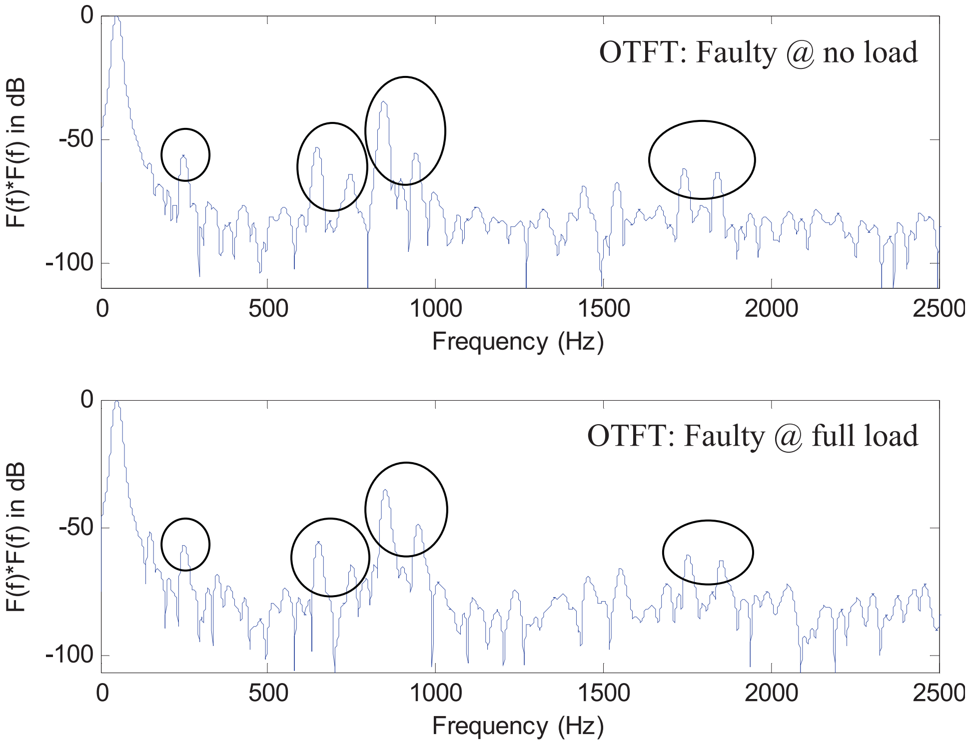

Figure 8.7 - Power spectra (with OT technique) of the rundown induced voltages of the faulty motor with 4 BRB running at no load (top) and at rated load (bottom).

There are 2 main advantages of using the OTFT technique. The first improvement is that the harmonic components are much easier to detect using the OTFT technique than the standard FT technique, especially at high loads. This is because the harmonics obtained from the OTFT technique have sharp peaks while the harmonics obtained from the standard FT have wider peaks (especially at high loads), which make them difficult to detect. The second improvement is that the magnitude of the harmonic component detected by the OTFT technique is more accurate than the magnitude detected by the standard FT technique. This is because the OTFT technique produces results with higher frequency resolution and less frequency smearing than the results produced by the standard FT technique.

For a harmonic component in the rundown induced voltage to be considered as a broken rotor bar feature, it must be detectable in the faulty motor signal and it must show consistent magnitude variation between healthy and faulty motors under different loading conditions. Figure 8.6 and Figure 8.7 show that there are seven strong components in the rundown induced voltage of the faulty motor that could potentially be used as broken rotor bar features. These seven components are identified to be the 5th, 13th, 15th, 17th, 19th, 35th, and 37th harmonics of the fundamental (highlighted in Figure 8.7). These components will be analysed below.

Figure 8.8 - Figure 8.9 present comparisons of the seven potential broken rotor bar features (harmonics) in the rundown induced voltage of the healthy and faulty motors under different loading conditions. Unfortunately, most of the harmonics cannot be considered as broken rotor bar features because they do not show consistent magnitude variation between the healthy and the faulty motors under the different loading conditions or they do not show consistent magnitude variation pattern between the different fault severities. Out of the seven harmonics, the 13th and the 17th harmonics are the better features because they show consistent magnitude variation between the healthy and the 1 BRB conditions under the different loading conditions (i.e. about 15 dB difference for the 13th harmonic and about 6 dB difference for the 17th harmonic). However, for the test motor, both harmonics do not show consistent magnitude variation pattern with increasing fault severity, where the magnitude does not increase with increasing fault severity.

As a comparison, the work in [96, 97] discovered that the magnitude of the fundamental harmonics could increase by about 5 – 20 dB between the healthy and the faulty motors. However, the previous work did not consider the consistency of their findings under different loading conditions and under different broken rotor bar fault severities. For example, this thesis found that there was about a 15 dB increase in the magnitude of the 15th harmonic from the healthy motor to the faulty motor with 4 BRB at no load. However, the magnitude variation was not consistent with increasing load and the magnitude variation pattern was not consistent with increasing fault severity.

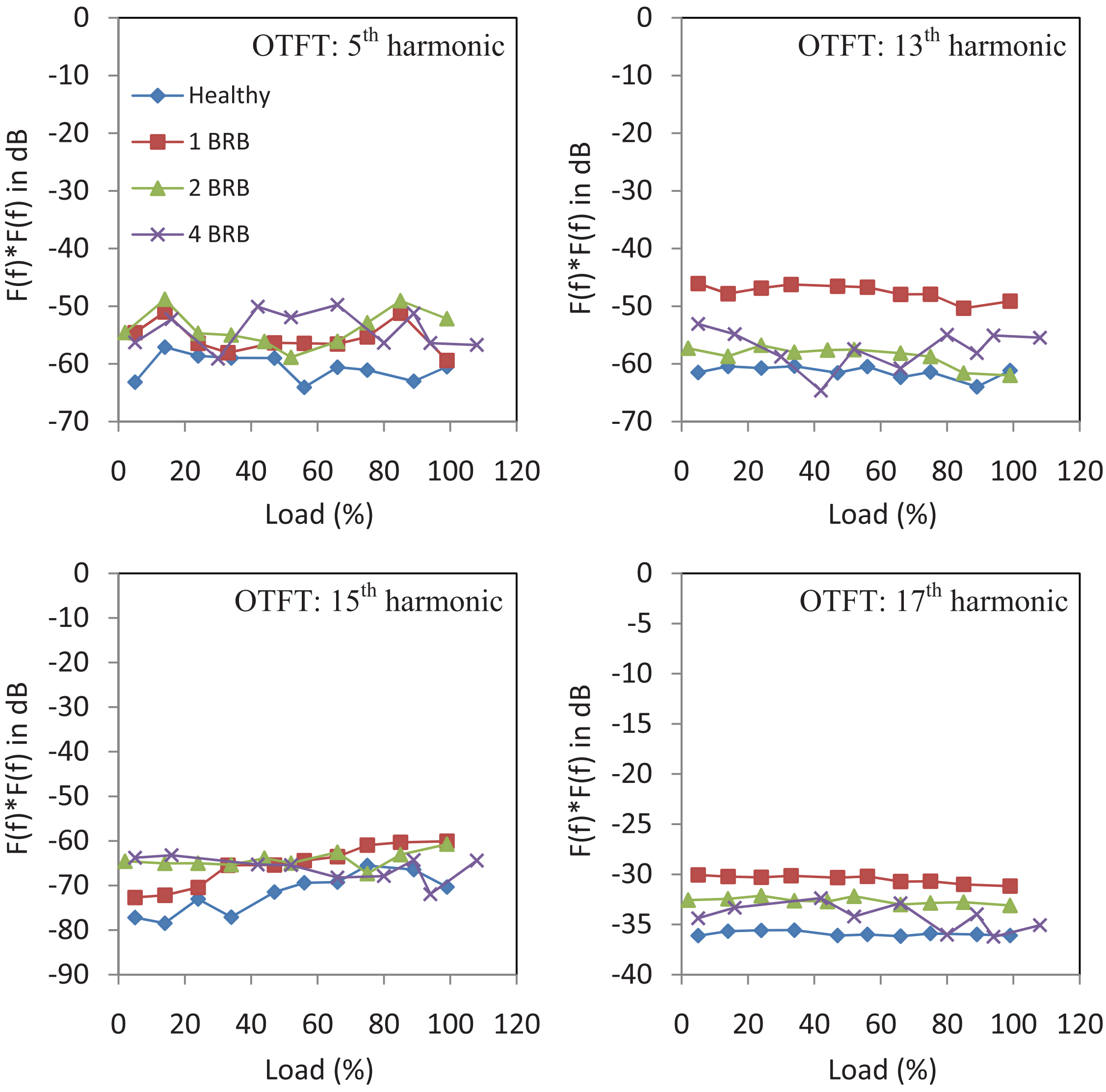

Figure 8.8 - Magnitude of the 5th, 13th, 15th, and 17th harmonics of the fundamental frequency using the OTFT technique as a function of load.

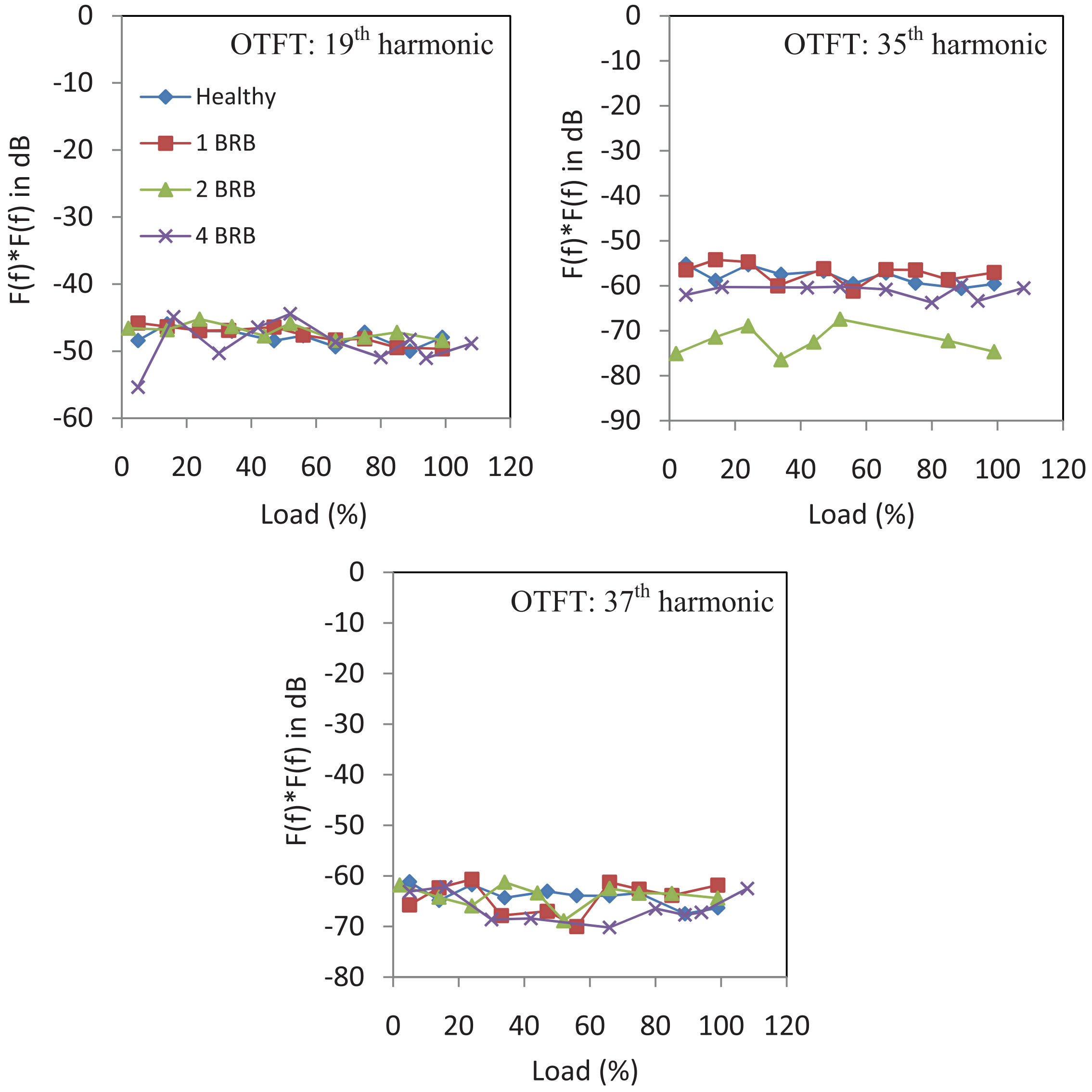

Figure 8.9 - Magnitude of the 19th, 35th, and 37th harmonics of the fundamental frequency using the OTFT technique as a function of load.

8.3.2. Rate of Decay of Rotor Speed for a Given Operating Slip

It was discussed earlier that broken rotor bar faults reduce the machine output torque for a given value of slip. This means that for the same value of slip, the load torque will be lower with a broken rotor bar fault, and hence the faulty rotor will take longer to slow down.

As the machine is acting as a synchronous machine after the supply is disconnected, the frequency of the induced voltage is directly proportional to the rotor speed. The rotor speed after supply disconnection decays at a rapid rate. As a consequence, the Fourier transform, which can only display the frequency information of a signal by using a fixed-size window, may not be the most suitable technique. In order to overcome these transient issues, the wavelet transform technique is utilised. The wavelet transform can provide both scale (which is related to frequency) and time information of a signal through its variable-sized window. As a result, the wavelet transform can be used to track the fundamental frequency, and hence the rotor speed, as a function of time. The wavelet function used for this analysis is “sym3” from the Symlet family (see *section 2.4*). The “sym3” wavelet is chosen because it was experimentally found to be suitable in extracting and highlighting the broken rotor bar features from the sensor signals.

The proposed technique begins by calculating the time taken for the amplitude of the rundown induced back-emf voltage to reach a certain threshold. This thesis set the threshold to be 2.5% of the rundown back-emf initial value. This particular value is chosen because the preliminary analysis shows that this value can highlight the differences in the rate of the decay of the rotor speed for a given slip between healthy and faulty (BRB) motors. The next step is to compute the wavelet transform of the rundown induced voltage. Then, to calculate the wavelet scale that corresponds to the maximum wavelet coefficient at the instant of supply disconnection and the wavelet scale that corresponds to the maximum wavelet coefficient at the time obtained from the threshold process. Note that these maximum wavelet coefficients correspond to the fundamental component of the signal, which is the rotor frequency component. Finally, the difference between the two wavelet scales, Δa, which is proportional to the change in the rotor speed from the speed at the instant of disconnection to the speed when the induced voltage has decayed to the threshold, is calculated. This difference is the proposed feature for detecting broken rotor bar faults.

8.3.2.1. Analysis of Results

Typical wavelet plots of the rundown induced voltage of the healthy and faulty motors running at no load and at rated load are shown in Figure 8.10 and Figure 8.11 respectively. Figure 8.11 shows that the fundamental component, which is the component highlighted between the dashed lines, changes its frequency with time. This frequency change is quantified by using the technique described in *section 8.3.2* and the results are given in Figure 8.12.

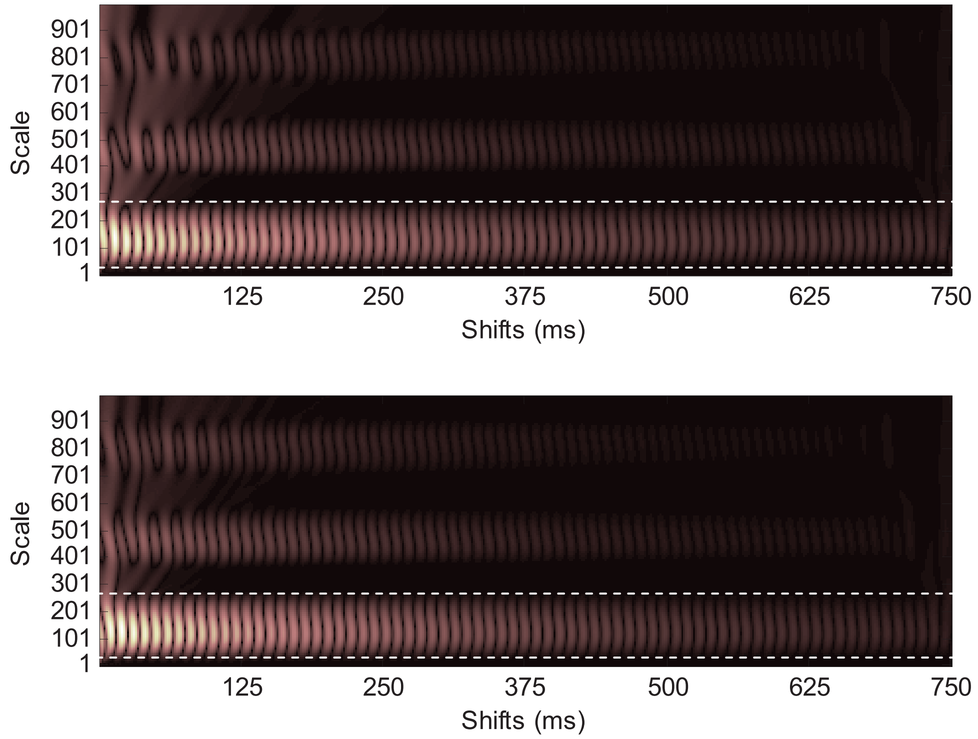

Figure 8.10 - Wavelet plots of the induced rundown voltage on the healthy motor (top) and the faulty motors with 4 BRB (bottom) running at no load.

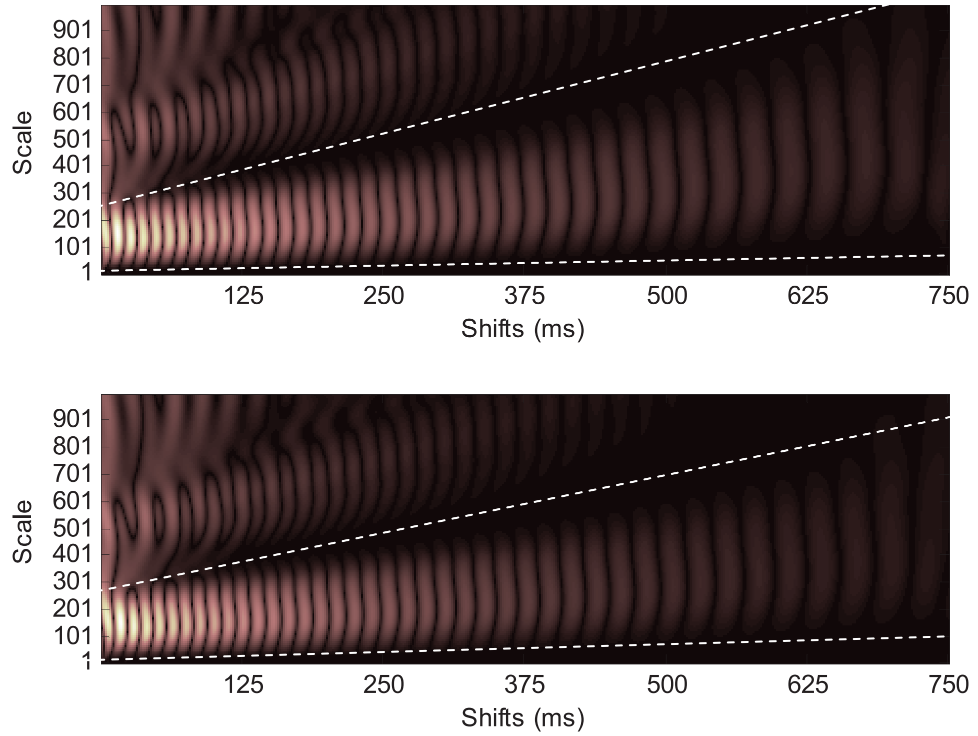

Figure 8.11 - Wavelet plots of the induced rundown voltage on the healthy motor (top) and faulty motors with 4 BRB (bottom) running at rated load.

As indicated in *section 8.2*, broken rotor bar faults reduce the motor torque and hence load torque for a given value of slip. Thus for a given value of slip, the rate at which the speed decays will decrease as the fault severity increases. Figure 8.12 shows how the change in wavelet scales, Δa, (that is the change in rotor speed) over a given time interval varies under different loading and broken rotor bar fault conditions. Figure 8.12 demonstrates that the change in wavelet scale, Δa, tends to increase proportionally with the slip (and hence load torque). This means that the rotor speed decays faster with increasing load. On the other hand, the change in wavelet scale, Δa, decreases as the severity of the broken rotor bar fault increases. This means that the rotor speed decays slower with the increasing fault severity. These findings are in agreement with the theory and they show that the change in wavelet scale, Δa, can be considered as a broken rotor bar feature for distinguishing and separating the different levels of broken rotor bar fault, especially at mid to higher (>20%) loads.

It should be noted that while this technique is promising, it does have some limitations when applied to practical systems. Firstly, it requires tests to be carried out with the motor in the healthy state to develop a baseline response curve of deceleration rate versus slip. This means that the technique can only be used in conjunction with trending of the feature but not setting a threshold for the feature. Secondly, the technique relies on estimating the motor torque based on the deceleration rate after supply disconnection and correlating changes in motor torque with the broken bar fault severity. Therefore, the approach may be sensitive to changes in system inertia, rotor temperature and supply voltage. In addition, the technique may also be sensitive to rapid fluctuations in load, as it inherently assumes that the load does not change between the steady-state operation just before supply disconnection, and the first few cycles of the run down period. As a consequence, this detection technique may be used by itself only if all its limitations have been taken into account (i.e. if the system inertia, the rotor temperature, the supply voltage, and the motor load remain relatively constant when capturing the sensor signal). Otherwise, the technique needs to be used together with other broken rotor bar detection methods.

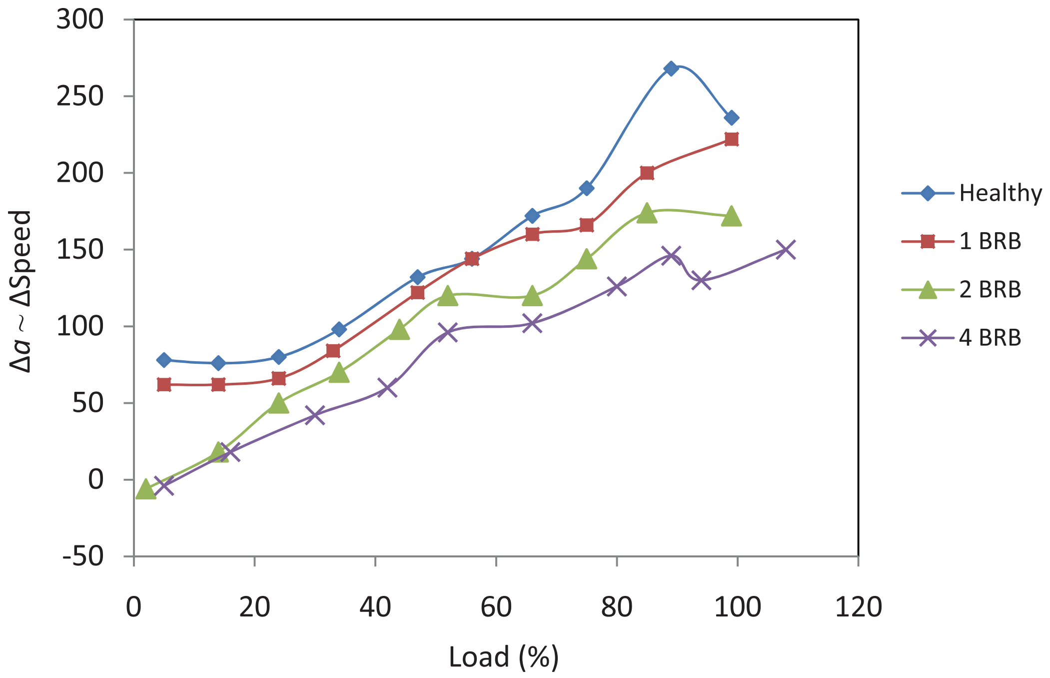

Figure 8.12 – Change in wavelet scale, Δ*a*, of the rundown induced voltage over a given time interval.

8.4. Analysis of Rundown Broken Rotor Bar Features Using Stator Flux Linkage

This section investigates the broken rotor bar features obtained from the stator flux linkage during motor rundown operation. The rundown stator flux linkage is calculated by integrating the rundown induced back-emf voltage as shown in (Eq. 8.1). However, the integration of the rundown induced voltage suffers from two main issues, which are DC drift and initial value condition [99]. The DC drift on the flux linkage signal occurs because a DC component is always present on the voltage signal due to the inability to completely remove the sensor offset errors. On the other hand, the initial value condition of the voltage signal may produce a DC component in the flux signal. These two issues can be avoided by basically removing the DC component in the voltage signal before the integration process, followed by removing the DC component in the integrated voltage signal (i.e. flux signal). However, due to the difficulties of measuring the DC level in a real system and due to the transient nature of the measured signal, it is found to be difficult to remove the DC offset in a real time measurement. Note that this problem could have been avoided if an analogue high pass filter was utilised. However, the present experimental setup did not include an analogue high pass filter. Its inclusion in the experimental setup may be considered in future studies.

$$\lambda(t) = -\int \varepsilon(t)\, dt \qquad \text{(Eq. 8.1)}$$

where $\lambda(t)$ is the stator magnetic flux linkage and $\varepsilon(t)$ is the induced back emf.

The method used in this thesis to obtain the flux linkage from the induced voltage is as follows:

1. Separating the induced voltage signal into its steady-state and rundown portions.
2. Removing the DC component in the steady-state portion by
    a. averaging the maximum and the minimum values of the portion and then subtracting it from the steady-state portion,
    b. integrating the steady-state portion, calculating the resultant DC drift, and then compensating for it in the steady-state induced voltage.
3. Integrating the steady-state portion of the DC removed induced voltage in order to obtain the steady-state flux linkage.
4. Removing the DC component of the steady-state flux linkage by using the method described in step 2.
5. Removing the DC component of the rundown induced voltage by
    a. using the DC component of the steady-state portion (step 2),
    b. integrating the rundown portion, calculating the resultant DC drift, and then compensating for it in the rundown induced voltage.
6. Integrating the rundown portion of the DC removed induced voltage by compensating the initial value condition in order to obtain the rundown flux linkage.
7. Finally combining the steady-state and the rundown portions of the flux linkage.

The stator magnetic flux linkage plots, calculated from the induced phase voltage plots in Figure 8.2 and Figure 8.3, are shown in Figure 8.13 and Figure 8.14. As mentioned before, the flux linkage is not dependent on the rotor speed. Therefore, the flux linkage removes the change in the shape of the envelope of the curves due to loading but it does not change the frequency variation with load. It can be concluded from Figure 8.13 and Figure 8.14 that the most obvious differences between the healthy and faulty motors is the decay rate of the stator magnetic flux-linkage at full load, where it decays faster in the faulty motor than in the healthy motor. The other effects may be present but are not easily determined by observation from the figures.

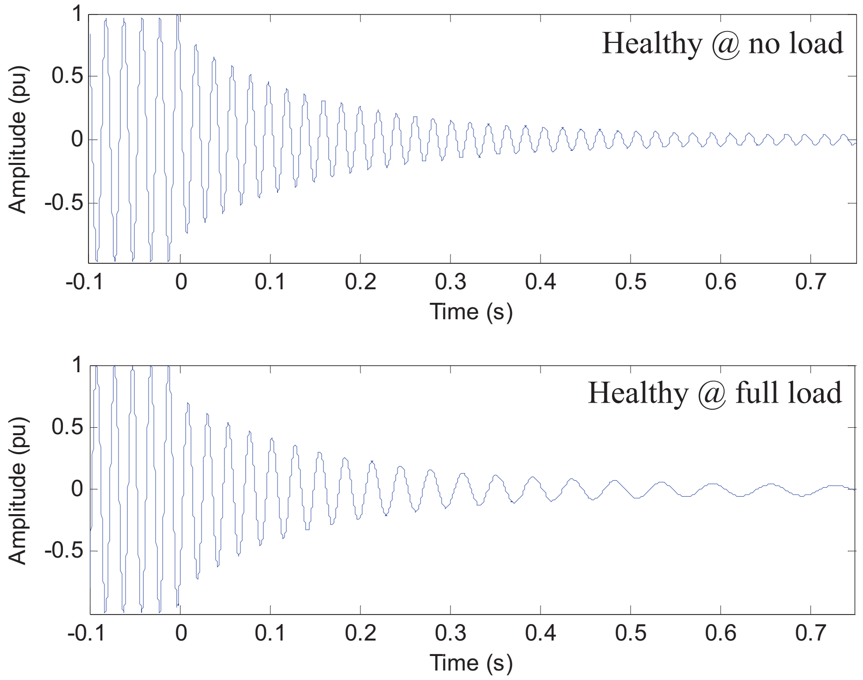

Figure 8.13 - Rundown stator magnetic flux linkage on the healthy motor when operating at no-load (top) and full-load (bottom) before and after the supply disconnection (at 0 s).

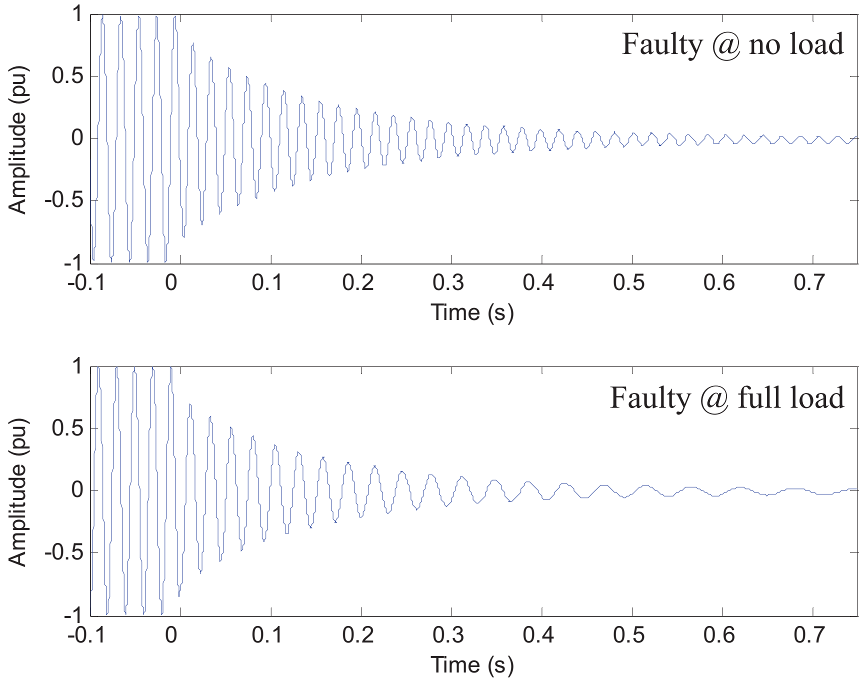

Figure 8.14 - Rundown stator magnetic flux linkage on the faulty motor with 4 BRB when operating at no-load (top) and full-load (bottom) before and after the supply disconnection (at 0 s).

8.4.1. Step Change in Magnitude of Flux Linkage on Disconnection

One of the features proposed earlier for detecting broken bar faults is the step change in the magnitude of the magnetic flux linkage on disconnection, which may be observed in Figure 8.13 and Figure 8.14. The step change in the flux-linkage magnitude can be calculated as the difference between the magnitude of the steady-state portion of the signal before disconnection and the magnitude just after disconnection. Determining the magnitude just after disconnection is complicated by the fact that this is a single-phase signal. In the analysis, the magnitude is estimated by fitting a curve to the envelope of the flux linkage peaks after disconnection. This curve is then extrapolated back to the instant of disconnection.

8.4.1.1. Analysis of Results

Figure 8.15 shows how the magnitude drop of the stator magnetic flux linkage at the instant of disconnection varies for different broken rotor bar fault severities under different loading conditions. The drop is generally found to increase with increasing loading condition and fault severity. However, it cannot be used to separate between the healthy, 1 BRB, and 2 BRB conditions because the magnitude variations between them are not large enough (<2.5%). The magnitude drop only starts to increase when there are 4 (or more) BRB present in the motor, where there is about 5 - 10% difference between the healthy and the 4 BRB condition. As a consequence, the step change in the magnitude of flux linkage on disconnection cannot be considered as a good broken rotor bar feature.

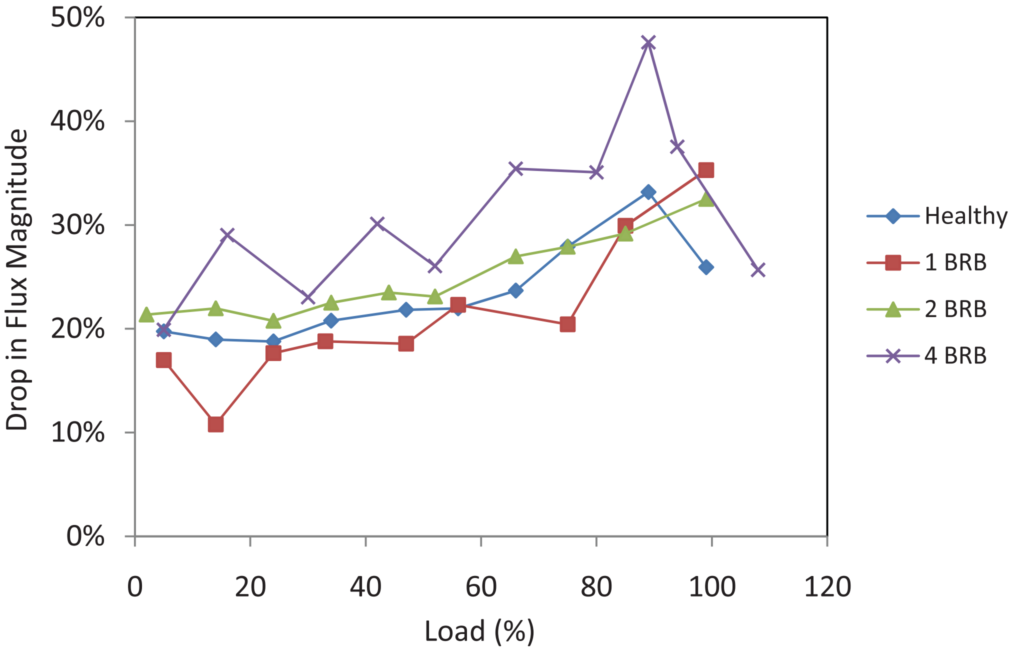

Figure 8.15 – Step change in the stator magnetic flux linkage at the instant of supply disconnection under different loading conditions.

8.5. Analysis of Rundown Broken Rotor Bar Features Using Space Vector of Stator Flux Linkage

This section investigates the broken rotor bar features obtained from the space vector of the stator flux linkage signal during motor rundown operation. The space (Park's) vector of the instantaneous stator flux-linkage is calculated by combining the three phases of the stator flux linkage using the transformation shown in (Eq. 8.2) and (Eq. 8.3) [68]. This space vector transformation can be utilised to determine the time constant of the decay of the flux linkage by monitoring the magnitude of the space vector over a period of time. In addition, the space vector of the flux linkage combines the information from all three phases of the flux linkage signal. Therefore the harmonic components in the space vector of the flux linkage should be more susceptible to broken rotor bar faults than the harmonic components in the single phase flux linkage signal.

$$\lambda_d(t) = \frac{\sqrt{2}}{\sqrt{3}}\lambda_a(t) - \frac{1}{\sqrt{6}}\lambda_b(t) - \frac{1}{\sqrt{6}}\lambda_c(t) \qquad \text{(Eq. 8.2)}$$

$$\lambda_q(t) = \frac{1}{\sqrt{2}}\lambda_b(t) - \frac{1}{\sqrt{2}}\lambda_c(t) \qquad \text{(Eq. 8.3)}$$

The locus of the space vector of the flux-linkage for the healthy and faulty machines (Figure 8.13 and Figure 8.14) at full load are given in Figure 8.16 and Figure 8.17. In the loci, the steady-state operation prior to disconnection is shown as the outer circle while the decay in the magnitude after disconnection is shown as a regular decaying spiral, and the disconnection transient joins the two.

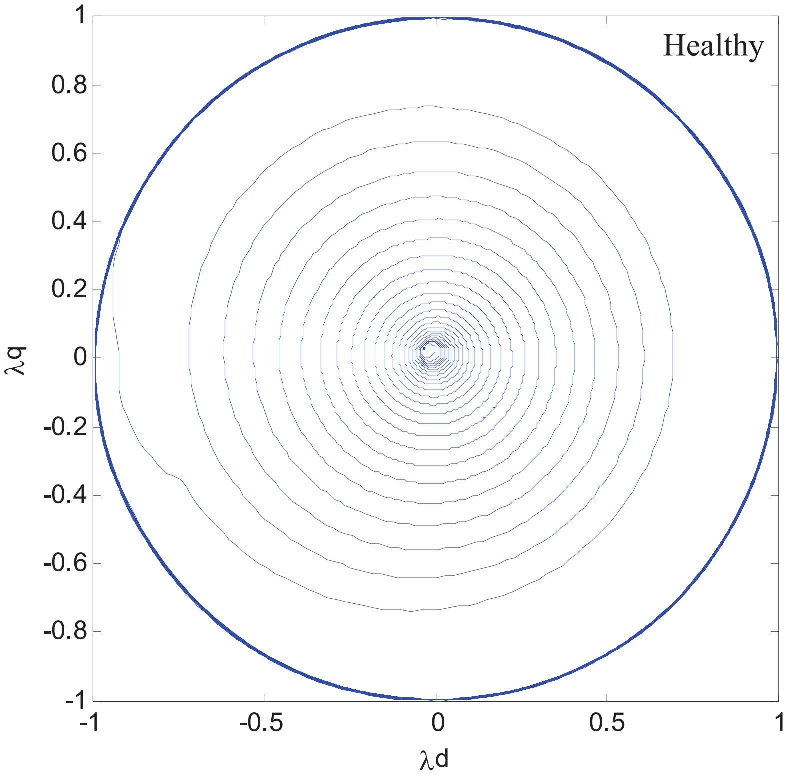

Figure 8.16 - Locus of the space vector of the stator flux-linkage for the healthy motor running at full load.

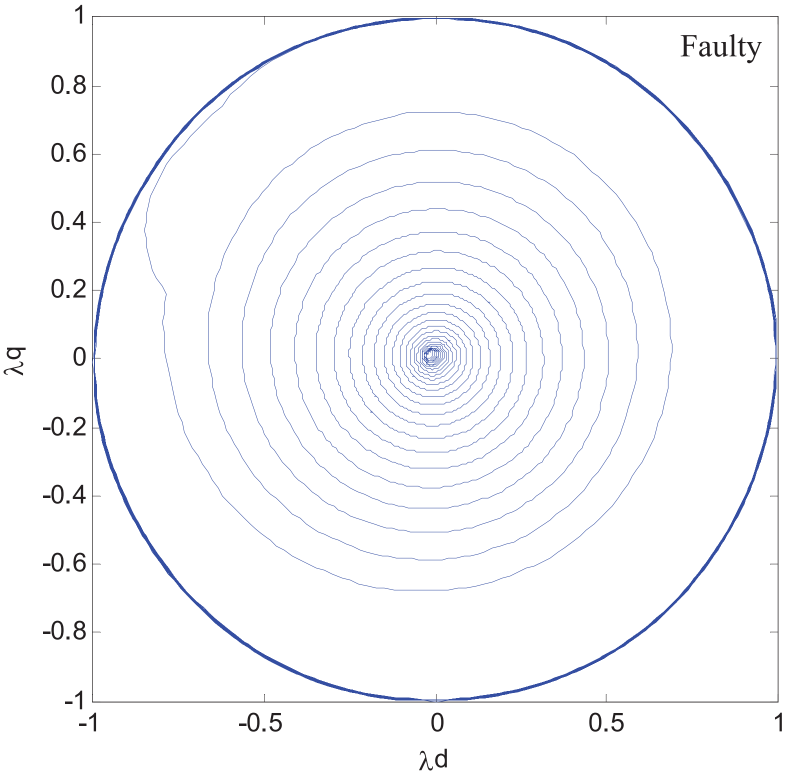

Figure 8.17 - Locus of the space vector of the stator flux-linkage for the faulty motor with 4 BRB running at full load.

8.5.1. Time Constant of Stator Magnetic Flux Linkage

From the locus of the space vector shown in Figure 8.16 and Figure 8.17, the space vector magnitude versus time can be plotted, as shown in Figure 8.18, for both the healthy and faulty motors when operating at full load. The figure shows the expected exponential decay for the two motors. Using curve-fitting techniques it is possible to estimate the time constant of the decay of the stator flux-linkage. This corresponds to the rotor winding time constant and forms the feature which will be investigated here. It is expected that the rate of decay of the rotor magnetic flux linkage is proportional to the effective rotor resistance and hence related to the severity of broken rotor bar faults. This proposition is supported in Figure 8.18 which shows that the space vector magnitude of the faulty motor decays at a faster rate than the space vector magnitude of the healthy motor. Note that the final space vector magnitudes in Figure 8.18 do not reach exactly zero due to the inability to remove DC offsets completely.

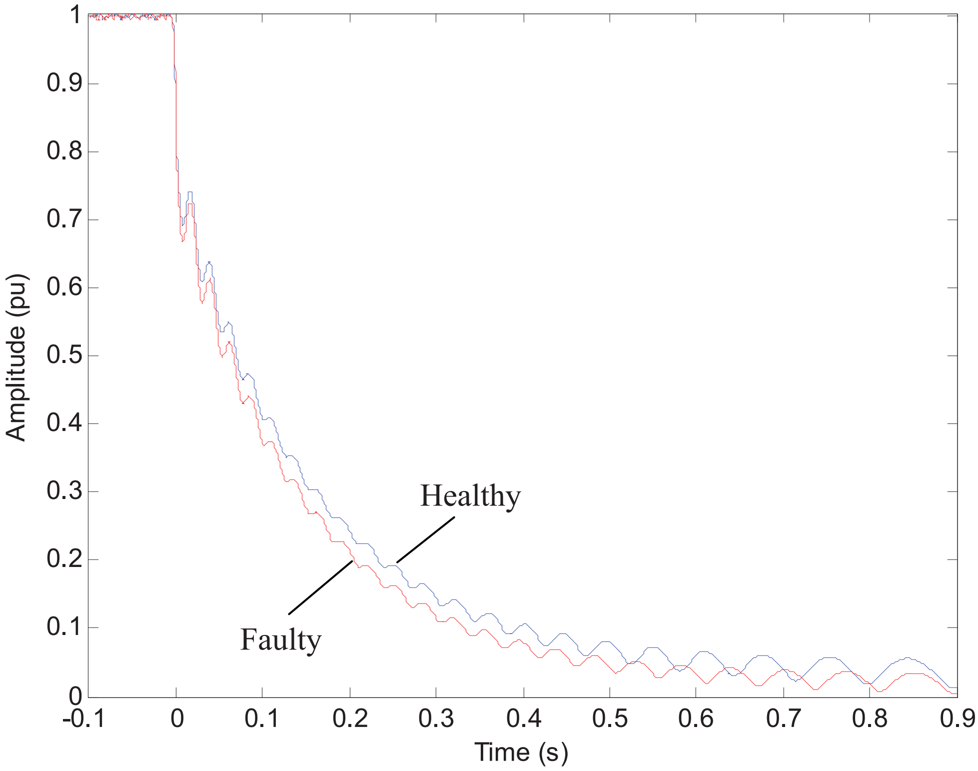

Figure 8.18 – Flux linkage space vector magnitude of the healthy and faulty with 4BRB motors running at full load.

8.5.1.1. Analysis of Results

The time constant of the magnetic flux linkage decay is expected to decrease as the severity of the broken rotor bar fault increases. This is because a BRB fault increases the effective rotor resistance and the decay rate depends on the rotor resistance.

Figure 8.19 shows that the time constant remains relatively steady under all loading conditions. This shows that the rate of decay of the flux linkage is nearly independent of the loading conditions, which is to be expected as the flux linkage is not affected by the rotor speed. In addition, Figure 8.19 also shows that the time constant tends to be smaller in the faulty motors than the healthy motor, especially when the motor load is greater than 60%. However, the time constant only starts to decrease when there are 2 or more broken rotor bars present in the motor. As a consequence, the time constant is not considered to be a good broken rotor bar feature.

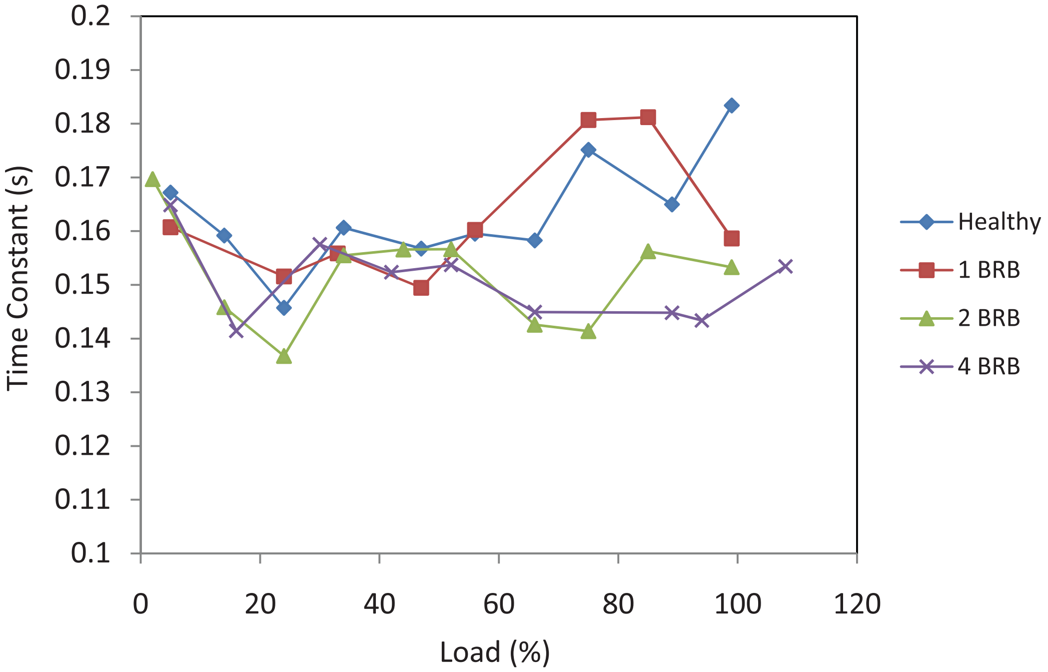

Figure 8.19 - Time constant of the stator magnetic flux linkage after supply disconnection under different loading conditions.

8.5.2. Harmonic Components

As in the case of the induced back-emf voltage, the presence of broken rotor bar faults is expected to introduce harmonic components in the stator magnetic flux linkage. These harmonic components, taking into account all three phases, will appear as spatially periodic disturbances in the magnitude of the flux linkage space vector.

These harmonics can be identified by applying the Fourier transform (FT) on the magnitude of the space vector shown in Figure 8.18. However, the magnitude of the space vector after disconnection is a transient signal, which has both a changing magnitude and a changing fundamental frequency, while the FT assumes steady-state operation. A similar solution as used when analysing the induced back-emf of a single phase (see *section 8.3.1*) can also be utilised here. The solution is to apply the FT to the first five fundamental cycles after disconnection in order to reduce the amplitude and frequency changes over the analysis period. This method is effective at light loads but it was found that if the motor load is high, the larger frequency change causes the signal peaks to broaden and make the spectra harder to interpret.

This poor frequency resolution at high loads can be minimised by normalising the magnitude of the space vector and performing a spatial FT (i.e. order tracking) analysis on the space vector. The magnitude is normalised by multiplying the signal by the inverse of the exponential decay function which was estimated from Figure 8.18. The spatial FT analysis is the process of re-sampling the space vector of the flux linkage such that each cycle of the space vector contains exactly the same number of samples separated by a fixed spatial (angular) interval rather than a fixed time interval. Effectively this is the same as synchronously re-sampling the flux-linkage with constant rotor position intervals. The FT of the resultant signal should show the harmonics of the fundamental more clearly.

8.5.2.1. Analysis of Results

For a harmonic component in the rundown space vector magnitude of a stator magnetic flux linkage to be considered as a broken rotor bar feature, it must be detectable in the faulty motor signal and it must show a consistent magnitude variation between healthy and faulty motors under different loading conditions. Figure 8.20 and Figure 8.21, which display typical power spectra of the space vector magnitude of the rundown flux linkage, show that the 18th harmonic (highlighted) is a strong harmonic in the motor signal. As a result, this thesis will monitor this harmonic component to see if it shows consistent magnitude variation between healthy and faulty motors under different loading conditions.

As in the case of the harmonic components in the back-emf voltage (*section 8.3.1*), the width of the harmonic peaks vary with the load. The width of the peak is found to increase with increasing load, which results in poor frequency resolution at heavier loads. In order to minimise this poor frequency resolution problem, the spatial FT technique (*section 8.5.2*) is utilised. The results of applying the spatial FT technique on the space vector spectra in Figure 8.20 and Figure 8.21 are shown in Figure 8.22 and Figure 8.23.

Figure 8.22 and Figure 8.23 show that the spatial FT technique has managed to reduce the poor frequency resolution problem, where the width of the 18th harmonic (highlighted) is now about the same, irrespective of the loading condition. These results suggest that the spatial FT technique allows the detection of the harmonic component with greater accuracy. However, the spatial FT technique involves interpolation of the input signal, which may introduce other signal components that are not originally present in the signal. Unfortunately the side effect of the spatial FT technique is strongly present in the harmonic spectra in Figure 8.22 and Figure 8.23. The side effect causes the 18th harmonic to have a lower SNR and may no longer be the most dominant component of the space vector harmonics. These interpolation errors are significantly worse for the spatial FT technique than the order tracking FT technique. This is because the order tracking FT technique only needs to interpolate one signal, while the spatial FT involves interpolation of three signals, which are the three phases of the flux linkage. The feasibility of using the spatial FT technique for detecting the harmonic component will be discussed later.

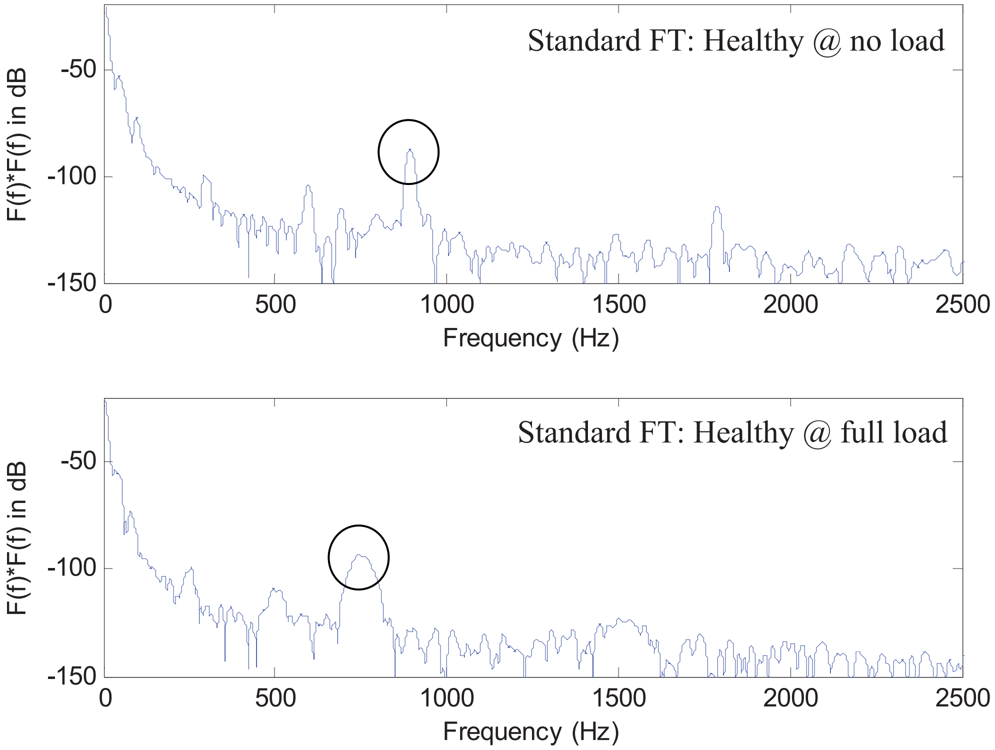

Figure 8.20 - Harmonic spectra of the space vector magnitude of the healthy motor running at no load (top) and full load (bottom) using the standard FT.

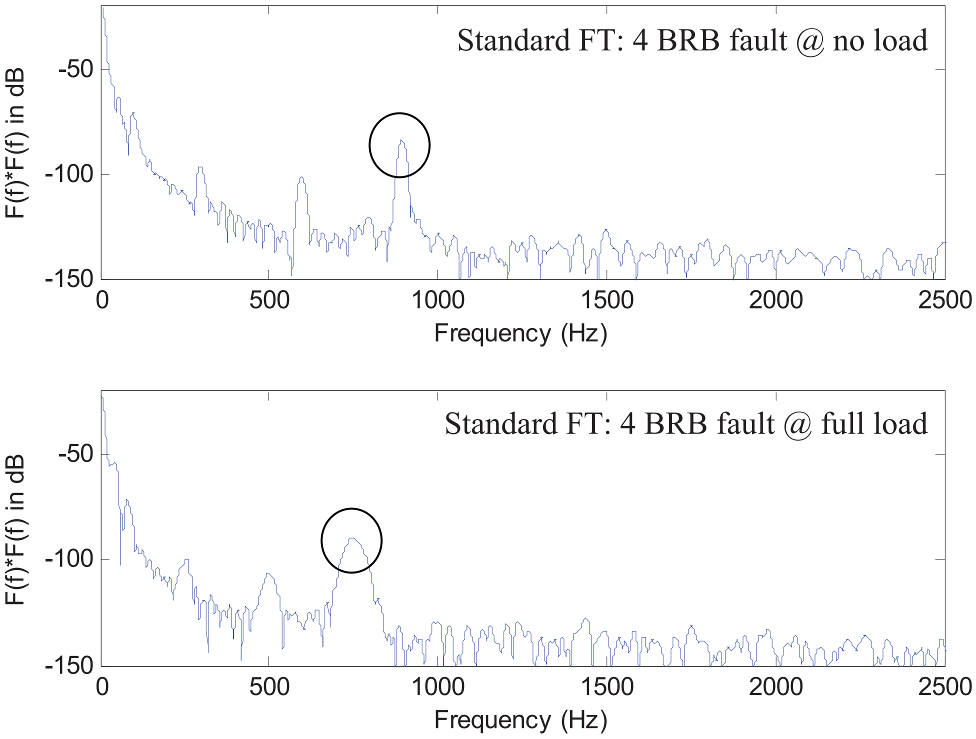

Figure 8.21 - Harmonic spectra of the space vector magnitude of the faulty motor with 4 BRB running at no load (top) and full load (bottom) using the standard FT.

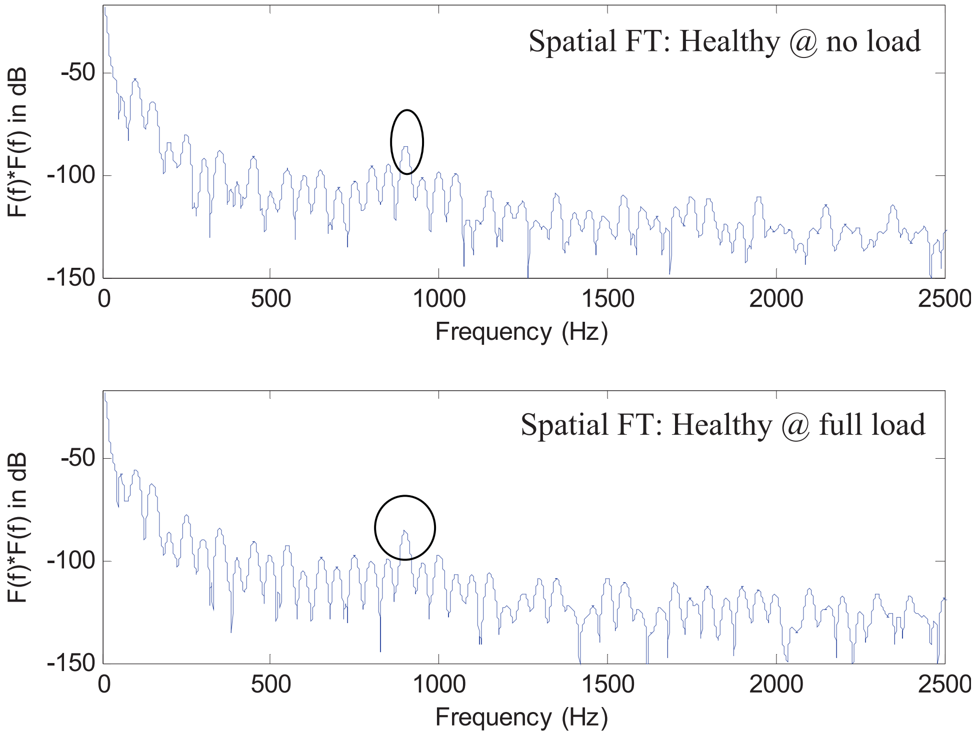

Figure 8.22 - Harmonic spectra of the space vector magnitude of the healthy motor as in Figure 8.20 using the spatial FT.

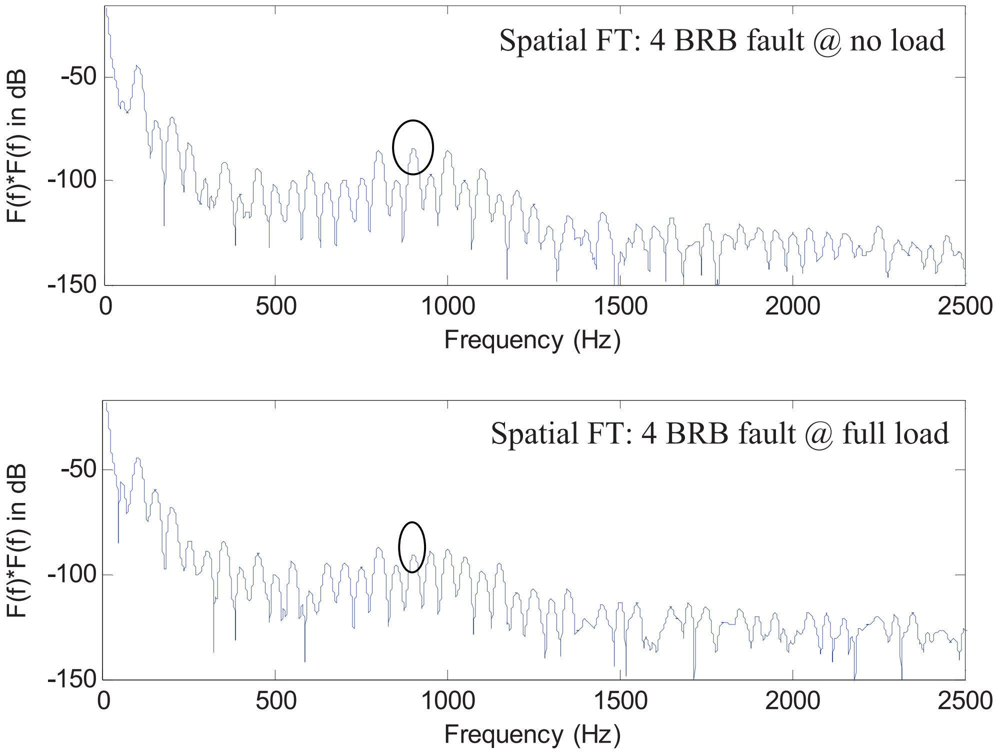

Figure 8.23 - Harmonic spectra of the space vector magnitude of the faulty motor with 4 BRB as in Figure 8.21 using the spatial FT.

Standard FT Results

Figure 8.24 shows the magnitude of the 18th harmonic component using the standard FT technique under different loading conditions. The magnitude of this component tends to decrease with increasing load (i.e. the magnitude drops by about 5 dB from no load to full load). This is because an increase in loading means an increase in the harmonic frequency change, which causes a poorer frequency resolution and hence a lesser measurement accuracy.

Figure 8.24 also shows that the magnitude of the harmonic tends to be higher in the faulty motors than in the healthy motor. However, the magnitude doesn’t necessarily increase proportionally with the fault severity. For example, it is found that the faulty motor with 1 BRB has the strongest magnitude (i.e. about 7 dB higher than the healthy motor), while the faulty motor with 4 BRB has the weakest magnitude among the faulty motors (i.e. less than 3 dB higher than the healthy motor). Hence, this detection method cannot be used to distinguish the different levels of BRB faults and it still needs more experimental data from different motors to make a conclusion about its ability to detect broken rotor bar faults.

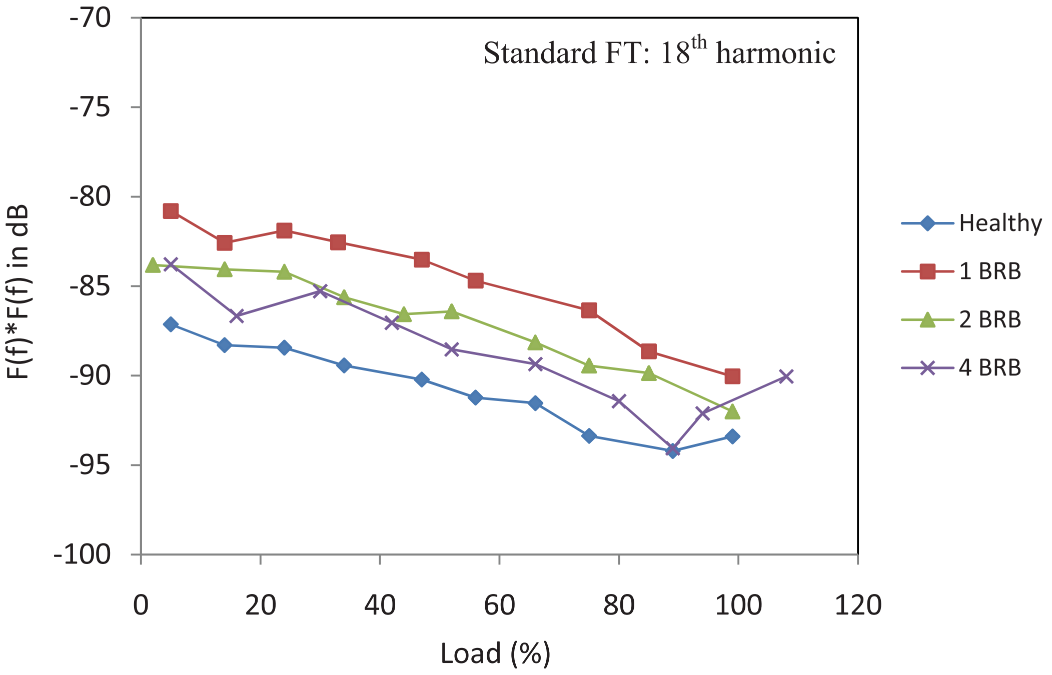

Figure 8.24 - Magnitude of the 18th harmonic from the standard FT under different loading conditions.

Spatial FT Results

Figure 8.25 shows the magnitude of the 18th harmonic using the spatial FT technique under different loading conditions. The figure shows that the harmonic magnitude generally shows a smaller reduction with increasing load, which highlights the benefit of the synchronous sampling approach. That is, an increase in loading does not translate to a poorer frequency resolution and a lesser measurement accuracy.

As in the standard FT results, the results from the spatial FT technique (Figure 8.25) show that the magnitude tends to be higher in the faulty motors than in the healthy motor, except for the faulty motor with 4 BRB. Note that the anomaly with the results from the 4 BRB motor is due to the interpolation errors of the spatial FT technique. Therefore, it is recommended to utilise the standard FT technique when analysing the harmonic components in the space vector magnitude of the rundown flux linkage.

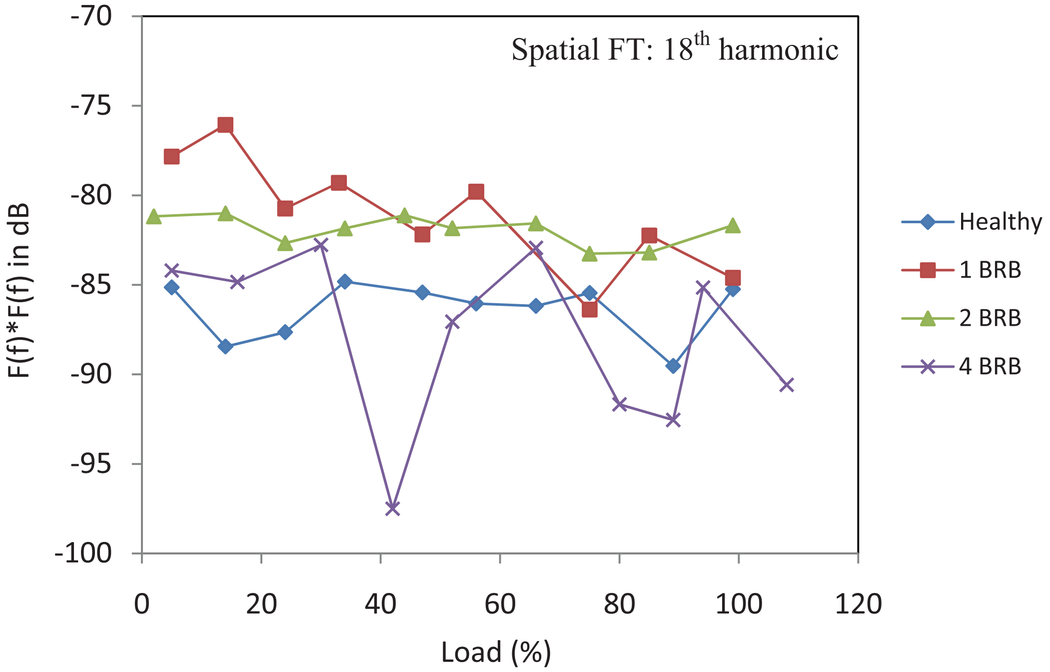

Figure 8.25 - Magnitude of the 18th harmonic from the spatial FT under different loading conditions.

8.6. Summary

This chapter investigated the use of the induced back-emf voltages and the stator magnetic flux linkages during motor rundown operation in order to detect broken rotor bar faults under different loading conditions. Five possible broken rotor bar fault detection features based on the rundown induced voltage, the flux linkage, and the space vector of the flux linkage were considered. These features include the harmonic components in the induced voltage, the rate of decay of rotor speed, the step change of flux linkage on disconnection, the time constant of flux linkage, and the harmonic component in the flux linkage. The analysis of the features were performed based on comprehensive experimental data under four different broken rotor bar fault severities and ten different loading conditions.

The harmonic components in the induced voltage and in the space vector of the flux linkage are found to be affected by broken rotor bar faults, especially the 13th and 17th harmonics in the induced voltage and the 18th harmonic in the flux linkage. The magnitudes of these three harmonics show an increase between the healthy and the faulty motors and they are consistent under different loading conditions. However, the magnitudes do not show a consistent variation pattern with increasing fault severities. Therefore, further experimental data from different size motors are required in order to make a reliable conclusion. It should also be noted that the order tracking FT technique presented here improves the detection of the harmonic components in the rundown induced voltage signal. However, the detection of the harmonic components in the flux linkage using the spatial FT technique is slightly worse than using the standard FT technique.

The broken rotor bar feature that is based on the rate of the decay of the rotor speed for a given slip is found to be the best feature in this investigation. The principle of the method is that broken rotor bar faults reduce the motor output torque for a given slip and hence reduce the change in the rotor speed over a period of time for the same slip. This change in the rotor speed is measured by utilising a new wavelet approach. This fault detection technique can potentially be used to detect different numbers of broken rotor bars, especially when the motor is operating at higher load (>20%). The technique however does have some limitations when applied to practical systems. It requires tests be carried out with the motor in the healthy state to develop a baseline response and is also sensitive to changes in load, system inertia, rotor temperature, and supply voltage.

The other two broken rotor bar features from the flux linkage; the step change of flux linkage on disconnection and the time constant of flux linkage, cannot be considered as good broken rotor bar features. This is because the feature based on the step change on disconnection only starts to become useful when there are four broken rotor bars in the motor, while the feature based on the time constant is useful when the motor has two or more broken rotor bars and the motor load is greater than 60%.

Chapter 9. Thesis Summary and Recommendation for Future Work

9.1. Introduction

Steady-state fault detection techniques for stator and rotor faults have been investigated extensively in the literature. However, previous studies mainly concentrated on a single fault type, using a single fault indicator (eg. a specific fault frequency component), using only one type of sensor signal (eg. a stator current signal), and under a limited range of loading and fault severity conditions. Therefore, the effects of load on the fault features have not been studied and no correlation has been made regarding the load levels and the fault severities that can be detected reliably by the fault features.

This thesis has examined a number of approaches to address the above issues in on-line condition monitoring of induction motors. In particular, the thesis has investigated: (a) techniques for estimating the rotor speed and the number of rotor bars, (b) a baseline study of induction motors, and (c) fault detection techniques for various stator and rotor faults, which include shorted turn faults, eccentricity faults, and broken rotor bar faults.

One of the major contributions of this thesis includes the performance comparison of various stator and rotor fault detection techniques under a wide range of loading and fault severity conditions in order to identify the most relevant features in detecting a particular fault. The thesis identified the relevant features, compared them against the results of the baseline study, and analysed the effects of loads. These processes were important to obtain a clear conclusion about the fault severities and the loads for which the features can be used reliably for detecting the faults. In addition, the thesis expands this idea further by examining how these relevant fault features behave under the presence of common faults, such as supply imbalance and misalignment.

Another significant contribution of this thesis includes an investigation of methods for combining the relevant fault features in order to improve the detection of particular faults. In addition, the thesis presents new techniques for detecting rotor faults during the transient operation of the motor (starting and rundown) to overcome the limitations of steady-state fault detection techniques.

9.2. Summary of Work

9.2.1. Experimental Setup

The experimental test setup and procedures utilised in this thesis were considered to be reliable and repeatable. The repeatability of the measurements results was ensured by installing the test motors using a torque spanner and a precision laser alignment tool. All movable parts of the test motors were also marked so that the motors could be disassembled and re-assembled with precision in order to ensure the repeatability and the consistency of the sensor signal measurements. In addition, some of the test motors included custom designed sections to be able to introduce a particular stator or rotor fault with various severities in isolation of other faults. These included shorted turn fault setup and eccentricity fault setup.

In the thesis, real data were collected from four different sensor signal types: the stator current sensors, the stator voltage sensors, the axial leakage flux sensor, and the motor vibration sensors. Each sensor signal was sampled at two different sampling rates; 400 Hz and 8 kHz, so that all relevant fault frequency components were captured. The sensor signal measurements of a test motor were usually performed under a wide range of fault severities and a wide range of loading conditions.

9.2.2. Rotor Speed Estimation

The rotor speed information in condition monitoring is necessary to estimate the load of a motor and to determine the fault frequency components that can be used for detecting stator and rotor faults. Chapter 3 of the thesis investigated the use of stator current, axial leakage flux and motor vibration signals in order to estimate the rotor speed accurately. The rotor speed was estimated by utilising (a) the eccentricity harmonics in the stator current and in the leakage flux signals, (b) the slip frequency in the leakage flux signal, and (c) the rotor frequency in the vibration signals. A comparison of these four rotor speed estimation techniques were presented in the thesis. It was found that the speed estimation technique based on the slip frequency in the axial leakage flux signal was not accurate for the loads less than 14%. On the other hand, the other techniques demonstrated accurate speed measurements even when the load was as low as 2%. The accuracy of the rotor speed detection in all four techniques was found to be less than 0.1% of the measured speed (using an optical tachometer), which was within the tachometer tolerance.

Signal to noise ratio (SNR) analysis of the four speed estimation techniques revealed that:

- the techniques based on the eccentricity harmonics were better at light loads as the SNR tended to reduce with increasing load. However, the techniques continued to maintain an acceptable SNR under all loading conditions,
- the technique based on the rotor frequency in the vibration signal showed good SNR under all loading conditions, and
- the technique based on the slip frequency failed at very light loads but showed good SNR at medium to higher loads.

9.2.3. Rotor Slot Number Estimation

Besides investigating the rotor speed estimation techniques, Chapter 3 also investigated techniques to estimate the number of rotor bars as it is required for determining the fault frequency components that can be used for detecting stator and rotor faults. Rotor slot number estimation techniques usually require data at several loading conditions or require a significant number of mathematical operations and iterations (i.e. computationally expensive). Therefore, this study proposed three simple and effective rotor slot number estimation techniques using the stator current, the axial leakage flux, and the motor vibration signals at a single operating point. The stator current and the leakage flux based estimation techniques utilised the first eccentricity harmonics, $Rf_r + f$, in the corresponding sensor signals. The experimental results showed that these techniques successfully identified the number of rotor slots on the healthy motor under all loading conditions. However, the SNR analysis of these techniques revealed that the technique from the current signal had a low SNR (less than 5 dB) when the load was less than 5% and the technique from the flux signal had a low SNR (less than 15 dB) at up to 25% load. However, both techniques showed good SNR at loads higher than the range mentioned above (about 45 dB for the current technique and about 25 dB for the flux technique). The vibration based rotor slot number estimation technique utilised the rotor slot passing frequency in the vibration signal. The experimental results showed that this technique failed when the load was less than 5% and it generally had lower SNR than the other two techniques (i.e. the SNR was about 20 dB).

The three rotor slot number estimation techniques were also tested against a faulty motor with 4 broken rotor bars. It was found that the broken rotor bar faults reduced the SNR of the three techniques by about 60% - 80%. In this case, the SNR averaged about 20 dB for the current technique, about 10 dB for the flux technique, and less than 5 dB for the vibration technique.

It was also shown that by combining the three techniques, the SNR can be increased dramatically by about 2 - 6 times in both the healthy and faulty motors. This approach allowed the accurate detection of the number of rotor slots regardless of the motor loads and the motor rotor bar condition.

9.2.4. Baseline Study

Chapter 4 described the baseline study of six identical healthy induction motors used in this research. The baseline study examined three main issues, which were the variation between current phases, the repeatability of the sensor measurements, and the variation between the identical motors, under different motor loading conditions. The baseline study investigated these three issues on the common stator and rotor fault frequency components, such as the broken rotor bar sidebands, the eccentricity fault frequencies, and the shorted turn fault frequencies. It was verified in the study that signal components at these fault frequencies exist even in healthy motors.

The baseline study demonstrated that most of the fault frequency components showed a good degree of repeatability between repeated measurements using the developed test setup. The magnitude variation of the frequency components among the repeated measurements was generally found to be less than 5 dB at a particular load. These findings suggested that trending of the fault features was possible. Similarly, the magnitude variation between the different current phases was found to be insignificant. These suggested that it was only necessary to examine one of the phases when investigating the fault frequency components in the stator current signals. On the other hand, most of the fault frequency components showed a significant degree of variability between the nominally identical healthy motors. The magnitude variation of the frequency components among the six healthy motors was likely to be between 10 - 15 dB at a particular load. These findings suggested that setting thresholds for the fault features in a given motor size would not be an easy task.

9.2.5. Shorted Turn Fault Detection

Chapter 5 investigated the performance of various shorted turn features from the stator current signals, the axial leakage flux signal, and the motor vibration signals in detecting both turn to turn and phase to phase turn faults under a comprehensive range of loading conditions (ten different loads) and fault severities (five different fault severities). The shorted turn features that were examined consisted of the fundamental sidebands of the rotor frequency harmonics, the twice supply frequency components, the rotor slot harmonics, the third harmonic of the fundamental, and the extended Park's vector approach (EPVA).

It was verified by the experimental results that the most suitable features in detecting the turn to turn faults were the fundamental sidebands of the rotor frequency harmonics with k(the integer variable) = 1 and v(the order of the stator time harmonics) = ±1, ±3 in the leakage flux signal and the extended Park's vector approach (EPVA) feature. In the test motor, the sideband components were found to vary (decrease) by about 5 - 15 dB between the healthy condition and the 7.1% fault (20 shorted turns), and the EPVA feature was found to vary (increase) by about 10 - 25 dB between the healthy condition and the 7.1% fault. Analysing these features against the results from the baseline study revealed that the EPVA feature was the best turn to turn fault feature because it can detect the faults under the most loading and fault severity conditions. It was found that the EPVA feature can detect turn to turn faults with a severity of 3.5% (10 shorted turns) or greater and at a load of 20% or greater.

Similarly, the experimental results showed that the most suitable features in detecting phase to phase turn faults were found to be the fundamental sidebands of the rotor frequency harmonics with $k = 1$ and $v = -1, +3$ in the leakage flux signal, the rotor slot harmonics with n_d(the integer variable) = 0, $k = 1$, $v = +1$ in the leakage flux signal, and the EPVA feature. These features were generally found to vary by about 10 - 20 dB between the healthy and the 7.1% fault. Analysing these features against the results from the baseline study revealed that the EPVA feature was the best phase to phase turn fault feature because it can detect the faults under the most loading and fault severity conditions. It was found that the EPVA feature can detect phase to phase turn faults with a severity of 1.7% (5 shorted turns) or greater under the entire loading conditions of the motor.

The analysis of the experimental results also suggested that estimating the severity of both turn to turn and phase to phase turn faults was difficult. This was because the magnitude of the shorted turn features did not show significant variation between one level of fault severity to the next.

9.2.6. Static Eccentricity Fault Detection

Chapter 6 compared the performance of various eccentricity features in the stator current signals, the axial leakage flux signal, and the motor vibration signals under a wide range of loading conditions (ten different loads) and fault severities (nine different fault severities). The eccentricity features examined consisted of the rotor slot harmonics, the rotor frequency sidebands of the fundamental, the rotor frequency sidebands of the twice fundamental, the third harmonic of the rotor frequency, the twice supply frequency components, the rotor frequency components, the second harmonic of the rotor frequency sidebands of the fundamental, and the RMS vibration value.

The experimental results showed that the better static eccentricity features were found to be the rotor slot harmonics with $n_d = 0$, $k = 1$, $v = \pm 1$ in the leakage flux signal, the rotor slot harmonic with $n_d = 1$, $k = 1$, $v = +1$ in the current signal, and the RMS vibration value. However, most of these features only varied by about 5 dB from the healthy condition to the 50% fault and the features were also found to be sensitive to the loading conditions. For example, the rotor slot harmonics with $n_d = 1$, $k = 1$, $v = +1$ in the current signal were found to be useful only when the load was greater than 25%. In order to improve the fault detection, the work in this chapter combined the better features by considering the loading conditions in which the features were considered useful. The results of combining the features were found to be very promising, where the technique (named WLC in this thesis) can detect static eccentricity faults at a load of between 15% and 25% with a fault severity of 50% or greater and at a load of greater than 25% with a fault severity of 25% or greater. The WLC technique generally showed magnitude variations of about 10 - 15 dB between the healthy condition and the 50% fault under most tested loading conditions. These findings showed that detecting eccentricity faults was possible. However, estimating the fault severity was found to be difficult. This was due to the fact that the magnitude difference of the WLC technique between one level of fault severity to the next was less than 5 dB.

The chapter also investigated the effects of mixing misalignment faults with static eccentricity faults, upon the misalignment features and the better eccentricity features. It was found that the third harmonic of the rotor frequency showed higher magnitude variation when both misalignment and eccentricity faults were present than if only the eccentricity faults were present. The magnitude variation of the third harmonic between the healthy and the 50% mixed faults was generally found to be about 15 dB. This demonstrated that the third harmonic of the rotor frequency can be considered as a good misalignment feature. Although, the presence of misalignment faults together with eccentricity faults was also found to slightly reduce the effectiveness of the eccentricity features in detecting eccentricity faults, the problem can be reduced by utilising the WLC technique.

It should also be noted that the features based on the rotor slot harmonics and the features based on the rotor frequency sidebands of the fundamental are good indicators for both eccentricity faults and shorted turn faults. Therefore, it is not possible to differentiate between the two types of faults just by analysing the common frequency components. However, if there is a fault feature that is only sensitive to one type of the faults (either eccentricity faults or shorted turn faults), then it is possible to distinguish between the two faults. For example, if the extended Park's vector approach (EPVA) feature, which is known to be sensitive to shorted turn faults, were not affected by eccentricity faults, then it could be utilised to distinguish between eccentricity and shorted turn faults. This may be investigated in future studies.

9.2.7. Broken Rotor Bar Fault Detection

Broken rotor bar (BRB) faults are usually detected by using steady-state condition monitoring techniques such as monitoring the magnitude of the BRB sidebands. However, these steady-state condition monitoring techniques are unreliable at light loads and they depend on the quality of the supply. In order to overcome these problems, Chapter 7 and Chapter 8 proposed new approaches in detecting broken rotor bar faults by utilising sensor signals during the transient operation (i.e. starting and rundown) of the induction motor.

Chapter 7 introduced a new approach to detect BRB faults that utilised the wavelet transform of the envelope of the starting current waveform. The advantage of using the starting current was that the starting current is usually much higher than the running current and hence rotor faults should be more evident in the starting current than the steady-state current. In the proposed method, the envelope of the starting current signal was extracted in order to remove the fundamental component in the signal that may interfere with the detection of BRB characteristics. The results of the wavelet transform were then processed in order to develop a normalised numerical parameter, called wavelet indicator. This was the feature used in the study for detecting broken rotor bar faults.

The experimental results presented in Chapter 7 showed that the wavelet indicator was sensitive to the broken rotor bar faults, where it increased as the severity of the fault increased. It was found that, at all tested loads, the increase was about 15 dB from the healthy to the 1 BRB faulty condition and about a further 10 dB increase with the 4 BRB fault. These findings showed that the wavelet indicator can be reliably used to detect any number of fully broken rotor bars under all loading conditions.

The wavelet indicator was also tested for possible variations under repeated measurements, among nominally identical motors, between different current phases, and in the presence of an unbalanced three phase supply. It was concluded from the experimental results that the proposed technique was not sensitive to the above changes under all tested loading conditions, which proved its reliability.

The analysis of the results in this thesis showed that detecting broken rotor bar faults was easier than detecting shorted turn faults or eccentricity faults. This was because the BRB fault feature showed greater magnitude variation between different fault severities than the shorted turn fault features or the eccentricity fault features. In addition, the BRB feature was found to be useful under all loading conditions, while the shorted turn or the eccentricity features were not.

Chapter 8 proposed several BRB fault detection techniques, which utilised the induced voltage in the stator windings after supply disconnection. These techniques were considered in an attempt to remove the effects of the AC supply when detecting BRB faults. The principle idea behind this approach is that when the AC supply is disconnected, the only source of the induced voltage in the stator windings is due to the rotor currents, which can be distorted by BRB faults.

The induced voltage is produced as a result of the rate of change of the stator magnetic flux linkage. Therefore, the flux linkage, which can be obtained by integrating the induced voltage, can also be used as a means to detect BRB faults. The advantage of using the flux linkage over the induced voltage is that it is independent of the rotor speed. Since the decay of the rotor speed with time during motor rundown operation is proportional to the motor load, the decay of the flux linkage amplitude with time is also independent of the loading condition.

The BRB investigation in Chapter 8 examined two features from the rundown induced voltage; the harmonic content and the change in the motor output torque for a given value of slip, and three features from the stator flux linkage and its space vector components; the step change on disconnection, the rate of decay with time, and its spatially correlated harmonic content. The experimental results showed that the harmonic components in both the induced voltage signal and the space vector of the flux linkage signals were affected by BRB faults, especially the 13th and the 17th harmonics in the induced voltage signal and the 18th harmonic in the flux linkage signal. The magnitude of these harmonics showed an increase between the healthy and the faulty motors. However, they did not consistently increase with increasing fault severities. Thus, further investigation is required to make a conclusion about the reliability of these harmonics to detect BRB faults.

The results of analysing the proposed wavelet approach for measuring the change in the motor output torque for a given value of slip were found to be promising, especially for the motor loads greater than 20%. The wavelet technique showed about 36% magnitude variation between the healthy and the 4 BRB conditions at full load. In addition, the technique also showed a consistent trend where the magnitude decreased as the severity of the fault increased. Therefore, the wavelet approach can be considered as a good method to detect any number of fully broken rotor bars when the load is greater than 20%.

The experimental results showed that the other two features from the flux linkage signals; the step change on disconnection and the time constant of the flux linkage decay rate, were also affected by broken rotor bar faults. However, they were not considered as good features because the feature based on the step change on disconnection was not found to be effective below the 4 BRB fault and the feature based on the time constant was found to be useful only when the motor had two or more broken rotor bars with a motor load of 60% or greater.

A comparison between the results from the starting current based broken rotor feature and the results from the rundown broken rotor bar features shows that both the starting and rundown features can be used to detect different numbers of broken rotor bars in a motor, including a motor with 1 BRB. However, detecting broken rotor bar faults during motor starting operation is easier and more reliable than during motor rundown operation. This is because the starting current based broken rotor bar feature shows a greater magnitude variation between healthy and faulty motors than the rundown broken rotor bar features. In addition, the starting broken rotor feature can be used under a wider range of loading conditions. Therefore, it is recommended to utilise the starting broken rotor bar feature whenever possible and to utilise the rundown broken rotor bar features to complement other broken rotor bar features.

It should be noted here that fault detection during motor transient operation can be used when a motor is in maintenance, a new motor is being tested during production, or a motor is turned off/on during day to day operation.

This thesis has provided comprehensive research work on the baseline study of the induction motors and on the detection of the stator and rotor faults under a comprehensive range of loading conditions and fault severities. It is foreseen that this research in conjunction with suitable data mining and fault classification techniques can be utilised to develop an advanced on-line condition monitoring system. However, it is believed that further research, which is discussed in the following section, may be required before this aim can be realised.

9.3. Future Work

The baseline study in this thesis provided comparisons of how the fault frequency components vary between the different current phases, between the repeated measurements, and between the identical induction motors. The study can be expanded further by investigating how the fault frequency components vary between induction motors of different power ratings. Analysing the fault frequency (feature) variations between motors of different ratings would allow a deeper understanding on how trending and thresholds can be set for each feature. In turn, this would allow a generalisation of a complete condition monitoring system which works not only for a particular rating of induction motors but also for motors of different ratings. This investigation can be undertaken if there is access to a variety of induction motors with different power ratings.

The study on the shorted turn faults and the eccentricity faults in this thesis compared the common steady-state condition monitoring techniques, gave recommendations as to which feature worked best, and then combined these better features in order to improve the overall effectiveness of the fault detection. However, the techniques examined were only for the motor steady-state operation. It may be of interest to investigate other techniques which utilise the starting current or the rundown induced voltage. The starting current has the advantage that it is less sensitive to motor loadings. On the other hand, the rundown induced voltage has the advantage of being independent of the quality of the supply. Both starting current and rundown induced voltage can be analysed using transient signal processing techniques, such as the short-time Fourier transform and the wavelet transform, because they can extract both time and frequency information of a signal.

The study on the broken rotor bar faults in this thesis proposed new techniques in detecting the broken rotor bar faults during motor transient operation (starting and rundown). It may also be useful to verify that these techniques are valuable not only for the tested motors but also for other motors with different power ratings. In addition, it may also be useful to extend the existing fault detection techniques such that they can also be used to estimate the location of the broken rotor bars. This may be achieved by considering the space vector of sensor signals. If each cycle of the space vector contains irregular patterns at consistent locations, these locations could theoretically be correlated to the actual locations of the broken rotor bars.

The study on the detection of the stator and rotor faults in this thesis was performed without the presence of the other stator and rotor faults. For example, the investigation on eccentricity faults was performed without the presence of shorted turn or broken rotor bar faults. This investigation can be expanded by introducing multiple stator and rotor fault types into a motor. The introduction of multiple faults in a motor will lead to new studies, such as investigating the effects of multiple faults on the useful stator and rotor fault features, investigating how the different fault types in the motor can be identified, and investigating how the fault severity of the different fault types can be estimated.